EMARC

ELECTRONIC MATERIALS APPLIED RESEARCH CENTER

Microporous and Thin Film Membranes for Solid Oxide Fuel Cells

Final Technical Report

Harlan U. Anderson

February, 2007

DE-FC36-01GO11084
Energy Efficiency Science Initiative

(Electronic Materials Applied Research Center) EMARC
University of Missouri-Rolla
Rolla, MO 65401
Email: harlanua@umr.edu

University of Colorado-Boulder
Department of Mechanical Engineering
427 UCB
Boulder, CO 80309-0427

Lawrence Berkeley National Laboratory
62-203
1 Cyclotron Road
Berkeley, CA 94720

National Renewable Energy Laboratory
1617 Cole Boulevard
Go9lden, CO 80401-3393

Aker Industries
952 57th Street
Oakland, CA 94608

UMROLLA

MICROPOROUS AND THIN FILM MEMBRANES
FOR SOLID OXIDE FUEL CELLS

Final Technical Report

TABLE OF CONTENTS

1.0: Status of Program

1) Executive Summary

One of the major limitations to the commercialization of solid oxide fuel cells is the expense of fabricating the required (anode/electrolyte/cathode) cells (currently planar or tubular). The current technology being employed by most of the producers of solid oxide fuel cells is essentially all the same in that it involves standard ceramic processing to make composite structures (either electrolyte or electrode supported). Each investigator/program has their own individual processing steps to produce the cells, but in the end, they all make these cells in a very similar manner. As a result only limited progress has been made towards cost reductions over the last 2-3 decades. It is our contention that major changes in the processing of cells need to be made before SOFCs can become economically feasible.

Over a decade ago, Aker Industries (AI) demonstrated that it was possible to imbibe metal salts into cellulose (paper, paper products, cardboard, etc) and subsequently pyrolize the resulting composites at relatively low temperatures, <1000 C, to form both microporous and dense structures which replicated the original paper structures. These results are very significant in the fact that they suggest that it might be possible to fabricate the cells needed for SOFCs by using the well established technology of the paper industry. If this is possible, then it may be the vehicle to allow the manufacturing cost of SOFCs to be significantly decreased.

The overall objective of this program was to expand the work of AI to: 1) learn how to synthesis both dense and porous cellulose films using cellulose polymer and/or cellulose derivatives; 2) develop the protocol to imbibe these films with metal salts to yield organic/inorganic hybrid (OIH) structures which can be pyrolized to form oxide replicas of themselves; 3) investigate the possibility of producing the trilayer (cathode/electrolyte/anode or PEN) SOFC structures and 4) demonstrate the innovative technology by fabricating a SOFC.

This program required a joint effort of a five-member team comprising the University of Missouri-Rolla (UMR), the Lawrence Berkeley National Laboratory (LBNL), the National Renewable Energy Laboratory (NREL), the University of Colorado-Boulder (UCB) and Aker Industries (AI). Each team member played a key role in the program: 1) NREL and UCB synthesized dense and porous cellulose films and developed the protocol for imbibing salts into the films; 2) UMR, UCB and NREL studied the pyrolysis of the OIH structures to form oxide films; 3) LBNL, UMR and AI focused on characterizing and producing the PEN structures and using them to produce SOFCs; and 4) UMR lead the program, developed cathode and anode compositions and studied alternate ways of preparing the PEN structures.

The results of the program were mixed so that not all of the goals were met:

Successes:

- NREL/UCB successfully synthesized dense and porous cellulose films from both Catcel-5 and Rayonier cellulose and were able to imbibe metal salts into the resulting films.

- NREL/UCB/UMR demonstrated that the imbibed films could be pyrolized to produce nanocrystalline zirconium oxide structures which were replicas of the imbibed films.
- UMR developed both cathode and anode electrode materials which could be used with the cellulose film technology.
- UMR demonstrated an alternate technology to prepare the required PEN structures.
- AI/UMR developed a glass system which can provide the glass seals and electrical isolation which is required by the SOFC structure.
- LBL/UMR demonstrated that Ebrite alloy could be coated by LaZnCrO3 and be used as the interconnect for the proposed SOFC system.
- Over 39 publications resulted from the program.

Failures:

- AI was unable to develop the equipment which would allow the conversion of the imbibed cellulose to the oxide replicas. As a result, we were not able to produce oxide films which were flat enough for use in PEN and SOFC structures.
- Due to the lack of success in producing flat membranes, we were unable to demonstrate a SOFC using imbibed cellulose technology.

The overall objective of the program was to demonstrate that imbibed metal salt cellulose technology is a viable candidate for the low cost production of SOFCs. Even though we were unable to complete this demonstration because of the inability to produce sufficiently flat oxide membranes to assemble a cell, the successes in producing both cellulose and nanocrystalline zirconia films suggests that exploiting "paper technology" can be utilized to produce SOFC structures.

2.0: Accomplishments/Goals/Objectives

- Showed that cellulose polymer (Catcel-5 and Rayonier) can be use do produce both dense and porous films
- Showed that both dense and porous nanocrystallineYSZ films can be made from the pyrolisis of metal salt imbibed cellulose film.
- Showed that IC (Ebrite stainless alloy) can be protected by perovskite film
- Showed that SOFCs can be made by thin film technique
- Developed cathode and anode materials which are compatible with cellulose technology
- Developed glass seal
- Produced 39 publications

3.0: Overview of Project

One of the major limitations to the commercialization of solid oxide fuel cells is the expense of fabricating the required (anode/electrolyte/cathode) cells (currently planar or tubular). The current technology being employed by most of the producers of solid oxide fuel cells is essentially all the same in that it involves standard ceramic processing to make composite structures (either electrolyte or electrode supported). Each investigator/program has their own

individual processing steps to produce the cells, but in the end, they all make these cells in a very similar manner. As a result only limited progress has been made towards cost reductions over the last 2-3 decades. It is our contention that major changes in the processing of cells need to be made before SOFCs can become economically feasible.

Over a decade ago, Aker Industries (AI) demonstrated that it was possible to imbibe metal salts into cellulose (paper, paper products, cardboard, etc) and subsequently pyrolize the resulting composites at relatively low temperatures, <1000 C, to form both microporous and dense structures which replicated the original paper structures. These results are very significant in the fact that they suggest that it might be possible to fabricate the cells needed for SOFCs by using the well established technology of the paper industry. If this is possible, then it may be the vehicle to allow the manufacturing cost of SOFCs to be significantly decreased.

The overall objective of this program was to expand the work of AI to: 1) learn how to synthesis both dense and porous cellulose films using cellulose polymer and/or cellulose derivatives; 2) develop the protocol to imbibe these films with metal salts to yield organic/inorganic hybrid (OIH) structures which can be pyrolized to form oxide replicas of themselves; 3) investigate the possibility of producing the trilayer (cathode/electrolyte/anode or PEN) SOFC structures and 4) demonstrate the innovative technology by fabricating a SOFC.

This program required a joint effort of a five-member team comprising the University of Missouri-Rolla (UMR), the Lawrence Berkeley National Laboratory (LBNL), the National Renewable Energy Laboratory (NREL), the University of Colorado-Boulder (UCB) and Aker Industries (AI). Each team member played a key role in the program: 1) NREL and UCB synthesized dense and porous cellulose films and developed the protocol for imbibing salts into the films ; 2) UMR, UCB and NREL studied the pyrolysis of the OIH structures to form oxide films; 3) LBNL, UMR and AI focused on characterizing and producing the PEN structures and using them to produce SOFCs; and 4) UMR lead the program, developed cathode and anode compositions and studied alternate ways of preparing the PEN structures.

The project was divided into four major tasks:

- Task # 1: Selection and Characterization of metal oxide compositions(UMR)
- Task # 2: Preparation and Characterization of Organic/Inorganic Hybrides (NREL, UCB)
- Task # 3: Preparation and Characterization of Interconnect (LBNL and AI)
- Task # 4: Preparation of Single Layers, Trilayers (PEN) and Stack Modules (AI)

Since each of these tasks is quite distinct from the others, each task will be discussed separately.

3.1) TASK #1 (UMR)

3.1.1) The Development and Selection of Electrode Compositions to be used in the Trilayers (PEN) Structures

3.1.1.1) Cathode Development

The cathode to be used in this program was developed using compositions and processing developed at UMR.

A composite consisting of (La, Sr)MnO_3 (LSM) -Y doped ZrO_2 (YSZ) was prepared by coating a YSZ colloidal suspension (initial YSZ particle size ~ 100 nm) and YSZ and LSM polymer precursors on dense substrates at 800^{o}C annealing temperature. The results of a symmetrical LSM-YSZ cell test showed that at 800^{o}C the for overpotential measured as the area specific resistance was found to be 0.14 Ωcm^2, which indicated that the composite LSM-YSZ might serve as a cathode in SOFCs. The performance of a cell using a 0.4 mm thick YSZ electrolyte with the composite LSM-YSZ and Ni-YSZ anode was investigated and the power density of about 0.26 Wcm^{-2} was obtained at 850^{o}C using hydrogen fuel.

Our group showed that a dense YSZ electrolyte could be prepared on porous substrates (anodes and/or cathodes) with processing temperatures as low as 400^{o}C using a combination of YSZ polymer precursor and YSZ colloidal particles (YSZ particle size ~ 100 nm). The process of this technique is as follows; first, a YSZ skeleton layer is prepared by the colloidal suspension, then the resulting porous layer is densified by filling it with the YSZ polymer precursor. This technique can be applied for the processing not only an electrolyte, but also electrodes by producing a porous composite consisting of suitable polymer precursors and controlling the concentration and size of oxide particles to be backfilled.

In this program, a new type of composite cathode has been prepared at temperatures <800^{o}C using (La, Sr)MnO_3 (LSM) polymer precursor and Y doped ZrO_2 (YSZ) colloidal suspension. The composite LSM-YSZ was examined as a cathode for SOFCs by making overpotential measurements using a symmetrical composite LSM-YSZ cell and as a fuel cell using a YSZ electrolyte and Ni/YSZ anode.

Experimental

A composite consisting of $La_{0.8}Sr_{0.2})_{0.9}MnO_3$ and Y doped ZrO_2 (LSM-YSZ) was prepared by coating YSZ colloidal particles (initial YSZ particle size ~ 100 nm) and LSM polymer precursor on to a dense YSZ substrate (0.4 mm thick). Commercially available YSZ powder (16% Y doped ZrO_2, Daiichiki Genso Co, Japan) was used for processing the required colloidal suspension. Figure 1 shows a scheme of the composite technology, which was used in this study. Preparation process is as follows;

(i) Preparation of the YSZ colloidal suspension
(ii) Preparation of the polymer precursors (YSZ and target cathode materials)
(iii) Coating the colloidal suspension onto the substrate to prepare a porous layer of YSZ.
(iv) Backfill the YSZ polymer precursor into the porous layer to provide adhesion of the YSZ particles to the substrate and each other.
(v) Backfill the LSM polymer precursor into the YSZ porous layer by spin coating several times. After each backfill, the resulting polymer coatings are converted to the oxide by heating to 380^{o}C to remove the hydrocarbons.
(vi) Annealing at 800^{o}C.

For the preparation of a symmetrical cell, the composite LSM-YSZ was prepared on both sides of a 0.4 mm thick YSZ substrate, which was used as an electrolyte. For preparation of a fuel cell, Ni-YSZ powder ink (Ni 45 wt%) was screen printed onto the YSZ substrate and sintered at 1400 ^{o}C for 1h. Then, the composite LSM -YSZ was prepared on the other side. The microstructures of the resulting cells were analyzed using a Hitachi S4700 Scanning Electron Microscope. Impedance spectroscopy techniques were utilized to investigate the performance of the composite LSM-YSZ symmetrical cell using a Solartron 1470 Battery Tester and a 1255B Impedance Gain Phase Analyzer with 4-probe configuration.

The fuel cell performance was evaluated in the double chamber configuration (Fig. 2) using forming gas (10 vol% H_2 in N_2) on the anode side and air on the cathode side. A mixture of Ag paste and YSZ powder was used as a current collector, which was applied to give electrode area of 0.28 cm^2.

Results and Discussion

Figure 3 shows an SEM image of the resulting 2 μm thick LSM-YSZ composite cathode. As can be seen, the LSM coated the YSZ particles very well. The porosity of the composite layer can be controlled by the number of applications of the polymer precursor and the oxide content of the polymer.

Figure 4 shows the electrical conductivity of the composite LSM-YSZ as a function of reciprocal temperature along with the conductivity of YSZ and LSM. Compared to the literature, the composite LSM-YSZ showed lower conductivity simply due to lower concentration of LSM in the composite. However, the composite LSM-YSZ does have sufficiently high conductivity to make it attractive for use as a cathode.

Figure 5 shows the impedance spectra of the symmetrical cell obtained in air at 700-800^{o}C. Two semi-circles were observed in the impedance spectra, which are typically interpreted as the charge transfer and gas diffusion process, namely R_2 and R_3, respectively (Fig. 5). High frequency resistance, R_1, corresponds to the resistance of the YSZ substrate.

Figure 6 shows the area specific resistance for the LSM-YSZ symmetrical cell determined from the impedance spectra in Fig. 5. The overpotential resistances are low compared to the electrolyte resistance, however the resistance due to the gas diffusion processes, R_3, was relatively large due to the dense structure of the composite LSM-YSZ. (This can be adjusted by changes in microstructure.) The total overpotential resistance for the LSM-YSZ composite cathode can be estimated to be 0.14Ωcm^2 at 800^{o}C and 0.3 Ωcm^2 at 700^{o}C for a single electrode.

Fuel cell performance of the composite LSM-YSZ (cathode)/ YSZ/ Ni-YSZ (anode) cell was investigated using a forming gas (10 vol% H_2 in N_2) (Fig.2). Figure 7 shows the discharge profile of the cell at the temperature range from 650 to 850^{o}C. The results showed that a maximum power density of about 0.26 Wcm^{-2} was obtained at a temperature of 850^{o}C with a current density of 0.65 Acm^{-2}. The impedance spectra for this cell are shown in Fig. 8. The spectra showed distorted semi circles with relatively higher high frequency resistance

corresponding to the thick YSZ electrolyte. The area specific resistances of the cell are shown in Fig. 9. The overpotential ASR of the cell was estimated to be 0.3 Ωcm^2 at 800^oC, which is the sum of the ASR for both the anode and cathode. The good correlation of the ASR obtained by the symmetrical cell and fuel cell measurements, suggests that the performance of the cell was mainly limited by the electrolyte resistance, which can be easily improved by reducing the thickness of an electrolyte. Further investigation is ongoing to improve the microstructure of the composite to decrease the overpotential from gas diffusion process, as well as searching for new materials for a cathode.

Summary

A composite of LSM-YSZ was prepared by combining YSZ colloidal particles (initial YSZ particle size ~ 100 nm) and, YSZ and LSM polymer precursor coatings. This composite technique allows the preparation of fuel cell components at temperatures < 800^oC, which makes it possible to use a variety of materials and cell configurations. The composite LSM-YSZ prepared under 800^oC showed sufficiently high conductivity to be useful as an electrode. The results of the symmetrical cell test showed that the area specific resistances (ASR) for overpotential were 0.14 and 0.3 Ωcm^2 at 800 and 700^oC, respectively, mainly due to the gas diffusion process.

The performance of the composite LSM-YSZ as a cathode for SOFC was investigated. It was obtained a maximum power density of about 0.26 W cm^{-2} at 850^oC using 0.4 mm thick YSZ electrolyte and Ni-YSZ as an anode, with the ASR for total overpotential was about as 0.17 Ωcm^2 at 850^oC.

Figure Caption

Figure 1: The schematic diagram of composite technique.
Figure 2: Fuel cell test configuration
Figure 3: SEM image of $(La_{0.8}Sr_{0.2})_{0.9}MnO_3$ -YSZ composite cathode
Figure 4: Electrical conductivity of the composite LSM-YSZ along with the conductivity of bulk YSZ and $La_{0.8}Sr_{0.2}MnO_{3-\delta}$
Figure 5: Impedance spectra of $(La_{0.8}Sr_{0.2})_{0.9}MnO_3$ -YSZ composite cathode (symmetrical double sided cell, electrode area = 0.28cm^2).
Figure 6: Area specific resistance of $(La_{0.8}Sr_{0.2})_{0.9}MnO_3$ -YSZ composite symmetrical cell
Figure 7: I-V discharge profile and I-P characterization for a cell with LSM compoiste chathode.
Figure 8: Impedance spectra for LSMcompoiste chathode cell.
Figure 9: Area specific resistance of $(La_{0.8}Sr_{0.2})_{0.9}MnO_3$ -YSZ composite cathode-YSZ-Ni-YSZ cell.

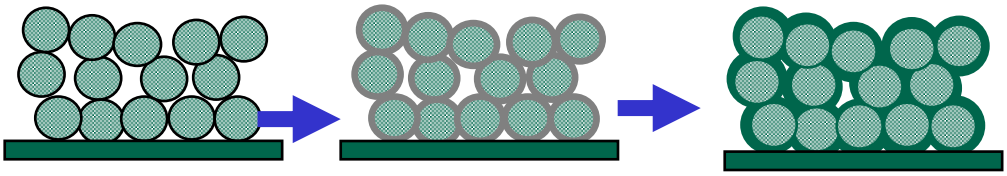

YSZ skeleton from YSZ slurry YSZ polymer precursor coating LSM polymer precursor coating

Figure 1

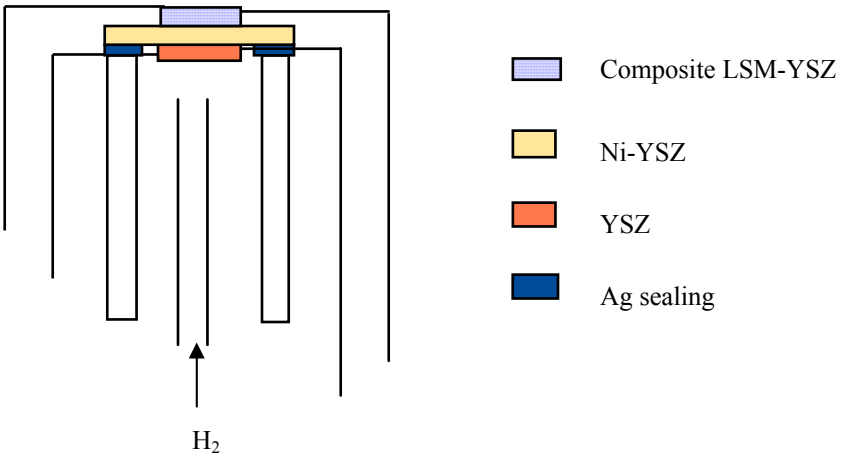

Figure 2

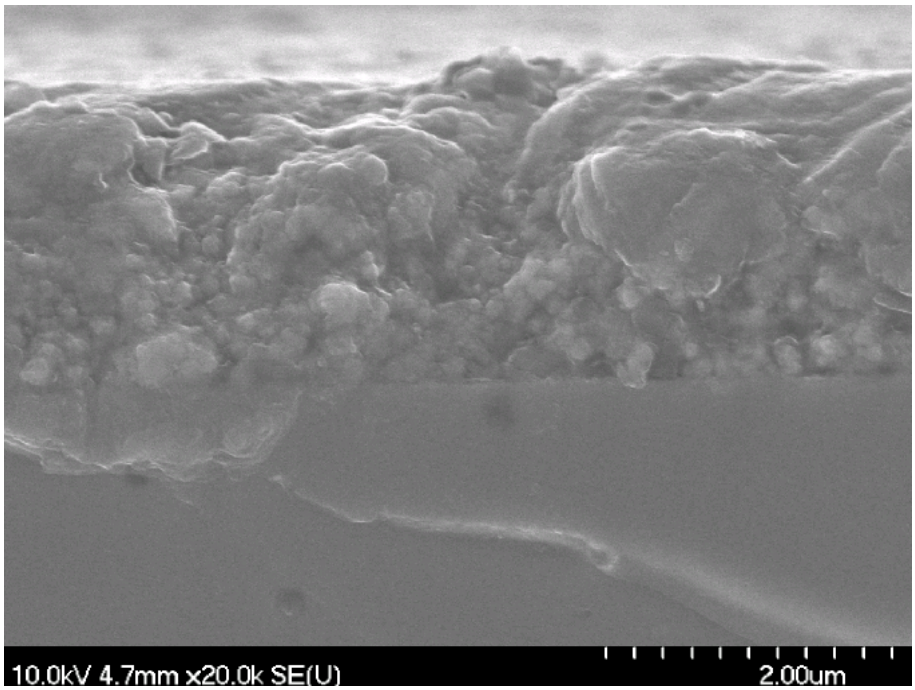

Figure 3

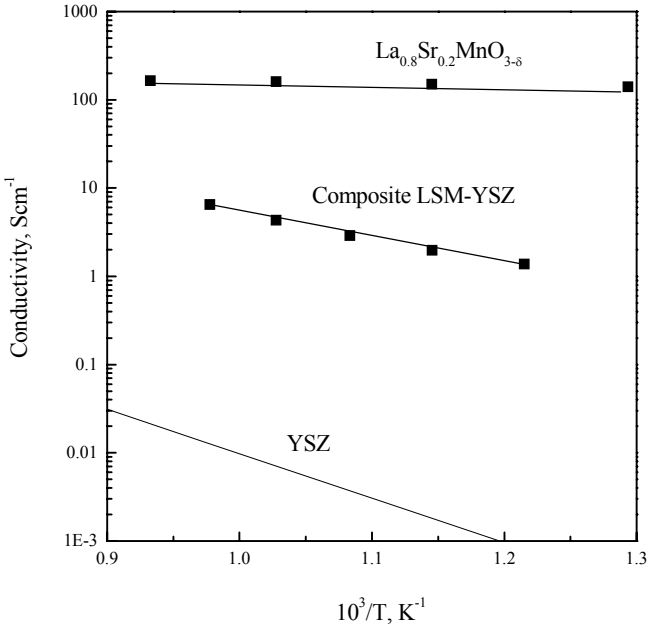

Figure 4

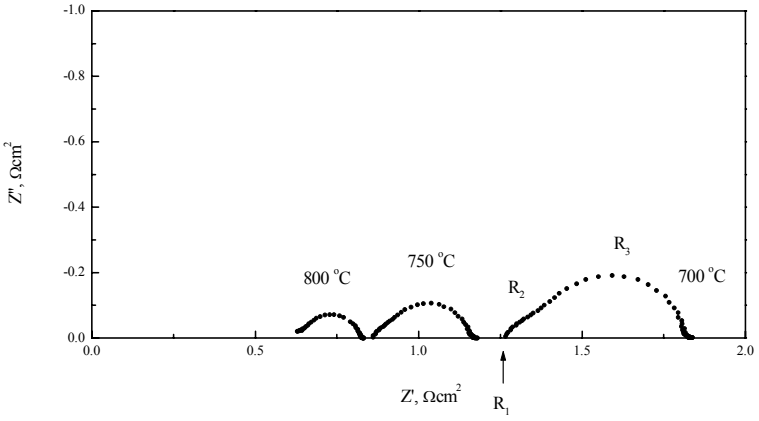

Figure 5

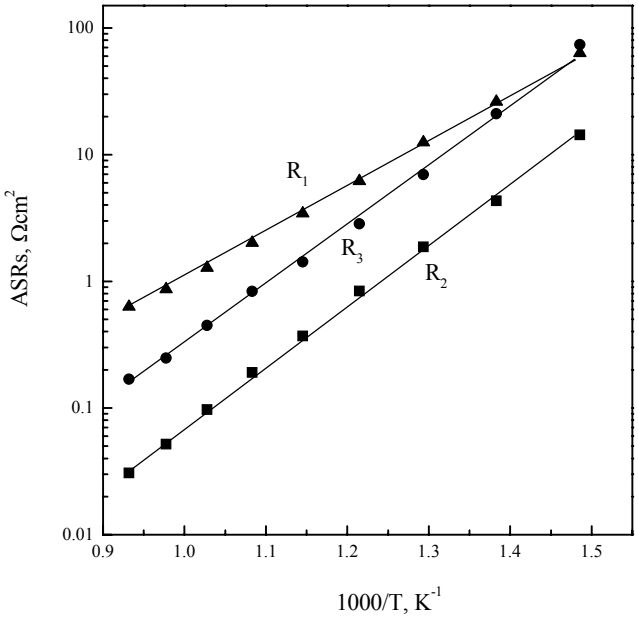

Figure 6

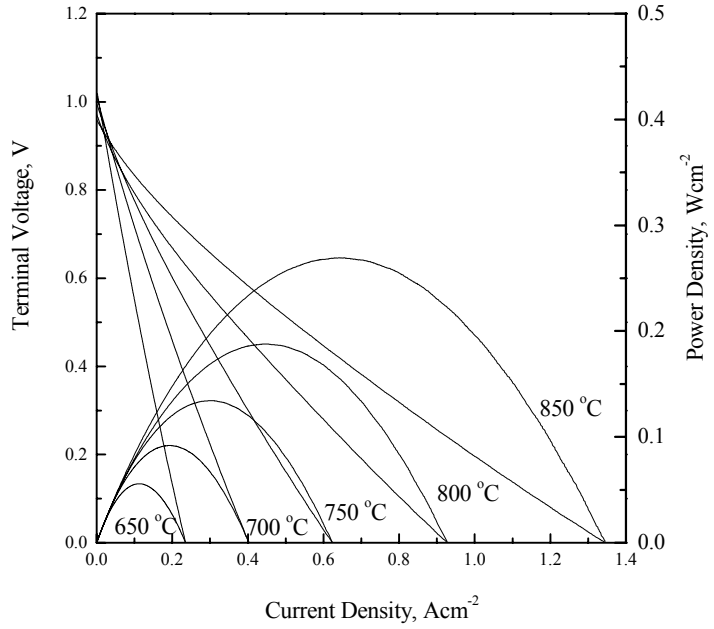

Figure 7

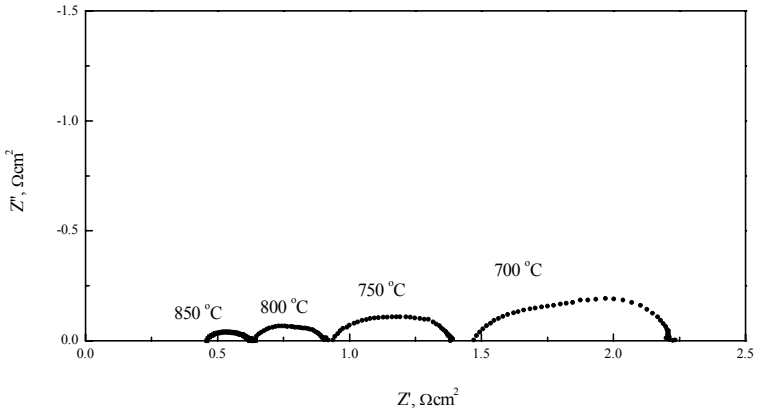

Figure 8

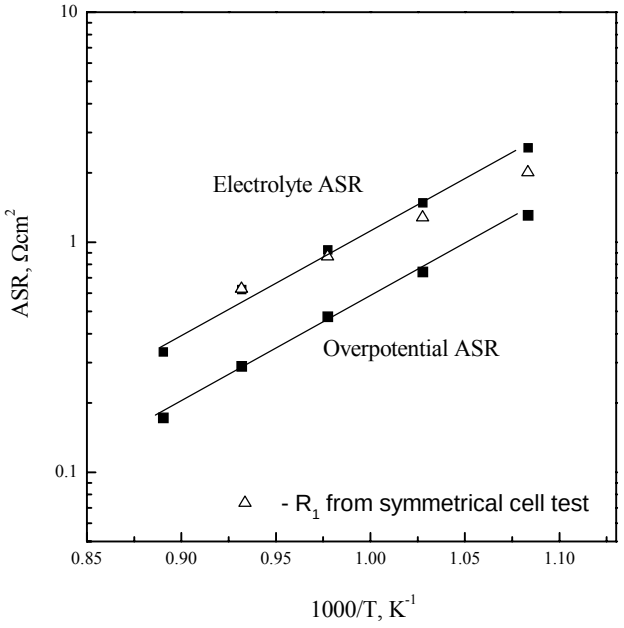

Figure 9

3.1.1.2) Anode Composition Development

A cermet composite Ni-Y doped ZrO_2 (YSZ) composite was prepared by depositing a 1-50 micometer thick coating of YSZ particles from a colloidal suspension (initial YSZ particle size ~ 100 nm) onto a sapphire substrate followed by impregnation by Ni polymer precursors into the coating and annealing at 800^{o}C. The electrical conductivity at 700^{o}C of the composite Ni-YSZ was found to be 0.1 Scm^{-1} in air and above 100 Scm^{-1} in reducing atmosphere. Redox cycle and life time testing showed stable performance and the conductivity at 800^{o}C was as high as 300 Scm^{-1} after 800 h operation in reducing atmosphere. These results suggest that the Ni-YSZ cermet composite is a viable candidate for use as an anode in the PEN structure.

A low temperature processed cermet Ni-YSZ composite was prepared using a polymer precursor technique which we have shown to be suitable for the preparation of oxides at temperature < 800^{o}C. Figure 1 shows a graphical schematic of the composite processing method which was used in this study.

The cermet Ni-Y doped ZrO_2 (YSZ) composite was prepared by: 1) depositing a 1-50 micron thick coating of YSZ colloidal particles (initial YSZ particle size ~ 100 nm) onto a dense substrate (sapphire). {Commercially available YSZ powder 16% Y doped ZrO_2, Daiichiki Genso Co, Japan was used for processing the colloidal suspension}; 2) backfilling the resulting porous YSZ coating with a Ni containing polymer precursor by spin coating for 30 times; 3) heating at 380 ^{o}C after each deposition to remove organic matter.; 4) annealing at 800^{o}C after completion of the depositions.

The microstructures of the resulting Ni-YSZ composites were analyzed using a Hitachi S4700 field emission gun (FEG). Figure 2 shows fracture surface SEM images of the composite Ni-YSZ on the sapphire substrate (a) before reduction of the Ni0 to Ni and (b) after reduction in 10% H_2 in N_2 gas at 700^{o}C (Ni-YSZ). Open channels were observed in the reduced specimen as shown in Fig. 2(b), which allows gas permeation through the electrode. As can be seen, the thickness of the composite Ni-YSZ was about 3 μm. Note that the thickness of the composite Ni-YSZ can be easily controlled up to 50 μm by multiple coating of the YSZ colloidal suspension.

The electrical conductivity of the composite Ni-YSZ was investigated using a Solartron 1470 Battery Tester with 4-probe configuration in the oxidizing (air) and in the reducing atmosphere (forming gas; 10% H_2 in N_2). Figure 3 shows the conductivity of the composite Ni-YSZ for an initially oxidized sample in the reducing atmosphere, and an initially reduced sample in the oxidizing atmosphere measured both in elevated temperatures. As can be seen, the transition temperature from NiO to Ni (or Ni to NiO) of the composite Ni-YSZ appeared to be about 350^{o}C. The conductivity of the cernet Ni-YSZ composite was above 100 S/cm in the reducing atmosphere for all the temperature range, showing that it is suitable to use as an SOFC anode.

Figure 4 shows oxidation and reduction cycle behavior of the composite Ni-YSZ at 700^{o}C. The sample was cycled through reducing and oxidizing atmospheres with a l h hold for each. The conductivities in both reducing and oxidizing atmospheres were stable after the third cycle.

Figure 5 shows the results of a life test at 800^{o}C in reducing atmosphere where the conductivity was monitored for over 800 h. As can be seen the conductivity decreased to about half of the initial value during the first 50 h. However, after 50 h, the rate of conductivity decrease stabilized at about 0.02%/h. After 350 h, the sample was exposed to the oxidizing atmosphere for 1 h and then, brought back into the reducing atmosphere several times. The arrows in Fig. 5 indicate when the oxidizing process took place. As can be seen, the conductivity in the reducing atmosphere increased after the oxidizing process to a value about 25% higher than it was prior to the life test and showed a decay rate of about 0.02%/h until the test was terminated at about 800 h. This reasons for this behavior is certainly not well understood.

Figure 6 shows X-ray diffraction patterns of Ni (111) for the composite Ni-YSZ, which was placed in the reducing atmosphere for 3 h and 800 h at 800^{o}C. It can be seen that after 800 h in the reducing atmosphere the intensity of Ni (111) peak increased. The grain size of the Ni crystallites was determined using the Scherrer equation. Despite the changes in the intensity, the calculated grain size of Ni crystallites in the two samples turned out to be about the same (70~80 nm). That is, there does not appear to be any significant grain growth of the Ni crystallites after 800 h operation in the reducing atmosphere. However, the increase in the intensity of the Ni(111) peak after 800 h exposure to reducing atmosphere does suggest that the concentration of Ni crystallites has increased. This suggests that a substantial quantity of the Ni was initially in the amorphous state and it crystallized to form stable Ni crystals in the 70-80 nm range.

In summary, the composite Ni-YSZ was successfully prepared by combining YSZ colloidal particles (initial YSZ particle size ~ 100 nm) and Ni polymer precursor coatings. This composite technique allows the preparation of fuel cell components at temperatures < 800^{o}C, which makes it possible to use a variety of materials and cell configurations. The results of conductivity measurement of the composite Ni-YSZ showed that stable electrical conductivity above 300 S cm^{-1} could be attained at 800^{o}C in the reducing atmosphere for periods of time over 800 h, as well as after a number of redox cycles. This indicates that the composite Ni-YSZ can be a potential candidate for an anode for SOFCs. Currently there is no explanation for the increase of the conductivity which was observed in the composite Ni-YSZ after several redox cycles. It does not appear to be due to Ni migration since the grain size is stable. This issue is under investigation and hopefully careful electron microscopy will reveal the solution.

Figure Caption

Figure 1: The schematic diagram of composite technique.
Figure 2: SEM images of composite Ni-YSZ (a) before reduction (b) after reduction using forming gas in 700 ^{o}C.
Figure 3: Electrical conductivity of the composite Ni-YSZ in the reducing and oxidizing atmosphere.
Figure 4: The results of the redox cycle test for the composite Ni-YSZ.
Figure 5: Life test for composite Ni-YSZ at 800 ^{o}C in the reducing atmosphere. Arrows indicate when the redox process was taken place.
Figure 6: X-ray diffraction pattern of Ni (111) for the composite anode, after 3 h and 800 h in the reducing atmosphere at 800 ^{o}C.

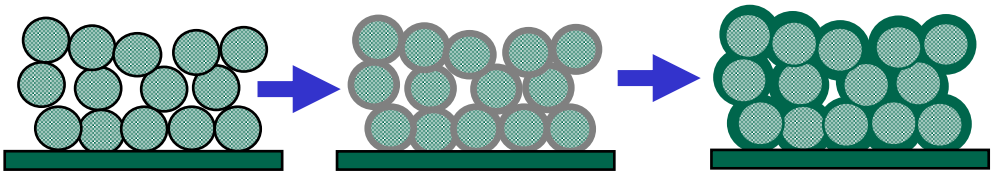

Figure 1

(a)

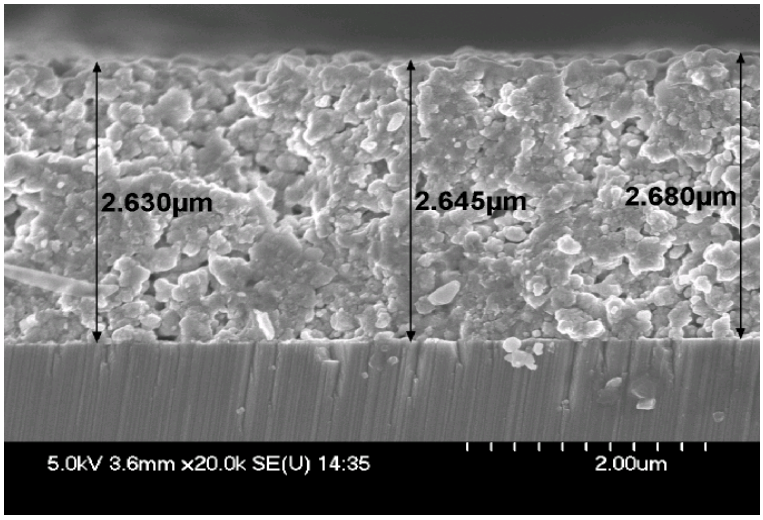

(b)

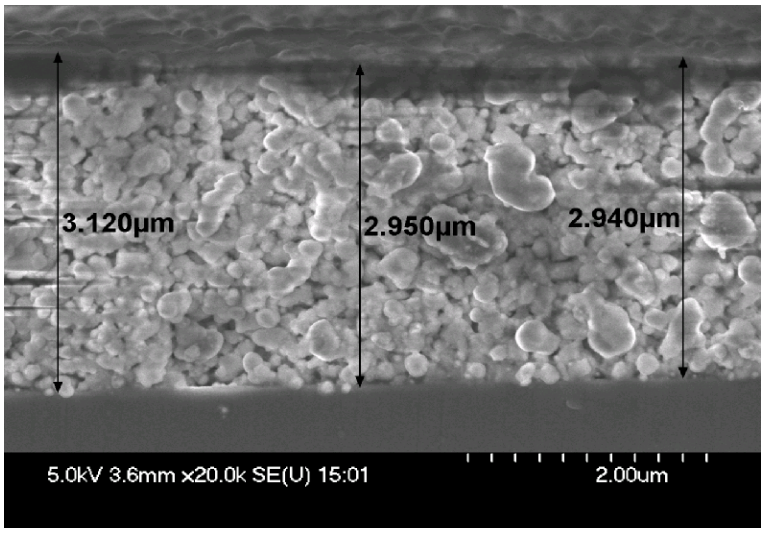

Figure 2

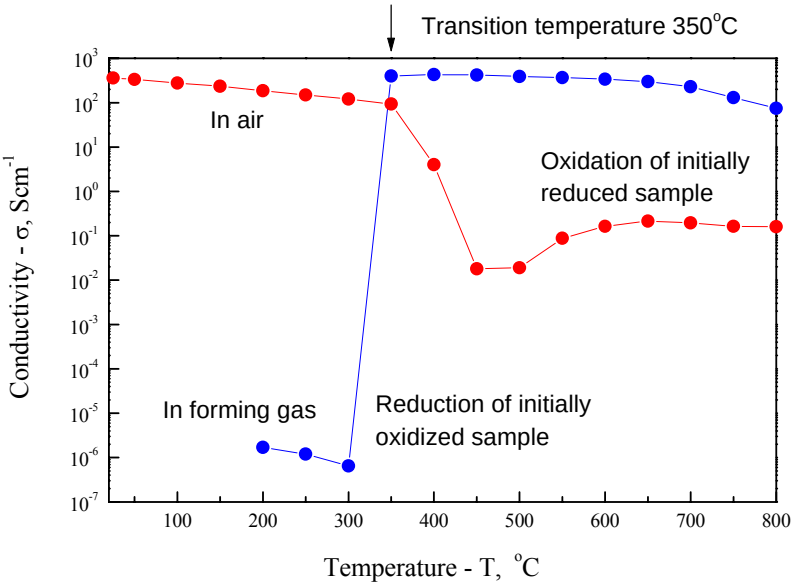

Figure 3

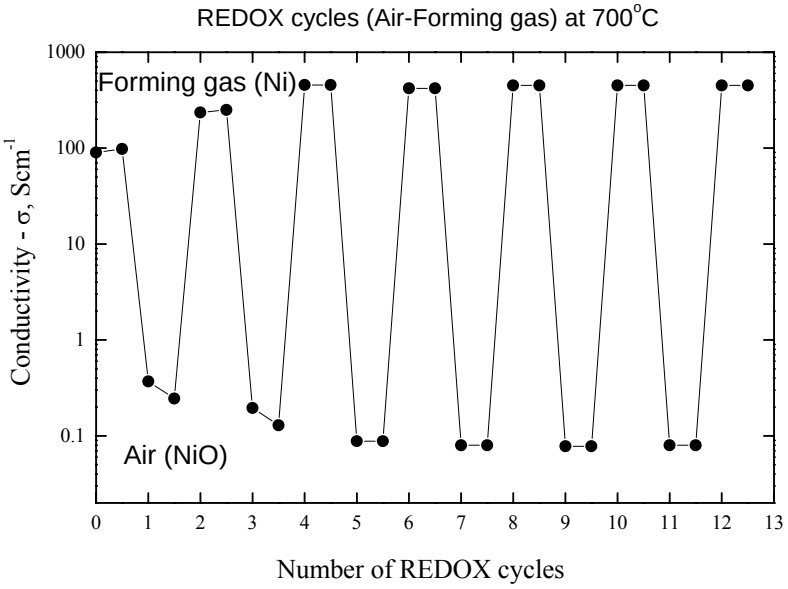

Figure 4

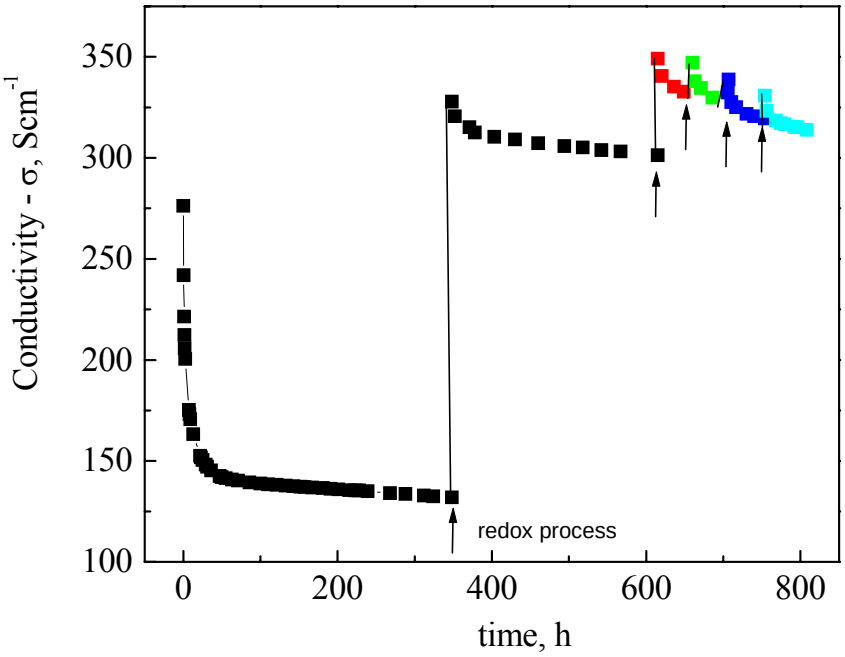

Figure 5

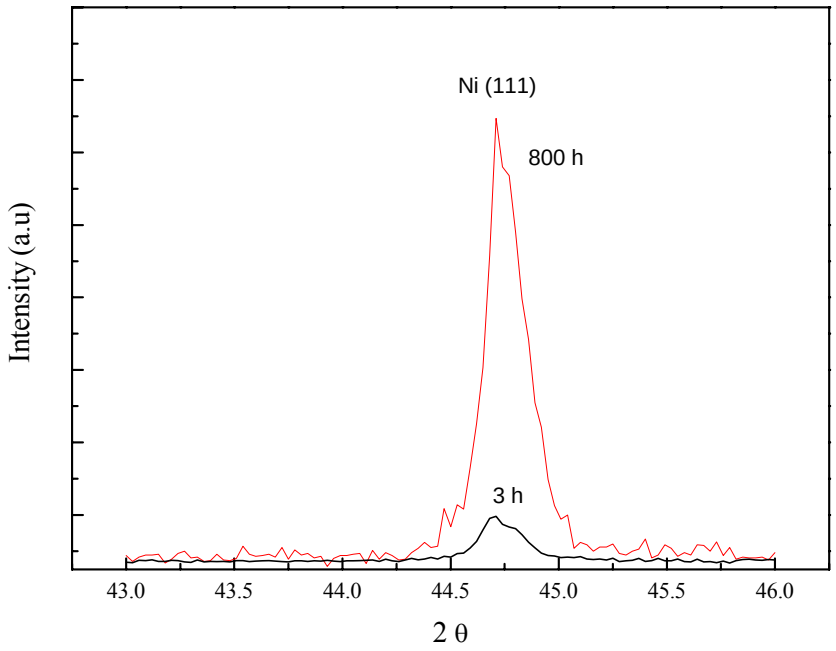

Figure 6

The cathode and anode compositions shown above are adequate for the PEN structure proposed in this program and were used to prepare single cells, However these compositions were never used in the cellulose derived PEN structures since such structures were never prepared due to the inability to make flat oxide structures.

3.1.2) Characterization of the Oxide Films Resulting from the OIH Composites

UMR was provided dense and microporous membranes (Rayonier or Catcel-5) (from NREL/UCB) imbibed with metal oxides and mixed oxides for pyrolysis and densification studies. For pyrolysis and densification, UMR dried the cellulose films and later annealed or sintered them at 600, 800 and 1000^{o}C. The heating and cooling processes were accomplished in a box furnace with heating and cooling rates of 3^{o}C/min and 2 hours of holding time at a designated temperature. After the sintering process, the cellulose films imbibed with $ZrOCl_2$ solution became zirconia films and the cellulose films imbibed with $YCl_3/ZrOCl_2$ solution became YSZ films. However, during the drying process the films are subjected to shrinkage and significant shape change occurs. The shape changes resulted in distortion with some of the films forming roll-like structures.

According to NREL (National Renewable Energy Laboratory) and UCB (University of Colorado, Boulder) the cellulose films were cast on glass plates. Therefore the side of the films which touched the glass surface was smoother than that exposed to evaporation (glossy vs. dull) – see Figure 1.

(a) (b)

Figure 1. Images from sample #2912-909-8 after drying in air at room temperature: (a) glossy surface (b) dull surface

During the drying and sintering processes, surface tension or compression mismatch between the two sides of the films seemed to cause the cellulose films to distort. This problem was discussed in the January 27th meeting at UMR and it was agreed that the problem eventually would be taken care of during the fabrication of multi-layered composite films with sandwiched electrolytes and electrodes. Since the macro-defects on the surface of the cellulose films due to the surface tension or compression mismatch probably affected the microstructure of the films, UMR has tried to make cellulose films as flat as possible during the drying and sintering

processes to simulate the same microstructure of the films which will eventually be obtained after fabricating the multi-layered structure.

A number of trial and error drying processes involving soaking the films with water, alcohol or acetone and without applying any pressure on the films have been tried, but with only limited success. Therefore, we tried a new film drying process which involves the addition of pressure. In this process the cellulose film after soaking water, alcohol, acetone and butoxy-ethanol was inserted between two glass plates and placed on a hot plate. Magnets were placed on the top of the glass plates to apply pressure on the film as illustrated in Figure 2.

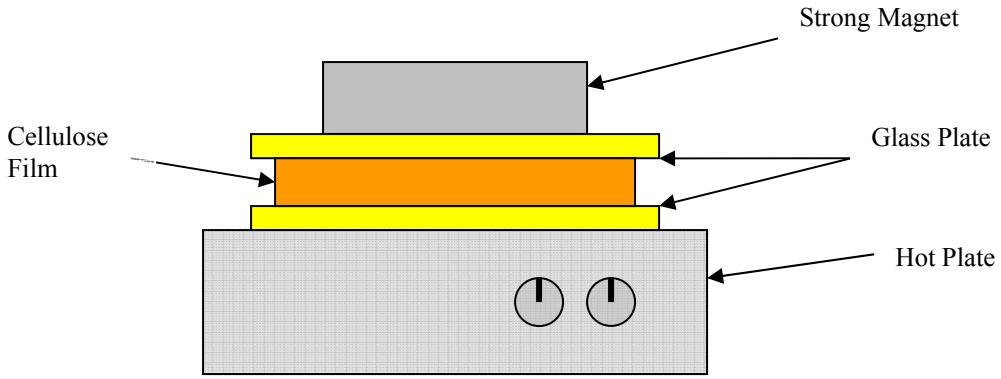

Figure 2. Schematic diagram of drying process

The temperature of the hot plate was set to above the boiling point of the particular solvents. This process was intended to change the surface structure of the cellulose films by decreasing the surface tension or compression mismatches between the two surfaces of the films so that the films would maintain their flat shape after the drying and sintering processes. This process seems to be working since almost all of the cellulose films that were treated were successfully flattened after heating in the temperature range between 150 and 250^{o}C on the hot plate.

However, the efforts to flatten the films turned out to be not totally successful since some of the films distorted again after sintering above 250^{o}C in a furnace. Therefore, the cracks observed in the SEM micrographs on the surface of the distorted films after sintering process should be regarded to be due to the surface tension or compression mismatch of the two sides of the films and be ignored in evaluating the structure of the cellulose films.

UMR also investigated films from AI who used a different processing procedure than that which UMR used to make dense films. The detailed drying and sintering process is shown in Table 1. After drying for 24 hours in a chamber in which dry nitrogen was flowing into the chamber at room temperature, the dried cellulose films were later burned out or sintered in the box furnace by following the temperature-time ramp schedule in Table 1.

Table 1. The detailed schedule of burnout and sintering

Process	Temperature Profile	Time (hr)
Stabilization	Heat to 60°C @ 40°C/hr Hold @ 60°C for 2 hr	1 2
Burnout	Heat to 360°C @ 10°C/hr Hold @ 360°C for 8 hrs	30 8
Dehydroxylation and Crystallization	Heat to 600°C @ 10°C/hr Hold @ 600°C for 8 hrs	24 8
Sintering	Heat to 800°C @ 10°C/hr Hold @ 800°C for 10 hrs	20 10
Cool Down	Cool to 350°C @ 30°C/hr Cool to 50°C @ 150°C/hr	15 2
Total time	5 day cycle	120

The two different methods were compared by UMR who found that the new procedure provided by AI which involves drying in chamber with flowing nitrogen gas did not result in flat membranes. However, they were subjected to the sintering process as scheduled and were compared with the films sintered by following the UMR procedure.

2. Rayonier vs. Catcel-5

The cellulose films soaked in butoxyethanol for drying resulted in flatter films than in other solvents. (Figure 3) It appears that the flatness was related to the higher boiling point of butoxyethanol (170 ~172°C) which prolonged the drying process and gave enough time to change the surface structure of the films.

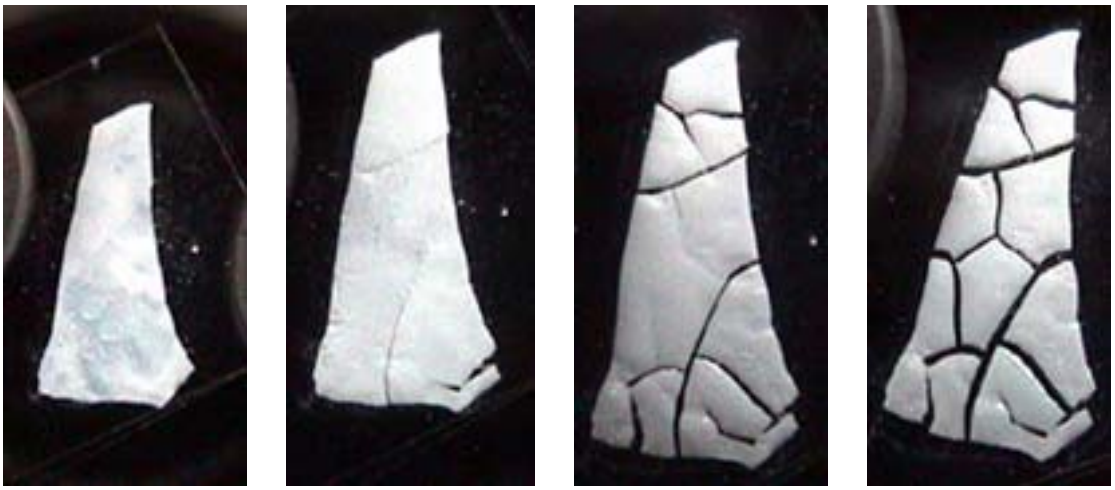

(a)

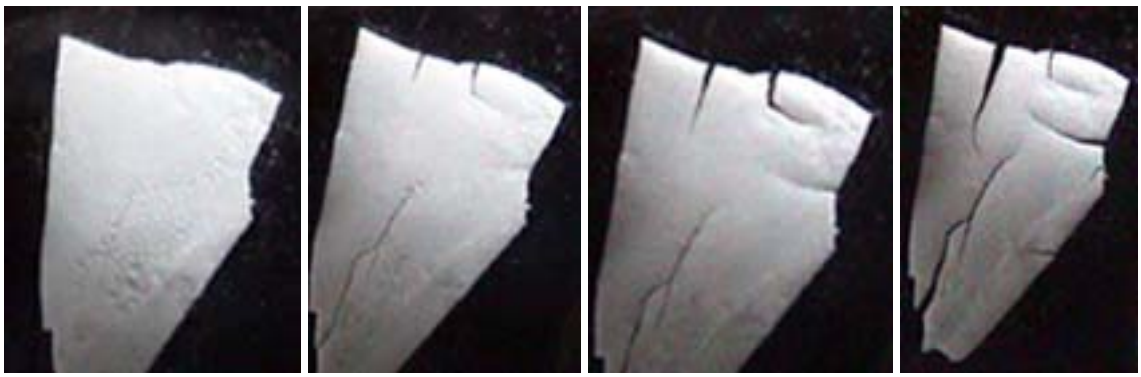

(b)

(c)

Figure 3. Images from sample #2912-909-8 after drying in air at 200^{o}C: The films soaked in water (b) in acetone (c) in butoxyethanol

The Rayonier films were broken into several big pieces during this process while Catcel-5 porous films maintained their original shapes. The color for the Rayonier films was changed from white to yellowish and from white to brownish for Catcel-5 porous films. After this process, the samples were annealed for 1 hour at 250, 350 and 450^{o}C in the furnace following the UMR sintering procedure. It was found that the Rayonier films which broke during drying maintained their broken shapes up to 1000^{o}C during heating. It appears that nearly all of the organic had been removed during the annealing stage. On the other hand, the Catcel-5 films when heated, underwent rapid deterioration, which resulted in badly distorted films that had been subjected to severe shrinkage for temperatures above 250^{o}C. The reason that the Catcel-5 porous films underwent more distortion and shrinkage than the Rayonier films may be because the Catcel-5 films have higher polymer content (7.5 wt%) than the Rayonier films (2.5 wt%) and the pores in the Catcel-5 films seem to have collapsed after sintering. They are illustrated in Figures 4, 5, 6 and 7. Therefore the higher solid content resulted in flatter films which qualitatively exhibited the higher mechanical strength.

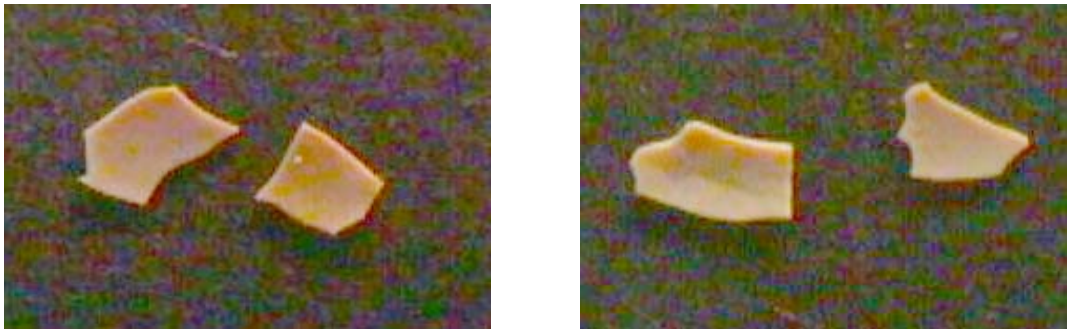

1 cm

(a) (b)

(c) (d)

Figure 4. Image of sample #3058-017-6 (Rayonier, Zirconia, High Molecular Weight, 85% of Solid Content)
(a) heated at 350°C on the hot plate for 5 minutes
(b) sintered at 250°C in the furnace for 1 hour
(c) sintered at 350°C in the furnace for 1 hour
(d) sintered at 450°C in the furnace for 1 hour

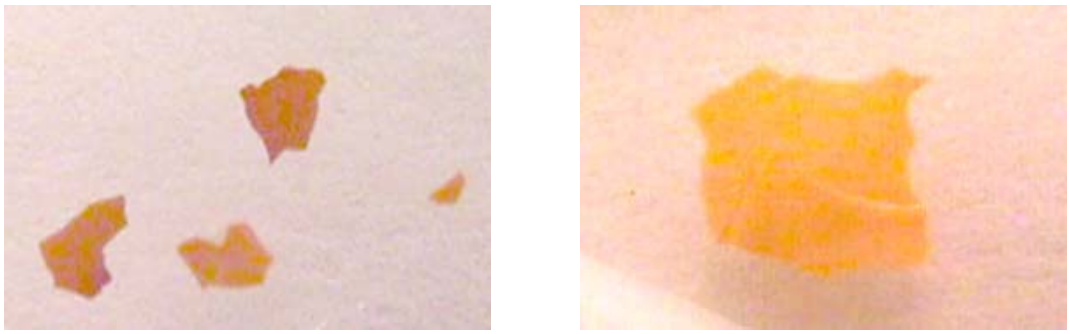

1 cm

(a) (b)

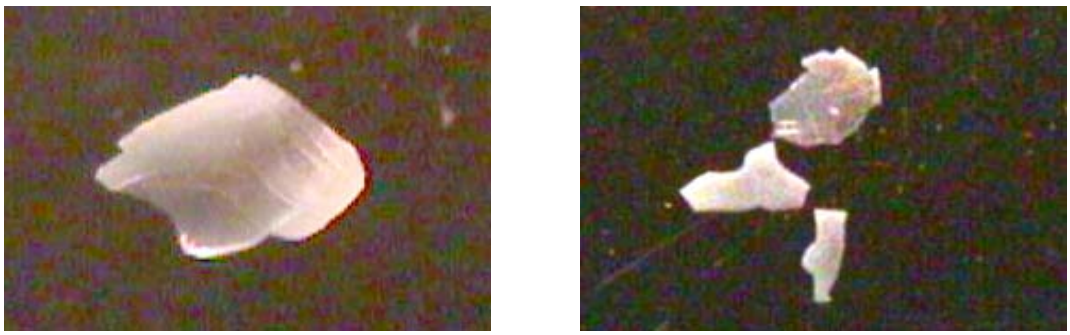

(c) (d)

Figure 5. Image of sample #3058-021-1 (Rayonier, YSZ, High Molecular Weight, 70% of Solid Content)
(a) heated at 350°C on the hot plate for 5 minutes
(b) sintered at 250°C in the furnace for 1 hour
(c) sintered at 350°C in the furnace for 1 hour
(d) sintered at 450°C in the furnace for 1 hour

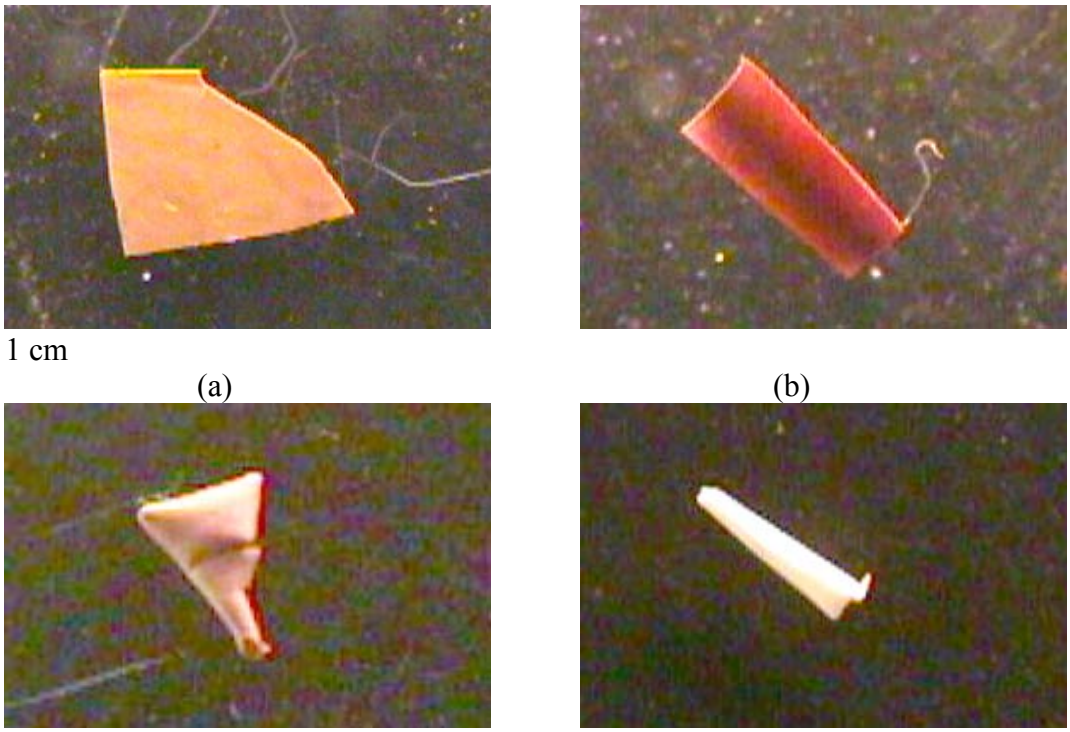

1 cm

(a) (b)

(c) (d)

Figure 6. Image of sample #3058-022-5 (Catcel-5, Zirconia, High Molecular Weight, 60-70% of Solid Content)
(a) heated at 350°C on the hot plate for 5 minutes
(b) sintered at 250°C in the furnace for 1 hour
(c) sintered at 350°C in the furnace for 1 hour
(d) sintered at 450°C in the furnace for 1 hour

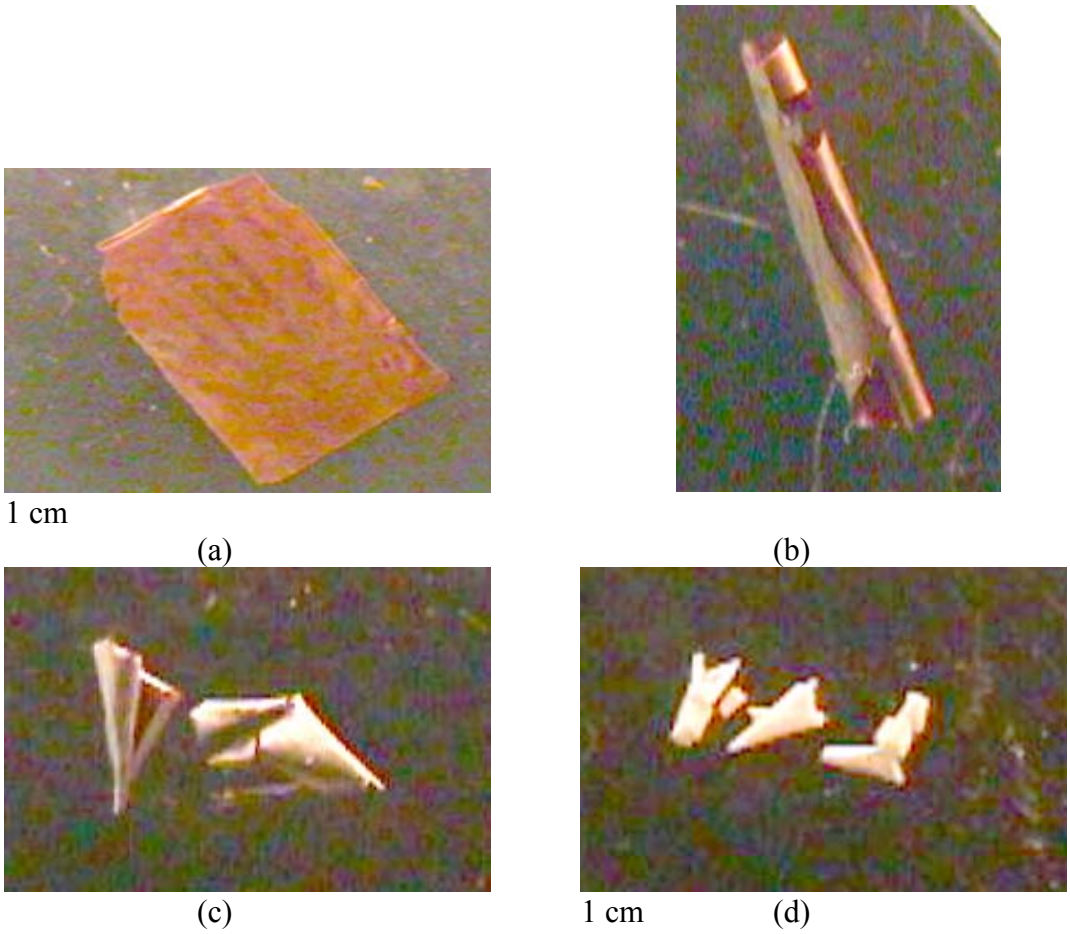

Figure 7. Image of sample #3058-023-2 (Catcel-5, YSZ, Low Molecular Weight, 28-44% of Solid Content)
(a) heated at 350^{o}C on the hot plate for 5 minutes
(b) sintered at 250^{o}C in the furnace for 1 hour
(c) sintered at 350^{o}C in the furnace for 1 hour
(d) sintered at 450^{o}C in the furnace for 1 hour

3. Evaluation of the thin films after sintering Process

After comparing the data from the fabrication of the cellulose films and the TGA results provided by NREL, UMR found that the cellulose films with higher polymer content yielded thinner films after the sintering process, which gave rise to more distortion and lower solid content. In other words, the cellulose films with higher solid content after the sintering process made thicker films which were less distorted than the films with the lower solid content. The TGA results shown in Figure 8 elucidate this point together with Figures from 4 to 7.

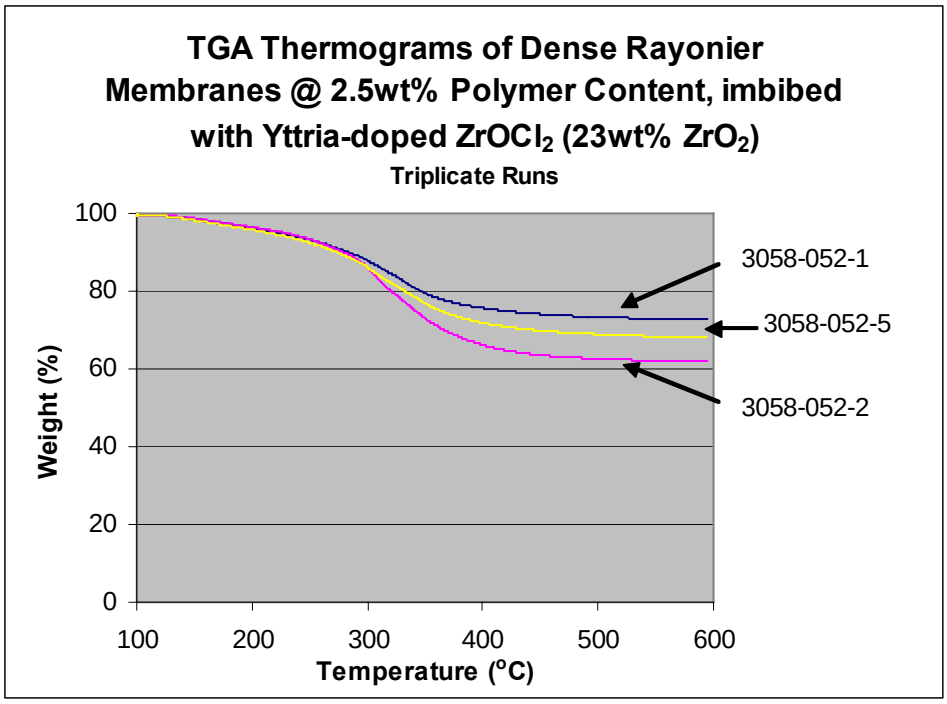

(a)

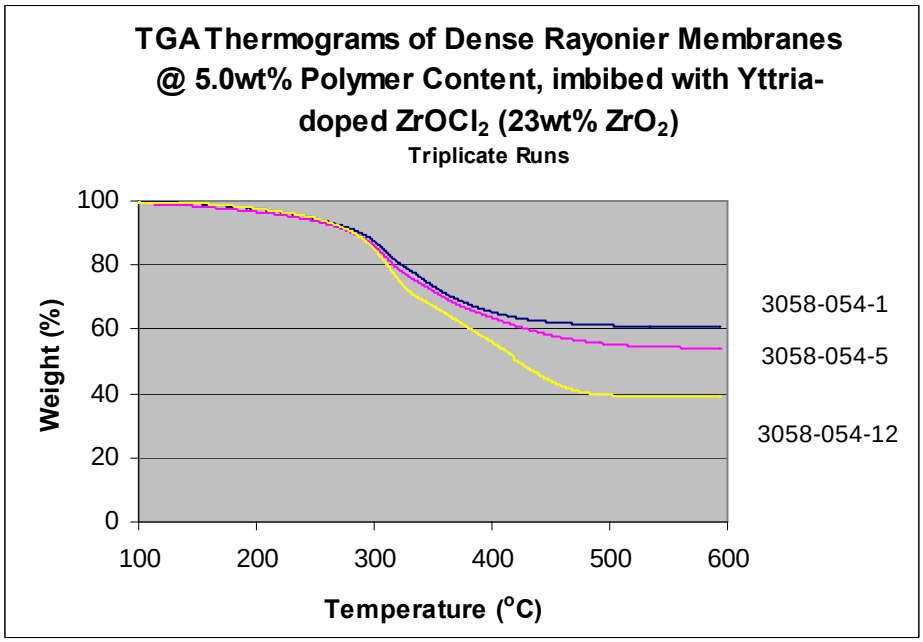

(b)

Figure 8. TGA thermograms of dense Rayonier membranes imbibed with Yttria-doped $ZrOcl_2$ (23 wt% ZrO_2) at
(a) 2.5 wt% Polymer content,
(b) 5 wt% Polymer content

The zirconia film made with aged solution also exhibited larger grain size and well-defined grain boundaries compared with the film made with non-aged solution. (Figure 9) Therefore, it is assumed that the aged solution give rise to the faster development of grains in the films than non-aged solution.

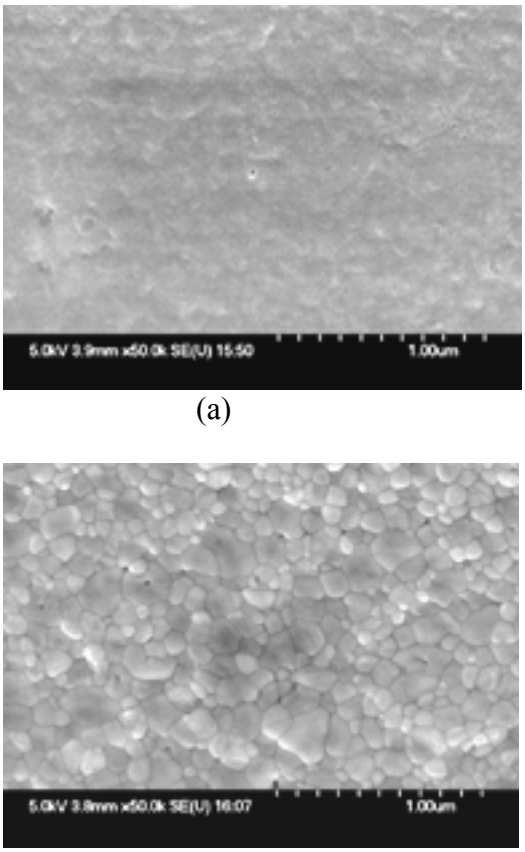

(a)

(b)

Figure 9. SEM micrographs (X50,000) of zirconia films sintered at 1000^{o}C for 2 hours from

(a) #3058-017-7 (Solution non-aged)

(b) #3058-017-25 (Solution aged for 2 days prior to casting)

The cracks observed in Figure 10 were created because of the distortion occurring during drying or sintering process and ended up with curled structures such as those shown in Figure 6 and 7. These cracks as previously mentioned we might be ignore when evaluating the microstructure of the sintered cellulose films, but it is recommended that the microstructure changes induced by surface tension or compression mismatch should be made on flat films.

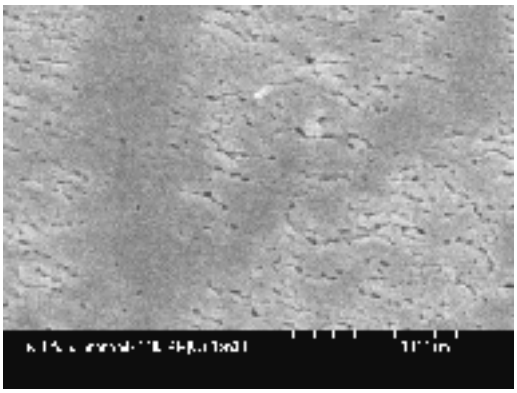

(a)

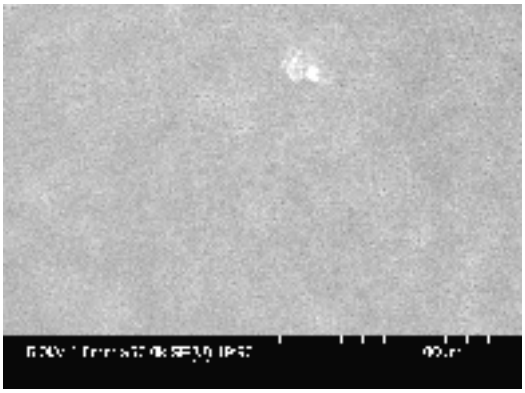

(b)

Figure 10. SEM micrographs (X50,000) of YSZ films sintered at 1000^{o}C for 2 hours from
(a) #3058-021-6 (Solution Not-aged)
(b) #3058-021-10 (Solution aged for 2 days prior to casting)

4. Microstructure of thin films

In this section, all the films followed the UMR procedure (mentioned in the previous section) during sintering unless it was specified as Dr. Benson's schedule. Figure 11 exhibits SEM micrographs of YSZ film #3058-021-6 (from Non-aged solution) after sintering for 2 hours at 1000^{o}C. In Figure 11, (a) shows the microstructure of dull-side and (b) shows glossy side. The dull side is always more porous than the glossy side because when the cellulose films were cast on the glass plate, the dull side was exposed to evaporation. In the Figure 11 (b), the cracks on the glossy side of the film were due to deformation during the drying and sintering process.

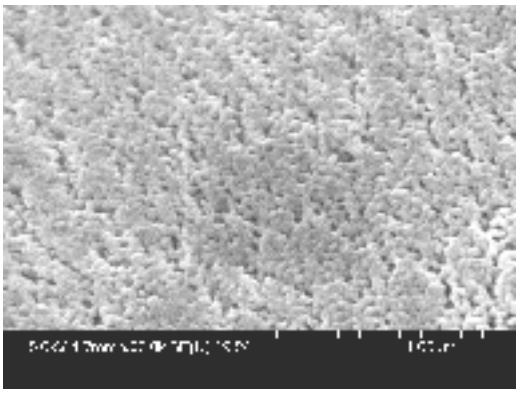

(a)

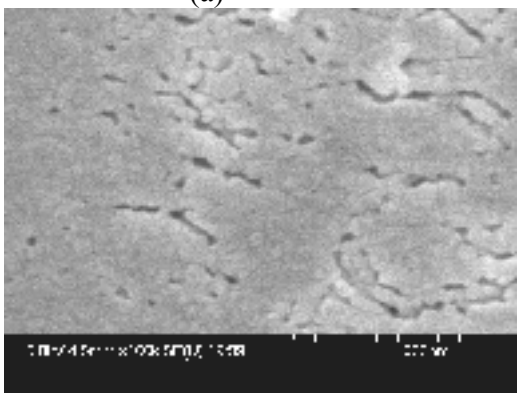

(b)

Figure 11. SEM micrographs (X50,000) of YSZ films sintered at 1000^{o}C for 2 hours from (from Non-aged solution)
(a) #3058-021-6 (Dull Side)
(b) #3058-021-6 (Glossy side)

Figure 12 shows that the SEM micrographs of sintered YSZ film #3058-021-10 (from Aged solution). When compared with film #3058-021-6 (from Non-aged solution) in Figure 11, it was observed that the film fabricated from aged solution exhibited a more uniform surface and less porous microstructure. This also might be related to the polymer and solid content of the films. The films # -021-6 has higher polymer content and lower solid content than the film # -021-10. Therefore, more study is required to evaluate the films which were fabricated from the cellulose films with high or low polymer content, imbibed by the aged and non-aged solution.

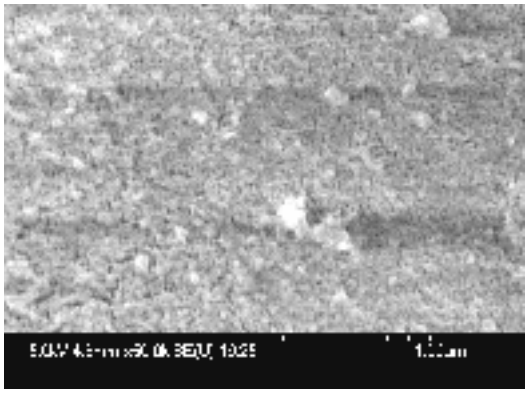

(a)

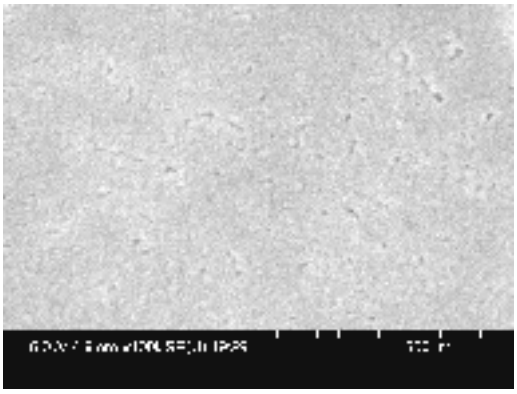

(b)

Figure 12. SEM micrographs (X50,000) of YSZ films sintered at 1000°C for 2 hours from (from Aged solution)
(a) #3058-021-10 (Dull Side)
(b) #3058-021-10 (Glossy side)

SEM micrographs show that the films from #3058-017-7, 25 (Figure 13) exhibited a microstructure with more uniform, larger grains and well-defined grain boundaries than the films from #3058-021-6,10 (Figure 11 and 12). It was observed that the grain size is about 0.1 μm or less at 1000°C from the glossy side in Figure 13 while the grains were still being developed in Figure 11 and 12. From the data for fabrication of cellulose films in Appendix A, the difference between the two films is as follows: (1) -021 was soaked in $YCl_3/ZrOCl_2$ solution and -017 was soaked in $ZrOCl_2$ solution; (2) -017 (about 80 ~ 85% of solid content) has about 10% of more solid content than -021 (about 70 ~ 75% of solid content).

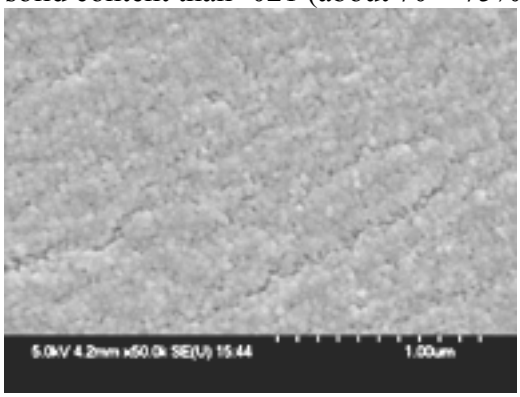

(a)

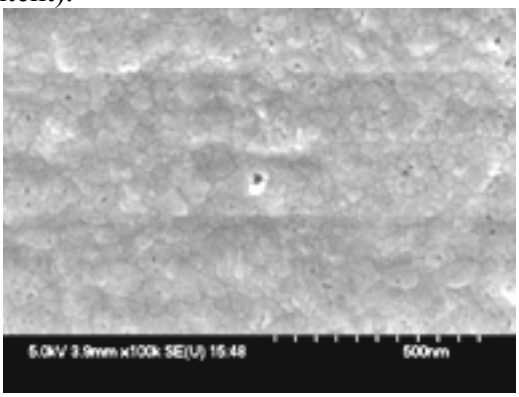

(b)

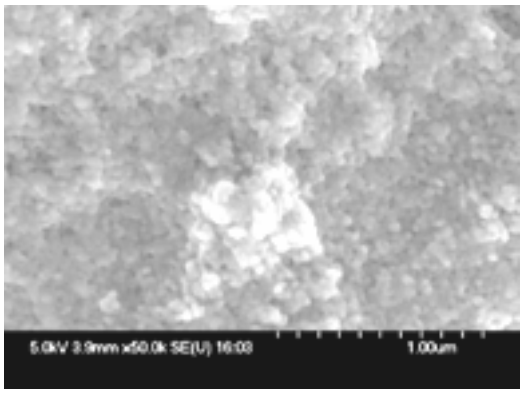

(c)

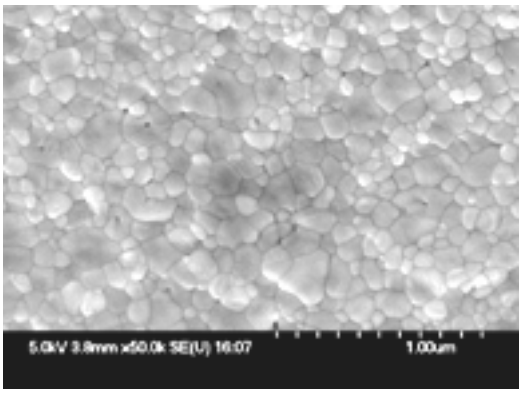

(d)

Figure 13. SEM micrographs (X50,000) of Zirconia films sintered at 1000°C for 2 hours from Non-aged solution for (a,b) and from Aged solution for (c,d)
(a) #3058-017-7 (Dull Side)
(b) #3058-017-7 (Glossy side)
(c) #3058-017-25 (Dull Side)
(d) #3058-017-25 (Glossy side)

Figure 14 shows the microstructure evolution of zirconia films as a function of increasing temperatures at 600, 800 and 1000°C. From the both glossy and dull surface at aforementioned temperature, the grains were not observed except on dull side at 1000°C. Although it was very difficult to evaluate grains and grain boundaries on the glossy side we could find some evidences of the development of grains at 1000°C. The films from dull side became more porous with increasing sintering temperature in the films shown in Figure 14.

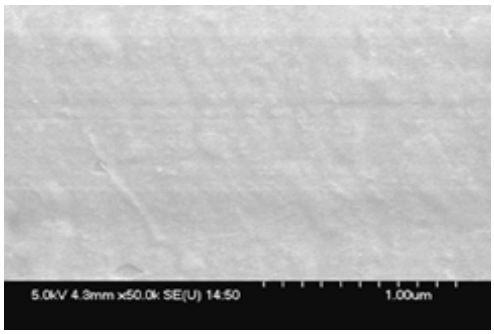

(a) Glossy at 600°C

(b) Dull at 600°C

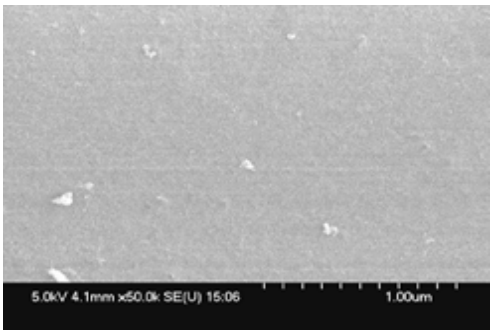

(c) Glossy at 800°C

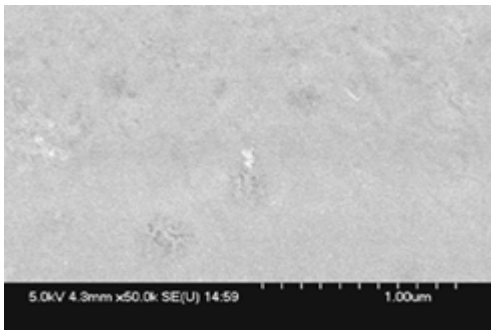

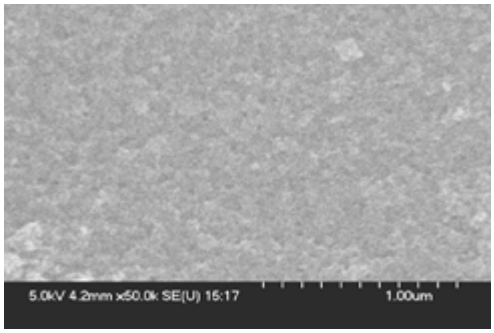

(d) Dull at 800°C

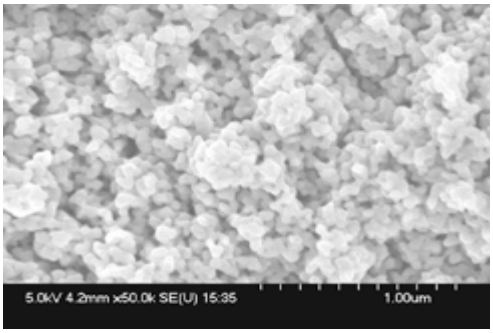

(f) Dull at 1000°C

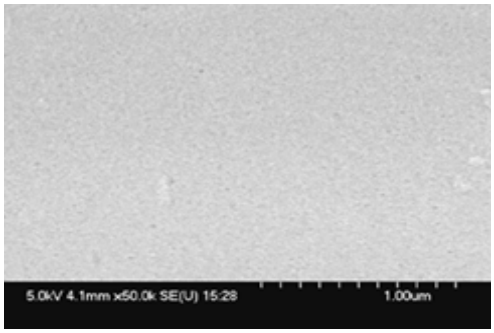

(e) Glossy at 1000°C

Figure 14. SEM micrographs (X50,000) of Zirconia films (from Non-Aged solution) with UMR sintering process for

(a) #3058-017-3 (Glossy Side) sintered at 600°C
(b) #3058-017-3 (Dull side) sintered at 600°C
(c) #3058-017-3 (Glossy Side) sintered at 800°C
(d) #3058-017-3 (Dull side) sintered at 800°C
(e) #3058-017-3 (Glossy Side) sintered at 1000°C
(f) #3058-017-3 (Dull side) sintered at 1000°C

Figure 15 shows the development of microstructure when the same film was sintered with the two different sintering schedules: one from Dr. Benson (a, b, c) and the other from UMR (d, e). The films numbered as 017-3 and 017-4 are basically from the same film batch. The only difference between the two films is 1 or 2 minutes of time delay before they were rinsed with solvent or water after they were soaked in metal salt solutions. From the comparison of glossy surface shown in Figure 15 (a) and (d), it was observed that the surface was textured in (a) which was not observed in (d). However, texturing was not found on the dull-side as shown in Figure 15 (b) and (c). More porous microstructure was observed in the films sintered by following Dr. Benson's schedule (Figure b and c). Therefore, it is assumed that the prolonged sintering process probably increased the porosity of the film and also induced different surface morphology on the glossy surface by development of texturing.

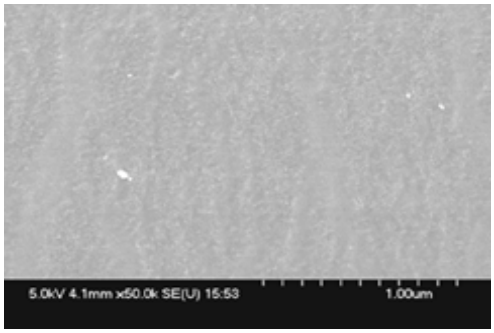

(a) Glossy at 800°C

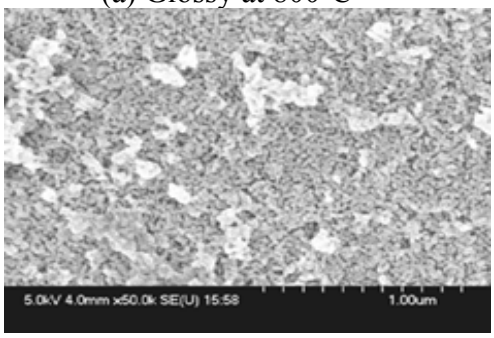

(b) Dull at 800°C

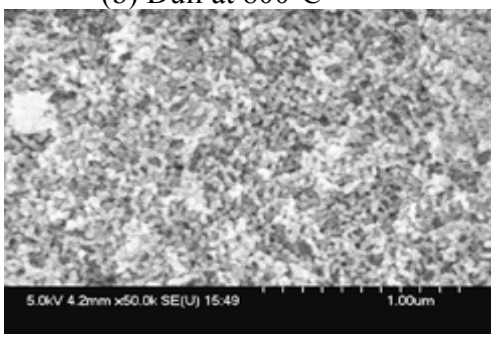

(c) Dull at 800°C

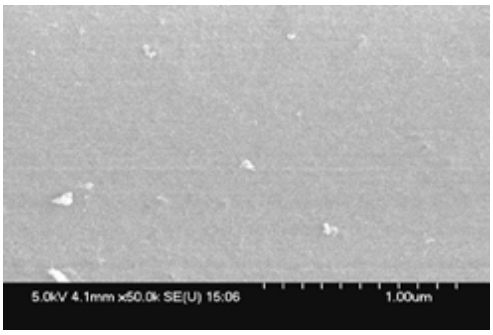

(d) Glossy at 800°C

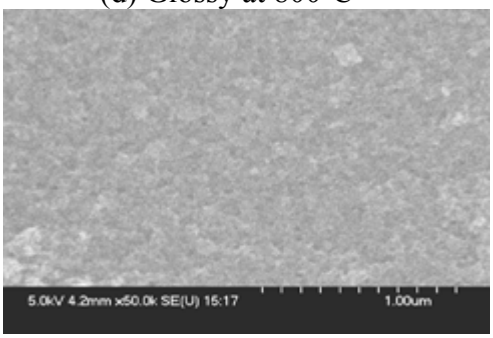

(e) Dull at 800°C

Figure 15. SEM micrographs (X50,000) of Zirconia films (from Non-Aged solution) with Dr. Benson's (a,b,c) and UMR (d,e) sintering schedule for

(a) #3058-017-4 (Glossy Side) sintered at 800°C
(b) #3058-017-4 (Dull side) sintered at 800°C
(c) #3058-017-3 (Dull side) sintered at 800°C
(d) #3058-017-3 (Glossy Side) sintered at 800°C
(e) #3058-017-3 (Dull side) sintered at 800°C

The microstructures exhibited by zirconia films formed from cellulose films imbibed by non-aged solution show that the density increases when the sintering temperature is increased. (Figure 16) However, the grain size was little influenced by the processing temperature.

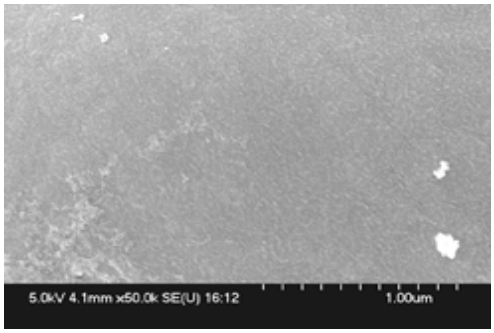

(a) Glossy at 600°C

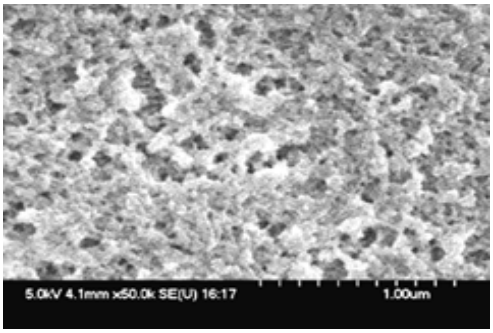

(b) Dull at 600°C

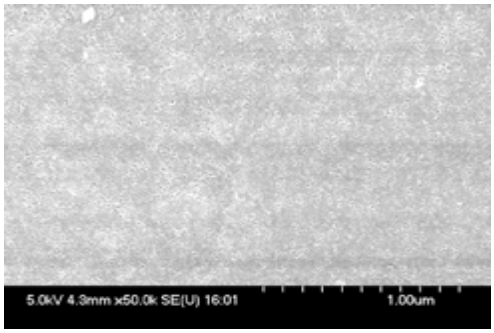

(c) Glossy at 800°C

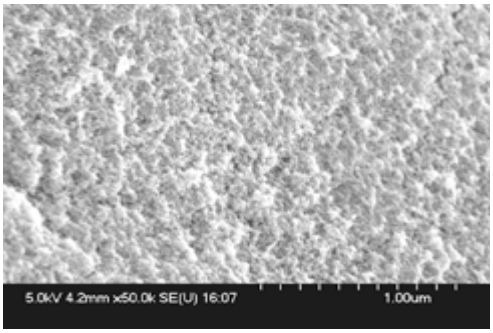

(d) Dull at 800°C

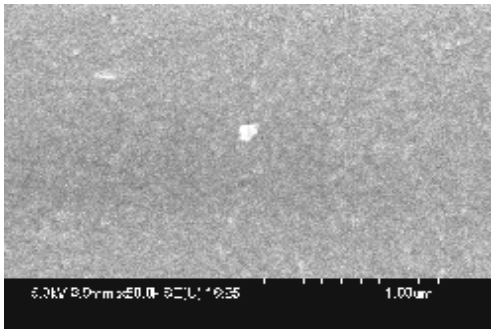

(e) Glossy at 1000°C

Figure 16. SEM micrographs (X50,000) of Zirconia films (from Non-Aged solution) with UMR sintering process for

(a) #3058-041-40 (Glossy Side) sintered at 600°C
(b) #3058-041-40 (Dull side) sintered at 600°C
(c) #3058-041-40 (Glossy Side) sintered at 800°C
(d) #3058-041-40 (Dull side) sintered at 800°C
(e) #3058-041-40 (Glossy Side) sintered at 1000°C

Figure 17 compares the microstructure of zirconia films resulting from the same batch of imbibed cellulose films (the difference between 041-47 and 041-40 is the time delay of rinsing after soaking the films in the metal salt solution) which were sintered by following Dr. Benson's schedule (a, b) and the UMR schedule (c, d). The microstructure of the zirconia films sintered by Dr. Benson's schedule shown in Figure (a, b) exhibited texturing and more porosity on both the glossy and dull surface.

(a) Glossy at 800°C

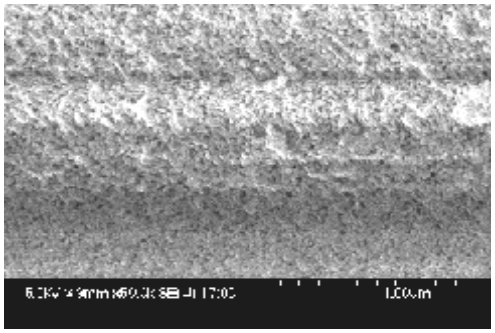

(b) Dull at 800°C

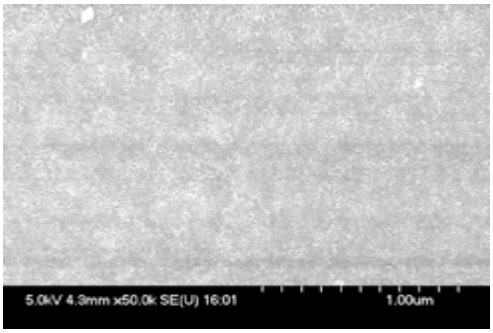

(c) Glossy at 800°C

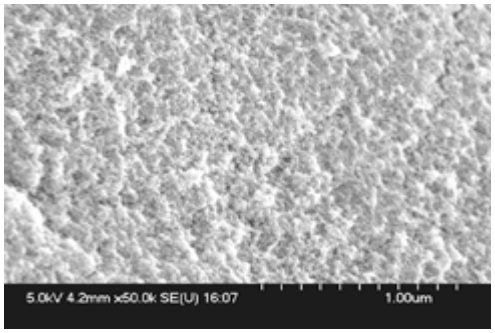

(d) Dull at 800°C

Figure 17. SEM micrographs (X50,000) of Zirconia films (from Non-Aged solution) sintered at 800°C with Dr. Benson's (a,b) and UMR (c, d) sintering schedule for
(a) #3058-041-47 (Glossy Side)
(b) #3058-041-47 (Dull side)
(c) #3058-041-40 (Glossy Side)
(d) #3058-041-40 (Dull side)

Two thin films shown in Figure 18 were fabricated from the cellulose films which have the same polymer content and were soaked in the same salt solution. The only difference was the fabrication date and therefore the sample numbers. However the film shown in (b) is more porous than (a). This difference is probably due to the fabrication process of the cellulose films in NREL or UC.

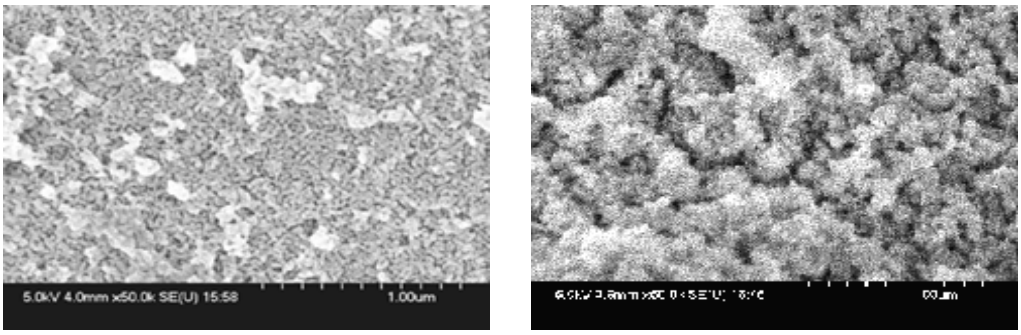

(a) Dull at 800°C (b) Dull at 800°C

Figure 18. SEM micrographs (X50,000) of Zirconia films (from Non-Aged solution) with Dr. Benson's sintering schedule sintered at 800°C for
(a) #3058-017-4 (Dull Side)
(b) #3058-041-16 (Dull side)

5. Conclusion

a. If we produce thin films which have less polymer content and more solid content and also if we cast the thin films with aged salt solutions, we might have flatter, mechanically stronger, less defected and dense cellulose thin films.
b. Since the porous Catcel-5 films qualitatively exhibited poor mechanical stability and were subjected to the significant shrinkage and distortion during drying and sintering, the improvement of the fabrication process of the Catcel-5 films is recommended.
c. It is also recommended that the porous Catcel-5 films may be replaced by the porous Rayonier films.
d. Since all the porous Catcel-5 films were severely distorted and very fragile, we could not take any SEM micrographs from them.
e. The fabrication process of cellulose films should be improved and standardized as well as the drying and sintering process.
f. The visible evidence of development of grains in thin films was observed at the sintering temperature of 800°C, however it was not clear until the temperature reached to 1000°C.
g. It is obvious that the ZOC imbibed cellulose can produce both dense and porous oxide structures with grain size in the nanocrystalline range which replicate the initial cellulose structures well.

3.3.3) Characterization of the PEN Structures

The problem of the distortion and cracking prevented the fabrication of the PEN structures and their subsequent testing as single and multi-cell SOFC structures. Developing the equipment and process to produce flat films was part of Task 4 (AI.), which even after two extensions was never completed due to equipment problems.

3.1.4) Investigation of Alernate Routes to Fabricate PEN Structures

Application of Composite Technology for SOFCs

Composite technology is a new approach to solid oxide fuel cell (SOFC) fabrication. It is based on the net shape processing, which uses a combination of colloidal suspension and polymer precursor techniques. Different elements of SOFC can be prepared and optimized using this approach and the flexibility of the net shape processing. The goal of this research was to develop net shape procedures for different elements of SOFC, to show the real possibility preparing all these elements of SOFC and to investigate the advantages of composite technology. A nickel-YSZ composite was prepared and investigated as the prospective anode material. High electronic conductivity and stability in REDOX cycles were shown for this material. Different cathode compositions were prepared using composite technology and tested. It was shown, that these materials ensure low overpotentials and are time stable at operation temperature up to 800^{o}C. All three SOFC designs were tested: anode, cathode and electrolyte supported SOFCs. It was possible to achieve low resistance of SOFC structure for all designs, but electrode supported SOFCs had limitation in the current connected with the gas diffusion through thick electrode substrates. The best performance was achieved on an electrolyte supported system with 100 μm YSZ electrolyte and composite anode and cathode: 0.75W/cm^2 power density at 0.6 V at 800^{o}C.

The intent of this research was to develop a low temperature method for deposition of 1 to 10 μm thickYSZ electrolyte using combination of YSZ powder and YSZ polymeric precursor (net shape processing). In this process the powder is first deposited onto the surface to provide a framework of connected grains into which the polymeric precursor impregnates to form an oxide particle / organic polymer film. Upon heating to 300^{o}C, the polymer decomposes to yield a nanocrystalline layer of YSZ, which fills the space between the grains, so dense material can be prepared without shrinkage during further annealing. One of the goals of this research was to show the possibility to deposit dense electrolyte layers at low temperature using net shape processing, to investigate structural stability of these layers at elevated annealing temperatures and to compare electrical properties with those for YSZ electrolytes prepared by commonly used techniques (high temperature sintered bulk ceramics).

Low electrode overpotentials are required for the low temperature SOFC applications. Composite technology allows the formation of electrodes with higher effective surface area, increases efficiency of the exchange reactions, and, consequently, decrease electroded overpotentials.

Different three-layer structures were prepared using net shape processing: anode, cathode and electrolyte supported. Impedance spectroscopy and direct SOFC measurements were used to characterize these structures.

Experimental

Nanocrystalline powders with the grain size 50 to 100 nm and metal organic polymeric precursors were used for the preparation of all composite materials investigated.

Scanning Electron Microscopy (SEM) images were obtained using Field Emission Scanning Electron Microscope Hitachi S-4700 and Battery Tester Solartron 1470 together with Impedance Gain Phase Analyzer Solartron 1255 was used for impedance measurements and SOFC performance testing.

Dense YSZ coatings were successfully prepared on different substrates including dense (sapphire, platinum foil) and porous (YSZ-Ni anode and LSM cathode). It was shown that the thickness range 1 to 10 μm can be overlapped by net shape processing, and, what is important, the preparation temperature for the dense YSZ electrolyte can be decreased to 400^{o}C. SEM images of the structure cross-sections for ~2 μm coatings on LSM substrate are shown in Fig.1 as an example. These coatings were initially prepared at 400^{o}C and than annealed at 900^{o}C to ensure stability of the YSZ layers at elevated temperatures. It can be seen from the figure, that net shape processing allows the preparation of dense coatings on porous substrates and exhibits good planarization properties: it is possible to prepare smooth, defect free coating with the thickness less than 2 μm on porous substrates which have pore size of several microns. The electrical properties of the coatings are close to the properties obtained with high temperature sintered ceramic materials and are stable with the further high temperature annealing (Fig.2): up triangles in Fig.2a shows Ahrrenius plot for as-prepared (un-annealed sample) and down triangles refer to the sample annealed at 900^{o}C. Fig.2b illustrates the fact that net shape processing can yield the same value of conductivity of composite YSZ with the annealing temperature below 600^{o}C as dense ceramic YSZ sintered above 1200^{o}C.

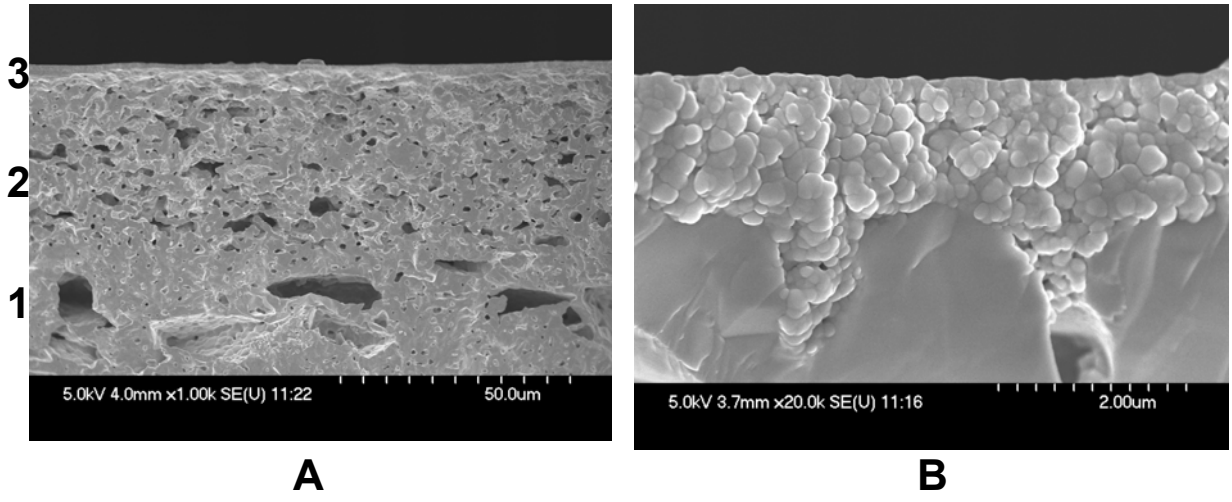

Fig.1. SEM images of the cross-sections for dense composite YSZ films on porous LSM substrates.

A – Low magnification; B – High magnification.

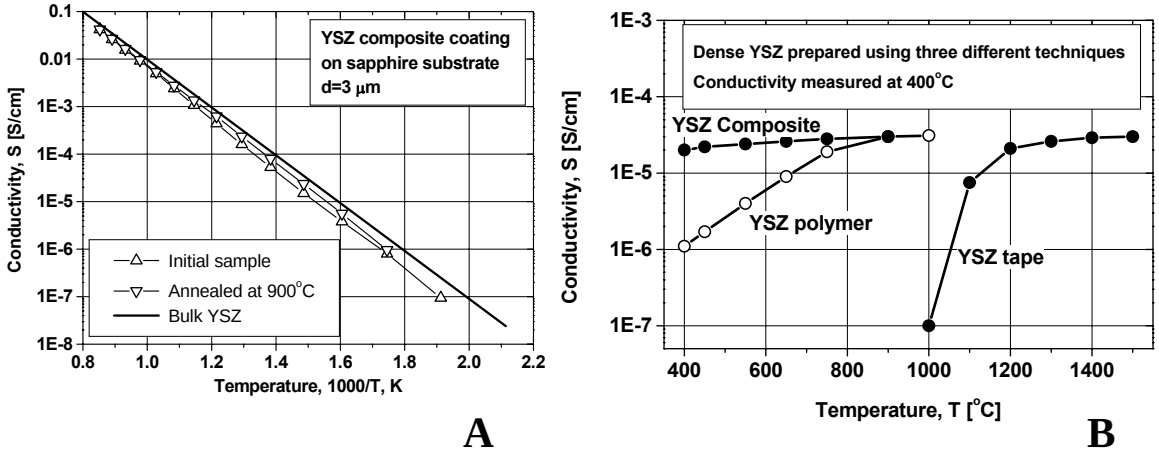

Fig.2. Electrical properties of composite YSZ coatings.
A – Temperature dependence of the conductivity for composite YSZ;
B - Conductivity of YSZ prepared by different techniques as a function of sintering temperature.

Ni-YSZ composite coatings were prepared on different substrates to investigate an applicability of the net shape processing for SOFC anodes. Fig.3 shows the results obtained for composite coatings on sapphire substrate. It can be seen from Fig.3a that the conductivity of YSZ/NiO composite in air is higher than that of YSZ by itself. Upon reduction Ni conductivity increased to ~500 S/cm. It is important that composite Ni-YSZ cermet shows stability as it undergoes REDOX cycles, which is illustrated in Fig.3b.

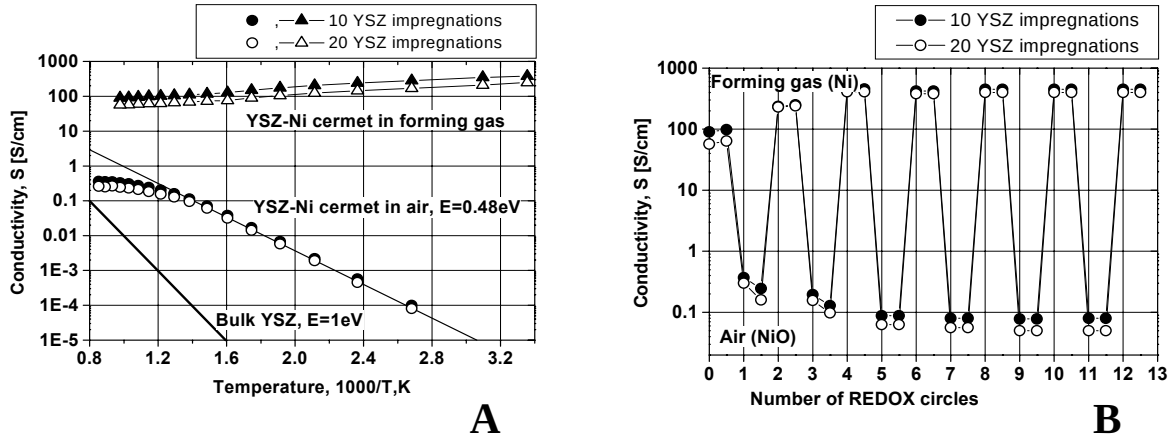

Fig.3. Electrical properties of net shape processed YSZ-Ni composite.
A – Temperature dependence of the conductivity in air (NiO phase) and in forming gas (Ni phase);
B – REDOX stability of composite Ni-YSZ cermet.

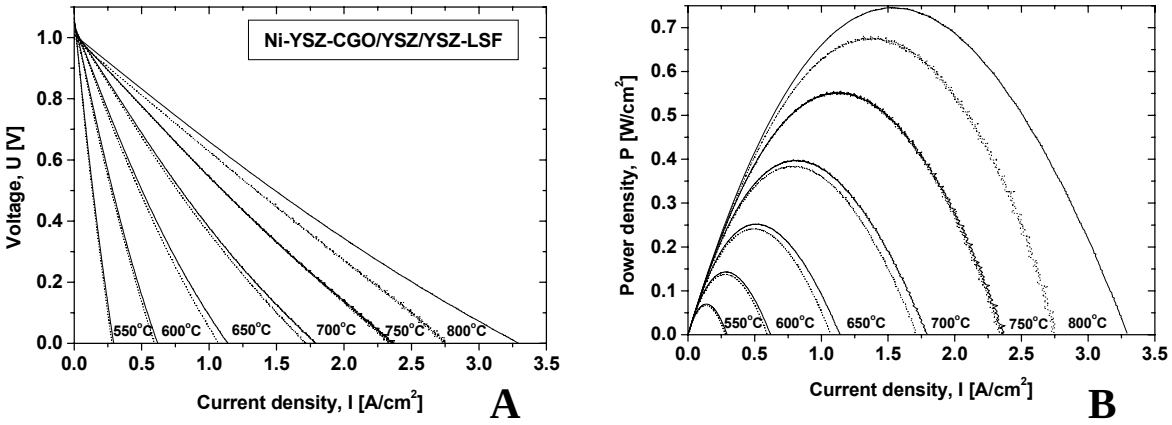

Fig.4. SOFC testing results. Electrolyte supported design with 100 μm YSZ electrolyte, Ni-YSZ-CGO composite anode and YSZ-LSF composite cathode.
A – Current to voltage characteristics in the temperature range 550 to 800°C;
B – Power density in the same temperature range.

Different composite cathodes were also prepared and tested including LSM-YSZ, LSF-YSZ, LSCF-YSZ and SSC-YSZ compositions. It was shown by investigation of the symmetrical structures cathode-electrolyte-cathode that these cathodes have low resistance (on the level of 0.05 Ohm.cm^2 at 800°C) and show resistance towards degradation.

Fuel cell testing was accomplished on anode, cathode and electrolyte supported SOFC structures with all elements prepared using net shape processing. It was shown that overall resistance of SOFC structures is low (on the level of 0.25 to 0.3 Ohm.cm^2 at 800°C), but gas diffusion through the substrate did limit maximum current density on electrode supported samples. The best results were achieved on electrolyte supported SOFCs with 100 μm YSZ electrolyte (Fig.4). It can be seen that I-V characteristics are almost linear and power density is on the level of 0.75 W/cm^2 at 800°C. REDOX cycles were provided at each temperature investigated (see dotted and solid lines in Fig.4). It can be seen that composite SOFCs are stable in REDOX cycles up to ~750°C.

Summary

The possibility of using net shape technology for preparation of the trilayer (anode/electrolyte/cathode) elements of a SOFC was shown. The features of net shape processing (possibility to prepare and to densify the material at very low temperature and precise control of the composition) allow deposition of dense electrolytes (thickness range 1 to 10 μm) on pre-sintered substrates and efficient electrodes (anode and cathode). Net shape processing opens additional ways for optimization of SOFC elements and could be helpful for different designs of the SOFC.

3.2 TASK # 2: Preparation and Characterization of Organic/Inorganic Hybrides

This was a NREL/UCB task which involved: 1) preparation of novel cellulose derivatives, 2) synthesis of both dense and porous cellulose films and 3) development of protocol for imbibing salts into the films.

Initially the focus was on testing the reproducibility of the microporous structures obtained from Rayonier (cellulose) and Catcel polymers. The polymer concentration in the dope solution was varied over the range 3.5 – 9.5 wt%. Typically, the pore size and porosity in the Catcel porous films were ~ 4 μm and 45%, respectively. On the other hand, the Rayonier porous films had larger pores (> 5.5 μm) and greater porosity (> 55%). After discussions at the review meetings, the decision was made to focus on Rayonier cellulose polymer because:

1. Given the very low cost of Rayonier cellulose polymer, obtaining porous microstructures using cellulose would be much more desirable than using other cellulose derivatives.
2. Rayonier was producing asymmetric anisotropic porous structure with a thin dense skin, supported by a porous substructure that incorporated systematically increasing pore size in the direction away from the skin is ideally suited for fuel cell applications.

Consequently, we focused on and succeeded in obtaining the desired asymmetric microstructure in Rayonier porous films. Representative micrographs are shown in Figure 1. These micrographs correspond to two different porous Rayonier films cast on two separate days under identical processing conditions from dope solutions containing 7.5 wt% polymer. The figures demonstrate that the fabrication protocol that is now employed enables us to cast films that possess morphologies with a reasonably high degree of reproducibility.

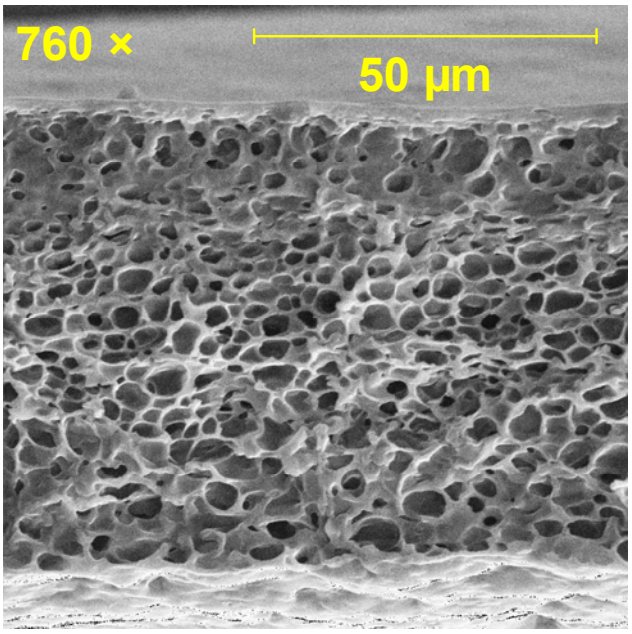

(a)

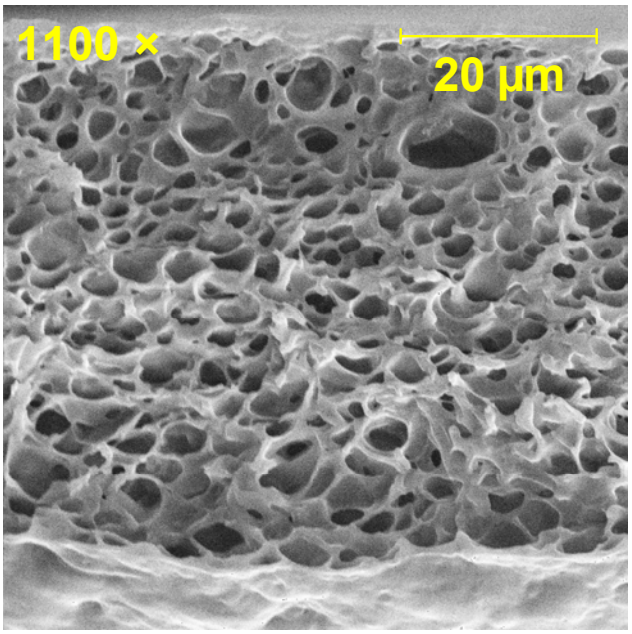

(b)

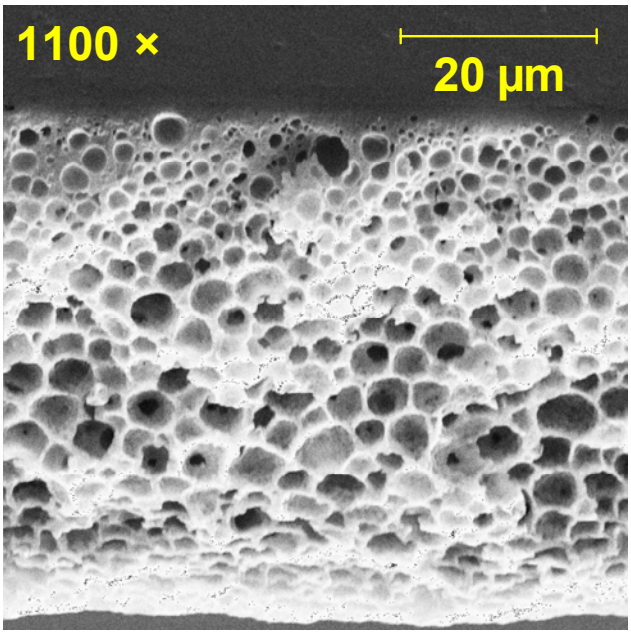

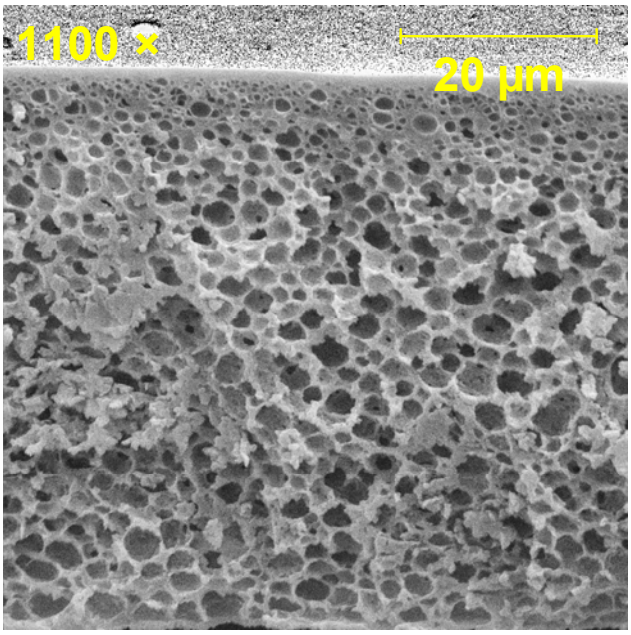

(c) (d)

Figure 1: Scanning electron micrographs of the cross sections of two porous Rayonier cellulose films cast on different days under identical processing conditions. The micrographs in (a) and (b) are different magnification views of a sample cast on day 1; (c) and (d) are corresponding micrographs of a physically different sample cast on the following day under identical conditions. The asymmetric and anisotropic morphologies of the samples are quite similar and indicate a high level of reproducibility.

In general, all of the subtasks were completed. A protocol was developed for making both porous and dense cellulose films and imbibing metal salts into the cellulose structures. Imbibed structures were supplied to UMR and AI for conversion into oxide films.

The work which was done in this program, with the exception of the metal salt imbibing process is well represented by the manuscript which was submitted to the Journal of Applied Polymer Science for publication. This manuscript is shown as follows:

Journal:	*Journal of Applied Polymer Science*
Manuscript ID:	APP-2005-03-0465
Manuscript Type:	Research Article
Date Submitted by the Author:	30-Mar-2005
Keywords:	membranes, morphology, phase separation

Synthesis and Characterization of Dense and Porous Cellulose Films

Vivek P. Khare[1,*], Alan R. Greenberg[1], Stephen S. Kelley[2], Heidi Pilath[2], Il Juhn Roh[3], and Jeff Tyber[1]

[1] *Department of Mechanical EngineeringNSF Membrane Applied Science and Technology CenterUniversity of Colorado at Boulder, Boulder CO 80309-0427.*

[2] *National Renewable Energy LaboratoryGolden CO 80401-3393.*

[3] *Hydranautics, Inc.401 Jones Road, Oceanside CA 92054.*

Abstract

Cellulose derivate polymers such as cellulose acetate, cellulose triacetate, and cellulose nitrate are routinely used as membrane materials for applications involving microfiltration, ultrafiltration and gas separation. However, the cellulose polymer itself is not directly used to synthesize dense or porous films for membrane applications. Recently, N-methylmorpholine N-oxide (NMMO) and dimethylacetamide (DMAc)/lithium chloride (LiCl) have been successfully employed for dissolution of unmodified cellulose. There is thus a strong rationale for re-examining the possibility of cellulose membrane fabrication using these solvents.

By a judicious selection of solvents, casting conditions, solution composition, and solvent exchange steps, we have successfully cast dense as well as skinned asymmetric porous cellulose films. The porous films were obtained from a range of cellulose solution concentrations. The pore size and porosity decreased systematically with increasing cellulose concentration. SEM analysis of the cross sections revealed an asymmetric skinned structure with a monotonically increasing pore size away from the skin. Quantitative image analysis techniques revealed that the measured pore diameters are in the range 1.8–4.8 μm. Mechanical testing indicated that the dense cellulose films possessed tensile properties comparable to those of cellulose acetate (CA) films. Transport measurements indicated that whereas the nitrogen permeability values were comparable for cellulose and CA dense films, the cellulose permeability depended upon the type of drying protocol employed. These results demonstrate that processability need not be a constraint in the use of cellulose polymer for membrane fabrication. In selected applications, cellulose membranes could become a cost-effective, environmentally friendly alternative to other more commonly employed membrane polymers. Keywords: membranes; cellulose; morphology; phase separation; natural polymers;

Introduction

Cellulose derivatives – cellulose acetate (CA), cellulose triacetate (CTA), and cellulose nitrate (CN) are routinely and extensively used as membrane materials. For example, CA membranes are used in gas separation, reverse osmosis (RO), ultrafiltration (UF), and microfiltration (MF) [1–3]; CTA membranes are used in RO and UF [1,2]; and CN membranes are used in MF applications [1]. These membranes are typically made using phase inversion techniques whereby a solution containing the polymer is cast in the desired shape, and phase inversion is effected by incorporation of a nonsolvent, removal of the solvent, or by changing the temperature of the polymer solution. The ability to obtain a moderately viscous homogeneous polymer solution is an important precondition to such membrane formation techniques. CA, CTA, and CN readily dissolve in numerous ketone and ester solvents such as acetone, methyl acetate, and polar aprotic solvents such as dimethyl acetamide (DMAc), n-methyl pyrrolidone (NMP), and dimethyl sulfoxide (DMSO) [4]. As is well recognized, a variety of membrane microstructures can be prepared from these cellulose derivatives.

Unlike cellulose derivatives, the cellulose polymer itself is not viewed as a good membrane material because its unique structure (Figure 1) severely limits the processability of the cellulose polymer. Cellulose is a polysaccharide composed of glucosidic rings linked through oxygen bridges with a repeat unit having three hydroxyl groups and an acetal linkage. Strong hydrogen bonding between the hydroxyl groups make cellulose a highly crystalline, insoluble polymer that degrades before melting [5,6]. Since cellulose is not soluble in common solvents, casting by standard methods is not possible and the relatively low degradation temperature precludes melt processing [6].

From a broader perspective, cellulose is a relatively inexpensive, biodegradable, and sustainable polymer. Hence, there is a strong rationale to use the cellulose polymer itself as a raw material for making porous and dense membranes. Since the early 1990s, new processes based on organic solvents – N-methylmorpholine N-oxide (NMMO) and dimethylacetamide (DMAc)/lithium chloride (LiCl) – and more recently ionic liquids such as 1-butyl-3-methylimidazolium chloride have been explored to produce regenerated cellulose films [7,8]. The use of such solvents for making cellulose films and fibers has several important advantages. Since cellulose dissolution involves purely physical unit operations, no chemical bi-products requiring disposal as waste products are formed. Moreover, the solvents can be recycled completely, which makes the cellulose-dissolution-based processes environmentally friendly. Not surprisingly, the dissolution-based processes are increasingly being adopted to obtain cellulose products. For example, the Lyocell process utilizes the NMMO solvent to obtain regenerated cellulose fibers [9]. The Lyocell process is receiving considerable interest because of its environmentally friendly characteristics, simplicity, and the special properties of the resulting fibers. Compared to viscose fibers, the Lyocell fibers have higher tenacity, higher modulus, lower shrinkage in the dry state, and lower tenacity and modulus reduction in the wet state [10].

While there has been considerable effort in obtaining fibers using cellulose solutions, reports describing the preparation of cellulose films are relatively scarce. Wu and Yuan [6] measured the gas permeability of dry as well as water-swollen cellulose films obtained by

precipitating films of NMMO-cellulose solution in a water bath. The water-swollen films showed high CO2/N2, CO2/CH4, and CO2/H2 separation factors. Zhang and coworkers [11] measured the permeation of bovine serum albumin (BSA) through cellulose membranes prepared by coagulating films of NMMO-cellulose solution in aqueous NMMO-water baths. The scanning electron micrographs (SEMs) as well as pore size calculations indicate either dense films or films possessing extremely small pores (pore size ~ 15-40 nm). The researchers determined that BSA permeability decreased and BSA rejection increased with increasing solution cellulose concentration. Abe and Mochizuki [12] investigated the water permeation and sieving of dextran in flat hemodialysis membranes prepared from films of NMMO-cellulose solution coagulated in NMMO-water baths. While no morphological characteristics of the membranes were reported, our experience suggests that their casting protocols generated dense cellulose films. The authors indicate that water permeation increased with temperature and decreased with increasing cellulose concentration in the solution. In addition, they determined that the sieving coefficient (SC) for dextran (defined as the ratio of dextran concentration in the permeate to that in the feed solution) decreased with increasing temperature. However, the SC decrease was much less for smaller cellulose concentrations in the solution.

In contrast to the use of NMMO as a solvent, Zhou and Zhang [11] utilized an aqueous solution of urea and sodium hydroxide (NaOH) for dissolving regenerated cellulose. They prepared cellulose solutions by dissolving approximately 4.3 wt% cellulose polymer in a 6 wt% NaOH/4 wt% urea solution. Phase inversion was achieved by using aqueous H2SO4 solutions of varying concentrations as the coagulation bath. SEM analysis indicated that the films had an isotropic structure with very small pores (< 1μm).

This literature review indicates that research has focused on dense films or films with very small pore sizes. Even for the dense films, the information available in the open literature is rather meager compared to that for cellulose derivatives such as CA. If native cellulose is to be treated as a more common starting material for membrane formation, then protocols and methods to obtain porous cellulose films of specified pore size, porosity, and morphology need to be established. Clearly, the cellulose membrane morphologies reported to date do not seem suitable for NF, UF or MF separations.

In this work we have focused our attention on fabrication of porous cellulose films with morphologies suitable for NF/UF applications. By a judicious selection of solvents, casting conditions, solution composition, and solvent exchange steps, we have successfully cast dense as well as skinned asymmetric porous cellulose films. In this paper, we present details of the casting process and the resulting film characteristics including mechanical properties, N2 permeability, and pore size/porosity.

Materials and Methods Materials and casing solution preparation

All membranes were prepared from a hardwood acetate grade dissolving cellulose supplied by Rayonier Performance Fibers, Inc in the form of flat sheets. After vacuum drying at 80°C, small pieces (~ 1 mm × 3 mm) cut from the sheets were used to prepare the cellulose solution. Solid NMMO (97%) obtained from Sigma-Aldrich was used as the starting material for preparation of the cellulose solvent. Since NMMO is hygroscopic and forms a stable complex

with water, it was stored in a desiccator in a refrigerator. Whenever the NMMO bottle was opened, the space within the bottle was purged with dry N2 prior to closing. DMSO (analytical grade, Fisher) was the cosolvent, and was used as received; deionized (DI) water was used as a cosolvent for the NMMO. The polymer content (x) was varied in the range 4–12 wt%, and the casting solution composition was x wt% cellulose, 45 wt% NMMO, (100-x) wt% DMSO, and 5 wt% water. The water content of 5 wt% in the casting solution was chosen empirically, recognizing the fact that NMMO-water complexes (water:NMMO molecular ratio < 1) are direct solvents for cellulose [13].

A clear homogeneous cellulose solution was obtained by adding the above components to a glass conical flask, and heating the flask in a silicone oil bath at 135°C under constant stirring for 20 min. At such a high temperature, degradation reactions occur that form several byproducts that, in turn, can provoke severe effects such as the degradation of cellulose, and accelerated decomposition of NMMO [13]. To prevent these side reactions and to stabilize NMMO, a small quantity of propyl gallate (PG, Sigma-Aldrich, 97%, 0.005g/g of cellulose) was added to the cellulose solution. Water evaporation from the casting solution during heating can change the composition of the casting solution and seemed to adversely affect film morphology. Hence, evaporation of water was limited by piercing a Pasteur pipette through the septum that sealed the conical flask; the evaporated water condensed in the pipette and dripped back into the casting solution.

Dense Film casting

To obtain dense cellulose films, the cellulose solution was poured on a clean glass plate between 200-μm steel shims, and a film was cast using a casting knife. The glass plate was then immersed in a DI water bath. Generally, the cellulose films peeled off the glass plate within 5 minutes of immersion. The films were washed by successively transferring them to two additional water baths for 30 minutes each, and finally stored in a third water bath overnight. The dense films so obtained were significantly swollen with water, and underwent significant shrinking and deformation upon drying. The dried films were extremely brittle, greatly distorted, and unsuitable for analytical testing. The shrinkage-induced deformation was prevented/minimized by using two different drying protocols:

(1) After cutting off all the edges, the films were placed on glass plates and exposed to ambient conditions. Since the films adhered to glass strongly, they retained their flat shape even after the water had evaporated. When the corners started peeling, the glass plates were immersed in a water bath, and the films peeled-off. These films were placed on paper towels, and after wiping off the excess water, kept in a vacuum oven at room temperature for 24 hr. The residual stresses were relieved by placing the films in a vacuum oven at 110°C for 24 hr. The dry film thickness was 14 ± 0.5 μm.

(2) The filmswere transferred and stored in an isopropyl alcohol (IPA) bath for 24 hr. Subsequently, slow drying was conducted by placing the films in a 1 mm gap between two glass plates and keeping them in a vacuum oven for 48 hours at room temperature. Again the residual stresses were relieved by keeping the films in the vacuum oven at 110°C for 24 hours. The dry film thickness was 14 ± 0.5 μm.

Porous Film Casting

To obtain porous films, the glass plate was immersed in an acetone bath. Acetone is a nonsolvent for cellulose, and the ensuing mass transfer involving acetone, NMMO, DMSO, and water led to the formation of porous films. Due to the high surface energy of water, the pores invariably collapsed when the films were simply air-dried. In order to preserve the morphology, solvent exchange steps were incorporated into the protocol. After immersing the films in acetone for 20 minutes, the films were placed in an isopropyl alcohol bath for 20 minutes. Subsequently, they were stored in a heptane bath for 24 hours. The films were then dried by placing them on glass plates and exposing to dry ambient conditions. In order to ensure complete removal of residual solvent, the films were finally stored in a vacuum oven at 80°C.

Cellulose Film Characterization

SEM analysis (Aspex Instruments, Tungsten filament with a 15 keV beam energy), tensile testing (Instron 8500 with a 5000 N load cell), and N2 permeability measurements were utilized to characterize the dense films. Cross sections of the dense films for SEM analysis were obtained by standard freeze-fracturing. For tensile testing, small strips (50 mm × 3 mm) of the dense films were attached to a specially designed fixture and extended under a constant rate of 0.1 mm/sec. The force-elongation data were converted to corresponding engineering stress-strain values using the initial specimen dimensions, and the tensile modulus, failure stress, and failure strain were determined. N2 permeability was obtained via the permeate pressure-rise technique. Small circular samples (diameter 25 mm) were placed in a permeation cell that was pressurized to 552 kPa (80 psi), and the rise in permeate pressure with time was recorded.

The effect of the polymer concentration on the porous film morphology was studied by casting porous films from 4, 7, and 11 wt% cellulose in the casting solution. The morphology was characterized in terms of the skin layer thickness, pore-size distribution, and total porosity. Commercial image analysis software (Sigmascan) was used to obtain these three parameters from SEM micrographs of the film cross sections.

Results and Discussion Dense film studies Microscopy

The dense films obtained by the aforementioned procedure were transparent and had a thickness of 14 ± 0.3 μm. Figure 2 shows SEM micrographs of typical dense film cross sections. The micrographs indicate the expected unremarkable film structure with no pores apparent within the resolution limit of the SEM (~ 0.1 μm). However, the films might still possess small pores of the order of a few nanometers. No evidence of significant differences in microstructure or thickness was obtained among the dense films obtained via the two drying protocols. We obtained good control over the final thickness of the films, which could be easily varied by using shims of different dimensions.

Mechanical property measurements

The tensile properties of the dense films were measured using a mechanical test system in order to ascertain the processability of the films in conventional fabrication equipment. For

comparison, CA films fabricated in our laboratory via dry casting from a binary 15/85 wt% CA/Acetone solution were also tested. The measurements were conducted on 14 samples of cellulose films dried via protocol 1, four samples of cellulose films dried via protocol 2, and 10 CA film specimens. Table 1 summarizes the mechanical properties obtained including the tensile modulus (E) and the stress (σf) and strain (εf) at failure. The cellulose films dried via protocol 2, *i.e.*, initial immersion in an IPA bath followed by slow drying between two glass plates, evidenced higher ductility than those dried via protocol 1. Since the films had been thoroughly dried to remove all of the volatile IPA, it is unlikely that residual solvent plasticized the films. We believe that the higher ductility of these films is caused by IPA conditioning. Since cellulose-water interactions are stronger than cellulose-IPA interactions (as reflected in the liquid retention values [5]), differences in the drying process likely produce differences in the inter-and intramolecular hydrogen bonding patterns for the cellulose hydroxyl group. A lower degree of intermolecular hydrogen bonding between the cellulose chains for the IPA-dried films could account for the higher ductility.

In general, the only significant difference in mechanical response of the specimens was the more brittle nature of cellulose as compared to the CA films. This is expected, since cellulose films will have a significant degree of crystallinity, while CA has only limited crystallinity. The failure strain values in the range 5–10% agree with those reported in the literature for regenerated cellulose fibers [5]. The larger variability in the failure strain of the cellulose films appears to be caused by residual non-uniformity in the cellulose film samples. Despite the rigorous drying protocols employed, some of the films still contained small folds and creases. We observed that the more uniform cellulose samples evidenced somewhat greater failure stress and smaller failure strain values. Nonetheless, the mechanical property values obtained suggest that the dry cellulose films compare favorably to the CA films, and most likely possess sufficient mechanical integrity to enable processing on conventional fabrication equipment after casting and drying.

Gas permeability measurements

Prior to conducting nitrogen permeability measurements, the cellulose dense films were placed in the permeation cell and both sides of the films were exposed to nitrogen pressurized to 552 kPa (80 psi) for 12 hours. Permeability testing was initiated after the films had been equilibriated with nitrogen in this fashion. Multiple permeability measurements were performed on each cellulose film sample, since the film permeability was found to decrease with each progressive measurement. This suggests collapse of nanopores or the presence of residual solvent. Typical permeability values obtained on a single cellulose film are shown in Figure 4. Whereas the initial values were high, film permeability seemed to attain a constant value after six consecutive runs. Consequently, 10 successive measurements were conducted on each cellulose film sample. Figure 5 shows the consolidated nitrogen permeability data obtained from three films dried via protocol 1 and protocol 2, respectively, as well as three CA films. The data indicate that the film permeability depends upon the drying protocol. Films that were immersed in isopropyl alcohol prior to slow drying evidenced lower permeability values than the films that were simply air-dried (protocol 1). The relatively modest difference may reflect small differences in the nanostructure or in the degree of crystallinity.

Porous film studies

Effect of the presence of water on film morphology

Subtle variations in the composition of the ternary cellulose solvent system can have a significant effect on the morphology of the resulting cellulose films. Figure 6a shows the structure of a porous film that was cast from a cellulose solution in which the evaporated water was not recycled, *i.e*. returned to the solution. These films had a dense structure with small pores, in which the larger pores likely have collapsed. In contrast, when the evaporated water was returned to the casting solution, the films (Figure 6b) had a well-defined pore structure. While the exact mechanism for this behavior is unclear, we believe that the pore collapse is related to the kinetics of the phase inversion process. The solutions with slightly lower water content are in a "poorer" solvent for the cellulose polymer and thus precipitate more rapidly when immersed in the non-solvent bath. Pore collapse is generally associated with rapid phase inversion during the coagulation step [15-17], whereas slow mass transfer in the solutions with high water content leads to the formation of a more spongy porous structure (Figure 6b).

Effect of cellulose concentration on film morphology

Having established the importance of controlling the water concentration in the cellulose solvent system to prevent pore collapse, we cast several porous films using water recycle during cellulose dissolution and studied the influence of cellulose solution concentration on the porous film morphology. As expected, the pore size as well as the porosity decreased with an increase in the casting solution cellulose concentration (Figures 7 and 8). The lowest cellulose concentration of 4 wt% yielded films with large pores having a mean diameter of 4.8 μm. The pore diameter monotonically decreased to 2.9 μm and 1.8 μm when the cellulose concentration was increased to 7 wt% and 10 wt%, respectively. Figure 9 shows the pore-size distribution obtained from image analysis of multiple films at each cellulose concentration. The distribution was wide at a 4 wt% cellulose concentration due to the presence of large pores with diameters greater than 10 μm. The distribution progressively became narrower with increasing cellulose concentration, indicating much smaller differences in the pore sizes. The similarity of the pore-size distributions of multiple samples at the same solution cellulose concentration indicates the reproducibility of the porous film formation protocols. Thus, films with a mean pore diameter in the range 1.8–4.8 μm can be produced by simply using a solution with the appropriate cellulose concentration.

Figure 10 shows the morphology of films made from the three cellulose solution concentrations. The cross-section micrographs (Figures 10b, 10e, 10h) reveal that the porous films possess a skinned asymmetric structure, with small pores immediately beneath the skin, and pore size increasing away from the skin. Even though all of the films possessed a skin, the top surface of films made from 4 wt% cellulose concentration evidenced isolated small pores, probably formed because the thin skin layer is not strong enough to withstand the large interfacial stresses created during skin formation.

Conclusions

The availability of new solvents such as NMMO, DMAc/LiCl, and 1-butyl-3-methylimidazolium chloride provides potential new routes for the synthesis of membranes directly from unmodified cellulose polymer. By using a judicious selection of solvents, cosolvents, non-solvents and casting solution composition we were able to reproducibly cast dense films as well as porous cellulose films with mean pore diameters in the range 1.8–4.8 μm. Compared to dense CA films, the dense cellulose films were somewhat more brittle with similar N2 permeability values. Interestingly, the mechanical behavior depended upon the drying protocol employed, with films undergoing an IPA exchange step evidencing a slightly more ductile response. This dependence is most likely due to changes occurring in the hydrogen bonding at the intra- and inter-molecular level during the drying process.

Subtle changes in the composition of the ternary cellulose solvent system significantly affected the porous structure. Porous films with a skinned asymmetric structure, and anisotropic porosity, i.e., small pores beneath the top skin and pore size increasing away from the skin, could easily be obtained. The mean pore size of these films can be altered by appropriate variation in the cellulose concentration of the casting solution.

Although the porous morphologies obtained would be suitable for ultrafiltration applications, some significant limitations for water-based uses exist since cellulose swells significantly in the presence of water and is especially susceptible to biological fouling. However, given the advantages of low cost and an environmentally friendly material, porous cellulose films might well find a niche in non-aqueous separation applications.

Acknowledgements

The authors gratefully acknowledge support of this research by the US Department of Energy through award DE-FC01G011084 and the technical support provided by the NSF Industry/University Cooperative Research Center for Membrane Applied Science and Technology (MAST) at the University of Colorado.

References

[1] Lloyd, D.R.; Meluch, T.B. In Materials science of synthetic membranes, D.R. Lloyd, Ed.; ACS Symposium Series, 269, 1985.

[2] Cardew, P.T.; Le, M.S. Membrane processes: A technology guide; The Royal Society of Chemistry: Cambridge, 1998.

[3] Koros, W.J.; Fleming, G.K. J Membrane Sci 1993, 83, 1.

[4] Baker, R.W. Membrane technology and applications, 2nd ed.; John Wiley: West Sussex, UK, 2004.

[5] Klemm, D.; Philipp, B.; Heinze, T.; Heinze, U.; Wagenknecht, W. Comprehensive cellulose chemistry, Vol 1. Fundamentals and analytical methods; Wiley VCH: Germany, 1998.

[6] Wu, J.; Yuan, Q. J Membrane Sci 2002, 204, 185.

[7] Fink, H.P.; Weigel, P.; Purz, H.P.; Ganster, J. Prog Polym Sci 2001, 26, 1473.

[8] Swatloski, R.P.; Spear, S.K.; Holbrey, J.D.; Rogers, R.D. JACS 2002, 124, 4974.

[9] Liu, R.; Shen, Y.; Shao, H.; Wu, C.; Hu, X. Cellulose 2001, 8, 13.

[10] Peng, S.; Shao, H.; Hu, Z. J Appl Polym Sci 2003, 90, 1941.

[11] Zhang, Y.; Shao, H.; Wu, C.; Hu, Z. Macromol Biosci 2001, 1, 141.

[12] Zhou, J.; Zhang, L.; Shu, H.; Chen, F. J Macromol Sci – Physics 2001, B41, 1.

[13] Biganska, O.; Navard, P. Polymer 2003, 44, 1035.

[14] Rosenau, T.; Potthast, A.; Adorjan, I.; Hofinger, A.; Sixta, H.; Firgo, H.; Kosma, P. Cellulose 2002, 9, 283.

[15] Machado, P.S.T.; Habert, A.C.; Borges, C.P. J Membrane Sci 1999, 155, 171.

[16] Kang, Y.S.; Kim, H.J.; Kim, U.Y. J Membrane Sci 1991, 60, 219.

[17] Vandenburg, G.B.; Smolders, C.A. J. Membrane Sci 1992, 73, 103.

Table 1: Mechanical Properties of Porous Cellulose and CA Films.

Polymer	Tensile Modulus (GPa)	Failure Stress (MPa)	Failure Strain (%)
Cellulose	1.6 ± 0.6	64.9 ± 18.3	6.5 ± 1.5
CA	2.0 ± 0.6	60.1 ± 11.6	13.1 ± 8.0

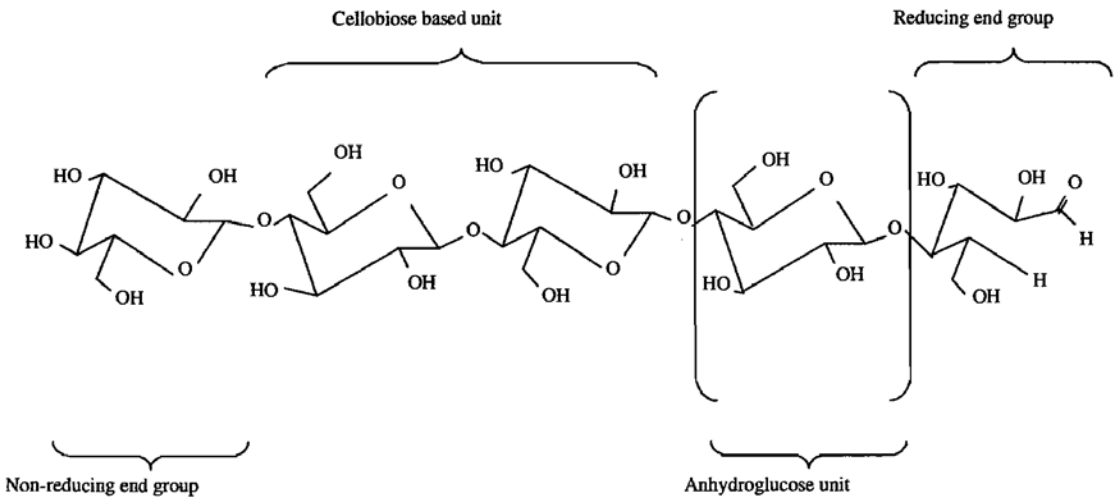

Figure 1: Molecular structure of cellulose. Cellulose is a linear syndiotactic homopolymer composed of D-anhydroglucopyranose units (AGU) linked together by β-(1→4)-glycosidic bonds. If the dimer cellobiose is considered as the basic unit, then cellulosecan be considered as an isotactic polymer of cellobiose.

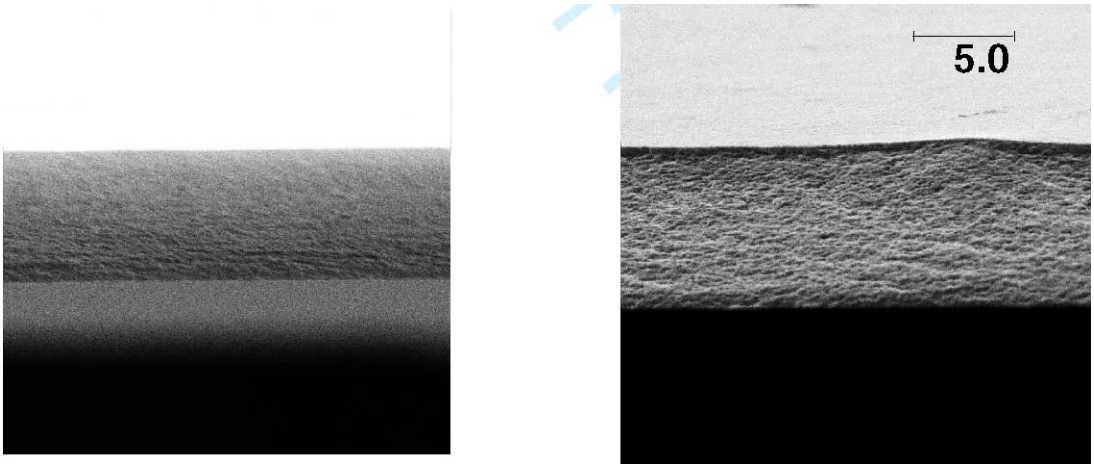

(a) (b)

Figure 2: SEM micrographs of the cross-sections of two identical dense films obtained using a 4wt% cellulose solution concentration and the following drying protocols: slow constrained air-drying (a) and IPA exchange followed by slow air-drying (b). Films of thickness 14 ± 0.3 μm could be reproducibly obtained, and no pores could be observed in the cross section within the resolution limit of the SEM (~ 0.1 μm). However, nitrogen permeation measurements suggested that the films might contain smaller pores, i.e., on the order of a few nanometers.

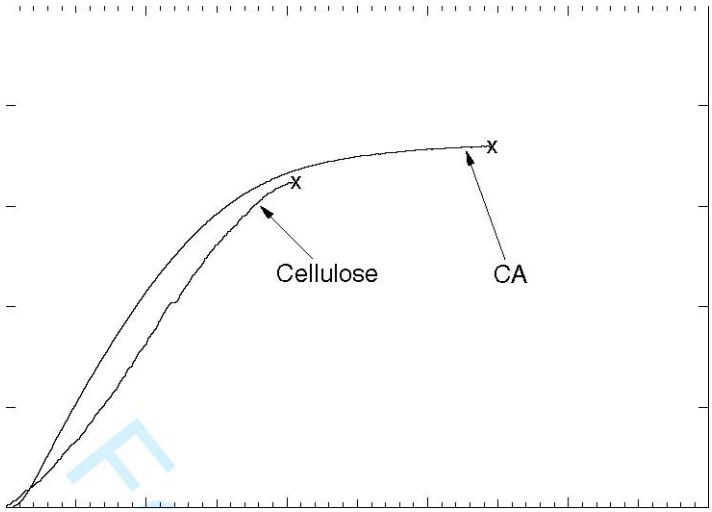

Figure 3: Representative stress-strain responses of a cellulose and CA film: X indicates failure.

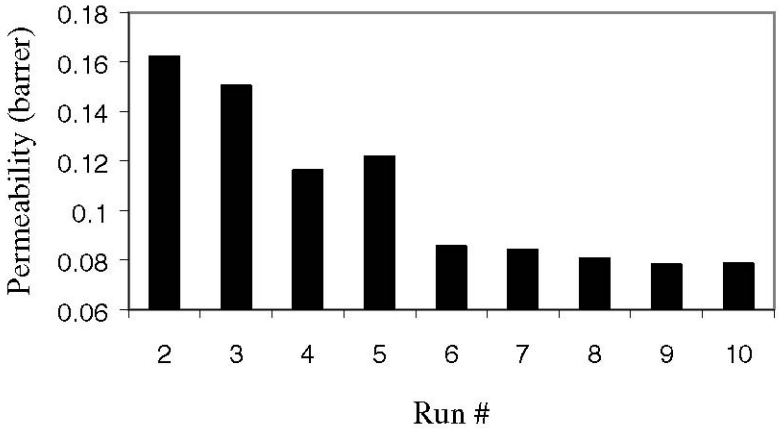

Figure 4: Results of permeability measurements conducted on a single cellulose film sample.Successive measurements yielded progressively decreasing permeability values. However, film permeability attained a relative constant value after six successive runs.Consequently, 10 runs were conducted on each sample, and the mean of the final fourruns was taken as the sample permeability.

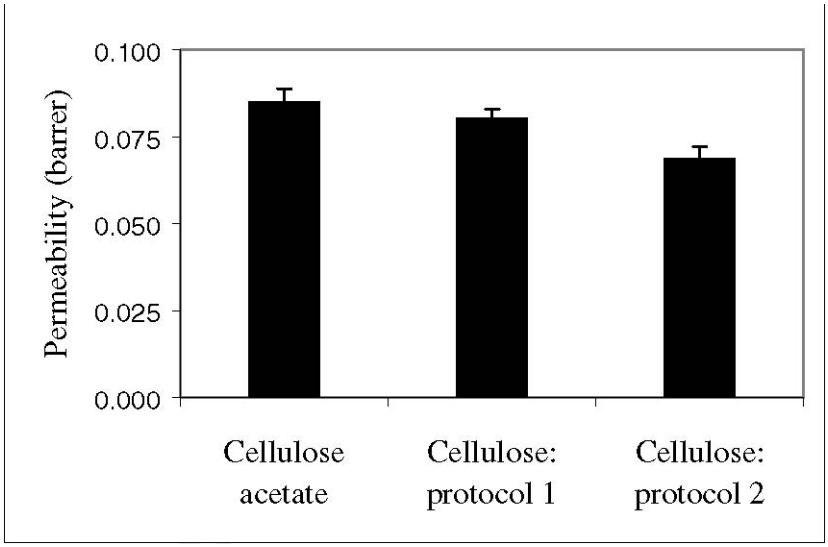

Figure 5: Consolidated nitrogen permeability data obtained from three samples each of cellulose films dried via protocols 1 and 2, as well as CA dense films. Cellulose films dried via protocol 2 (isopropyl alcohol immersion prior to slow drying) evidence the lowest permeability values.

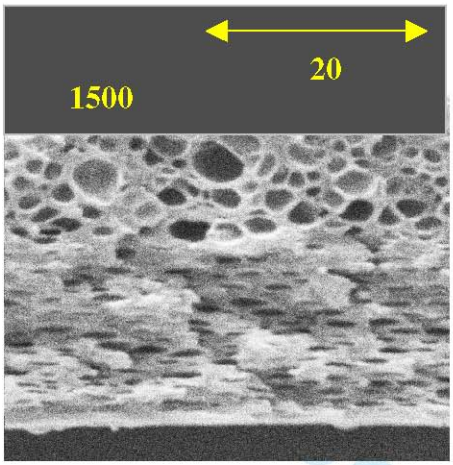

(a)

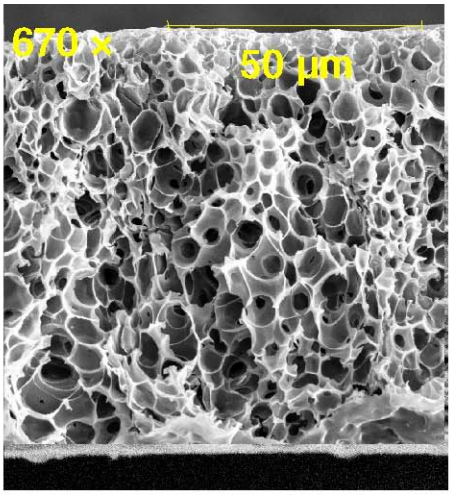

(b)

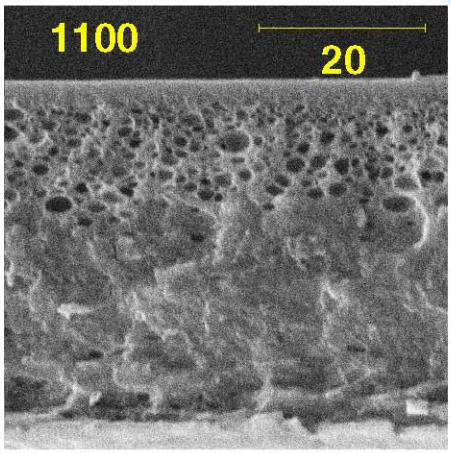

(c)

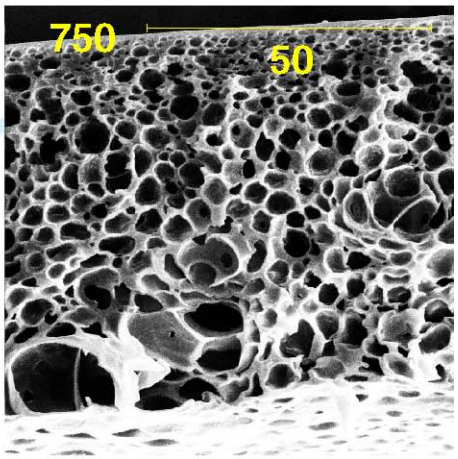

(d)

Figure 6: SEM micrographs of porous film cross-sections with (a and c) and without (b and d)water recycle during dissolution. For the films in (a) and (b), the solution contained 7 wt% cellulose, while for (c) and (d), the solution contained 10 wt% cellulose. The morphologies shown in (a) and (c) indicate that the loss of water via evaporation leads to pore collapse during drying.

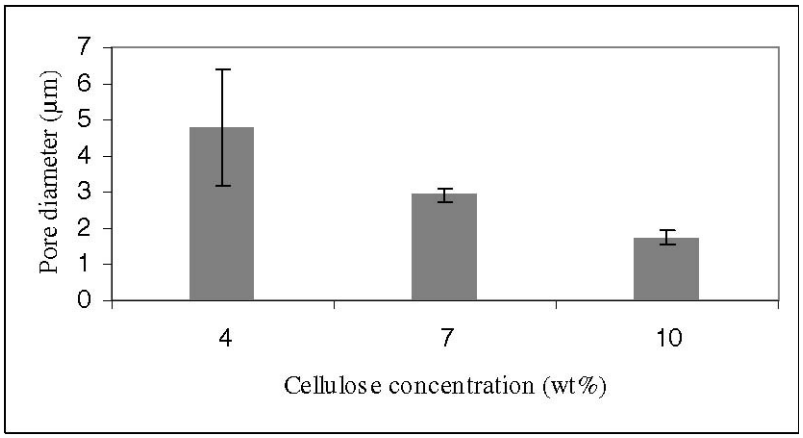

Figure 7: Influence of the cellulose concentration in the solution on the mean pore diameter.

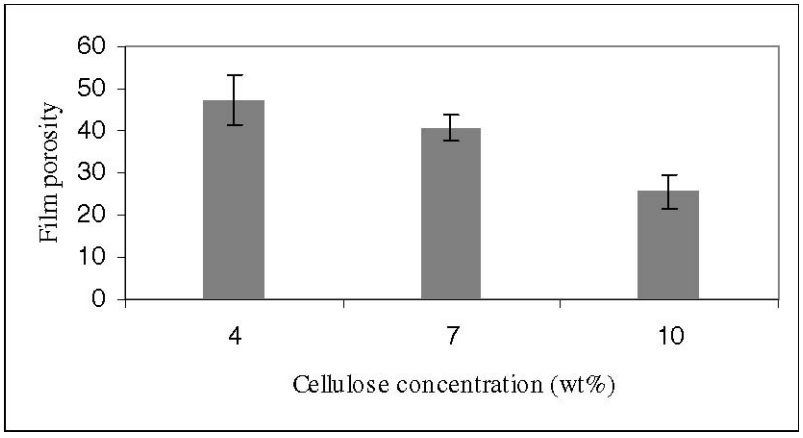

Figure 8: Influence of the cellulose solution concentration on film porosity. (b)

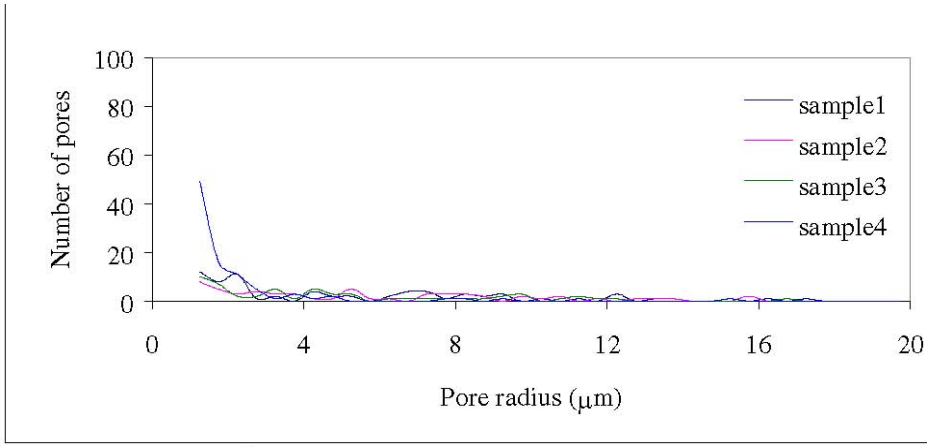

(a)

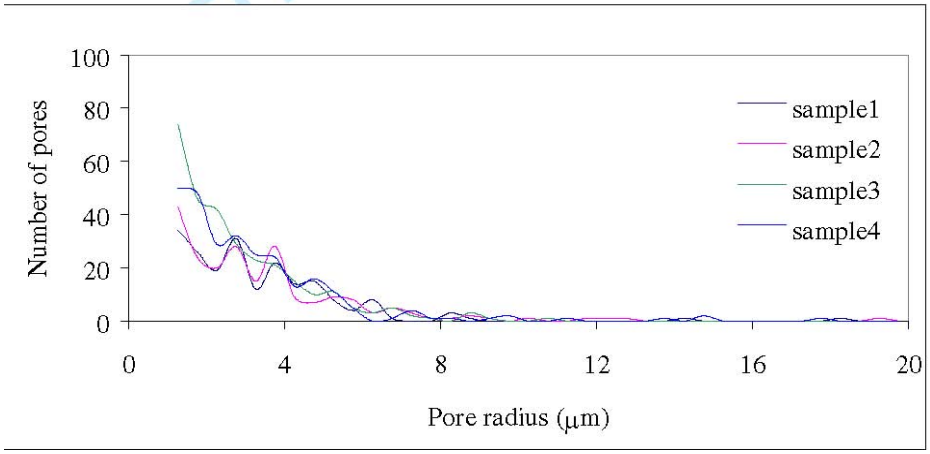

(b)

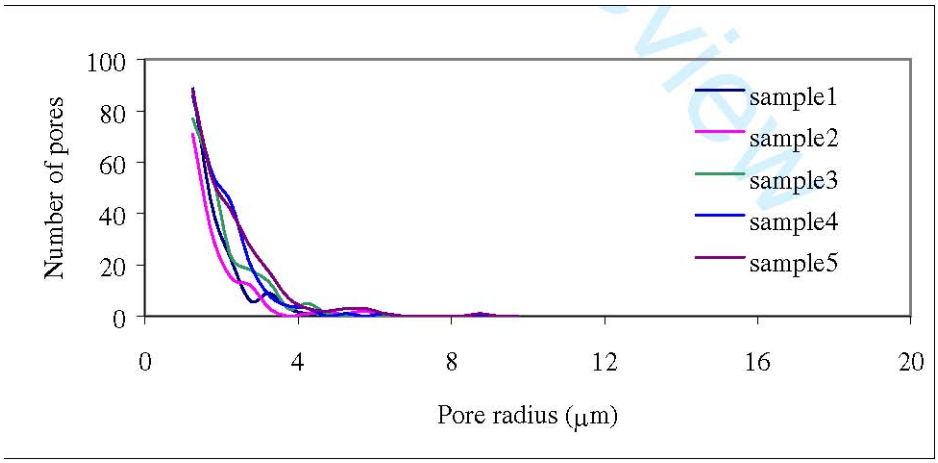

(c)

Figure 9: Pore-size distribution graphs for porous films made from 4 wt% (a), 7 wt% (b), and 10 wt% (c) cellulose concentrations. The figures show a systematic decrease in the poresize with an increase in the cellulose concentration in the solution. At each concentration, tests were conducted on multiple films so that the reproducibility of theporous film formation protocol could be established.

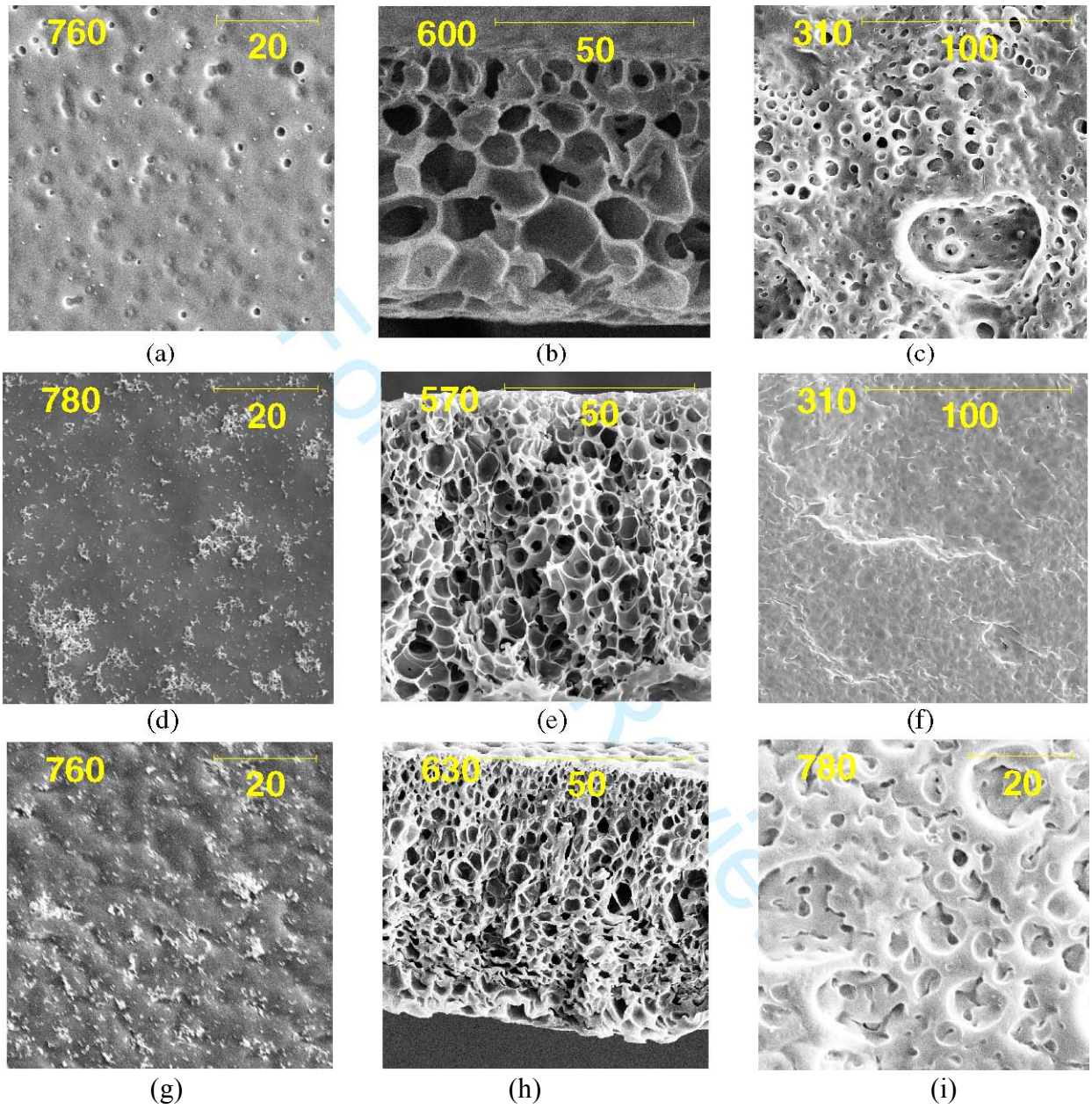

Figure 10: SEM micrographs showing the morphology of cellulose films prepared from solutions with different cellulose concentrations. Figures (a), (d), and (g) correspond to the topsurface of films cast using 4, 7, and 10 wt% cellulose in the solution, respectively.Likewise, figures (b), (e), and (h) correspond to the cross-section, and figures (c), (f),and (i) correspond to the bottom surface at the three cellulose concentrations. The skin at the top surface is non-porous, and the micrographs indicate the precipitation of some polymer at the higher (7 and 10 wt%) cellulose concentration. The cross sections reveal a skinned asymmetric structure.

3.3) TASK # 3 Preparation and Characterization of Interconnect (LBL/Ai)

3.3.1) Optimization of alloy for use as interconnect

Initally, the intent was to develop an alloy based on AI's past experience. This was to be done through a subcontract to Colorado School of Mines (CSM). As can be seen in the report which follows, this was not possible due to problems at CSM. As a result, the decision was made to focus on Ebrite as the interconnect.

ACSEL
Advanced Coatings and Surface Engineering Laboratory

Report no: CSM/MT/ACSEL/003/008

PROJECT REPORT

MOLTEN SALT ELECTRODEPOSITION AND PVD SPUTTERING OF La-Sr-Cr THIN FILMS & DEVELOPMENT OF Fe-Cr-Nb-La FERRITIC STAINLESS STEEL ALLOY

Contract Number: ***4-49886***
PERFORMANCE PERIOD: ***12.15.01 – 11.30.02***

Submitted to

Dr. Glen M. Benson
President
Aker Industries
952-57 th Street
Oakland, CA 94608-2842

Submitted by

Brajendra Mishra
Iman Maroef
Dalong Zhong

ADVANCED COATINGS & SURFACE ENGINEERING LABORATORY
DEPARTMENT OF METALLURGICAL & MATERIALS ENGINEERING

FEBRUARY 15, 2003

RESEARCH PROJECT REPORT

Task Description:

The Colorado School of Mines was assigned three tasks by Aker, Inc.:

(1) Produce 5-10 μm coating of co-deposited La-Sr-Cr thin film by electrodeposition.

Parameters: pulse dc-power deposition
Film composition in the range of Cr-$La_{(0.8\text{-}0.9)}$-$Sr_{(0.2\text{-}0.1)}$ at%
Anhydrous $LaCl_3$, $CrCl_2$, $SrCl_2$ molten salt electrolyte
Ferritic Fe-Cr-Nb-La alloy substrate (cathode)
Inert atmosphere
Removal of adherent salt and protective coating of samples

(2) Produce 1/8" thick strips of Fe-Cr-Nb-La Ferritic steel.

Parameters: Alloy composition: 22-24% Cr, 2% max. Nb and 0.1-0.2% La
Vacuum melting and cooling
Annealing for homogenization
Hot rolling to 1/8" thickness
Annealing and polishing

(3) Produce 5-10 μm coating of co-deposited La-Sr-Cr thin film by PVD sputtering.

(This task was later changed to a deposition of La-Sr-Cr-O film due to the difficulties in producing a La-Sr sputtering target experimentally and commercially.)

Parameters: Co-sputtering from La_2O_3-SrO mixed-oxide & chromium targets
Ferritic Fe-Cr-Nb-La alloy substrate

The products in each of the three tasks required chemical/optical and electron-microscopic analysis.

Results:

(2) Task 2 was taken up first due to the delay in the procurement of a dc-electroplating pulsed power supply.

General Practice:

The general practice to produce the ferritic stainless steel alloys for the metal interconnect is described below. The differences and variations in the three experiments are highlighted.

a. Vacuum melting of alloying elements, added either as pure elemental powders or as sheets, was performed with closely matching compositions to the desired

final product. Vacuum melting was done under low vacuum (50 mTorr), with several cycles of vacuum and argon gas purging applied to displace residual air in the vacuum furnace chamber before heating up to peak temperature. Temperature profiles, on an average, consisted of 5 hours heating time to 1700 C, 5 hours holding time at temperature of 1700 C, and finally 5 hours cooling time down to room temperature. The crucible used to contain the molten alloys was initially alumina, which was then replaced by magnesia due to a noticeable contamination of the alloy with aluminum. 4" dia x 8" tall crucibles were used for melting.

b. The ingots were cut in to smaller pieces for better mixing of the alloy during the subsequent vacuum re-melting. This step was considered necessary due to the limitation of the vacuum furnace to cast the molten alloy. Using the standard heating elements made of graphite electrode and connected by molybdenum pins in the high temperature vacuum furnace, opening the furnace door for casting purposes was not possible. Thus, alloys were slow cooled over five hours of cool down time during solidification. With such a limitation, gravitational segregation of elements was the major problem that required cutting and re-melting.

c. Vacuum re-melting was performed on the alloy with the same temperature program as in step (a). Cut pieces of the alloy were stacked in an order to obtain the best mixing of the elemental addition. At this stage, a crucible with a larger diameter of 6" was used to give additional mixing action by spreading of the re-melt.

d. Preparation for hot rolling was done by cutting off some material from the top and bottom sides of the second ingot to remove agglomerates of oxides and attached crucible pieces. The ingot was cut in to 1" thick pieces for rolling.

e. Hot rolling was done with a start temperature of 1200 C. The ingot was annealed in air furnace for at least half an hour at the 1200 C before hot rolling. Hot rolling was done with a reduction of 10 to 15 pct. per pass. A maximum of four passes were allowed at one hot rolling schedule to maintain the hot deformation at red-hot temperature regimes. At least two intermediate annealing, also at 1200 C, were needed to get the alloy to reach the final thickness of less than 0.1 inch.

f. The thin plates were ground and polished for the subsequent oxidation tests at Lawrence Berkeley Laboratories and for molten salt electro-deposition substrates.

Three batches of process development were undertaken to reach a final product.

Melt 1:

Initial effort to make the alloy was carried out by using high-chromium ferritic stainless steel sheets provided by Allegheny-Ludlum. This stainless steel was not the preferred AISI 446, as known to have been provided by the same company in the past. AISI 446 was considered ideal because the chromium is

already well mixed. As an alternative, an alloy AL29-4C was offered by the company because it contained 29 wt. % Cr and without the presence of nickel. This alloy, however, contained 4 wt.% Mo, which was found to be high for the intended high temperature application of the product alloy. Nb and La were added as flakes and small chips, respectively. The composition of the first melt is: (in wt. %):

0.021 C,	0.33 Mn,
0.022 P,	0.0011 S,
0.27 Si,	28.91 Cr,
0.27 Ni,	0.031 Al,
3.77 Mo,	0.079 Cu,
0.37 Nb,	0.11 V,
0.17 Ti,	0.023 N.

The composition of the alloy, after hot rolling process, is shown in Table 1.This batch failed to meet the specification due to the high content of Mo, Cr, and Nb.

Melt 2 :

The second batch was prepared by direct powder addition of chromium to pure iron sheets, in addition to Nb and La. The composition of the pure iron sheets is (in wt. %)

0.007 C,	0.010 Mn,	0.002 P,	0.0015 S,	0.13 Cu,	0.042 Ni,
0.003 Cr,	0.005 Cb,	0.006 Mo,	0.001 Si,	0.009 Co,	0.001 Pb,
0.10 Sn,	0.003 Al.				

As in the case of the first melt, La and Nb additions were in the form of flakes and chips. It was anticipated that this alloy should only have Fe, La, Nb, and Cr in its chemical composition. However, aluminum contamination was detected and was considered unacceptable. It was thought that lanthanum melted at appreciably lower temperature than the others and had a lot of chance to deoxidize the alumina crucible. Another unacceptable microstructural feature from this alloy was the distribution of the alloying elements, which was severely non-uniform. Many second phase precipitates with high content of Nb and Cr were found by LBL to cause non-uniform oxidation potential on the metal interconnect surface. It was thought that the melting of the Nb flakes was incomplete because the peak heating temperature during the vacuum melting was only 1700 C, which was about 700 C lower than the melting point of pure Nb. Pure Nb particles might have also remained in the alloy in the addition to Nb-rich second phase precipitates. The as hot-rolled composition of this alloy is also shown in Table 1.

Melt 3 :

The third batch was made by a process very similar to the 2nd batch, with some changes necessary to prevent undesirable results obtained earlier. Magnesia crucible was used to replace alumina ones to contain the melt. Better stability of magnesia was expected to prevent the contamination similar to that occurred

due to alumina reduction by La. An additional melting step was applied in between the first and the second vacuum re-melting. In this intermediate melting process, the ingot was tungsten arc melted, with pure argon shielding gas and with 200 amperes current. In this intermediate process, the alloy experienced a temperature approximating the boiling point of the alloy (2000 – 2500 C). With this level of heating, complete melting of Nb should be easily accomplished. High level of current during the tungsten arc melting should also provide significant magnetic stirring of the molten pool. After this process, the arc-melted ingot was then vacuum re-melted back at peak temperature of 1700 C. Small volume of finely distributed Nb-Cr rich second phase was still observed from the as-hot rolled product. It was possible that the slow cooling rate after the vacuum re-melting precipitated these second phase particles. Slow cooling rate is one of the limitations of the vacuum furnace. The chemical composition of the third alloy, shown in Table 1 (top and bottom surface compositions), reflects the success of mixing provided by the arc melting. A further 24-hour annealing at 1100 C, followed by water quenching, of a sample cut from the final hot-roll product was found to significantly dissolve this second phase.

Table 1. Composition of the three batches of alloys for the metal interconnect.

	Batch 1		**Batch 2**		**Batch 3**	
	(top)	(bottom)	(top)	(bottom)	(top)	(bottom)
Fe	65.44 ± 0.64	62.27 ± 0.67	76.09 ± 0.68	72.83 ± 0.70	73.72 ± 0.47	73.08 ± 0.47
Cr	29.09 ± 0.33	28.26 ± 0.34	21.26 ± 0.20	17.87 ± 0.20	24.19 ± 0.15	24.52 ± 0.21
Nb	1,33 ± 0.16	2.72 ± 0.17	2.29 ± 0.20	5.06 ± 0.23	1.69 ± 0.14	1.92 ± 0.14
La	0	0.1 ± 0.15	0.23 ± 0.14	3.93 ± 0.34	0.22 ± 0.10	0.26 ± 0.10
Mo	3.14 ± 0.16	3.80 ± 0.19	0	0	0	0
Mn	0.62 ± 0.20	0.89 ± 0.20	0	0	0	0
Si	0.38 ± 0.04	1.95 ± 0.06	0.12 ± 0.04	0.31 ± 0.04	0	0
Al	Detected NA	Detected NA	Detected NA	Detected NA	0.12 ± 0.03	0.14 ± 0.03

NA : not analyzed

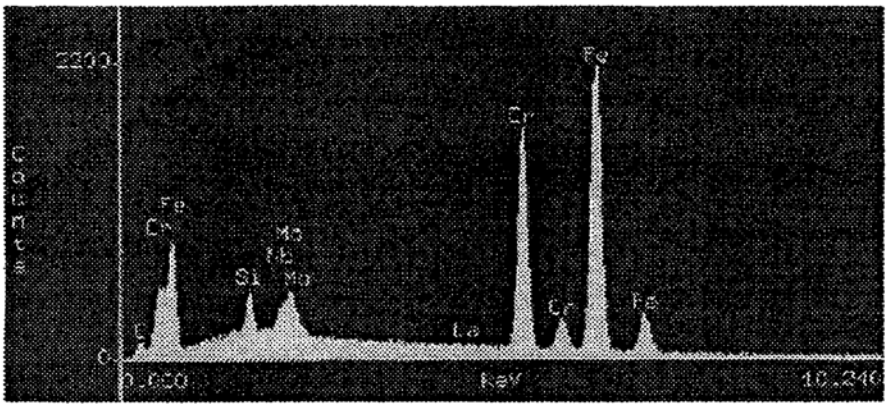

Fig.1. Energy Dispersive Spectrum [EDS] of the first alloy (measured from the bottom surface).

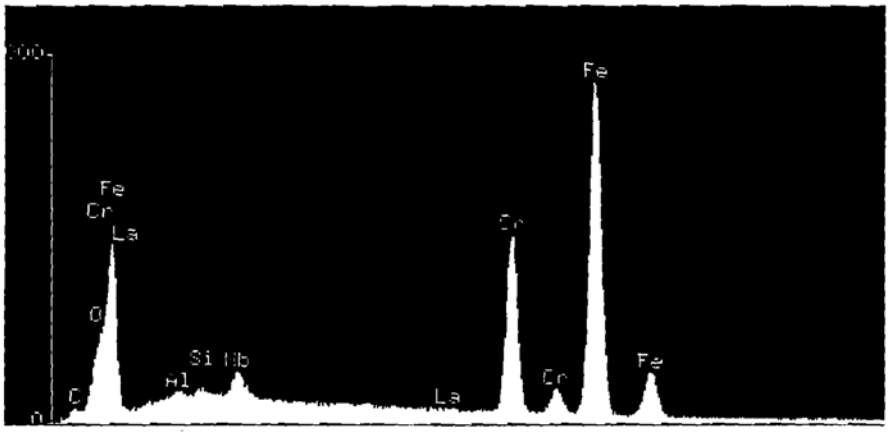

Fig.2. EDS of the second alloy (measured from the bottom surface).

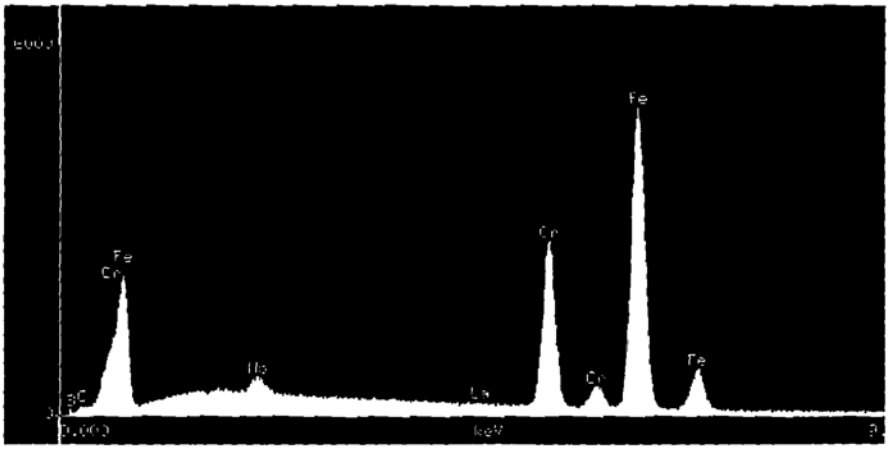

Fig.3. EDS of the third alloy (measured from the bottom surface).

Figure 4 shows the oxidation test results of Melt-3 alloy, as reported by LBL. It was reported that Melt-3 contained non-uniform La distribution and had oxidation kinetics similar to the commercial 446 Alloy comprising primarily of chromium tri-oxide layer.

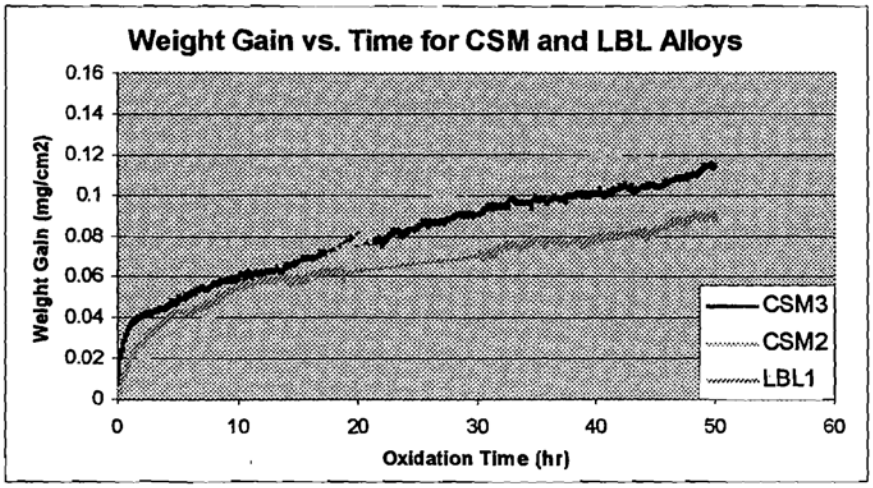

Figure 4: Oxidation kinetics of CSM's Melt-2 and Melt –3 alloys compared with the alloy produced by LBL.

(3) Task 3 was designed to produce a La-Sr-Cr thin film alloy containing high amounts of oxygen by using PVD co-sputtering from a La_2O_3-SrO composite target and a metallic chromium target. As the first attempt, La-Sr-Cr films were planned through PVD sputtering.

Target Preparation:

La-Sr targets could not be procured commercially as the target vendors were unable to produce such a target due to the high reactivity of the metals. CSM attempted to produce the target of La-Sr first by vacuum melting the metals, but the oxidation was excessive and the mixing of metals was poor. Hot pressing of these metal powders was not possible as lanthanum is not available in the powder form.

The lanthanum oxide-strontium oxide powder mixture was hot pressed at 1500 C under vacuum and a pressure of 20 Mpa. The powders pressed well, but the target strength was limited. Additionally, the oxides were found to be extremely hygroscopic and crumbled when stored in a desiccator.

The third successful attempt to make the target employed chromium metal as the binder for the oxide powders to achieve better hot pressed strength and room temperature stability. 20 wt. % Cr metal powder was used along with oxide powders in the ratio of 80 at % La_2O_3 and 20 at % SrO. A good 2.5" dia. X 3/16" thick target was produced with adequate strength for handling.

PVD Sputtering

DC magnetron sputtering using two cathodes at 37° angle was tried. The cathodes comprised of the pressed La_2O_3-SrO-Cr target and a metallic 5" chromium metal target procured commercially. Adequate sputtering rate of 0.2 μm/min was achieved from the chromium target. However, the system failed to generate a sustained plasma from the oxide composite target even at the highest power setting of 1900 kW and in spite of pulsing the cathode. Plasmas could only be sustained for 30 to 45 seconds during which negligible deposition occurred from the target. It should be note that the system is able to generate a sustained plasma from an alumina target at these power levels, albeit the slow deposition rate of 2 μm/hr.

It was thus, concluded that the oxide target has a very high resistance (simple multi-meter measurement indicates infinite resistance), which does not allow a plasma generation. Thus, PVD sputtering of even a La-Cr-Sr-O thin film was unsuccessful by dc magnetron sputtering.

It is suggested that a RF sputtering from oxide target can be successfully employed. RF sputtering is used for insulator deposition and for materials with very high resistance. However, the CSM RF sputtering unit is not capable of using the 2.5" dia target and requires 5" x 15" rectangular targets. CSM could not make such as target or commercially procure it with the allotted time, resources and equipment availability. RF sputtering of the material, never the less, remains a possible method to obtain thin films of La-Sr-Cr-O.

(1) Molten salt electrodeposition of La-Sr-Cr from a molten chloride salt mixture at high temperature (> 950°C) was researched to produce a 5-10 micron thick uniform film of Cr-$La_{(0.8-0.9)}$-$Sr_{(0.2-0.1)}$ at% . The following process-steps were used:

a. A 3.0" diameter and 5" tall graphite crucible (anode) was used to melt a mixture of anhydrous $LaCl_3$, $CrCl_2$, and $SrCl_2$. The anode connection to the crucible was established by clamping a stainless steel wire to the side of the crucible. The starting composition of the salt mixture was not known. Therefore, it was approximated on the basis of thermodynamic stability of various compounds and the desired product. The calculations are shown in Appendix A.

b. The crucible was heated in a cylindrical resistance-heated furnace. The furnace chamber is made out of Inconel tube and has the inner dimensions of 6" diameter and 14" height. A uniform heating zone of approx. 8" is obtained in this furnace in the temperature range of 800-1000°C. Inert, dry high purity argon gas is flown through the furnace well during melting, deposition and cooling stages. The entire furnace assembly is attached to an inert atmosphere glove-box with moisture and nitrogen control. The glove-box enables the insertion and removal of cathode substrates for electrodeposition under a protective environment. The samples after deposition are brought into the glove-box environment.

c. The graphite crucible is placed on ceramic bricks inside the Inconel tube to place it within the uniform heating zone. A protective alumina crucible is placed between the graphite crucible and the inconel well.

d. A 1"x1"x0.125" inch 304 stainless steel coupon (later on replaced with the experimental alloy produced in task 2) was used as the cathode surface. A stainless steel rod was spot welded to the top edge of the coupon and inserted centrally inside the furnace tube but well above the molten salt mixture. The stainless steel wire attached to the anode crucible and the rod attached to the cathode were tightly sealed through the lid of the furnace. Only these two wire-rods and the ceramic thermocouple sheath protrude inside the glove-box chamber where the furnace-lid is flush with the bottom floor of the box. A schematic diagram of the arrangement is shown in Figure 5.

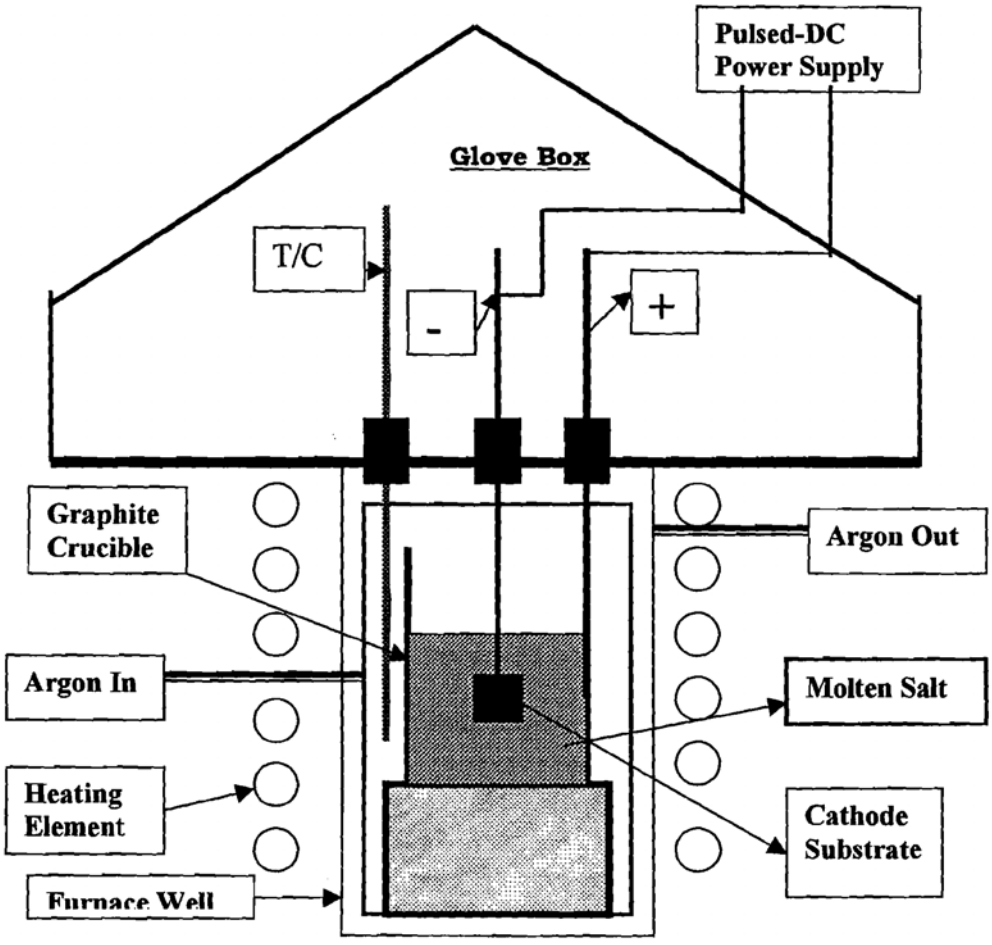

Fig. 5: Schematic Diagram of the Electrodeposition System.

e. The salt mixture was prepared inside the glove-box and added to the graphite crucible. The crucible was heated at a rate of approx. 200°C/hr to protect the graphite and the back-up ceramic crucibles. Once the temperature reached 950°±10°C, the cathode sample was lowered into the salt melt including approx. 1 inch of the connecting stainless rod.

f. Anode and cathode wire rods were then connected inside the glove-box to a E-Wave Bi-Polar Pulsed DC Power supply. The power supply has three independent channels, 1500W peak power, 400 W continuous power with a 75 Amp current range and is air cooled. The power supply does not have a front control panel and is only operated through a RS 232 computer interface.

g. Three deposition variables were used: pulse-frequency, current and duration of deposition for a given salt composition maintained at a fixed temperature.

h. Following the deposition for a pre-determined length of time, the sample was pulled out of the salt melt and the salt was allowed to drip off while the salt was cooled down before opening the furnace chamber. The sample was taken out inside the glove-box. The Stoichiometric theoretical time required to get a 5 micron deposit using faraday's law was estimated to be 50 seconds at 2 amps continuous current supply. Under the pulsed condition and assuming a 90 percent current efficiency, the deposition time was estimated at 350 secs or approx. 6 minutes.

i. Once the sample was separated from the wire-rod, cleaning of salt from the surface was attempted using various cleaners.

j. Samples were analyzed using a SEM-EDS system for the determination of deposit chemistry and variation in composition.

Tables 2-4 list the electrodeposition experiments conducted and the observations made. Table 2 lists the cell parameters of current, voltage, pulsing condition, deposition time and temperature. The cathodic current density, salt composition and film thickness are listed and Table 3. Table 4 shows the film and entrapped salt composition, as determined by SEM-EDAX.

Experimental Basis: Some of the initial parameters selected for electrodeposition experiments were based on the background work done at Aker Inc. in the past and provided to CSM at the start of the project. These parameters included, use of graphite crucible as the anode, selection of cathodic current density at 72 mA/cm^2, salt melt temperature in excess of 950°C, pulse-frequency of 30 Hz and an on-time of 5 msec and off-time of 28 msec, and electrodeposition using high temperature active electrolyte. Additional initial parameters selected were the use of the ferritic stainless steel substrates produced at CSM. Under these conditions, it was envisaged that chromium metal will deposit first due to the low thermodynamic stability of chromium chloride with respect to other chlorides (see Appendix A) and will be followed by a co-deposition of lanthanum and strontium in liquid form. It was reported in the report provided by Aker that the liquid co-deposited film will diffuse into the solid chromium deposit.

Table 2: Operating Parameters for Molten Salt Electrodeposition Experiments

Expt. No.	Current (Amp)	Voltage (V)	Pulse on (ms)	Pulse off (ms)	Temp., (°C)	Dep. Time (sec.)
1	2.0	1.32	5	28.3	970	360
2	2.2	1.58	5	28.3	970	420
3	2.1	1.47	5	28.3	950	2160
4	2.1	1.66	5	28.3	970	1800
5	2.3	1.79	5	28.3	980	1200
6	2.0	1.73	5	28.3	1000	600
7	4.0	4.4	15	18	1100	240
8	2.1	1.88	15	18	980	300
9	4.0	3.3	15	18	1010	900
10	8.0	5.2	15	18	990	300

Table 3: Operating Parameters for Molten Salt Electrodeposition Experiments

Expt. No.	Current Density (mA/cm^2)	Film thickness (μm)*	Substrate	$LaCl_3$ (wt%)	$SrCl_2$ (wt%)	$CrCl_2$ (wt%)	Total salt wt. (g)
1	153.8	15	α-SS	57	37	6	400
2	169.2	20	α-SS	57	37	6	380
3	161.5	120	α-SS	57	37	6	350
4	161.5	100	α-SS	66	28	6	400
5	176.9	65	α-SS	75	21	4	400
6	153.8	40	α-SS	75	20	5	375
7	307.7	10	Ta	76	20	4	350
8	171.3	10	α-SS-Cr plated	52	35	13	400
9	307.7	5	α-SS-Cr plated	80	16	4	380
10	614.8	0	α-SS-W plated	60	35	5	360

Observations:

Table 4 and figures 6-20 show the experimental results. It is shown on Tables 2 and 3 that the current density, pulsing parameters (on/off time), salt composition and substrate materials were varied in order to achieve a uniform stoichiometric film with La/Sr/Cr ratio of 1:0.176:1.11 (by wt %). This desired elemental ratio translates to a La/Sr ratio of 5.67 and a La/Cr ratio of 0.90. These two ratios for the deposited films are shown on Table 4.

Table 4: Chemical composition of La-Sr-Cr films formed by Molten Salt Electrodeposition

Expt. No.	La	Sr	Cr	Fe	Cl	La/Sr**	La/Cr***
1	17.42	11.45	19.92	32.28	17.41	1.52	0.87
2	20.66	13.21	21.36	23.44	11.83	1.56	0.97
3(A)	22.1	10.11	22.75	27.93	13.02	2.19	0.97
3(B)	56.01	2.87	0.78	4.28	33.29	Salt	Salt
3(C)	10.71	9.11	17.02	38.77	5.69	1.17	0.63
3(D)	1.66	0	18.09	78.08	1.32	substrate	substrate
3(E)	6.52	18.16	23.48	25.93	18.24	0.36	0.28
4	9.82	4.06	26.99	30.86	22.66	2.42	0.36
5	12.3	6.02	7.56	51.48	17.82	2.04	1.63
6	9.66	4.94	15.03	52.45	17.49	1.96	0.64
7	31.26	22.23	6.14	3.09 & 1.73-Ta	29.16	1.41	5.09
8	1.3	8.44	61.2	12.14	16.92	0.15	47.07
9[A]	22.58	7.19	5.18	0.14	64.67	3.14	4.36(salt)
9[B]	12.91	2.04	25.64	34.1	24.58	6.33	0.50
9[C]	0.88	1.55	22	68.5	6.27	0.56	Substrate
10	Trace as chloride	Nil	substrate	substrate			

* Measurement of film thickness is done on SEM and due to the undulations on the surface, is approximate values. In most samples, there is salt entrapment, and, therefore, the thickness measurement includes the trapped salt.

** The target La/Sr in films is 5.67

***The target La/Cr in films is 0.90

Over the range of variation of parameters, it is evident that:

a. Elemental ratio of the desired metals is not obtained.
b. Elemental ratio of the elements varies along the film thickness, since the film is developed by interdiffusion of elements deposited sequentially.
c. Iron is present in large quantities, indicating a very rapid interdiffusion from the substrate.
d. Chlorine is present in all the films, indicating the entrapment of salt.
e. La/Sr ratio improves by increasing the $LaCl_3$ content in the bath.

The lack of smoothness and compositional consistency was not overcome in any of the experiments that are compounded by the salt entrapment. Presence of salt in Figure 6 on the top surface after cleaning (salt removal) indicates incomplete cleaning by the recommended solutions and/or salt trapping by the deposited metal. Presence of iron in the surface salt is evident. Figure 7 shows the cross-sectional view of the deposit which clearly indicates the changing composition as a function of time and the

presence of chlorine (salt). Figures 8 and 9 show the roughness and salt trapped within the deposited metal. Figure 10 shows the top surface morphology where the roughness is evident. All the samples for microscopy and phase analysis were prepared by first removing the salt as far as practicable using the suggested solutions. Figures 6 to 10 are representing analytical data on Sample No. 3. Coating was non-planar and dendritic, giving rise to porosity and hence salt entrapment. High iron content at the top surface of the coating and high strontium content in the substrate suggests partial melting of the substrate followed by rapid interdiffusion.

Figures 11 (Expt. No. 4) and 12 (Expt. No. 5) show solidification porosity. Figure 13 (Expt. No 6) shows two areas of the cathodic reaction product where salt has been embedded into the metal. This could be caused by the incipient melting of the cathodic product at the interface leading to the formation of embedded sat salt. Figures 14 (cross-section) and 15 (top-view) show the product formation on the tantalum substrate (Expt. 7]. This experiment goes on to indicate that some fraction of the chromium obtained in the films in samples deposited on ferritic stainless substrate is from the diffusion from substrate and not from the electrodeposition. Thus, the total chromium content is a sum of the two sources and, therefore, is expected to vary along the film thickness.

PVD of Chromium: Since the amount of deposited chromium was lower than the desired level, in spite of the diffusion from the substrate, it was decided to coat the substrates with chromium metal and then deposit a liquid film of lanthanum and strontium. It was anticipated that the liquid film would diffuse into the deposited chromium layer providing the desired film composition. Initially, aqueous bath electrodeposition of chromium from a hexavalent chromium solution was planned but was not carried out due to environmental and health concerns.

A 4200 nm PVD layer of chromium was then deposited at a rate of 42 nm/min. Prior to deposition a 350V bias 64 mTorr argon sputtering was used for 20 minutes to sputter-etch the surface for good adhesion. Experiment Nos. 8 and 9 used the substrate with the chromium PVD layer. Lower current density (2 amps current) for a shorter time of 5 minutes with the standard salt composition was used in Experiment No.8. While chromium appeared to show a vast improvement in preventing iron diffusion from the substrate, very little diffusion of lanthanum or strontium was observed. There was more penetration of strontium than lanthanum. Therefore, in Expt. No.9, the current density was doubled and the deposition time was increased to fifteen minutes. Salt composition was adjusted to have very high levels of lanthanum and strontium chloride, since chromium was not desired for electrodeposition. A 4 micron layer of chromium existed on the surface that was found to be intact in Expt. No. 8. Figures 16-18 show the results with substrates coated with chromium in Expt. No.9. It is apparent that (a) cathodic product in form of a continuous layer is not formed, (b) PVD coated chromium mostly remains undissolved and (c) possible metallic Sr penetration into chromium as well as deep into the substrate is observed. Thus, PVD coated Cr acted as a diffusion barrier for elements in the substrate to some extent, but did not successfully promote continuous coating (as a layer) of the expected cathodic product.

Figure 16 shows the analysis at three positions of the formed layers. The outer adherent area A is predominantly the salt and corresponds to the salt composition of

$LaCl_3$-$SrCl_2$. The PVD chromium layer (area B) shows significant iron penetration in fifteen minutes. La/Sr ratio is closer to the desired value of 5.5 but the La/Cr value is low due to iron diffusion. Area C analysis on the substrate also indicates penetration of strontium and small amount of chlorine. Figures 17 and 18 indicate that the product layer (PVD-chromium after electrodeposition) is not a continuous layer of Cr-La-Sr and has variation in strontium, iron and chlorine content. Thus, using a chromium-plated surface for the deposition of lanthanum-strontium alloy has limitations with respect to strontium diffusion and iron back diffusion.

In addition to the PVD Cr-coated substrates, one sample of stainless steel substrate was also coated with tungsten to isolate the substrate chromium diffusion into the film. 8 micron layer of tungsten was used (Figure 19) for electrodeposition. However, complete lack of wetting was seen on this surface (Figure 20), and hence no diffusion of lanthanum/strontium film was recorded after the molten salt deposition in Expt. No. 10.

In addition, to these reported completed experiments, three experiments had to be aborted due to detachment at the spot-welded joint and the cracking of the crucible.

Since the top deposited surface was thought to be a liquid held on the surface by capillary action, the removal of the sample from the salt melt was expected to bring along a surface layer of the salt. Following the removal of the sample, the salt had to be cooled down to room temperature. The part of the surface adherent salt that could not drip-off while suspended above the melt during cool down, required to be removed by chemical methods. The suggested method for removal of the salt was either pyridine or dry acetone. Subsequent to the removal of the salt layer, the sample as had to be coated with mylar for protection. The salt cleaning and protective coating methodologies were provided to CSM by Aker, Inc.

CSM was required to perform a deposit chemical analysis prior to the application of the protective coating to check its suitability.

Removal of Salt: The removal of $CrCl_2$-$SrCl_2$-$LaCl_3$ salt mixture could not be removed by pyridine, ethanol or dry-acetone. This cleaning process was repeatedly verified by dip coating a substrate without any electrodeposition. However, water and warm glycerine were found to be successful cleaners.

It is suggested that a proper solution to clean the salt should be a non-polar solution. This observation was supported by the fact that warm ethanol was successful in removing the salt. Use of water, however, caused concerns of corrosion of the metallic layer.

SUMMARY

A. The experimental ferritic stainless alloy was produced within the compositional specification by vacuum melting, vacuum cooling, annealing and hot rolling. Some segregation was observed for lanthanum. Double annealing after hot rolling, minimized the segregation but oxide precipitation of niobium oxide was

observed. The oxidation tests performed on the Melt-3 samples by LBL, indicated the fabrication of a satisfactory alloy requiring further fine-tuning.

B. The dc-magnetron PVD sputtering was not successful due to a very high resistance of $SrO\text{-}La_2O_3$ target that failed to generate a sustained plasma. Sputtering of La-Sr metallic films could not be attempted due to the unavailability of a commercial or fabricated La-Sr target. It is recommended that a RF-sputtering method be employed to sputter the highly resistive oxide.

C. The co-deposition of a stoichiometric, uniform, adherent, non-porous 5 micron thin film of **Cr-$La_{(0.8\text{-}0.9)}$-$Sr_{(0.2\text{-}0.1)}$** layer by active high temperature (> 950°C) molten salt electrolysis from chloride melts was not accomplished and the experiments failed to give an acceptable product. Primary technical factors impeding the co-deposition of the desired film are:

   a. Diffusion of large amounts of iron and chromium from the substrate into the film at temperatures above 950°C.
   b. Dendritic growth of La-Sr-Cr film.
   c. Salt entrapment within the dendrites, preventing complete removal of salts from the film.
   d. Large deviation from the desired stoichiometry and variation of metal composition through the film thickness due to the lack of activity coefficients data. Assumption of Henrian activity and variation of $CrCl_2$ around the predicted composition did not allow adequate chromium to be deposited.
   e. Non-uniform surface profile due to dendritic growth and salt adherence. Formations of La-Sr, La-Fe, and Sr-Fe intermetallics that are accompanied by deep eutectics and exothermic heats, can give rise to dendritic growth.

Formation of oxy-chloride salt slag over repeated use of salt melts was also observed, in spite of the maintenance of high purity argon during deposition. Physical integrity of the system, i.e. spot-welded joint, electrical contact at the graphite crucible, strength of ceramic components, etc., also deteriorates with increase in temperature. It should be noted that lanthanum chloride that constitutes the majority of salt by weight, has a boiling point of only 1000°C in anhydrous condition. This fact makes the liquid salt somewhat unstable at the operating temperatures.

These problems are easily avoided at lower temperatures, however, can be surmounted by careful operation at higher temperatures. Nevertheless, several experiments had to be aborted and repeated due to the above mentioned physical system problems.

It is concluded that the feasibility of co-electrodeposition of uniform, leveled, stoichiometric **Cr-$La_{(0.8\text{-}0.9)}$-$Sr_{(0.2\text{-}0.1)}$** film using a high temperature active electrolyte is extremely limited when (a) one salt component is very thermodynamically unstable compared with the others, (b) diffusion rates for metals from the cathode are high, (c) deposits are not in the same physical state, (d) the desired film is developed by interdiffusion of sequentially deposited elements that have different diffusion coefficients in the substrate/chromium (e) the salt composition is not fully characterized due to the lack of activity coefficients in the ternary.

Recommendation:

It is recommended that the co-deposition of La-Sr-Cr film be done using inert electrolytes, such as LiCl-KCl or LiCl-NaCl-KCl melts. This process can be operated at temperatures around 400^{o}C where the salt is expected to be very stable. Diffusion from the substrate can be minimized. Fluidity of these salts is much improved compared with the active ternary salt used in this research. Thus, salt entrapment should be avoided in this arrangement as all the deposited metallic layers would be solid. Lanthanum and strontium should be introduced as chlorides into the melt. Their co-deposition is relatively easy owing to their similar thermodynamic stabilities. Chromium should be introduced as solid chromium metal anode rod with $CrCl_2$ addition to the salt only as a seed.

The dc pulsed power-supply unit purchased by Aker, Inc. for CSM is a 3-channel power supply that can be concurrently set-up to perform in a pulsed mode, without having to open the deposition chamber. In this manner, electrodeposition of chromium from an active anode and the La-Sr deposition from an inert anode can be independently controlled and accomplished. The scheme will also allow the deposition of a layered structure that can be subsequently annealed or completely co-deposited to form the desired alloy film.

APPENDIX A

The initial salt composition was based on the following calculations. Since activity and interaction coefficients of components are not known, Henrian activity was assumed for the calculation:

Substrate (cathode) area: 13 cm^2
Current: 1 amp
Current density: 77 mA/cm^2

Based on Faraday's Law:

1 faraday charge ≡ 26 g Cr; 46.3 g La and 43.8 g Sr

Total volume deposited: 5μm x 13 cm^2 = 65 x 10^{-4} cm^3

Desired composition:

50 at % Cr ⇒ 26.0 g ⇒ 28.8 wt % ⇒ 4.0 cm^3 ⇒ 22.5 vol % ⇒ **14.6 x 10^{-4} cm^3**
40 at % La ⇒ 55.6 g ⇒ 61.5 wt % ⇒ 10 cm^3 ⇒ 56.2 vol % ⇒ **36.5 x 10^{-4} cm^3**
10 at % La ⇒ 8.80 g ⇒ 9.70 wt % ⇒ 3.8 cm^3 ⇒ 21.3 vol % ⇒ **13.9 x 10^{-4} cm^3**

Desired wt. of metals in the film:

14.6 x 10^{-4} cm^3	⇒	105.0 x 10^{-4} g Cr	⇒	39.0 amp-sec for Chromium
36.5 x 10^{-4} cm^3	⇒	224.3 x 10^{-4} g La	⇒	46.7 amp-sec for Lanthanum
13.9 x 10^{-4} cm^3	⇒	35.30 x 10^{-4} g Sr	⇒	7.80 amp-sec for Strontium

Current shared:

Cr : La : Sr ≡ 0.8 : 0.94 : 0.16 in 2 amps.

Total charge required: 94 amp-sec. This requires a 47 second deposition time at 2 amps. Current.

Standard free energy of formation:

$CrCl_2$ = -356 kJ/mol (at RT) = -260 kJ/mol (900°C)
$LaCl_3$ = -800 kJ/mol (at RT) = -720 kJ/mol (900°C)
$SrCl_2$ = -781 kJ/mol (at RT) = -713 kJ/mol (900°C)

$LaCl_3 + 1½\ Cr = La + 1½\ CrCl_2$ ΔG^0 = 266 kJ/mol @ 900°C

Assuming a_{La} = 0.4; a_{Cr} = 0.5 (activity coeff. = 1)

a_{LaCl3} = 0.95 = mol. fraction $LaCl_3$
a_{CrCl2} = 0.05 = mol. fraction $CrCl_2$

Since the stability of lanthanum and strontium chlorides is comparable, the composition can be approximated in equal proportion.

Approximated initial salt composition:

45 at% (57 wt %) $LaCl_3$;
45 at% (36.7 wt %) $SrCl_2$;
10 at% (6.3 wt %) $CrCl_2$

Actual Budget: [12.15.01-11.30.02]

Cost Item	Budgeted ($)	Spent ($)
P.I.	13,391	0
Res. Assoc. (8.5 months) 6.5 months for alloy making + electrodeposition + 2 months for PVD $ 40,000 Annual + 27.5 % fringe + 27 % indirect	28,575	45,879
Technician (power supply interface)		762
Computer	0	1,400
Chemicals (27% indirect) incl. gas	8,890	3,304
+		
Target (Cr) (27 % indirect)		825
+		
Crucibles, T/c and other supplies		4,700
SEM-EDS Analysis (36 hrs @ $50)	6,604	2,286
+		
Vacuum furnace & rolling mill usage		4,572
Travel	2,540	0
Total Spent	**$60,000**	**$63,728**

Figure 6: TOP SURFACE OF COATING(Sample No. 3)

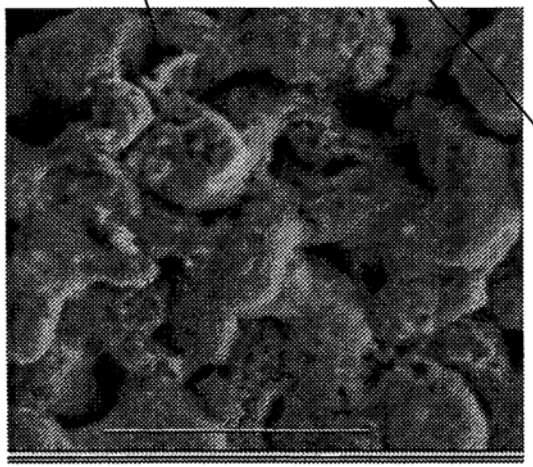

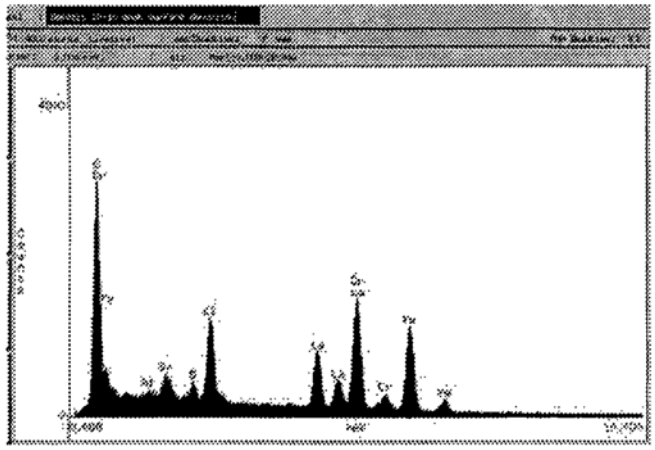

COAT

Element	Element Wt %	Wt % (1-Sigma)	Err.
Cl-K	13.02	+/-	0.17
La-L	22.1	+/-	0.59
Cr-K	22.75	+/-	0.39
Fe-K	27.93	+/-	0.52
S -K	2.13	+/-	0.12
Br-L	1.95	+/-	0.32
Sr-L	10.11	+/-	1.42
Total	100		

SALT

Element	Element Wt %	Wt % (1-Sigma)	Err.
Cl-K	33.29	+/-	0.47
La-L	56.01	+/-	1.01
Cr-K	0.78	+/-	0.23
Fe-K	4.28	+/-	0.49
S -K	0.09	+/-	0.16
Br-L	2.59	+/-	0.49
Sr-L	2.87	+/-	0.44
Total	100		

Figure 7: CROSS SECTION OF COATING (Sample No. 3)

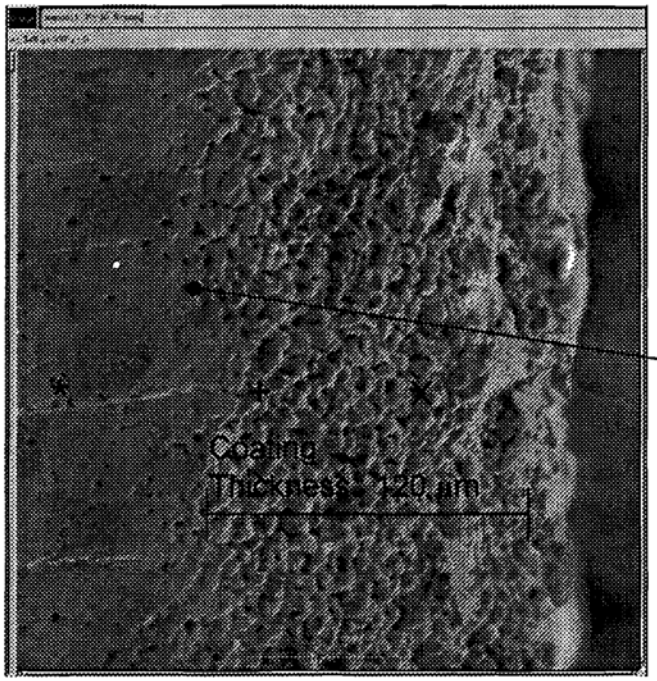

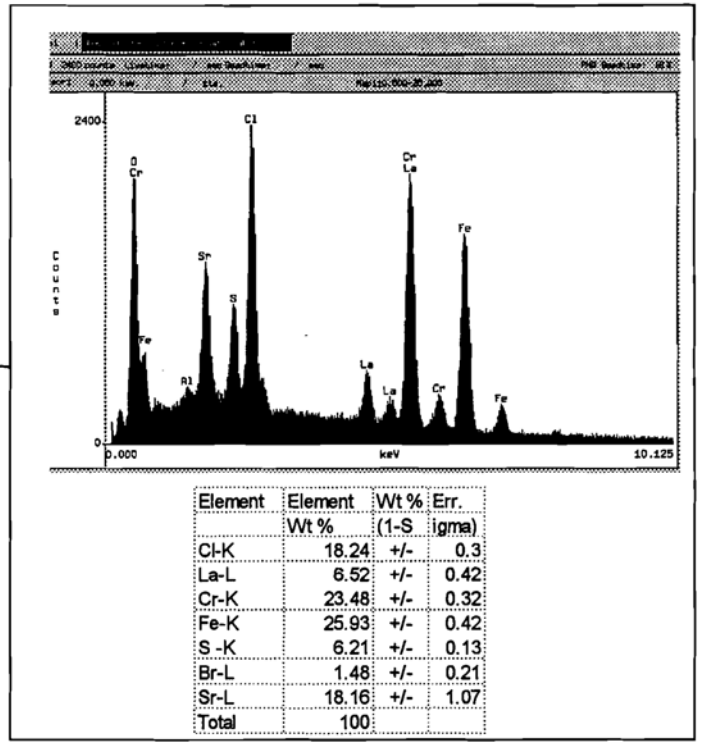

Element	Element Wt %	Wt % (1-S	Err. igma)
Cl-K	18.24	+/-	0.3
La-L	6.52	+/-	0.42
Cr-K	23.48	+/-	0.32
Fe-K	25.93	+/-	0.42
S -K	6.21	+/-	0.13
Br-L	1.48	+/-	0.21
Sr-L	18.16	+/-	1.07
Total	100		

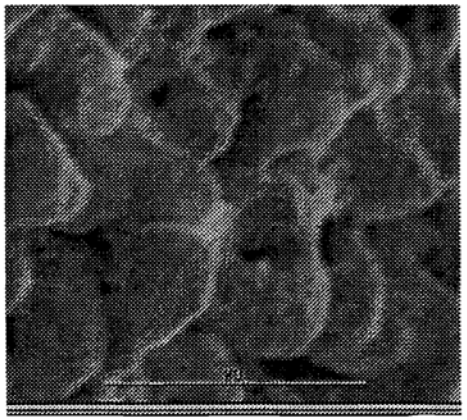

*

Element	Element Wt %	Wt % (1-S	Err. igma)
Cl-K	1.32	+/-	0.14
La-L	1.66	+/-	0.31
Cr-K	18.09	+/-	0.24
Fe-K	78.08	+/-	0.55
S -K	0	+/-	0
Br-L	0.92	+/-	0.2
Sr-L	0	+/-	0
Total	100		

\+

Element	Element Wt %	Wt % (1-S	Err. igma)
Cl-K	5.69	+/-	0.22
La-L	10.71	+/-	0.41
Cr-K	17.02	+/-	0.18
Fe-K	38.77	+/-	0.45
S -K	2.59	+/-	0.11
Br-L	16.12	+/-	0.55
Sr-L	9.11	+/-	0.97
Total	100		

X

Element	Element Wt %	Wt % (1-S	Err. igma)
Cl-K	6.54	+/-	0.11
La-L	9.88	+/-	0.38
Cr-K	12.76	+/-	0.15
Fe-K	59.06	+/-	0.48
S -K	1.06	+/-	0.1
Br-L	2.74	+/-	0.28
Sr-L	7.95	+/-	1.25
Total	100		

Figure 8: Sample No. 3

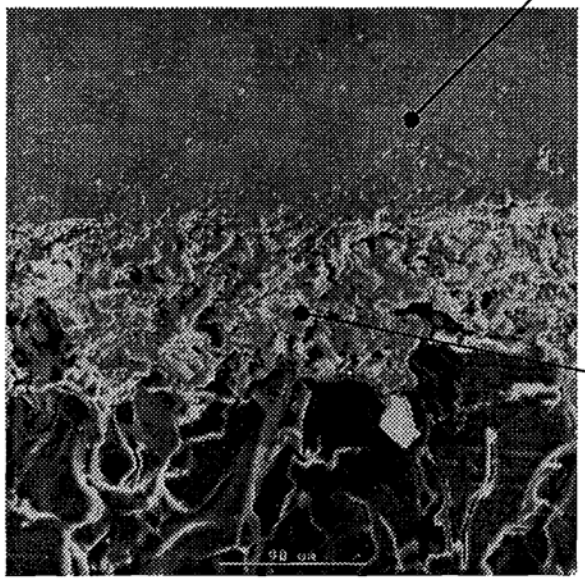

SUBSTRATE:
Composition (wt.%)
72±0.5 %Fe, 22.4 ±0.2%Cr, 2.81 ± 0.1% Nb 0.11 ±0.1%La, 0.1 ±0.06%Sr

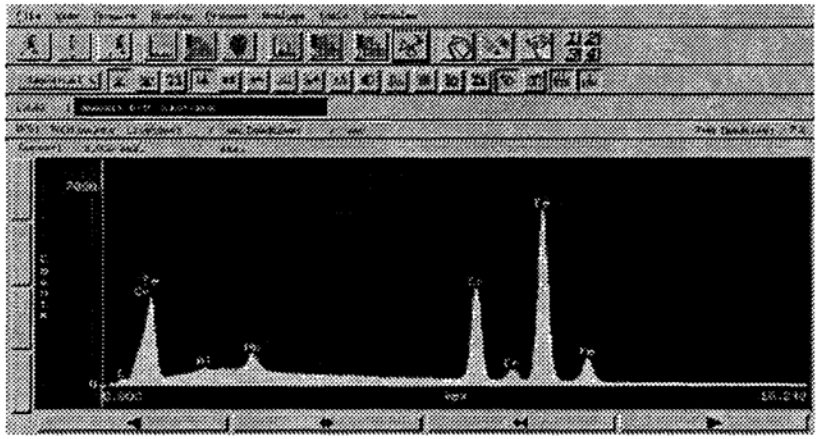

COATING:
Composition (wt.%)
47.08 ±0.57 %Fe, 5.01±0.51 %Ni, 5.49 ± 0.16 %Cr, 32.80 ±0.54 % La,
1.63 ± 0.16%Sr,0.30 ± 0.10%Nb, 7.71 ± 0.08Cl
Note : La/Cl ratio = 4.25 (In LaCl3 Compound, La/Cl =1.3
La/Sr/Cr ratio = 20/1/3.4

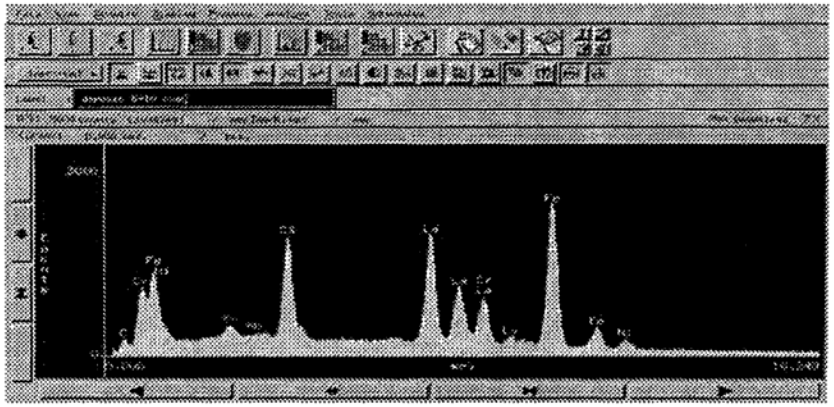

Figure 9: Cross Sectional View (sample no. 3)

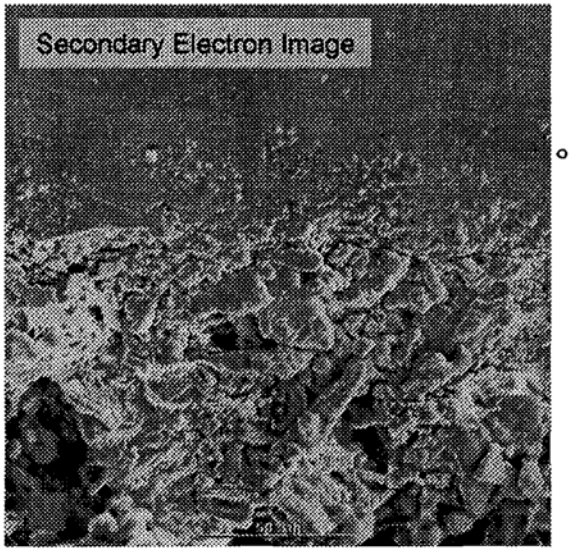

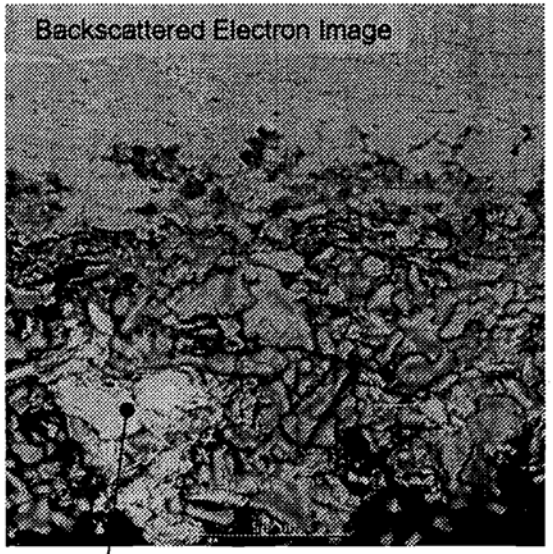

Substrate

Coating

Composition wt% : 7.67 ±0.53 %Fe, 0.52 ±0.31 %Ni, 6.13 ±0.25%Cr,
83.39 ± 0.91 % La,2.28 ± 0.28 %Sr (Cl is not quantified)

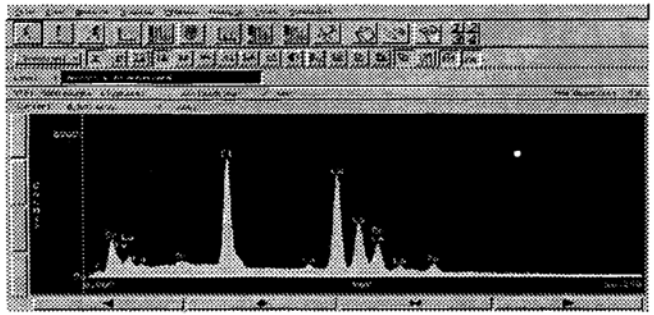

Figure 10: Coating Surface View (Sample No. 3)

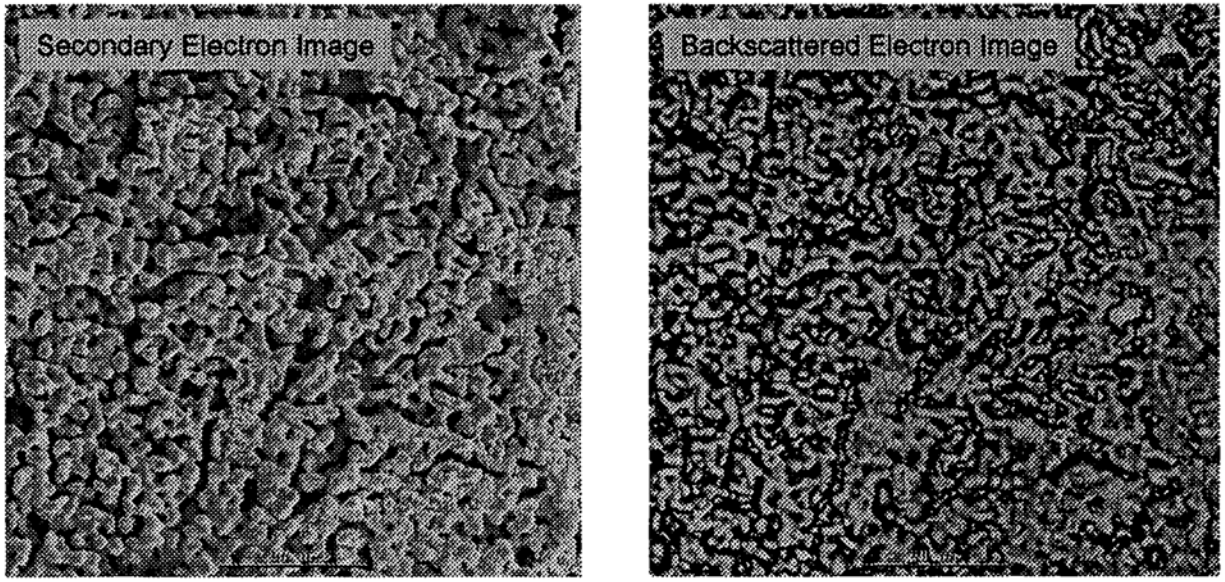

Figure 11: TOP SURFACE OF COATING

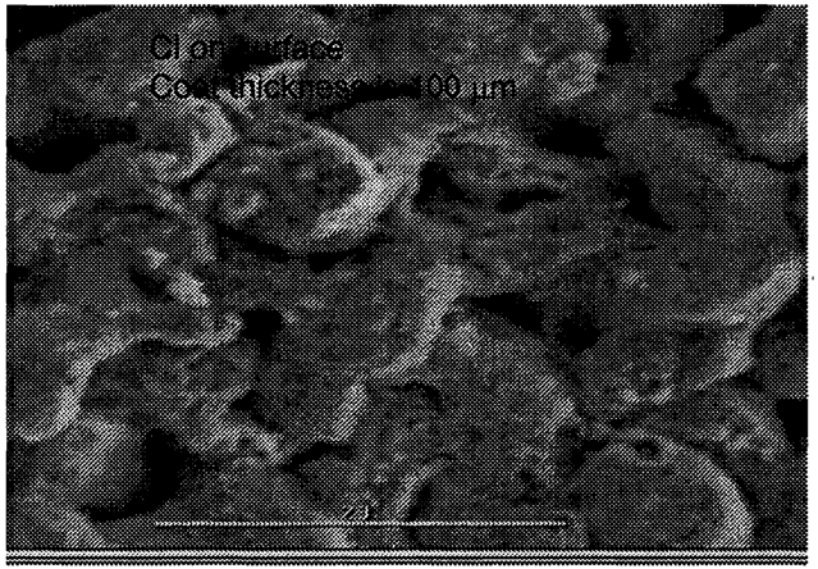

Sample No. 4

Element	Atom %
Cl-K	22.66
La-L	9.82
Cr-K	26.99
Fe-K	30.86
S -K	4.1
Br-L	1.5
Sr-L	4.06
Total	100

Salt	Weights (gr)	Comp (%)
$LaCl_3$	171	66.53696
$SrCl_2$	74	28.79377
$CrCl_2$	12	4.669261
Total	257	

	Actual	Target
La/Sr	2.418719	5.666667
La/Cr	0.363838	0.9

Figure 12: TOP SURFACE OF COATING

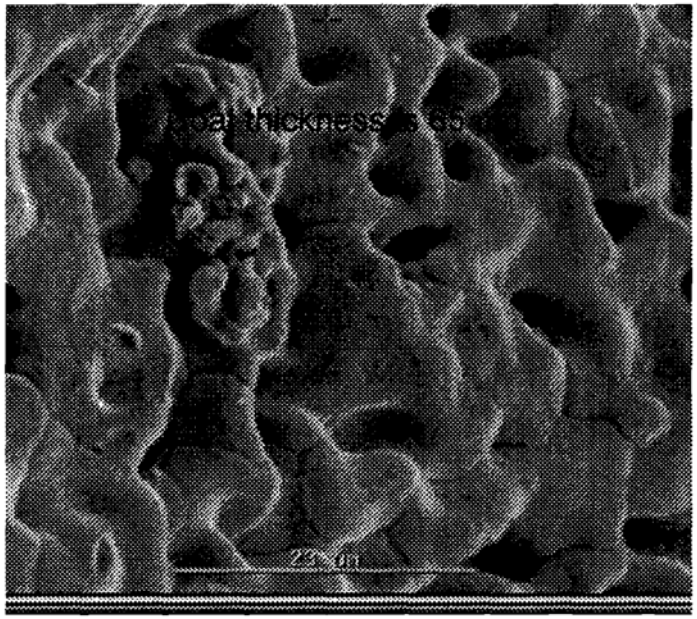

Sample No. 5

Element	Atom %
Al-K	0.66
Cr-K	7.56
Fe-K	91.1
Nb-L	0
La-L	0.5
Sr-L	0.18
Total	100

	Actual	Target
La/Sr	2.777778	5.666667
La/Cr	0.066138	0.9

Salt	Weights (gr)	Comp. (%)
$LaCl_3$	271	75.91036
$SrCl_2$	74	20.72829
$CrCl_2$	12	3.361345
Total	357	

Figure 13: CROSS SECTION OF COATING (Sample No. 6)

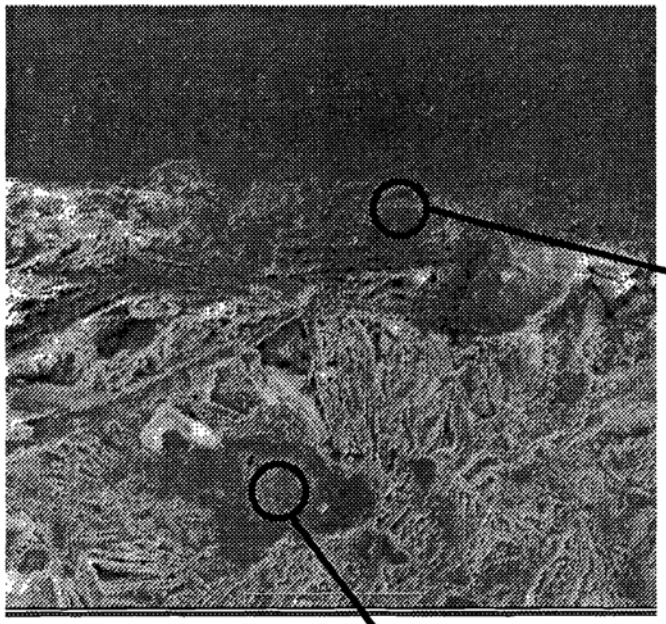

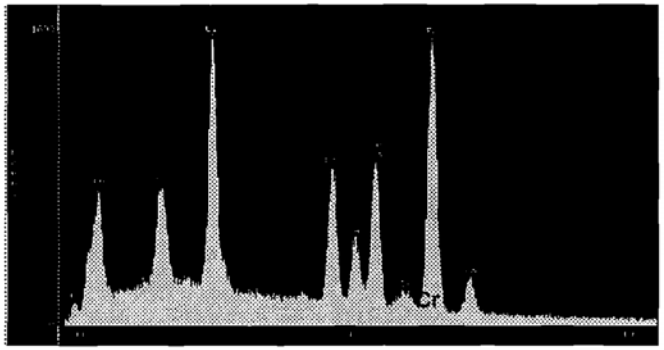

Cathodic Reaction Product
Embeded at the Interface

Element	Atom %
Cl-K	17.49
La-L	9.66
Cr-K	15.03
Fe-K	52.45
Nb-L	0.43
Sr-L	4.94
Total	100

Cathodic Reaction Product
Embeded in the Salt

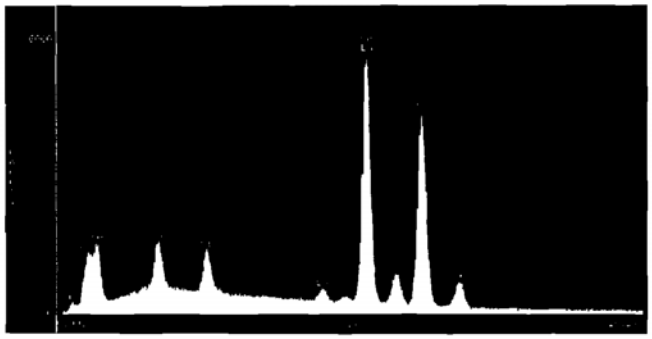

Element	Atom %
Cl-K	4.11
La-L	1.18
Cr-K	41.7
Fe-K	50.13
Nb-L	0.1
Sr-L	2.78
Total	100

Figure 14: CROSS SECTION

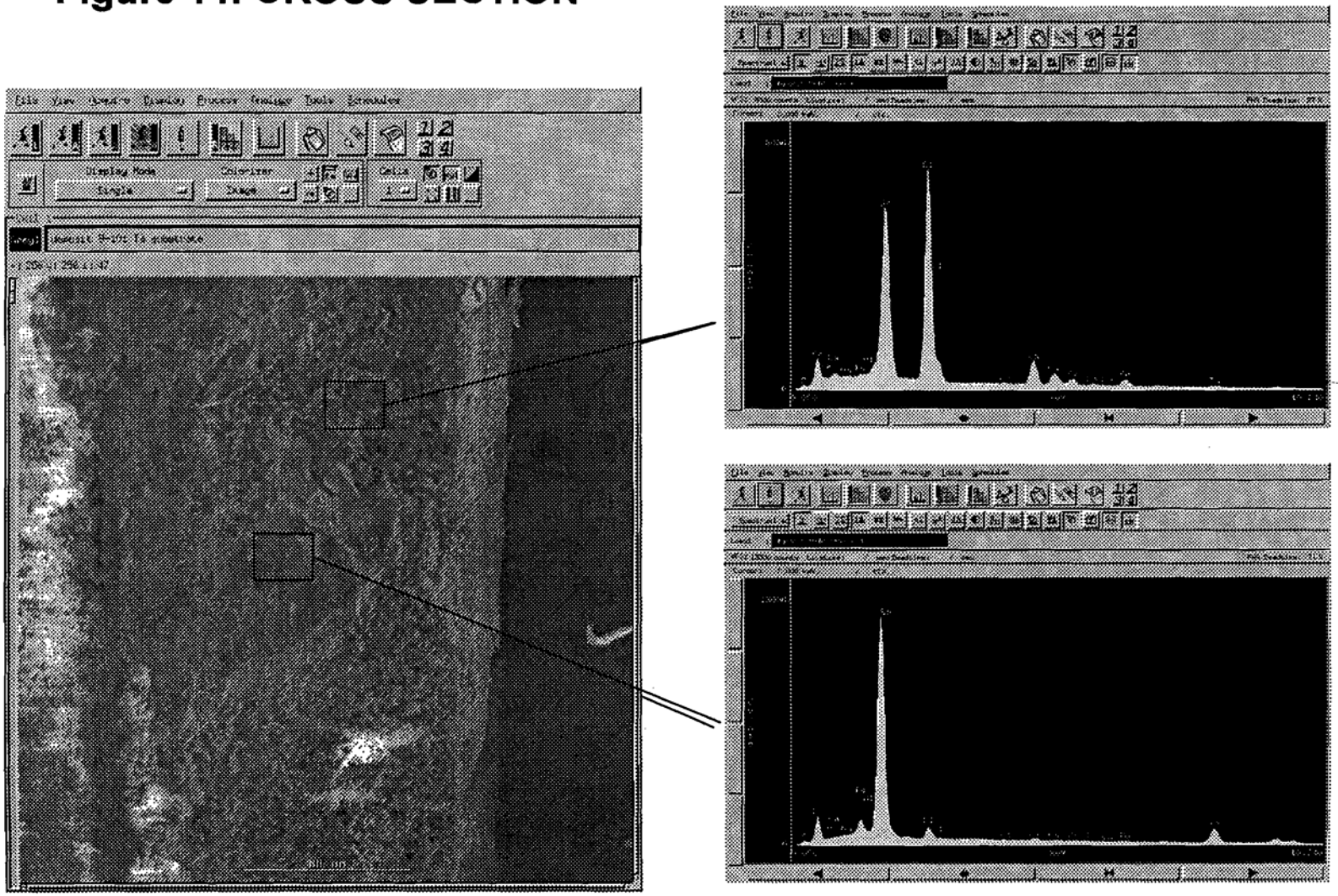

Figure 15: TOP SURFACE

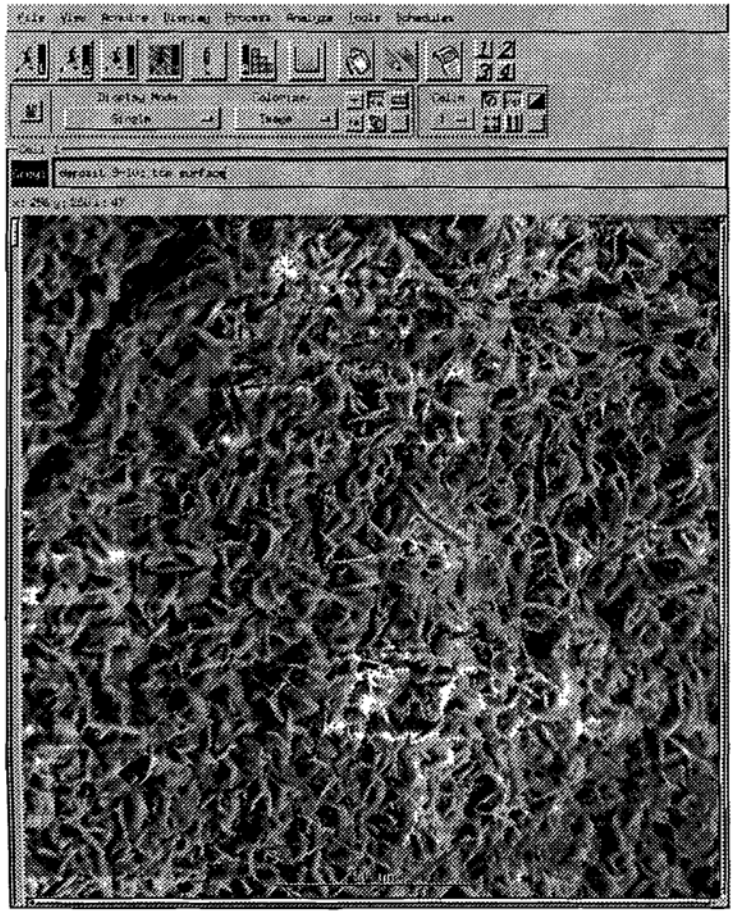

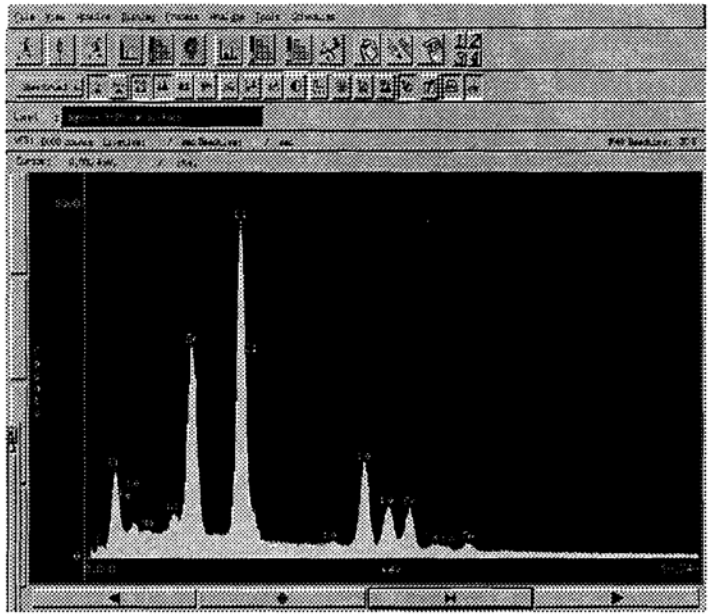

Element	k-ratio (calc.)	ZAF	Atom %	Element Wt %	Err. (1-Sigma)
Ni-L	0.0250	1.957	5.22	4.90	+/- 0.51
Ga-L	0.0057	2.057	1.05	1.17	+/- 0.29
Al-K	0.0022	1.536	0.77	0.33	+/- 0.09
Sr-L	0.1626	1.367	15.89	22.23	+/- 0.17
Cl-K	0.2580	1.130	51.51	29.16	+/- 0.20
La-L	0.2600	1.202	14.09	31.26	+/- 0.50
Cr-K	0.0634	0.968	7.40	6.14	+/- 0.15
Fe-K	0.0313	0.989	3.47	3.09	+/- 0.15
Ta-L	0.0133	1.299	0.60	1.73	+/- 0.77
Total			100.00	100.00	

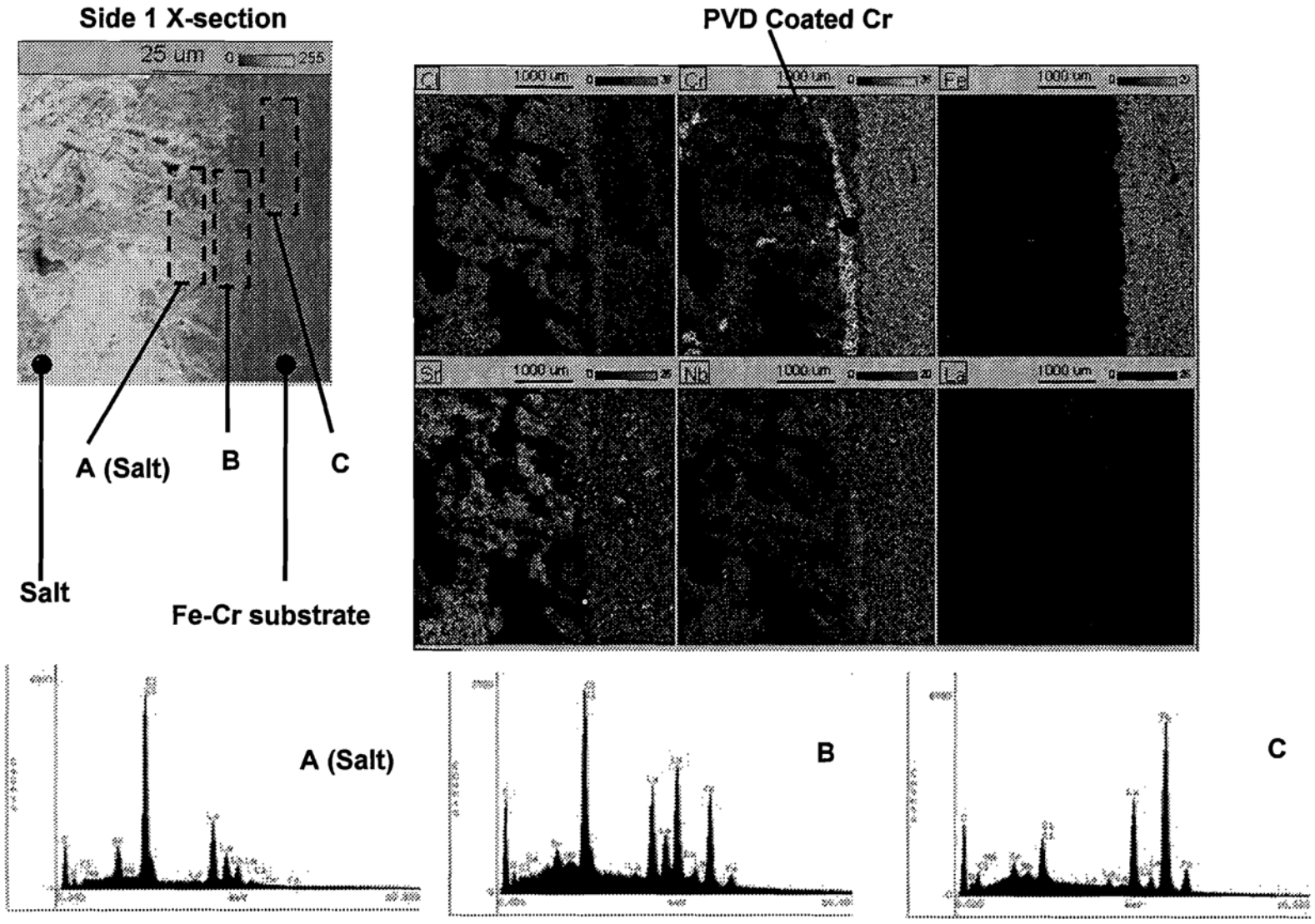

Figure 16: Salt, product and substrate analysis

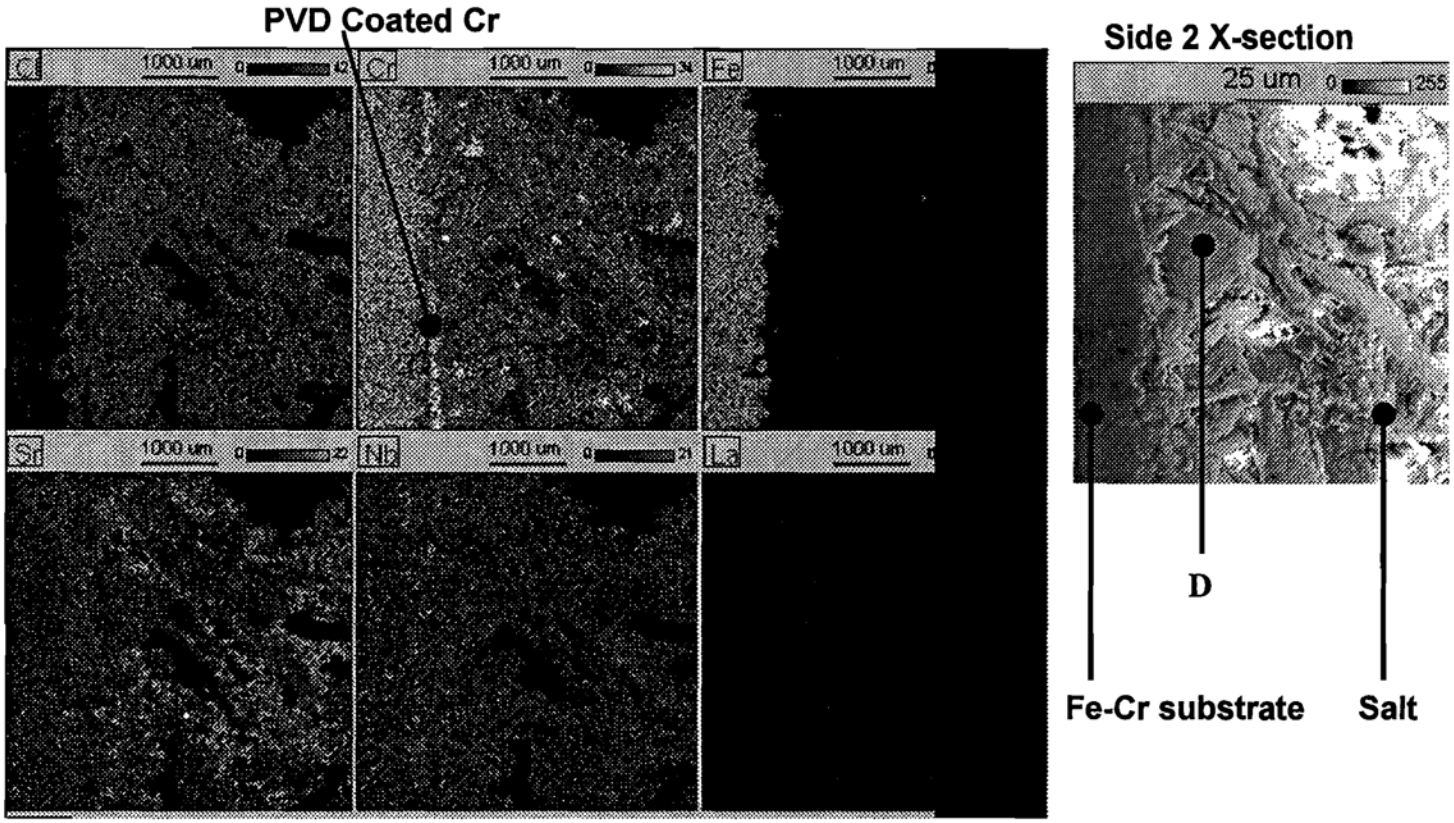

Figure 17: Point analysis of the PVD layer of chromium

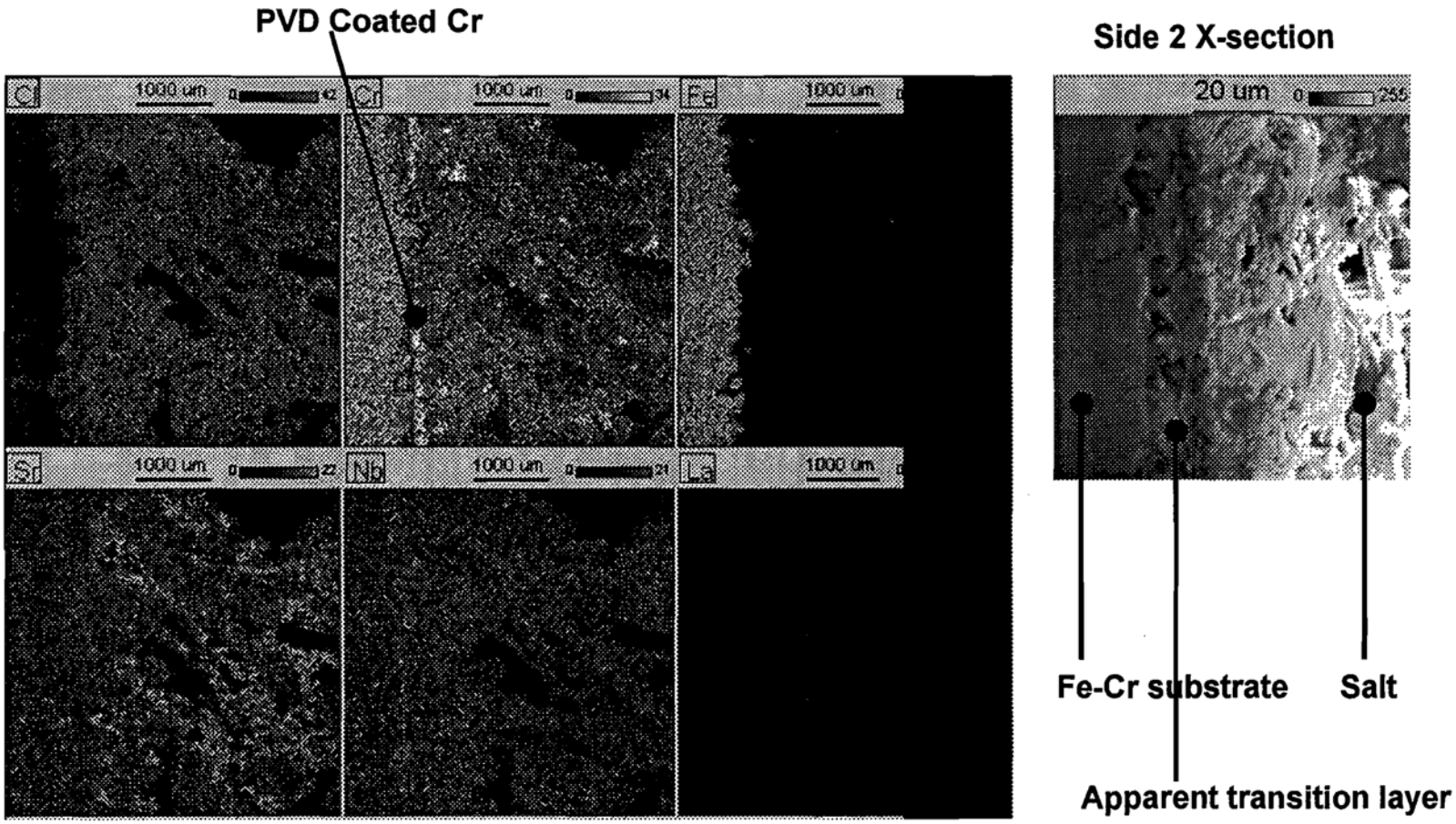

Figure 18: Elemental mapping showing the apparent transition layer

Figure 19: Molten Salt Electrodeposition on PVD tungsten layer

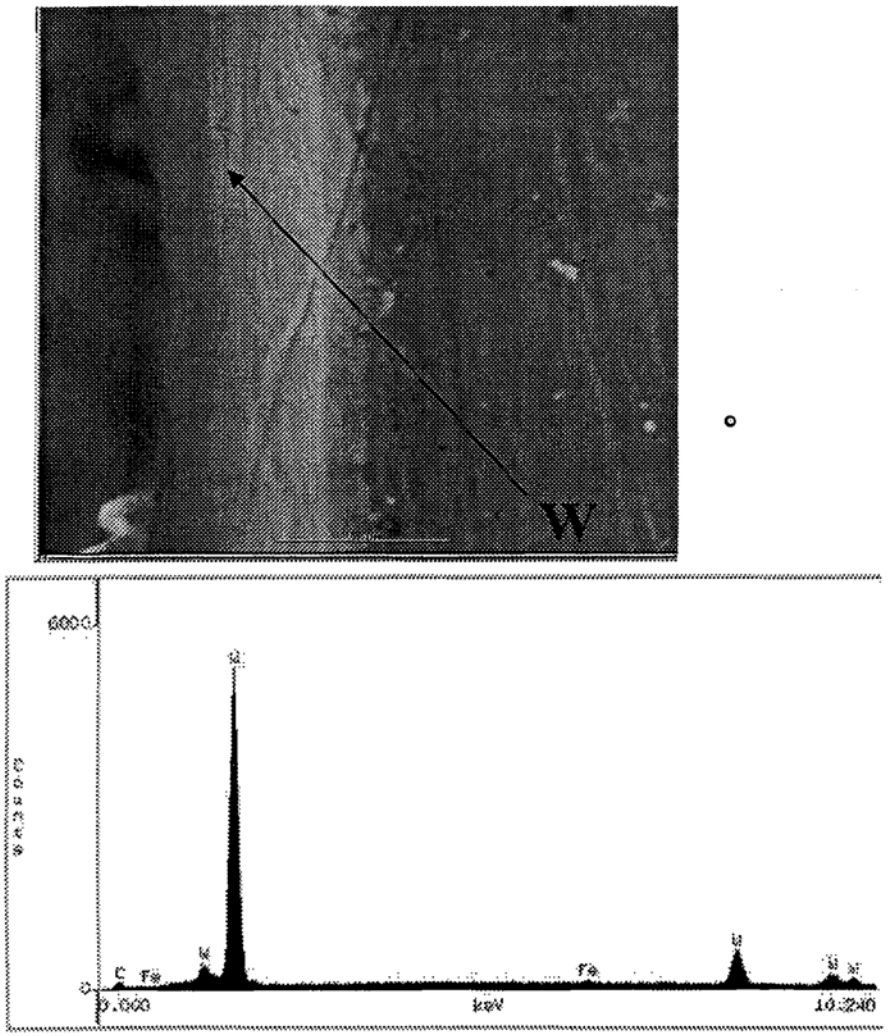

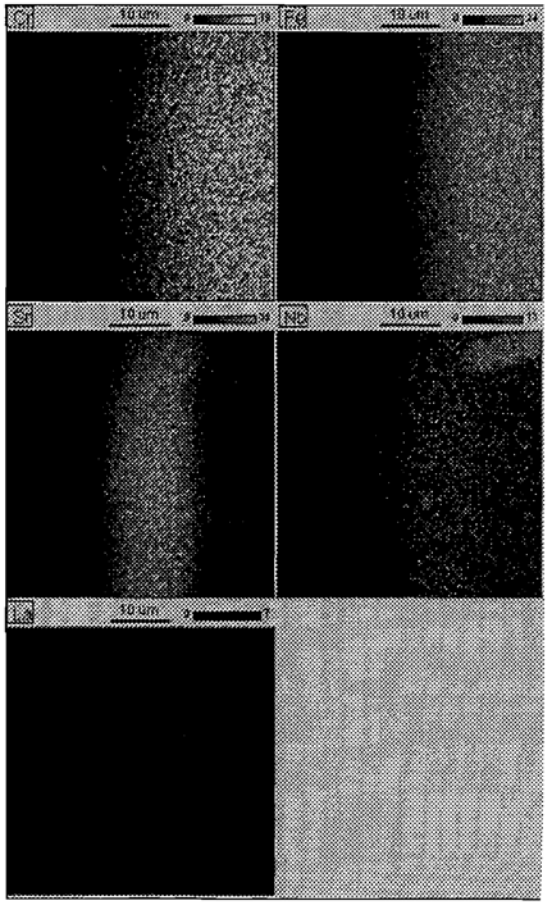

3.3.2 Characterization of coated ferritic alloys

Work was focused on studying Ebrite uncoated and coated with $LaZnCrO_3$, oxidized at temperatures of 750 and 850°C in air. The results showed that Ebrite alloy when coated with $LaZnCrO_3$ will yield an interconnect which will be adequate for the SOFC proposed in this program.

This study included

(1) Kinetics studies during isothermal oxidation
(2) 100-hour long-term oxidation with characterization using SEM/EDS and XRD
(3) Testing of oxide scale adhesion of the long-term oxidized samples
(4) Conductivity testing from 500-800°C on a $LaZnCrO_3$ coated sample.

I. Oxidation Kinetic

Oxidation tests were performed on 10x10x1 mm coupons. The steady state oxidation rate constants obtained from TGA experiments (in ambient air for 50 hours with 5°C/min heating rate) on coated and uncoated Ebrite alloys are summarized in Table 1 and plotted in Figure 1 with the rates of other alloys for comparison. The coated specimens were received in Jan. 04 from UMR.

Table 1. Oxidation rate constants ($g^2cm^{-4}s^{-1}$) for Ebrite alloy uncoated and coated with $La_{0.8}Sr_{0.2}CrO_3$ and $LaZnCrO_3$ films.

Sample Description (color of circle added onto Figure 1)	**Oxidation Temperature (°C)**	
	750	**850**
Ebrite alloy (yellow)	1.42×10^{-14}	7.65×10^{-14} 1.17×10^{-13}
Ebrite coated with $LaZnCrO_3$ (light green)	1.0×10^{-15}	6.50×10^{-14}
Ebrite coated with $LaSrCrO_3$	1.11×10^{-15}	

At 750°C, alloys coated with both types of coatings had very similar oxidation rates, and they are about an order of magnitude lower than that of the uncoated Ebrite. However, at 850°C, this beneficial effect diminishes and the rate constant of the $LaZnCrO_3$ coating approaches that of uncoated Ebrite. As will be seen in section II, this loss of protectiveness at the higher temperature is due to chromia overgrowing the deposited film. SEM micrographs in Section II show deposited film on the surface of the coated specimen after the 750°C oxidation, while after the 850°C tests, the entire specimen surface is covered with chromia.

II. Long-term Oxidation of $LaZnCrO_3$ coatings

Long-term oxidation was done on 2 x 2 cm^2 Ebrite samples received from UMR on 10/27/03. The oxidation was conducted in air first at 750°C for 100 hours, then again at 850°C for 100 hours. The sample was moved gradually (over 5-10 minutes) into a furnace that was already set at the desired temperature. After each oxidation, the sample was characterized by SEM/EDS and

XRD, followed by a tensile pull test to determine the interfacial fracture strength of the oxide scale.

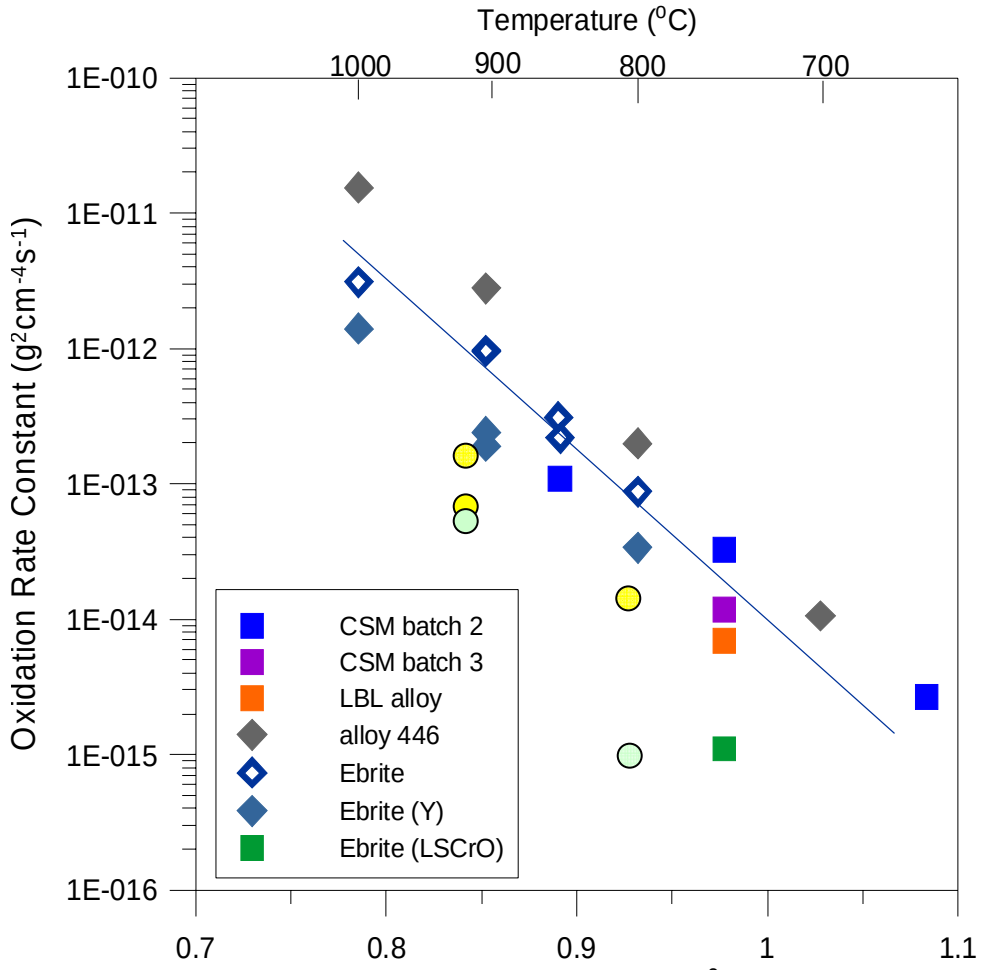

Figure 1. Oxidation Rate constants for various coated and uncoated alloys.

SEM photos of the sample surface as well as summary of sample composition obtained by EDS are shown in Fig. 2. Figures 2a and 2b show the surface of the coated specimen after 100 hours at 750°C. Table 2 presents a summary of the surface composition (in atomic %) obtained by EDS analysis. The big white particle in the bottom left corner of Fig. 2a is La-rich and has a bit more Zn. The black-looking particles have more Cr. The concentration of all elements, especially Zn, is not very uniform. The presence of the film (with its typical fine-grained morphology) on the specimen surface after this oxidation time is obvious, as seen in Fig. 2b.

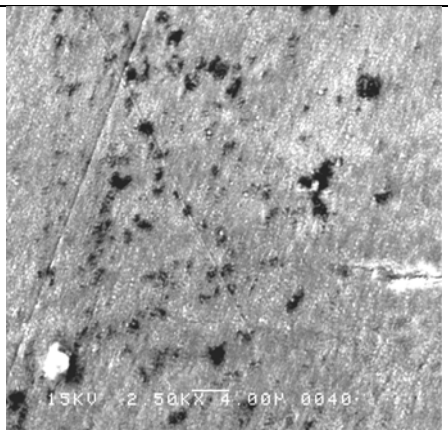

Figure 2a. Center of $LaZnCrO_3$ coated specimen after oxidation at 750°C for 100 hours. (2.5 kx)

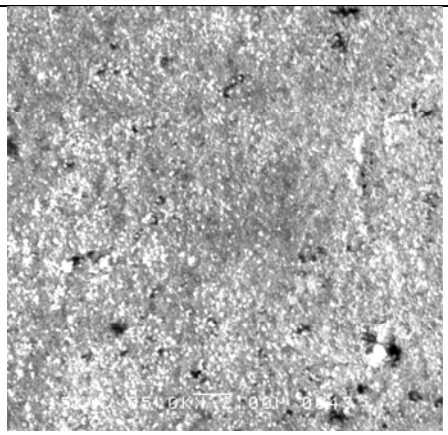

Figure 2b. Higher magnification of the sample surface (at 5 kx), after oxidation at 750°C for 100 hours.

La	1.8 ± 0.27
Cr	38.7 ±2.1
Fe	57.6 ±1.4
Zn	1.9 ± 0.73

Table 2. Overall surface composition (at%) of the coated specimen after 100-h at 750°C.

However, after another 100 hours at 850°C, the sample surface (see Figs 3a & b) looks as though chromia had overgrown the $LaZnCrO_3$ film completely. These chromia grains are 4-5 times bigger than after the 750°C oxidation (compare Figs 2b & 3b); they also vary in size greatly, with some as much as 10 times bigger than others.

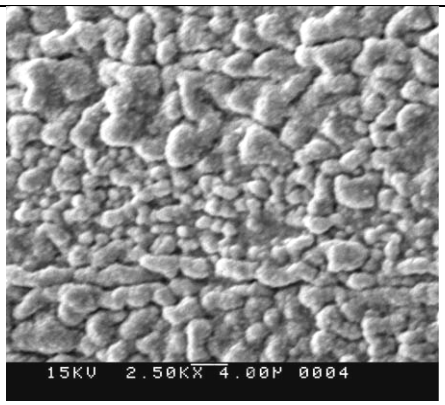

Figure 3a. Center of $LaZnCrO_3$ coated specimen after oxidation at 750°C for 100 hours followed by a 100h oxidation at 850°C. (2.5 kx)

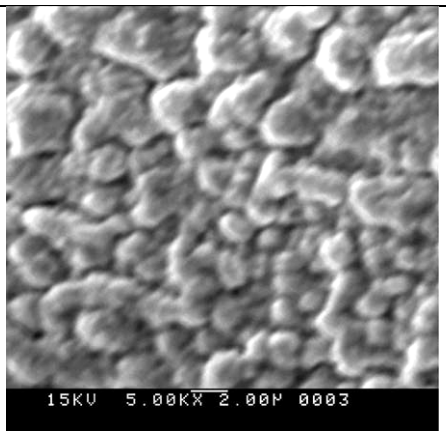

Figure 3b. Higher magnification of the same sample surface (at 5 kx).

In Figure 4b, white particles that can occasionally be found on the surface are shown. One of these is Zn-rich and another Fe-rich. From Table 3 it can be seen that the overall concentrations of La, Cr and Fe detected through the surface are more uniform, but the Zn concentration still varied more than others over the surface. Compare to the composition reported in Table 2 (after the 750°C oxidation), this surface oxide contains significantly more Cr. Since the Fe signal is from the substrate, the higher Cr content indicates a thicker Cr_2O_3 film. Concentration of the coating component, namely La and Zn, decreased a little but not much. This suggests that the coating was still incorporated in the Cr_2O_3 scale, although it is no longer at the surface as after the 750°C oxidation.

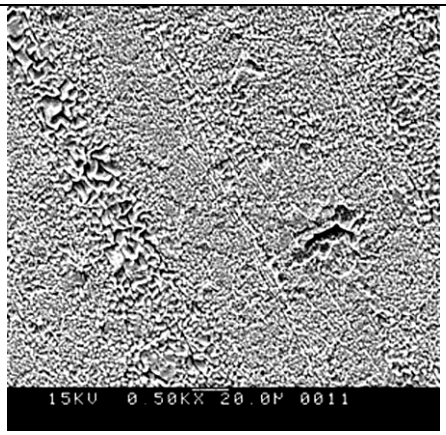

Figure 4a. Low magnification of the sample surface (500x) after oxidation at 750°C for 100h followed by 100h at 850°C.

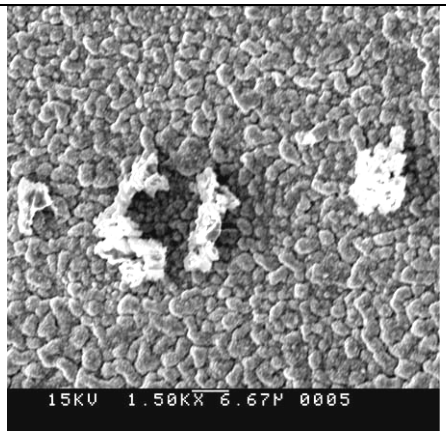

Figure 4b. White Zn & Fe particles, (1,500x) on the sample surface.

La	1.21 ± 0.14
Cr	89.2 ± 0.20
Fe	7.8 ± 0.65
Zn	1.77 ± 0.83

Table 3. EDS results (at%) of surface film formed on coated specimen oxidized at 750°C for 100h then 850°C for 100h.

Figure 4 shows XRD results of the $LaZnCrO_3$-coated specimen before and after the two oxidation stages. Moving down the three spectra, the growth of the Cr_2O_3 film can be witnessed. After 850°C, only Cr_2O_3 and the substrate Fe peaks are seen, and the Cr_2O_3 peaks are significantly stronger than before. Several peaks, which cannot be identified with current diffraction files on hand within our system, are seen on the as-deposited film and after 750°C oxidation. These are probably reflections from the coating. After the 850°C oxidation, they are no longer detected. This may be due to their incorporation into the growing chromia scale.

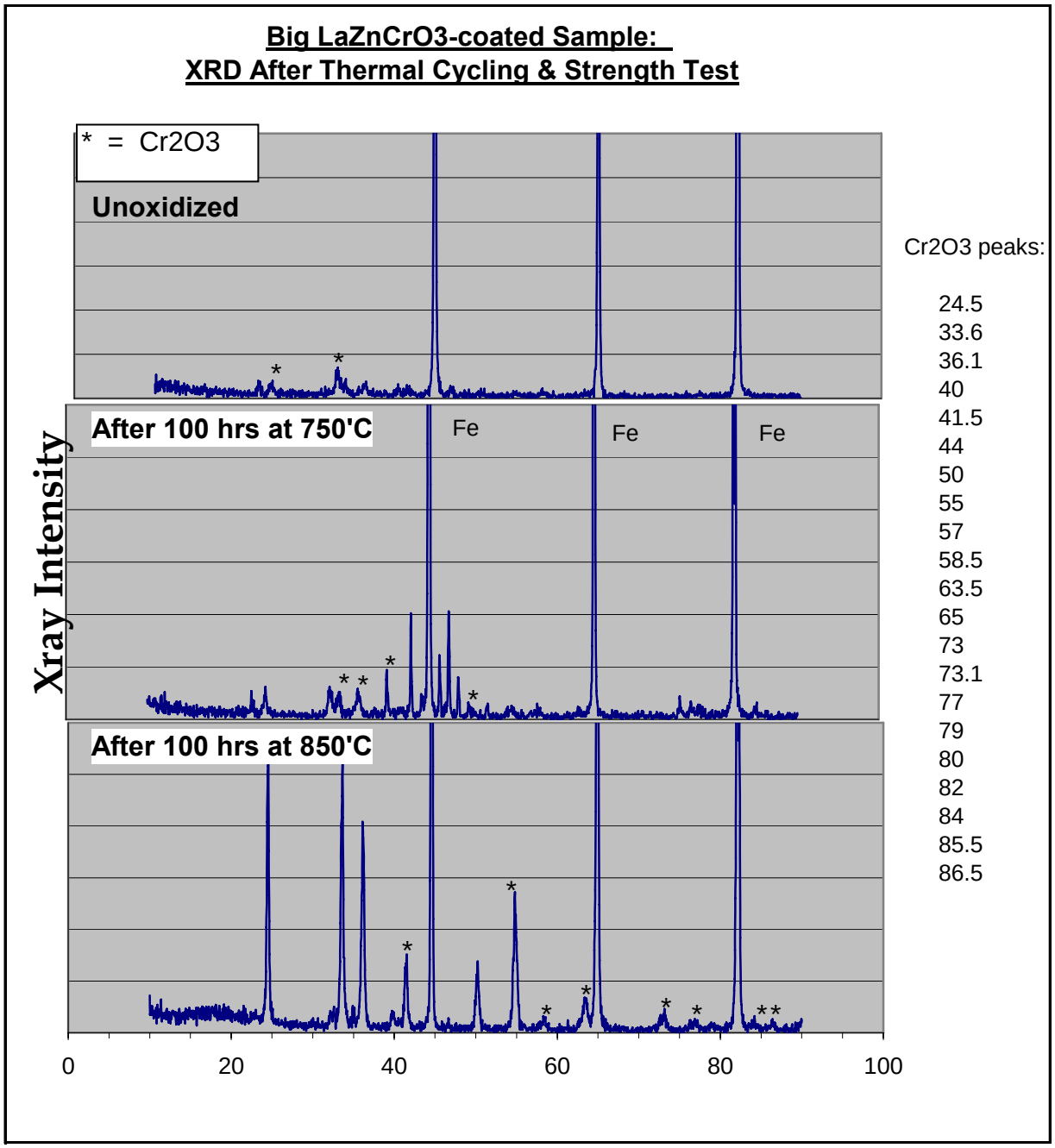

Figure 4. XRD of Ebrite coated with $LaZnCrO_3$ before and after oxidation.

III. Strength Testing of Ebrite uncoated and coated with $LaZnCrO_3$ film

The strength testing process involved several steps. First, a pull test stud with a thin layer of adhesive on it clamped to the sample put into an oven to cure at 150°C for about 1 hour and 15 minutes to cure the adhesive. After cooling, the stud was pulled off the sample using a Quard Group tensile pull tester. The force at which the stub separated from the specimen was recorded and the surface of the pull area on the specimen studied using a Keyence optical microscope.

As explained in Section II above, the large 2 x 2 cm^2 sample was oxidized at 750°C and 850°C for 100 hours each. After each 100 h oxidation, the specimen was tested for film adhesion. For comparison, an uncoated Ebrite of the same size was oxidized under the same condition and tested in the same way.

Table 4 summarizes the pull test results on the coated and uncoated Ebrite samples, and Figure 5 shows representative photos of the specimen surface under the pulled area.

None of the coated samples failed at the film/alloy interface, not even after 850°C oxidation for 100 hrs. The uncoated Ebrite also did not show any interfacial failure after 100 hrs at 750°C, but after 850°C, the film/alloy interface became significantly weaker than that of the coated sample. This can best be seen comparing Figs. 5a and 5c. The coated specimen failed mainly at the glue/stub interface or within the glue layer and showed no failure at the film/alloy interface, but the uncoated alloy showed substantial failure at the film/alloy interface. Since failure took place at different sites, the failure force listed in Table 4 cannot be used to compare the adhesive property of these various films. The results, however, do indicate a strengthening effect of the $LaZnCrO_3$ coating on Cr_2O_3 scales, even though at 850°C, the coating no longer reduces the Cr_2O_3 growth rate.

Table 4. Summary of tensile testing of Ebrite alloy uncoated and coated with the $LaZnCrO_3$ film after 750 and 850°C.

Sample	Oxidation Condition	Failure Force (lbs)	Observations
$LaZnCrO_3$ coated Ebrite	After 750°C, 100 hrs	64 88.2	Failed at glue-film interface and in glue layer
	After an additional 100 hrs at 850°C	101.3 109.4 109.9	Failed at glue-film interface and in glue layer (Fig. 5a)
Uncoated Ebrite	after 750°C, 100 hrs	120.9	Mostly failed at glue-film interface (Fig. 5b)
	After an additional 100 hrs at 850°C	111.7	~ 20% of the test area failed at the film-alloy interface
		112.3	~ 60% failed at the film-alloy interface (Fig. 5c)

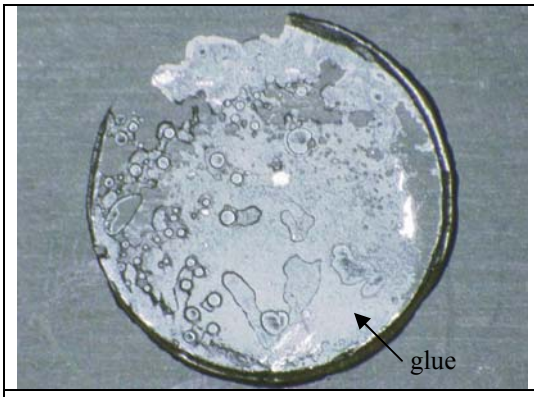

Figure 5a. Optical image of area under pull stub on Ebriete coated with $LaZnCrO_3$ oxidized at 750°C for 100h followed by another 100h at 850°C.

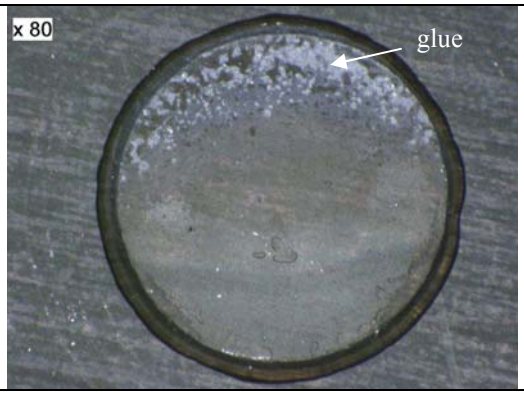

Figure 5b. Similar image from uncoated Ebriete oxidized after 100h at 750°C.

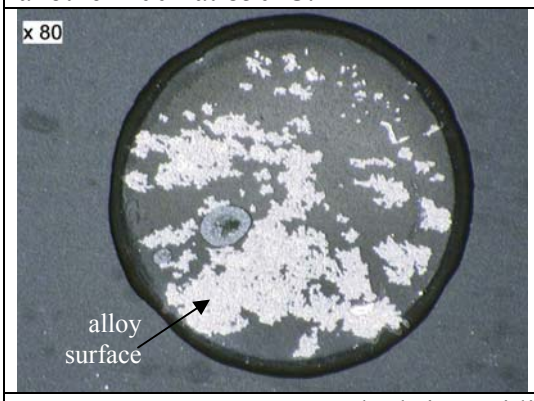

Figure 5c. From uncoated Ebrite oxidized after 100h at 750°C then 100h at 850°C.

IV. Conductivity Testing of $LaZnCrO_3$ film

For conductivity testing the coated sample was masked with high-temperature Kapton tape to expose about 30% of the area in the center. Gold was then evaporated onto the coated surface, and the same masking and evaporation was repeated on the uncoated back side. Pt-wire mesh, about 0.5x2cm, was attached on both sides of the Au coated areas with Au paste. After drying each side under the heating lamp, the sample, with meshes attached on both sides, was sintered at 850°C for 30 minutes (ramp up and down rate: 5°C/min). Pt wires were spot welded to the mesh as current and voltage leads.

Testing conditions were as follows: in an air atmosphere, the sample was taken up to 500°C with a heating rate of 5°C/min (the heating cycle). While the current was increased in 20mA steps up to 1000mA, voltage was measured to create an IV curve. This was repeated at 600, 700, 750 and 800°C. Then the sample was held at 800°C for 22 hours, and tested at the same temperatures (800, 750, 700, 600, 500) during cooling.

Sample 4 from the Jan. 04 batch, identified as having a thicker film, was used for this test.

Results of this conductivity run is plotted in Figure 6b, which show a difference in the heating and cooling cycles. The difference is most likely due oxide growth over the 22-hour holding period at 800°C, which makes the sample much more resistive. Compare to the behavior of an uncoated alloy and the one coated with $La_{0.8}Sr_{0.2}CrO_3$ that was also tested under a heating cycle (Fig. 6a), this $LaZnCrO_3$ coated sample had lower ASR to begin with (500°C on the heating cycle), but the resistance increased faster than the $LaSrCrO_3$ coating. At the end of the heating cycle, the ARS of the $LaZnCrO_3$ coated sample was 0.011 Ωcm^2, but only 0.004 on the $LaSrCrO_3$ coated on. After 22 hours at 800°C, the ASR of the $LaZnCrO_3$ coated sample at 800°C increased to 0.024 Ωcm^2. This level is still lower than that found on a ~2 μm thick Cr_2O_3 scale, but not much lower.

The apparently poorer behavior of the $LaZnCrO_3$ coating is really due to a different in experimental setup. Pt leads were spot welded directly onto the alloy on the back side of the previously tested $LaSrCrO_3$-coated sample, hence eliminated contribution of scale growth on uncoated alloy surfaces. The same welding method was attempted several times with this batch of coating, but each time, the circuit was shorted due to puncturing of the top film during welding. This faster increase and higher ASR's observed on this coated sample, therefore, is due to contributions from Cr_2O_3 growth on the back side of the specimen, which was uncoated.

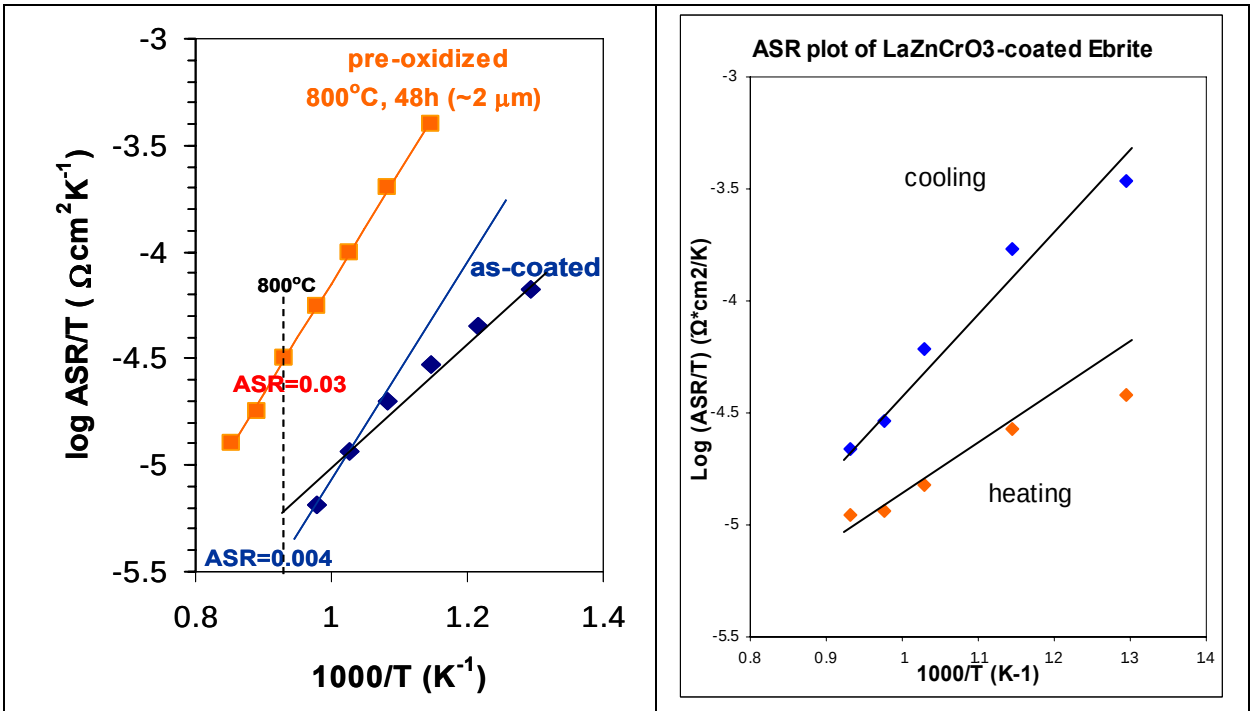

Figure 6a. Area Specific Resistance plot for oxidized Ebrite (red), and Ebrite coated with $La_{0.8}Sr_{0.2}CrO_3$ film (blue).

Figure 6b. Area Specific Resistance plot for Ebrite coated with $LaZnCrO_3$ film. Sample was heated to 800°C, held for 22 hours and then cooled.

Summary

- The $LaZnCrO_3$ coating is as protective as the $LaSrCrO_3$ coating at 750°C in air. Oxidation rate was reduced by an order of magnitude and Cr_2O_3 grew mainly under the film. At 850°C, the thin film is no longer protective but gave way to the faster out growth of Cr_2O_3. Similar behavior is expected for the Sr-containing coating. This raises a concern about the long term protectiveness of these thin films even at 750°C. Will the film remain protective after 40,000 hrs under operating conditions?
- Adhesion of the film was strong. Tensile pull test using an adhesive with a maximum failing load of 165 lbs was not able to detach the film from the alloy. This is true even after oxidation at 750°C for 100h followed by another 100h at 850°C. The presence of the coating element within the growing Cr_2O_3 scale probably strengthened the scale/alloy interface. In comparison, an uncoated alloy showed ~50% interfacial failure after the 100h 850°C oxidation.
- Conductivity of the coated Ebrite is lower than that of the uncoated when tested between 500-800°C in air. How much of this reduction is due to a reduction of Cr_2O_3 scale growth, and how much may be due to doping effect of the coating elements in Cr_2O_3 is unknown.

3.3.3) Selection of interconnects for PENs and SOFC stacks

As a result of our studies, Ebrite alloy which was coated with $LaZnCrO_3$ was chosen as the interconnect. No furthur testing was done since stacks were never produced.

3.4) TASK # 4 Preparation of Single Layers, Trilayers and Stack Modules (AI)

3.1 Development of methods to convert OIH structures to oxide replicas for use in SOFCs;
3.2 Development of coatings and bonding of metal interconnects to porous electrodes;
3.3 Designing a multi-staged- oxidation, reversed-counter-flow, planar SOFC stack, including fuel and air manifolding, ceramic-glass sealing and stack cooling;
3.4 Selection of glass to be used to provide seals within the stacks;
3.5 Fabrication of interconnects, manifolds and glass seals for the multi-cell SOFC stack;
3.6 Delivery of trilayer stack, a 2 layer planar stack and a multilayer SOFC stack for testing.

3.4.1) Development of methods to convert OIH structures to oxide replicas for use in SOFCs;

Components for the new ammoniator (ammonifier) were procured, and fabrication of machined parts continued. The metal honeycomb-supported porous metal disks (diffusers) used for confining and dynamically loading the membranes during ammonolysis and drying were rejected owing to improper manufacture. However, they were adequate for system checkout and hence were assembled and tested using the frictionless Airpot actuators, that are supplied with air controlled by electronic pressure regulators. These tests confirmed that the actuator forces could be controlled to within .05N, which corresponds to a membrane loading pressure of 5 Pa for a membrane area of 100 cm^2. In addition, testing with a porous metal sparger immersed in a water bath (necessary for capturing the ammonia exhausted from the ammoniator), which produces a

back-pressure in the bell jar, demonstrated that the upper movable diffuser could be floated above the membrane and then gently lowered onto the membrane with a force controlled within .05 N through use of the electronically controlled pressure regulators. Further, the lifting stroke of the actuator could be controlled to within 10 microns by use of an adjustable stop, which is sufficient to unload the membrane so as to permit in-plane stress relaxation of the membrane while preventing membrane curling during stress relief.

As a result of these successful tests, ZOC-imbibed dense and porous membranes, prepared by Aker, were ammoniated, water-washed and then dried by flowing dry nitrogen through the diffuser plates with the membrane sandwiched between. The resulting membranes were flat, strong, compliant and without cracks. However, the porous membranes exhibited excessive shrinkage, both in-plane and out-of-plane, whereas the dense membranes shrunk as calculated. To overcome this excessive shrinkage, two methods (previously employed by Aker) were tested using ZOC imbibed, ammoniated and water washed porous membranes. In the first method the membranes were impregnated with EF Klucel (food-grade hydroxy propyl cellulose) and allowed to gel prior to drying. In the second method the membranes were briefly soaked in a 5 w/o methylol melamine aqueous solution having 6 moles of formaldehyde per mole of melamine and then cured to provide crosslinking with the cellulose backbone of the ZOC-imbibed membranes. Both methods eliminated the excessive shrinkage previously produced in the porous membranes, inferring that collapse of the micropores in microporous cellulose gel-film was the cause of excessive drying shrinkage.

Drying tests were then conducted on ZOC-imbibed, ammoniated and water-washed porous samples prepared by UC/NREL. These tests showed that drying shrinkage in these samples was far more pronounced than for Aker's samples (prepared from regenerated cellulose acetate/nitrocellulose porous filters manufactured by Micron Separations – now Osmonics). The reason for this difference is attributed to the much higher wet strength of the Aker samples, which exhibited a water-wet/dry weight ratio of approximately two and hence a much higher concentration of cellulose backbone that provides the skeletal structure with higher wet strength.

Soaking the UC/NREL porous samples in the above described methylol melamine aqueous solution reduced drying shrinkage, but it was still excessive. Impregnating the UC/NREL samples with EF Klucel was difficult owing to their weak gel structure, but when successfully impregnated, excessive drying shrinkage was essentially eliminated. These tests confirmed that pore collapse was the cause of drying shrinkage in weak porous cellulose gel membranes.

The two methods for preventing excessive drying shrinkage of porous gel structures are: 1) supercritical extraction and 2) freeze drying, both of which avoid the presence of a liquid-vapor interface during drying and the resulting capillary forces thereby induced. Aker evaluated these methods some twenty years ago in making silica and carbon aerogels and later applied these methods to cellulose-based gels. For cellulose-based gels both methods prevented pore collapse whereas for polymeric gels, such as those formed from metal alkoxides, only supercritical drying was successful. The cause of this difference is that in the freeze drying of polymeric gels the growing crystals reject the gel network and grow in size until the gel fractures, whereas in cellulose-based gels the cellulose backbone prevents this, especially if the

gel is quickly frozen (which minimizes the size of ice crystals and the quantity of liquid evaporated during cool-down to freezing).*

As a result of the strong backbone, the high absorption of the liquid phase (water) by this backbone, and the low strength of the porous cellulose gels, they need to be quickly frozen between flat plates (maintained at a low compressive loading) and then need to remain frozen during ice sublimation (under controlled vacuum) in order to produce flat, unwrinkled dried porous membranes without excessive drying shrinkage. In production, chilled multiple rollers, that maintain controlled membrane tension, replace the flat plates used in batch processing.

---

*In a cellulose gel the continuous solid network is a regenerated infusible cellulose (or a cellulose derivative) which interpenetrates and supports a continuous liquid phase (absorbed by the polymer) comprising a metal salt aqueous solution which is converted to a hydrous metal hydroxide prior to drying. In a polymeric gel (sol-gel) the continuous solid network is a weakly-bond polymer, derived from solution precursors, that is dispersed in a continuous liquid phase from which the polymer has been derived. The cellulose gel has a strong fugitive backbone whereas the polymer gel has a weak backbone that gains strength through condensation and dehydroxylation reactions. As a result, the two gels exhibit properties and require processing steps (including sintering) that are markedly different.

Conventional freeze drying, in which the porous membrane is first frozen and then sublimated without geometrical restraint or controlled and continuous refrigeration, results in a highly wrinkled and curled porous cellulose membrane.*

The design of a flat plate freeze dryer for porous cellulose gel films is best met by using flat porous plates that initially permit rapid cool-down by use of cold dry nitrogen gas, produced from LN expansion through the plates, and then continuously cooling under vacuum using one of the plates as a refrigerant evaporator (to maintain the membrane frozen during vacuum drying) while the opposite-facing porous plate permits the water vapor (formed from ice sublimation) to escape to the vacuum pump).**

Concern of fracturing the porous cellulose gel during freezing (due to volume expansion of the absorbed water upon freezing) is unwarranted since: 1) the linear expansion produced in freezing of water is 3%, i.e. a linear tensile strain of .03 is produced when unconfined, which produces a cellulose tensile stress of 6 ksi (40 MPa) for re-wetted dried cellulose (having a tensile modulus of 200 ksi) and much less for cellulose gel-film which has a markedly lower but unknown tensile modulus, and 2) cellulose gel-film, upon immersion into LN, does not crack.

Freeze drying of cellulose gel-films, confined between flat plates, requires continuous refrigeration, even though sublimination is an endothermic reaction (requiring heat addition to maintain constant temperature). This is due to the heat loss from the flat plates being much greater than the heat absorbed by sublimination of the ice contained in the gel-film. For two flat disks of 5.00 in (12.7 cm) diameter mounted in a vacuumized glass bell jar the heat loss is calculated to be 33 Btu/hr (9.7 watts) whereas the heat absorbed by sublimating a cellulose gel-film of 5.00 in diameter and .010 in thickness is 8.0 Btu/hr (2.3 watts) if performed at a constant

rate for 1 hour. Hence, the refrigeration required to maintain constant temperature is 9.7 – 2.3 = 7.4 watts. Significantly higher refrigeration capacity would be needed if the flat plates and cellulose gel-film were not rapidly precooled by expanding LN.

Freeze drying of cellulose gel-films must be performed at a temperature between 12 and 18^{o}F (-11.1 and –7.8^{o}C), below which ice becomes brittle and above which its strength rapidly diminishes. Further, decreasing the temperature below 12^{o}F reduces the vapor pressure of ice (approx. 2 Torr @ 14^{o}F), which increases the time required for the complete drying of wet cellulose porous membranes.

---

* In the commercial production of cellulose porous membranes, the water content of the cellulose is significantly lower, resulting in a wet membrane that is sufficiently strong so as to resist the capillary forces produced during drying and therefore freeze drying is not required.

** The use of CO_2 for initial cool-down is undesirable since: 1) CO_2 forms snow (dry-ice) during its evaporation from liquid whereas LN does not, 2) liquid CO_2 pressure is much higher than cryogenically stored LN and 3) membrane-contained water will absorb CO_2 during cool-down which then must be removed during freeze drying thereby increasing the gas pumping load on the vacuum pump.

The refrigerant used in the cooled flat plate (acting as a refrigerant evaporator) should exhibit a pressure at ambient temperature (which occurs when the system is shut down) of approximately 100 psig in order to permit the use of flexible plastic tubing as refrigerant tubing that connects the movable evaporator flat plate to the fixed supply and discharge piping attached to the bell jar base plate. Commercial refrigerant R-134a satisfies this requirement, having a saturation pressure of 124 psig at 100^{o}F – a conservative temperature. Further, R-134a is compatible with commercial flexible nylon-12 tubing having a 150 pisg maximum operating pressure (burst pressure of 670 psig) at 140^{o}F.

Pre-cooling of the flat disks and cellulose porous gel-film, by use of expanding LN, is continued below 12^{o}F to insure sufficient chilling, after which the assembly must be heated to the temperature required for freeze drying (12 to 18^{o}F) and then maintained at this temperature throughout the freeze drying process.

Freeze Dryer Design

The above requirements dictate the design of the freeze dryer, which is described in the following discussion. This freeze dryer will utilize the design of the present dryer but use modified components and a mechanical refrigeration system.

Evaporator temperature control is to be achieved by: 1) use of a hot gas bypass line direct from the refrigerant compressor for heating (which is simpler than using a separately controlled heating plate) and 2) the use of an expanding refrigerant in the evaporator for cooling. Refrigerant expansion is to be performed by a combination solenoid-operated throttling valve in series with an adjustable metering valve in which expansion to evaporator pressure occurs. The

solenoid-operated throttling valve modulates the refrigerant flow by opening and closing in response to signals provided by a temperature controller which senses the evaporator temperature through use of an E-type thermocouple that is sealed to the evaporator and immersed in the liquid refrigerant contained therein. A flooded evaporator is to be used in which the internal face of the evaporator side, in contact with the cellulose gel-film, has a porous metal coating which produces uniform nucleate boiling across the face, thereby maintaining uniform temperature across the face that is in contact with the cellulose gel-film.

For evaporator heating, uncooled refrigerant vapor from the refrigerant compressor is to be injected directly into the evaporator through use of a solenoid-operated valve operated in response to signals provided by the temperature controller, but delayed by a delay-to-make relay which prevents excessive cycling between heating and cooling modes.

The refrigeration system is to use the smallest refrigerant compressor commercially available (Danfoss model PL30FX) with a rated cooling capacity of 60 watts at the required operating conditions of the freeze dryer. Since this cooling capacity is approximately eight times that required by the freeze dryer at steady-state condition, modulation of the compressor is required. This will be done by use of a solenoid-operated by-pass valve and a solenoid-operated suction valve. The by-pass valve unloads the compressor by circulating compressor discharge through an air-cooled heat exchanger back to the compressor suction line. The suction valve, normally open, is closed when evaporator temperature drops below the low temperature set-point, thereby raising evaporator pressure and quenching refrigerant boiling so as to prevent further heat extraction.

A glass bell jar, mounted on an O-ring sealed base plate, will provide the vacuum chamber, with the sealed plate manifolded to an oil-free mechanical vacuum pump for maintaining vacuum in the bell jar. Placed inside the bell jar will be pressing plates (one the evaporator and the other a metal honeycomb-supported porous metal disk) that slightly compress the porous cellulose gel-film during both freezing and freeze drying in order to keep the film flat. The compression force will be produced by a “frictionless” piston actuator (Airpot) that is supplied by air pressure, controlled by an electronic pressure regulator that is vented to the vacuum jar interior so as to act as a differential pressure regulator. Periodically, the supplied air pressure is increased, by use a 3-way solenoid-operated valve, which temporarily lifts the evaporator to unload the porous cellulose gel-film so as to allow the film to relax in-plane stresses prior to reclamping the film. Outgassing of the film during drying is to be provided by porous, hydrophobic, compliant Teflon sheets that sandwich the film and transmit to the film a uniformly low compressive force, provided by the Airpot actuator, so as to maintain film flatness.

Upon completion of freeze drying, the pressing assembly and dried film are heated to ambient temperature through use of hot bypass gas flow to the evaporator and then the dried film is removed from the bell jar after venting to atmosphere.

The dried film then will be rehydrated by exposing to humidified air. This step is necessary since the freeze-dried cellulose contains nanoporosity due to sublimination of the water originally contained in the dense portion of the cellulose. The natural water absorbency of

cellulose provides this rehydration without filling the micropores of the porous membrane. Without this rehydration the "dense" portion of cellulose will be porous and therefore more difficult to consolidate during pyrolysis and sintering.

After rehydration, the cellulose will be dried using dry nitrogen, during which process the nanopores will collapse and yield a dense cellulose that intercalates the hydrous metal hydroxides.

AI completed the designs of the pyrolizing/oxidizing furnace and reported the details at the September 12, 2003 review meeting held at NREL. Fabrication of the ammoniator, dryer and pyrolyzing/oxidizing furnace(except of the required skinned honeycomb silicon nitride pressing plates) was completed by the end of the contract. However flat oxide film was never produced because the required pressing plates were never deliver to AI by the chosen vendor.

3.4.2) Development of coatings and bonding of metal interconnects to porous electrodes

AI intended to develop both the coatings, metal interconnects and bonding procedure by means of a subcontract with Professor Mishra at the Colorado School of Mines. As was shown above in section **3.1**, this project was not successful, so the only interconnect coating and bonding occurred in the LBL program (**3.2)**

3.4.3) Designing a multi-staged- oxidation, reversed-counter-flow, planar SOFC stack, including fuel and air manifolding, ceramic-glass sealing and stack cooling;

AI worked on this, but at this time there was not sufficient documentation and time available to allow construction of a SOFC stack. Also the inability to produce flat oxide membranes prevented the incorporation of PEN structures into the system

3.4.4) Selection of glass to be used to provide seals within the stacks

The sealing glass was developed by UMR under a subcontract between AI and Professor Richard Brow. The results of the project were very promising and it appears that a glass was developed which could be used in this program. However, stacks were never produced so we were unable to confirm this.

The final report of this program follows:

Developing Sealing Materials for Solid Oxide Fuel Cells

Final Report

Prepared by

S. T. Reis and R. K. Brow

Ceramic Engineering Department

University of Missouri-Rolla

Rolla, MO 65401, USA

August 2004

1. SUMMARY

This report describes the thermal and chemical properties of 'invert' glasses and glass-ceramics developed for hermetic seals for solid oxide fuel cells (SOFC). Invert glasses are those with relatively low concentrations of glass-forming oxides (<45mol% SiO_2) and so possess structures with continuous networks of modifying polyhedra instead of glass-forming tetrahedral [1]. These compositions fall outside of ranges reported for other SOFC sealing systems which have generally greater silica contents and usually possess significant concentrations of BaO [1,2]. The glasses in this work were crystallized to form thermally stable pyro- and orthosilicate phases with the requisite thermal expansion match to the Y-stabilized ZrO_2 (YSZ) electrolyte and the glass-ceramics form strong bonds to the Cr-steel alloy 'E-brite' at 850ºC. Furthermore, the glass-ceramics appear to be stable for extended times (over 28 days) at 750ºC in reducing atmospheres. Finally, the extent of interfacial reactions between the glass-ceramics and E-brite appears to be much less than that reported for BaO-containing sealing glasses [1].

This report describes

- The evaluation of the properties of bulk glass-ceramic systems based on silicate glasses, including thermal and electrical properties;
- The evaluation of the characteristics and long-term thermal stability of the sealing systems, including weight loss measurements in forming gas, and differential thermal analyses (DTA) and x-ray diffraction (XRD) analyses;
- The evaluation of the thermal expansion match of the glass seals with YSZ coupons and E-brite substrates, including dilatometric analyses of as-sealed and heat-treated glasses.
- The evaluation of reactivity of the glass seals with YSZ, E-brite, and (La,Sr)CrO_3 coated E-brite substrates, including XRD and microscopic studies of interfaces.
- The evaluation of the electrical resistivities of 'sandwich seals' between glass-ceramics and E-brite in reducing environments and of simulated SOFC stacks with thin (~400 μm) glass seals.

2. EXPERIMENTAL PROCEDURES

Table 1: Batch compositions of the sealing glasses

Composition (mol%)

ID	SrO	CaO	ZnO	B_2O_3	Al_2O_3	SiO_2	GeO_2	BaO	TiO_2	ZrO_2	Cr_2O_3	La_2O_3
2	50.0	-	-	-	10.0	40.0	-	-	-	-	-	-
6	25.0	-	25.0	-	10.0	40.0	-	-	-	-	-	-
7	27.5	-	27.5	-	5.0	40.0	-	-	-	-	-	-
12	25.0	25.0	-	-	5.0	45.0	-	-	-	-	-	-
13	25.0	25.0	-	2.0	3.0	45.0	-	-	-	-	-	-
14	23.8	23.8	-	1.9	2.9	42.8	-	-	-	5.0	-	-
16	20.0	20.0	10.0	2.0	3.0	45.0	-	-	-	-	-	-
18	19.6	19.6	9.8	2.0	2.9	44.1	-	-	2.0	-	-	-
19	19.2	19.2	9.6	1.9	2.9	43.2	-	-	4.0	-	-	-
20	16.7	16.7	16.7	2.0	3.0	45.0	-	-		-	-	-
21	16.4	16.4	16.4	2.0	2.9	44.1	-	-	2.0	-	-	-
22	16.5	16.5	16.5	2.0	3.0	44.6	-	-	1.0	-	-	-
23	27.5	-	27.5	2.0	3.0	40.0	-	-		-	-	-
24	25.0	13.5	13.5	5.0	3.0	40.0	-	-		-	-	-
25	24.5	13.2	13.2	4.9	2.9	39.2	-	-	2.0	-	-	-
26	24.3	13.1	13.1	4.9	2.9	38.8	-	-	3.0	-	-	-
27	18.5	19.2	13.2	1.9	2.9	42.2	-	-	2.0	-	-	-
28	18.5	19.2	13.2	1.9	2.9	38.2	4.0	-	2.0	-	-	-
29	20.0	20.0	10.0	2.0	3.0	43.0	2.0	-	-	-	-	-
30	19.6	19.6	9.8	2.0	2.9	42.1	2.0	-	2.0	-	-	-
32	18.5	19.2	-	1.9	2.9	42.2	-	13.2	2.0	-	-	-
33	18.5	19.2	13.2	1.9	2.9	42.2	-	-	-	-	2.0	-
34	26.0	26.0	-	4.0	2.0	42.0	-	-	-	-	-	-
35	25.5	25.5	-	3.9	2.0	41.2	-	-	-	-	-	-
36	26.5	26.5	-	1.9	2.0	41.2	-	-	2.0	-	-	-
37	-	26.0	26.0	4.0	2.0	42.0	-	-	-	-	-	-
38	26.0	-	26.0	4.0	2.0	42.0	-	-	-	-	-	-
39	26.0	-	26.0	7.0	2.0	39.0	-	-	-	-	-	-
40	26.0	13.0	13.0	4.0	2.0	42.0	-	-	-	-	-	-
41	26.0	-	26.0	2.0	2.0	44.0	-	-		-	-	-
42	26.0	13.0	13.0	2.0	2.0	42.0	-	-	2.0	-	-	-
43	18.5	19.2	13.2	1.9	-	42.2	-	-	2.0	-	-	2.9

The glasses were prepared from mixtures of reagent grade alkaline earth carbonates and silica, with concentrations of other oxides added as indicated. The batches were melted in platinum crucibles in air for 4 hours, typically at 1550°C. A typical melt size was approximately 50 grams.

Melts were quenched on steel plates and glasses were annealed for 6 hours near the appropriate glass transition temperature. The starting compositions (mol%) and the sample identification are indicated in Table 1.

The SOFC component materials used for sealing experiments include the solid YSZ electrolyte (8 mol% Y_2O_3), prepared by tape casting, and the interconnect alloy E-brite, with the reported [5] composition (in wt%); 26.5 Cr, 0.15 Ni, 0.10 Mn, 0.21 Si, 1.01 Mo, 0.12 Cd, 0.05 Ti, 0.01 V, 0.05 Al, 0.05 Cu, 0.02 C, 0.01 N, 0.01 P, 0.01S, and Fe as the balance. (The E-brite samples were provided by *Aker, Inc*.)

Glass powders (sieved to 125 μm) were used for differential thermal analyses (DTA)[*], heating in air at 10°C/min to determine the glass transition temperature, T_g, and crystallization temperature, T_c. The estimated error for T_g and T_c is ±2°C. Glass powder was crystallized by heat treating at temperatures around T_c for two hours in an argon atmosphere. Powders of crystallized samples (ground and sieved to 45-75 μm) were characterized by x-ray diffraction (XRD)[†]. Glass and crystallized samples, approximately 25 mm long, were prepared for dilatometric[‡] analyses, heating in air at 3°C/min, to determine the coefficient for thermal expansion (CTE) and the dilatometric softening points (T_d). The CTE was calculated between room temperature (RT) and the 600°C for 'as made' glass and partially crystallized samples, and between RT and 750°C for fully crystallized samples. The crystallized samples were prepared for dilatometric analyses by first sintering, then crystallizing glass powders in graphite molds (25 x 10 mm) under argon for the indicated time and temperature.

Glass powders were bonded to E-brite alloy substrates with and without $(La,Sr)CrO_3$ coatings. (The coatings were deposited by Dr. Xiao-Dong Zhou (EMARC) and are intended to reduce the diffusion of Cr from the alloy under the SOFC operational conditions.) The glasses were ground and sieved to separate particles in the size range of 45-75 μm and the powder was mixed with a binder (polymer type PVB, Ferro BX018-16), to form a paste that was then applied to the coated and uncoated substrates. These reaction couples were heated to 500°C for 2 hrs in air to remove the binder, and then fired in an alumina muffle furnace for the desired sealing times and temperatures under flowing argon. E-brite/G#27 and E-brite/G#32 reaction couples were further subjected to long-term heating at 750°C in air and in forming gas (10% hydrogen and 90% nitrogen). Reaction couples were prepared for microscopic evaluation. Samples were cross-sectioned with a diamond saw, then polished to a sub-micron finish and evaluated by analytical scanning electron microscopy[§] and optical microscopy.

Glass pastes were also deposited and sintered on YSZ substrates and also on E-brite substrates in order to measure the glass electrical conductivity. The sample configurations are shown schematically in Figure 1 (a) and (b). After the binder decomposition step, samples were sintered at 800°C for 2h in argon. The top gold electrode and platinum wire were attached. After conductivity measurements at 800°C, the glass layers were crystallized at 850°C for 2h and the electrical measurements were repeated. Both AC and DC techniques were employed for sample

[*] Perkin/Elmer DTA 7
[†] Scintag XDS2000X
[‡] Orton Dilatometer model 1600D.
[§] Hitachi 4700 SEM with the Phoenix EDAX system

conductivity evaluation. Impedance spectra were measured with an SI 1296 dielectric interface and SI1260 impedance analyser in the frequency range from 100kHz to 0.1Hz, while an electrometer (Keithley 6517A) was used for DC resistance measurements. Samples were placed in the tube furnace and investigated in the temperature range from 550°C to 750°C. Measurement were performed in air, nitrogen and forming gas (10% hydrogen and 90% nitrogen).

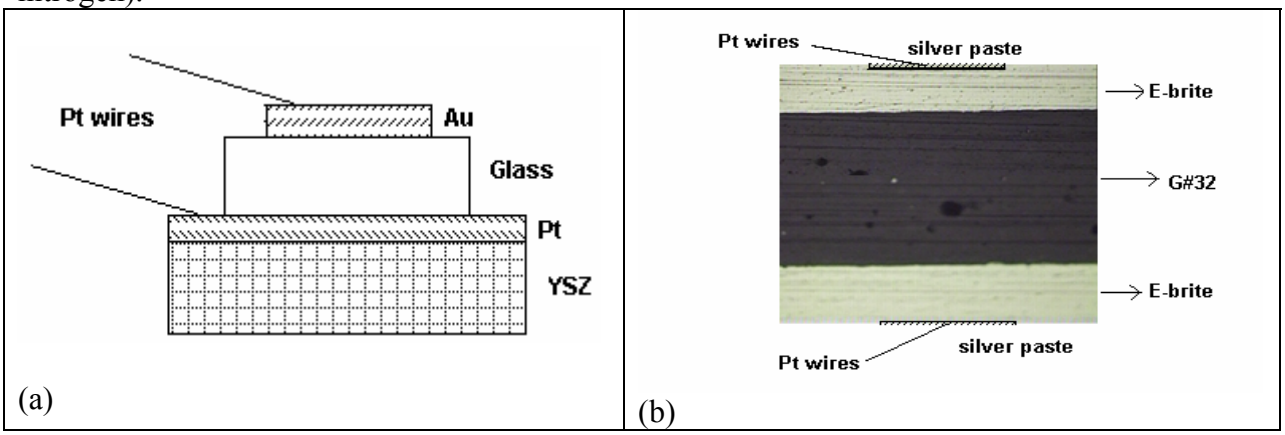

Figure 1: Schematic diagram of the electrical conductivity measurement configuration on (a) YSZ samples, and (b) E-brite/Glass/E-brite.

Chemical stability of crystallized glass samples in reducing environments was evaluated by measuring the weight loss from 'as-sealed' samples held in flowing forming gas at 750°C for 1 to 14 days. The samples were polished to 600 grit finish with SiC paper, cleaned with acetone and supported by a Nickel-Chromium wire in an alumina muffle furnace at 750°C under flowing forming gas. The measurements were made for each crystallized glass sample and the average weight loss, normalized to the glass surface area, was calculated from the sample weight loss measurements.

3. RESULTS

3.1 *Bulk Glass-Ceramic Systems*

The thermal properties of the glasses and resulting glass-ceramics prepared in this work are summarized in Table 2 and in Figure 2. The highlighted section in Figure 2 identifies the candidate sealing compositions with coefficients of thermal expansion (after crystallization) in the range 100-120x10^{-7}/°C and with sealing temperatures at or below 850°C. Table 3 provides a summary of the crystalline phases detected in the glass-ceramics by x-ray diffraction (XRD).

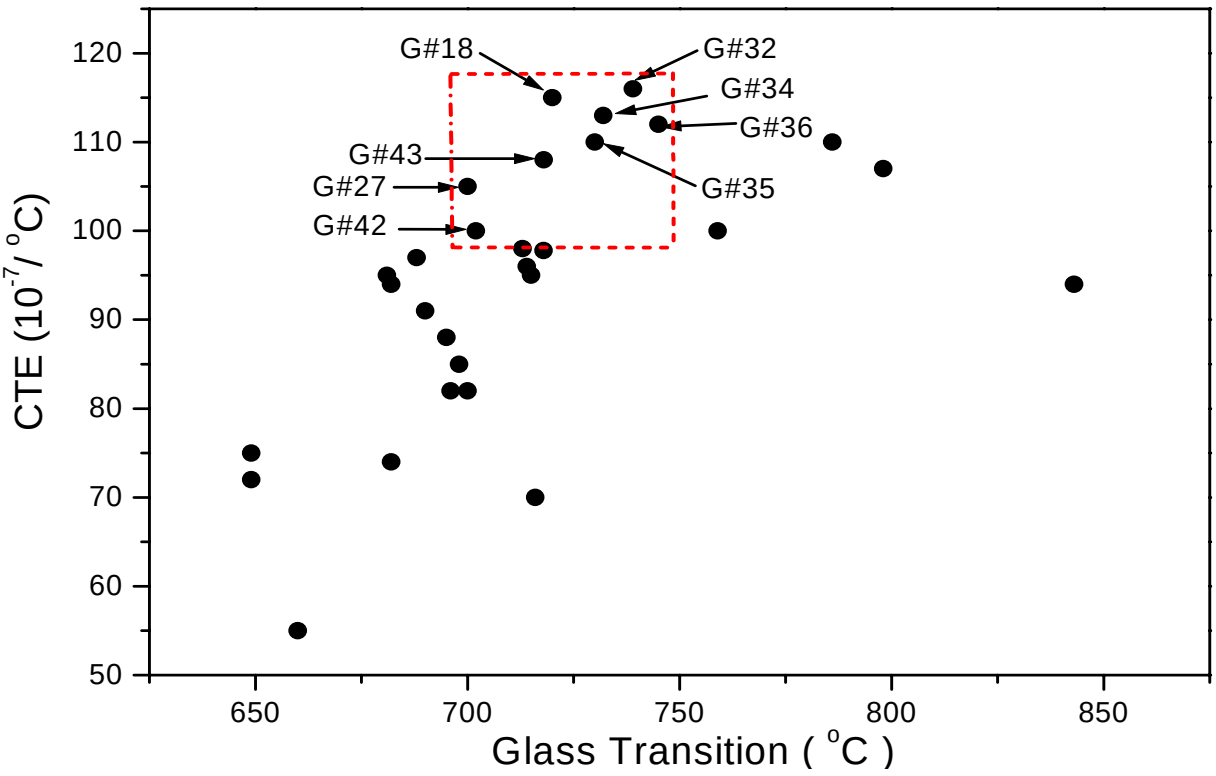

Figure 2: A summary of the glass transition temperatures and thermal expansion coefficients of the "invert" silicate sealing glasses. The highlighted area represents the preferred thermal properties for SOFC sealing glasses.

Table 2: Thermal properties of SOFC sealing glasses.

Properties

ID	Glass Transition Temperature (^oC)	**Softening Temp.** (^oC)	Crystallization Temperature (^oC)	Thermal Expansion (Glass, 100-600 ^oC) ($\times 10^{-7}/°C$)	Thermal Expansion (Crystal., RT to 700^o) ($\times 10^{-7}/°C$)
2	843	800	979	106	94
6	716	775	898	79	70
7	696	775	815/920	82	82
12	786	820	960	95	110
13	759	788	990	108	100
14	798	826	1040	107	106
16	720	751	929	100	104
18	720	755	920 - 940	102	120 - 115
19	720	755	908	100	102
20	700	730	922	86	90
21	695	732	845	86	88
22	700	736	911	90	82
23	690	723	818 - 897	89	91-78
24	681	704	864	93	95
25	682	717	862	93	94
27	700	730	904	95	105
26	688	719	790-881	97	97
28	456-705	735	820 - 904	95	-
29	713	704	911	92	100
30	715	746	890	91	95
31	698	733	808- 895	93	85
32	739	764	843	110	116
33	714	749	914	93	96
34	732	748	927	113	113
35	730	756	907	110	110
36	745	750	956	109	112
37	649	738	865 - 961	68	75
38	660	744	910	84	55
39	649	727	865	92	72
40	715	744	871	94	104
41	682	765	913	79	74
42	702	720	875	100	100
43	718	738	888	108	108

These results indicate some composition-property trends that are useful for the design of potential SOFC sealing materials. For example, the replacement of SrO by ZnO in the SrO-ZnO-Al_2O_3-SiO_2 system (e.g., glass #6, 7 and 37) and of CaO by ZnO in the CaO-ZnO-Al_2O_3-SiO_2 system (e.g. glass #38) decreases the T_g and so reduces the sealing temperature, but may also reduce the CTE of the crystallized samples to a value too low to be practical. (The low CTE appears to be related to the presence (Table 3) of the crystalline phase Zn_2SiO_4; CTE ~ 45 $x10^{-7}$/°C [6]. Table 2 also shows that replacing Al_2O_3 with B_2O_3 reduces T_g and increases CTE. B_2O_3 likely remains in a residual glassy phase and the reduction of the Al_2O_3 content prevents the formation of lower CTE phases like $CaAl_2Si_2O_8$ and Al_2SiO_5. Also mixed CaO/SrO compositions (glasses #16 - #19) with ZrO_2 or TiO_2 as nucleating agents produce crystallized materials with higher CTE. Crystallized glass #14 has a CTE in the range desired for some SOFC applications; however, with 5 mol% ZrO_2, the material has a preferred crystallization temperature which may be too high for some SOFC applications. TiO_2 appears to be a more effective nucleating agent than ZrO_2, decreasing T_x without significantly increasing T_g. The replacement of ZnO by BaO for G#32, ZnO by SrO and CaO in G#34, #35 and #36, produce crystallized materials with a higher CTE. Even though these crystallized glasses have a CTE (110 – 116 $x10^{-7}$/°C) in the range desired for some SOFC applications, the materials also have glass transition and crystallization temperatures which may be too high for some SOFC applications. G#42 has a high SrO content (26%mol) and a low glass transition and crystallization temperature, and also has a CTE in the range appropriate for some SOFC applications. The replacement of Al_2O_3 by La_2O_3 in the G#27 produces a composition (G#43) with a greater CTE and intermediate T_g which could be appropriate for some SOFC applications.

The thermal properties of the glasses G#25, #27 and #42 are promising (Table 2). The partial replacement of SiO_2 and CaO by SrO, ZnO and B_2O_3 decreases T_g, T_c, and T_d, while retaining CTEs for the crystallized samples that are similar to YSZ ($100x10^{-7}$/°C). Figure 3 shows the CTE curves for the glasses of compositions #25, #27 and #42 after a typical 'sealing run' (crystallization treatment at 850°C for 2hrs in argon), along with the dilatometric curve for YSZ. Each crystallized glass shows an excellent CTE match to YSZ. The "as sealed" samples exhibit inflections in their expansion curves near the respective T_g for the "as made glass". It seems likely that these inflections, which increase the nominal CTE, are due to the expansion characteristics of the residual glass in the crystallized samples.

Table 3: Crystalline phases identified by XRD in SOFC glasses crystallized in argon for 2h.

	T	Crystalline Phases (%)								
Glass ID	emp (°C)	Sr_2SiO_4 [6]	$SrAl_2Si_2O_8$ [7]	$CaAl_2Si_2O_8$ [6]	$CaSiO_3$ [6]	Zn_2SiO_4 [6]	$CaSrAl_2SiO_7$ [7]	$Ca_2ZnSi_2O_7$ [8]	Al_2SiO_5 [6]	$Ca_2BaSi_3O_9$ [9]
2	1000	×	×	-	-	-	-	-	-	-
6*	950	×	×	-	-	×	-	-	-	-
7	850	×	×	-	-	×	-	-	-	-
12*	950	×	×	-	×	-	-	-	-	-
13	950	×	-	-	×	-	-	-	×	-
14	940		-	-	-	-	-	-		-
16*	920	×	-	-	-	-	×	-	-	-
18	940	×	-	-	-	-	×	×	-	-
19	900	-	-	-	-	-	-	-	-	-
20	900	-	-	-	-	-	-	-	-	-
21	840	×	-	×	-	-	×	×	-	-
22	940	-	-	-	-	-	×	×	-	-
23	920	-	-	-	-	×	×	×	-	-
24	850	-	-	-	-	-			-	-
25	850	-	-	-	-	-	×	×	-	-
27	850	-	-	-	-	-	×	×	-	-
32*	850	-	-	-	-	-	-		-	×
33	914	-	-	-	-	×	×	×	-	-
34*	930	×	-	×	-	-	-		-	-
35*	900	×	-	×	-	-	-		-	-
36	956	×	-	×	-	-	-		-	-
37	950	-	-	-	×	×	-	×	-	-
40	850	-	-	-	-		×	×	-	-
42	850	-	-	-	-		×	×	-	-

* Partially crystallized

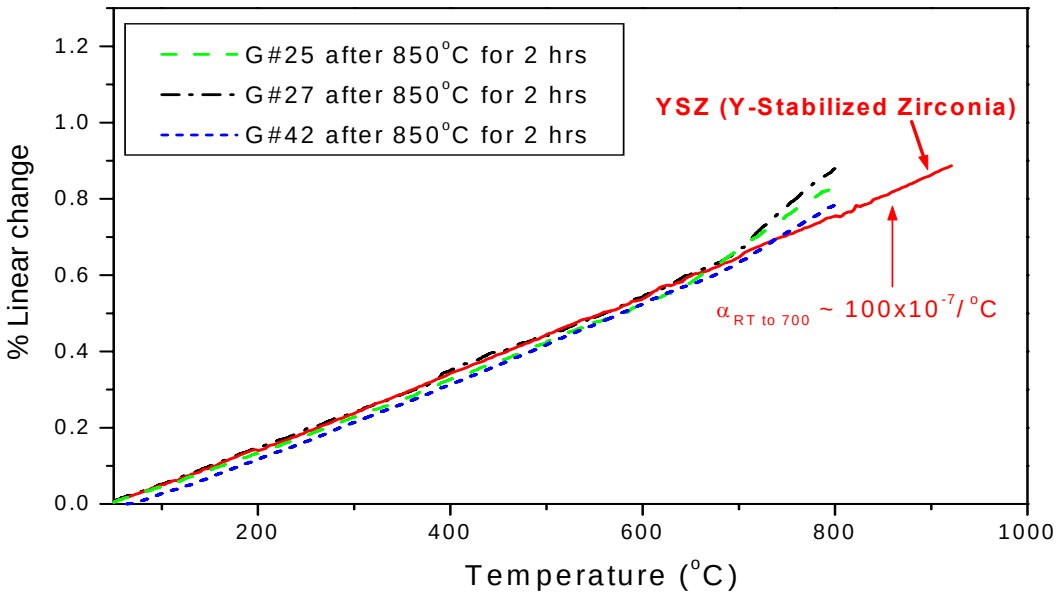

Figure 3: Dilatometric curves for glasses #25, 27 and #42 after crystallization at 850°C for 2hr. Also shown is the dilatometric curve for YSZ. Note the softening point in the CTE curves near T_g for the "as sealed glasses".

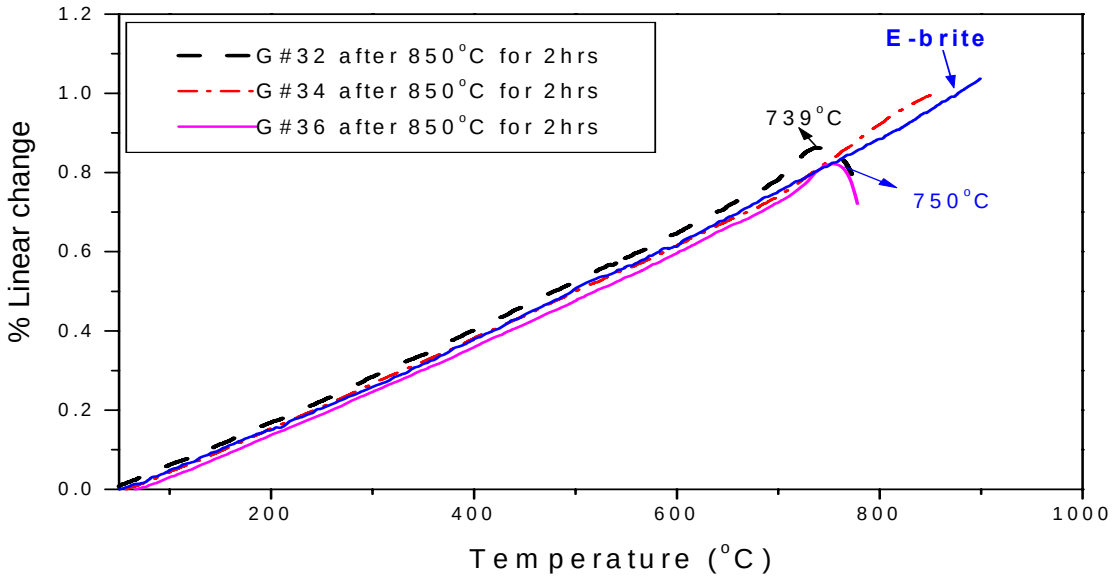

Figure 4: Dilatometric curves for glasses #32, #34 and #36 after crystallization at 850°C for 2hr. Also shown is the dilatometric curve for E-bright. Note the softening point in the CTE curves around 739°C for glass #32 and around 750°C for glass #36.

Figure 4 compares the CTE curves for G#32, #34 and #36 with that from E-brite. The glasses were heated to 850°C for 2hr, a typical 'sealing run' for these materials. G#32 and G#36 still

exhibit the dilatometric characteristics of a glassy material, whereas #34 is more completely crystallized. These samples have good CTE matches to E-brite.

Crystallized samples were characterized by x-ray diffraction (XRD) and the results of those studies are summarized in Table 3. Those crystallized samples with the phases Zn_2SiO_4[6] , $Ca_2ZnSi_2O_7$[7] and $CaSiO_3$[6], have relatively low CTE's, too low for most components proposed for fuel cell designs. The low CTE for crystallized glasses like G#6 (CTE~ $70x10^{-7}$/°C), G#37 (CTE~ $75x10^{-7}$/°C) G#38 (CTE~ $55x10^{-7}$/°C) and G#39 (CTE~ $72x10^{-7}$/°C) are related the dominant crystallized phases; Zn_2SiO_4 and $Ca_2ZnSi_2O_7$, respectively. The addition of nucleating agents like TiO_2 to the glass formulations promoted the formation of higher expansion phases, including, $CaSrAl_2SiO_7$ [7], $Ca_2ZnSi_2O_7$[8] and Sr_2SiO_4[6]. For example, Figure 5 shows the XRD patterns collected from glasses #27 and #42 after a typical "sealing run" for those "invert" glass ceramics, crystallizing at 850ºC for 2 hours in argon. The dominant phases are $CaSrAl_2SiO_7$ and $Ca_2ZnSi_2O_7$. The XRD data collected from glass #32 after two hours at 850°C (Figure 6) shows a typical glassy pattern which is consistent with the glassy CTE curve shown above in Figure 4. G#36 behaves in the same fashion. As shown in Figure 6, G#32 converts to a glass-ceramic when held at 750ºC and the XRD pattern indicates that $Ca_2BaSi_3O_9$ [9] is the primary crystalline phase.

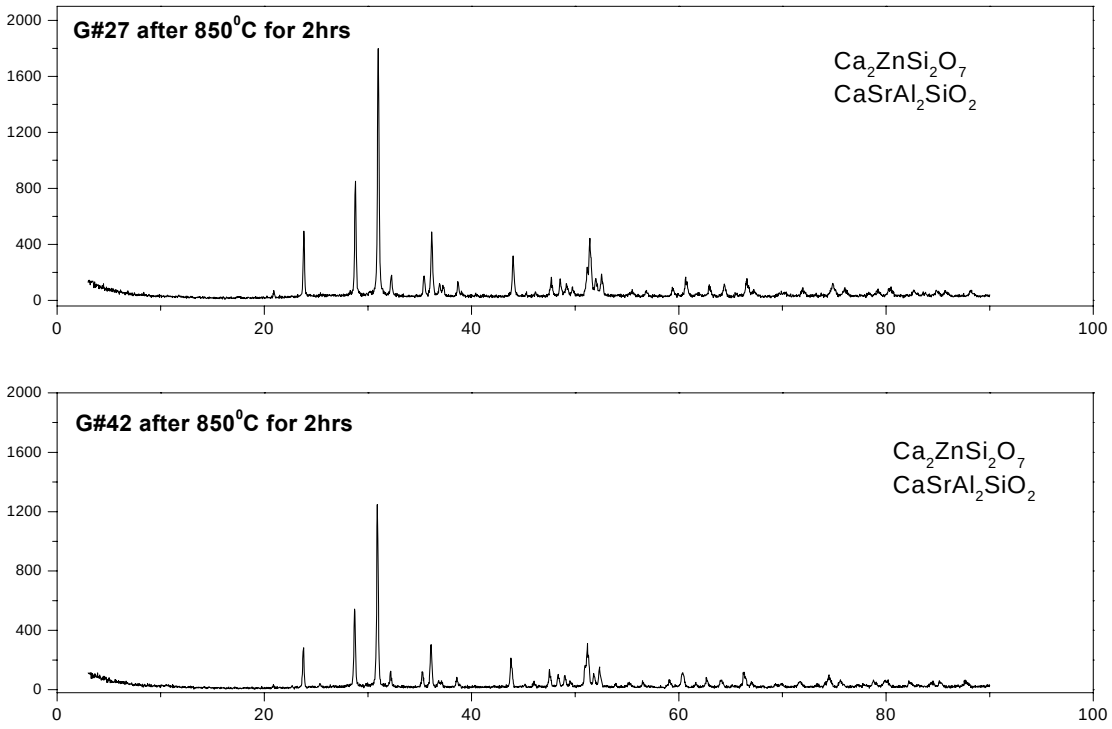

Figure 5: XRD analyses for glasses # 27 and #42 after thermal treatment at 850°C for 2 h in argon.

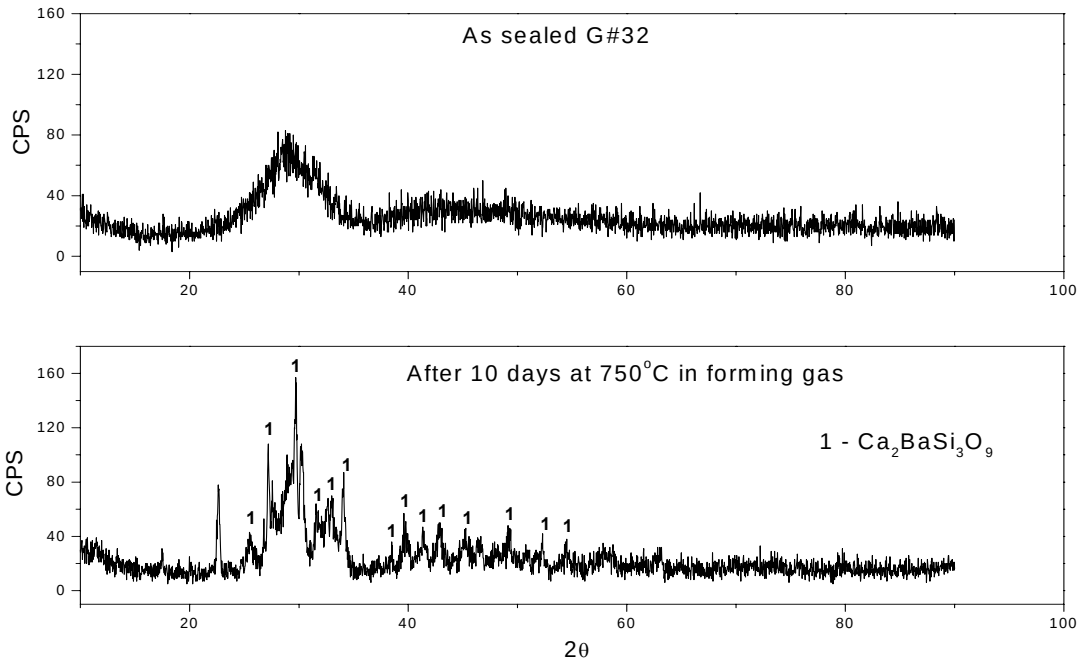

Figure 6: XRD pattern for glasses # 32 under "sealing run" and after held for 10 days at 750°C for 10 days in forming gas.

Figure 7 shows electron micrographs of the microstructures of G#25 and G#27 after two hour, 850ºC heat treatments. X-ray diffraction (Figure 5, Table 3) indicates that the dominant crystalline phases in these materials are $CaSrAl_2SiO_7$ and $Ca_2ZnSi_2O_7$.

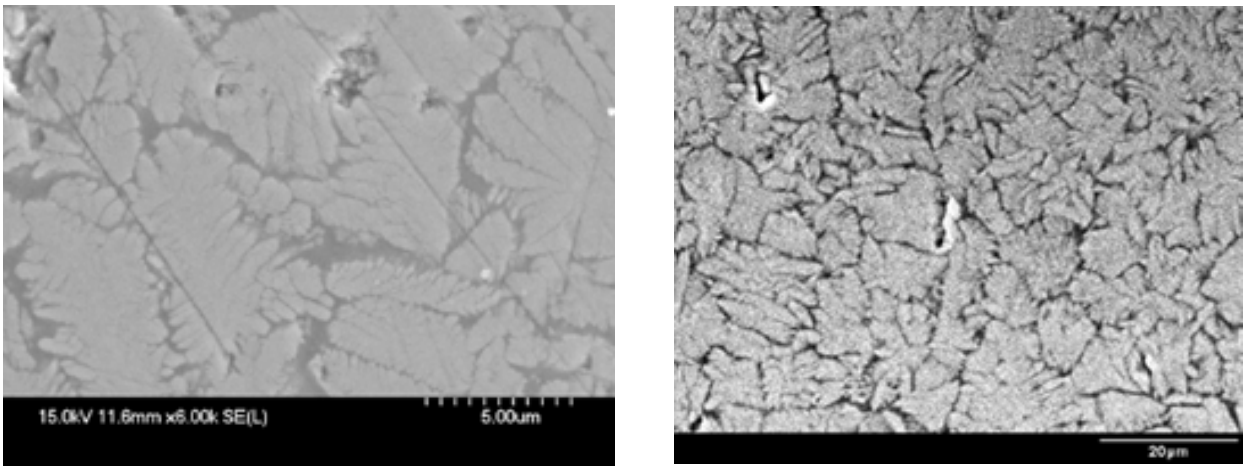

Figure 7: SEM micrograph showing the microstructure of the glass # 25 (left) and glass #27 (right) after an 850ºC, two-hour heat treatment.

3.2. Long-term thermal stability

Figure 8 (a) and (b) show the differences between the thermal expansion characteristics of YSZ and of G#27, and #42, respectively, heat-treated under various conditions. The thermal expansion difference between the glass-ceramics and the YSZ substrate are small between room temperature and about 650°C for the G#27 and 690°C for the G#42, and there is little substantial change in □CTE after the glass-ceramics were held at 750°C for up to 14 (G#42) or 28 days (G#27). The breaks in □CTE at the elevated temperatures are related to the presence of residualglass. The expansion coefficient of the residual glass increases above T_g. shows some small, but systematic changes in the □CTE behaviours for both systems at temperatures above the respective T_g's, indicating some change in the nature of the residual glass with time at 750°C.

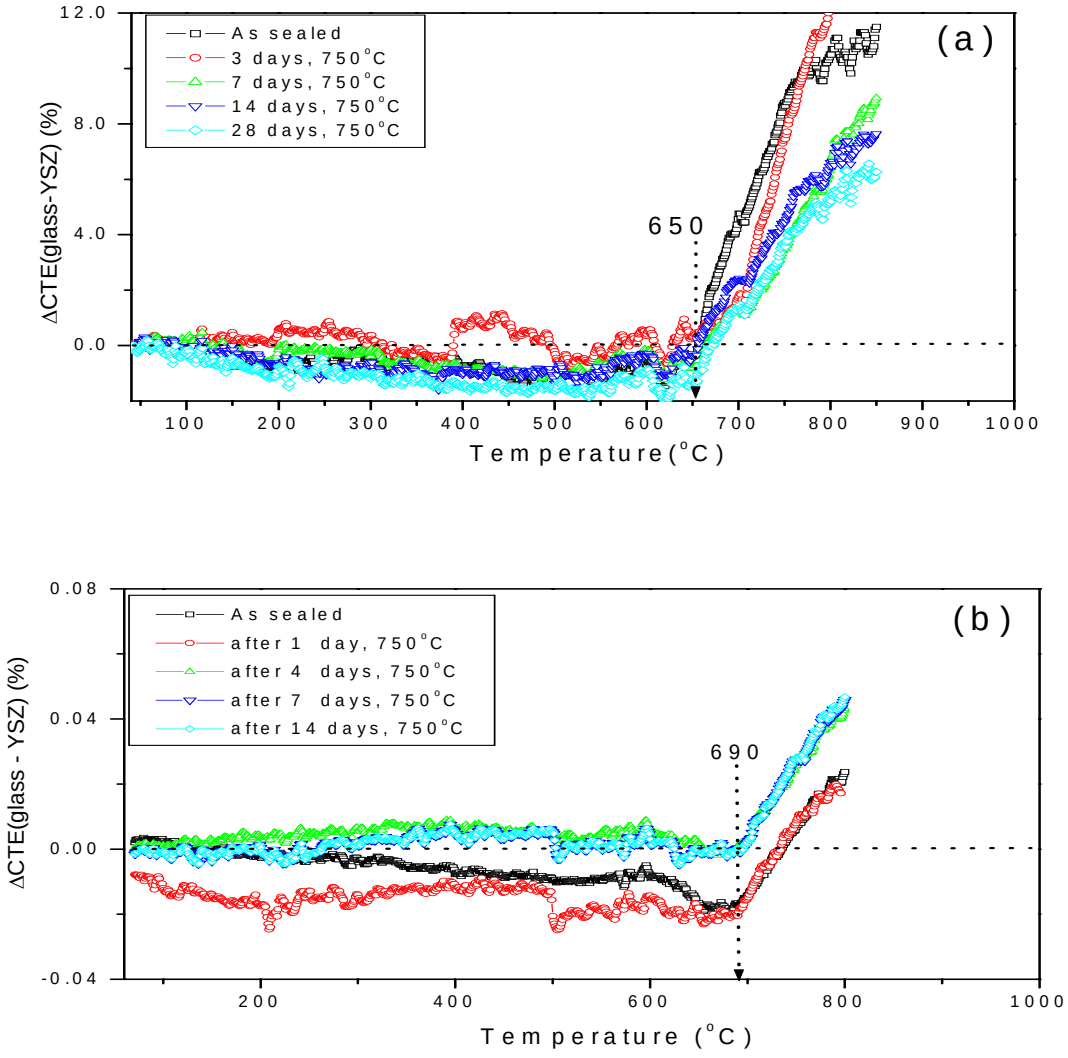

Figure 8: CTE difference curves between YSZ and glasses #27 (top) and #42 (bottom), held at 750°C for up to 28 days. The breaks in the □CTE curves near 650°C and 690°C are likely due to the expansion characteristics of the residual glassy phases at temperatures above each respective T_g.

Figure 9 shows the differences between the thermal expansion characteristics of an E-brite substrate and G#36 heat-treated under various conditions. For the 'as sealed' G#36 glass between room temperature and 600°C, the thermal expansion match with the E-brite substrate is close, with little change in the ΔCTE after the glass-ceramic was held at 750°C for up to 60 days. The large changes in ΔCTE above about 700ºC reflect the relatively large fraction of residual glass in this sealing material. In fact, this sample exhibits a dilatometric softening point near 750ºC even after 60 days at 750ºC.

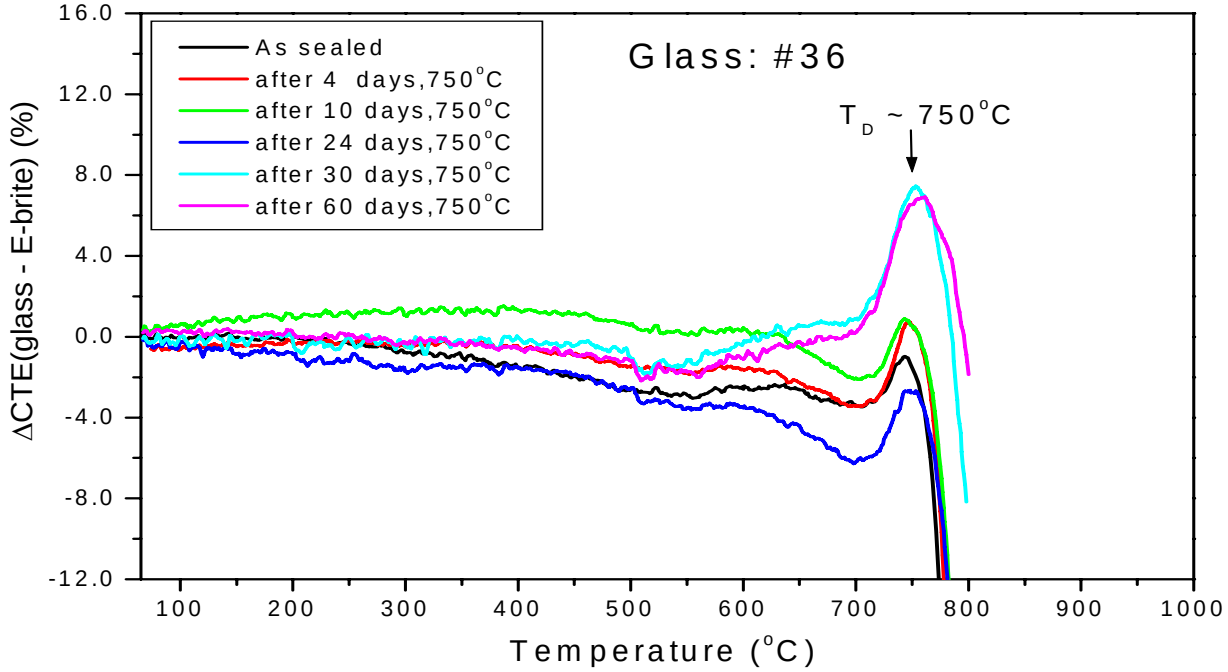

Figure 9: The differences in the CTE curves of an E-brite substrate and glass #36, held at 750°C for up to 60 days. The softening points in the □CTE curves near 750°C are likely due to the residual glassy phase in the partially crystallized G#36.

Error! Reference source not found. shows a scanning electron micrograph of a bond between YSZ and E-brite made with a paste of G#25, initially sealed at 850ºC, then held at 750°C for 14 days in air. The glass layer is about 200 microns thick. Figure 11 shows higher resolution SEM micrographs of the interfaces between glass #27 and uncoated and coated (with $(La,Sr)CrO_3$ films) E-bright. Both samples were initially sealed at 850ºC for 2 hours in argon, then held at 750°C in air for four days. Both bonding interfaces appear to be uniform and there are no obvious heterogeneities at either interface.

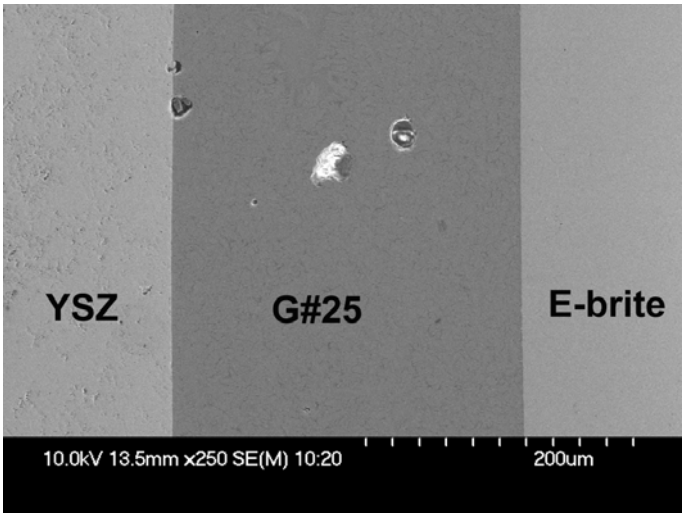

Figure 10 SEM micrograph of an Ebrite/G#25/YSZ assembly processed at 850°C for 4h in argon and then held at 750°C for 14days in air.

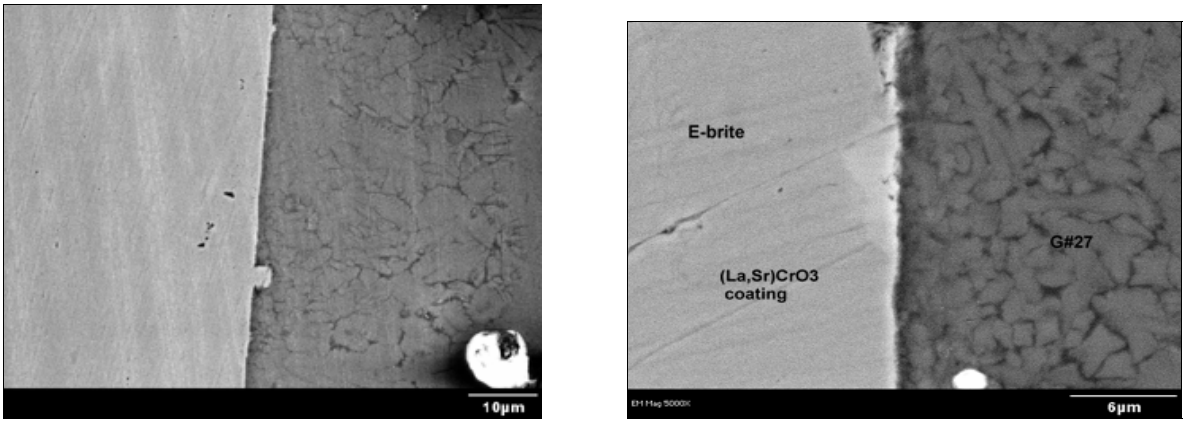

Figure 11: SEM micrographs of (left) an uncoated Ebrite/G#27 and (right) a (La,Sr)CrO_3 coated E-brite/G#27 reaction couple, both processed at 850°C for 2h in argon and then held at 750°C for 4days in air. Note that the image to the right was taken at a higher magnification.

Figure **12** shows a high magnification electron micrograph of an E-brite/G#25 interface after 14 days at 750ºC, along with the elemental profiles across the interface, obtained by energy dispersive x-ray spectroscopy. There is some indication for the presence of a Cr-rich layer at this interface, but this layer is far less apparent that the extensive interfacial reaction zones reported for BaO-containing glasses bonded to Cr-containing interconnect materials [**Error! Bookmark not defined.**]. Fully characterizing the extent and nature of the interfacial reactions that occur between these new sealing glasses and proposed interconnect materials is work that still needs to be done.

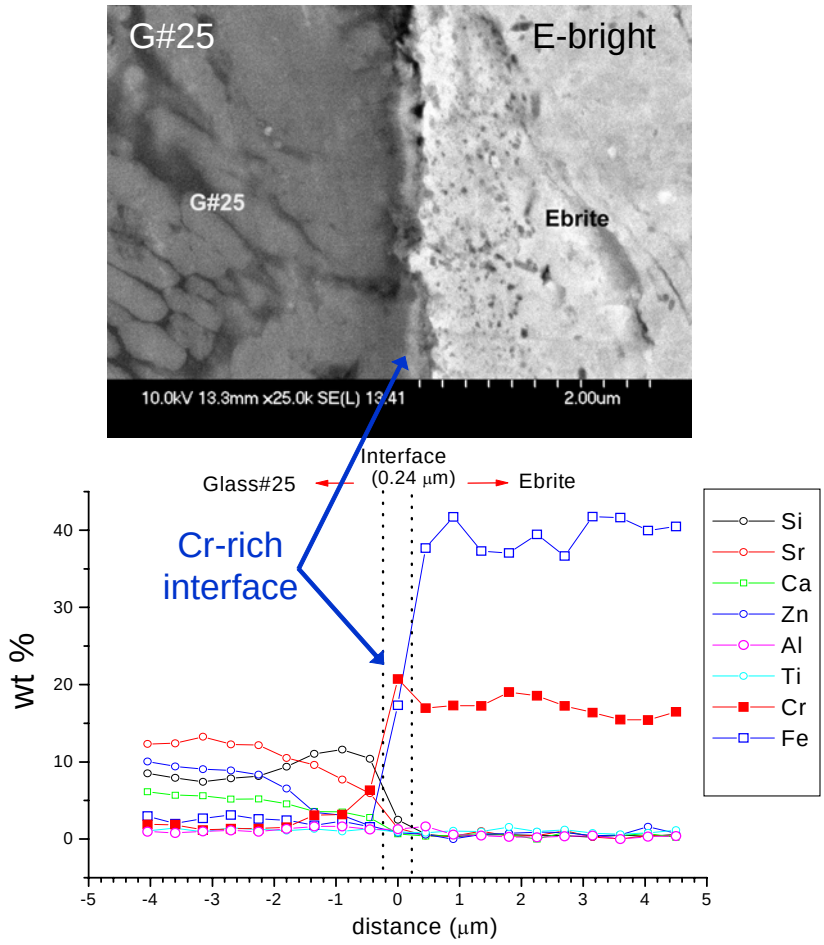

Figure 12: (Top) High resolution SEM micrograph of Ebrite/G#25 interface after 14 days at 750ºC; (below) elemental profiles by EDS across the interface showing the possible formation of a Cr-rich reaction layer, less than 1 micron wide.

3.3. Thermochemical Stability Tests

The weight losses (WL) from "as sealed" glasses #27, #32, #35, #36 and #42 in forming gas (90%Nitrogen, 10% Hydrogen) at 750°C, are shown in Figure 13. Some of these results are summarized in Figure 14, where it is shown that glasses with larger concentrations of B_2O_3 generally exhibit greater volatilization (weight loss) rates in reducing. In addition, it appears that the thermochemical stability of these sealing materials depends on the fraction of residual glass. For example, Figure 15 shows the weight losses at 750ºC in forming gas for two versions of G#27. The samples initially heated to 800ºC were significantly less crystallized than those initially heated to 850ºC, and the less crystallized samples have volatilization rates 2-4 times greater than the more crystallized samples. In addition, the volatilization rates of other samples with similar 'bulk' concentrations of B_2O_3 are greater from samples that have larger residual glassy fractions, as indicated by dilatometric analyses like those shown in Figure 4.

Figure 16 shows the weight loss from samples immersed in distilled water at 90ºC. There is little difference in the aqueous dissolution rates for "as made" and "as sealed" samples of glasses #25 and #27. Changes in solution pH are shown in Figure 17. The low corrosion rates and relatively insignificant changes in solution pH indicate that the chemical stability of these new glasses is excellent.

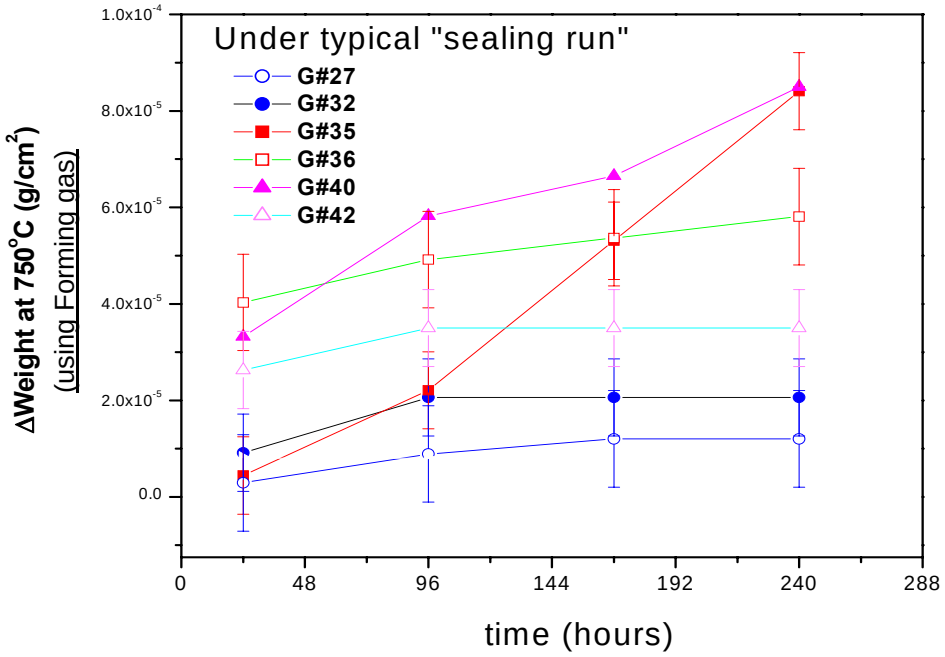

Figure 13: Weight loss rates (W_L) in forming gas at 750°C for glasses #27, #32, #35, #36, and #42, each after initial crystallization at 850°C for 2hr in argon.

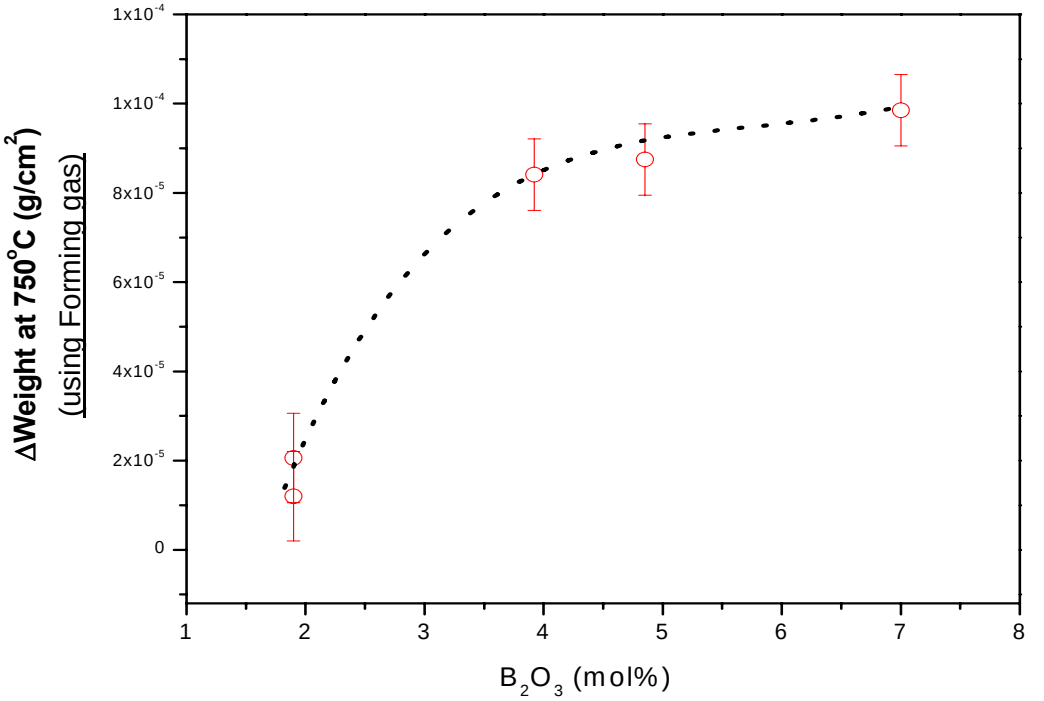

Figure 14: Sample weight loss (W_L) after 10 days at 750°C in forming gas.

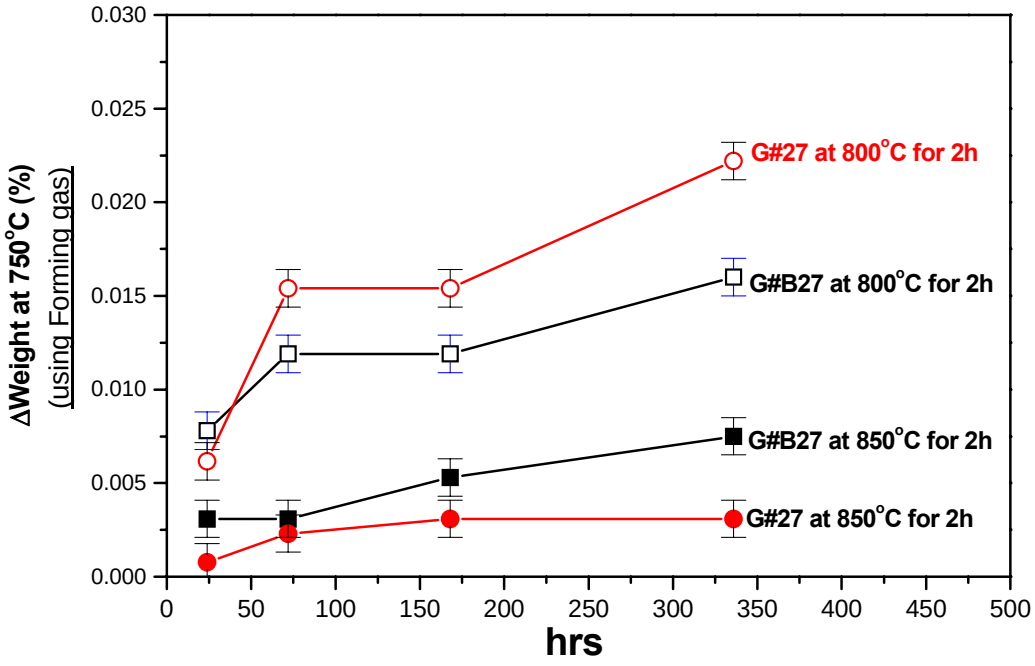

Figure 15: Weight losses in forming gas at 750ºC for two versions of G#27 heated to 800ºC for two hours (top) and to 850ºC for two hours. The samples initially heated to 800ºC are less-crystallized than the samples initially heated to 850ºC.

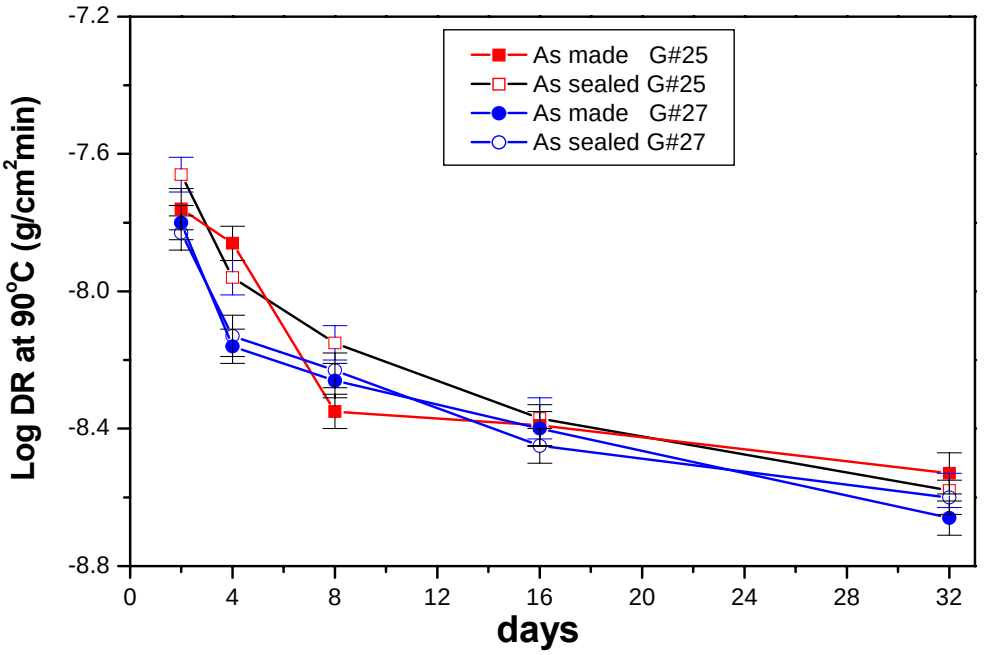

Figure 16: Dissolution rates (DR) in distilled water at 90°C for "as made" and "as sealed" glasses #25, and 27.

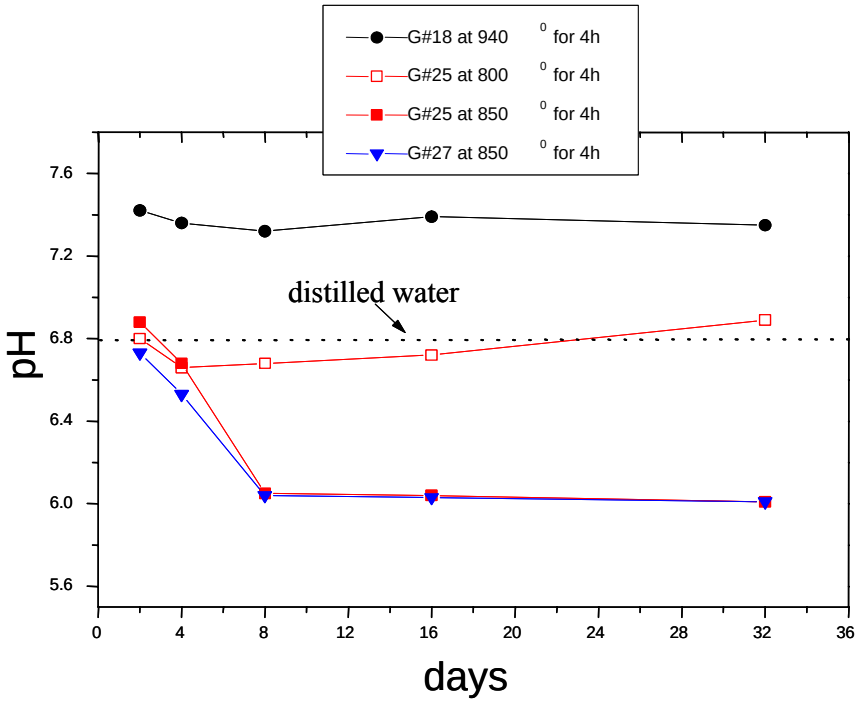

Figure 17: Changes in solution pH for glasses immersed in distilled water at 90ºC.

3.4 Electrical Resistivity

Figure 18 shows impedance spectra collected at 750°C from the reaction couples YZS/G#25 and YSZ/G#27, using the experimental configuration shown in Figure 1 (a). Changing the oxygen partial pressure from 0.2 atm (air) to 10^{-5} atm (nitrogen) and then to 10^{-20} - 10^{-27} atm (forming gas) influences the spectra. The lowest conductivity was obtained for nitrogen and the highest for forming gas. These changes, together with the value of calculated activation energy (from 1.9 to 2.2eV), suggest that the conductivity mechanism is not related to oxygen ion transport.

Figure 19 shows impedance spectra collected at 750°C from the reaction couples E-brite/Glass/E-brite with the glasses #32, #35 and #36, using the configuration shown in Figure 1b. The lowest conductivity was obtained for nitrogen and the highest for forming gas. The impedance spectra consist of one semicircle and a low frequency tail. The low frequency tail is especially pronounced in forming gas, where the semicircle is shifted to higher frequencies. The capacitance retrieved from the semicircle reflects the expected geometrical capacitance of the samples and therefore the low frequency intercept of semicircle with Z' corresponds to the resistance of the major charge carriers. The low frequency tail may be related to either electrode processes (electrode polarization effect) or diffusion of minor charge carriers. Both processes have very similar impedance spectra and therefore additional investigation is necessary to distinguish between those processes. The reaction couples were exposed over the period of 32 day to forming gas. An example of selected impedance spectra from G#32 recorded during this period is presented in Figure 20. These samples were then exposed to nitrogen at 750ºC for four days and in all cases the sample resistance increased. In Figure 21, conductivity values retrieved from the impedance spectra are presented as a function of exposure time at 750ºC to forming gas and nitrogen. It was observed that within the first five days, the conductivity of all glasses increased. After the first five days, the impedance spectra allow the monitoring of glass aging processes. In particular, the conductivity of glass #32 decreased, whereas glass #35 increased. The resistance of glass #36 stayed constant. The temperature dependence of conductivity after 32 days exposure to forming gas and after 4 days exposure to nitrogen is presented in the Figure 22. In all cases, the activation energy for conductivity is less in nitrogen than in forming gas.

Figure 23 compares the AC and DC conductivity for glass #35 and #36. Generally speaking, the difference between AC and DC conductivity is not significant.

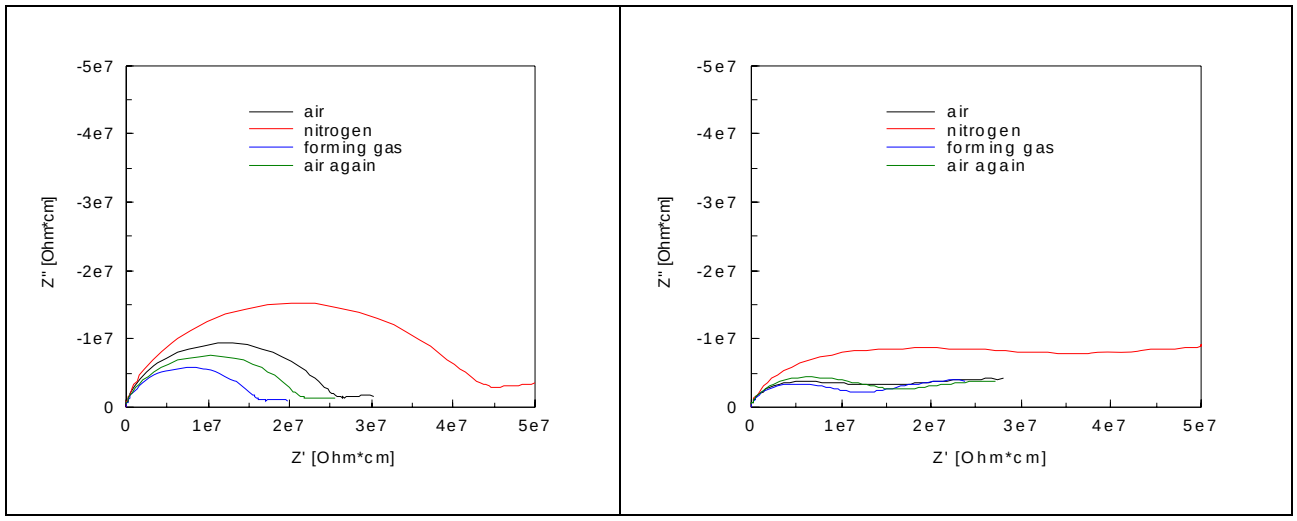

Figure 18: Impedance spectra of (left) glass #25 and (right) glass #27 at 750°C.

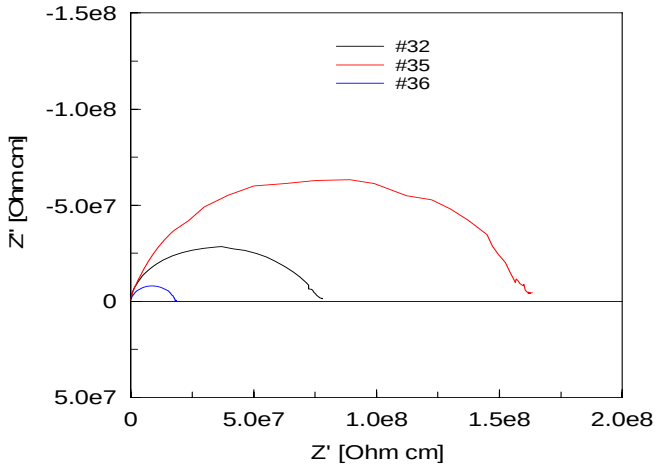

Figure 19: Impedance spectra of glasses #32, #35 and #36 in nitrogen at 750°C.

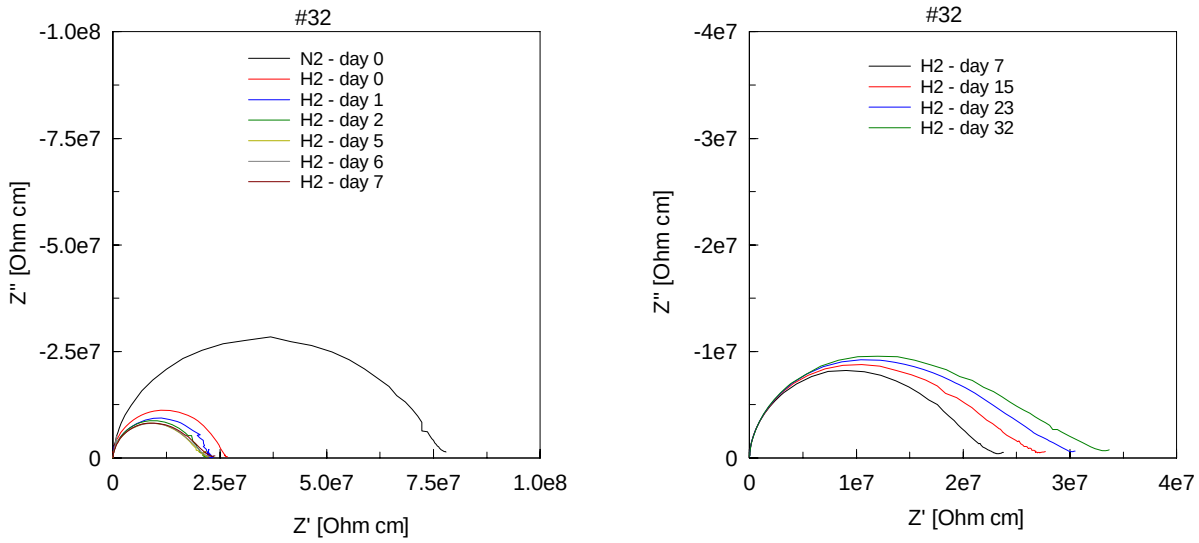

a. b.

Figure 20: Impedance spectra of glass #32 at 750°C after introducing forming gas (a) and in forming gas (b).

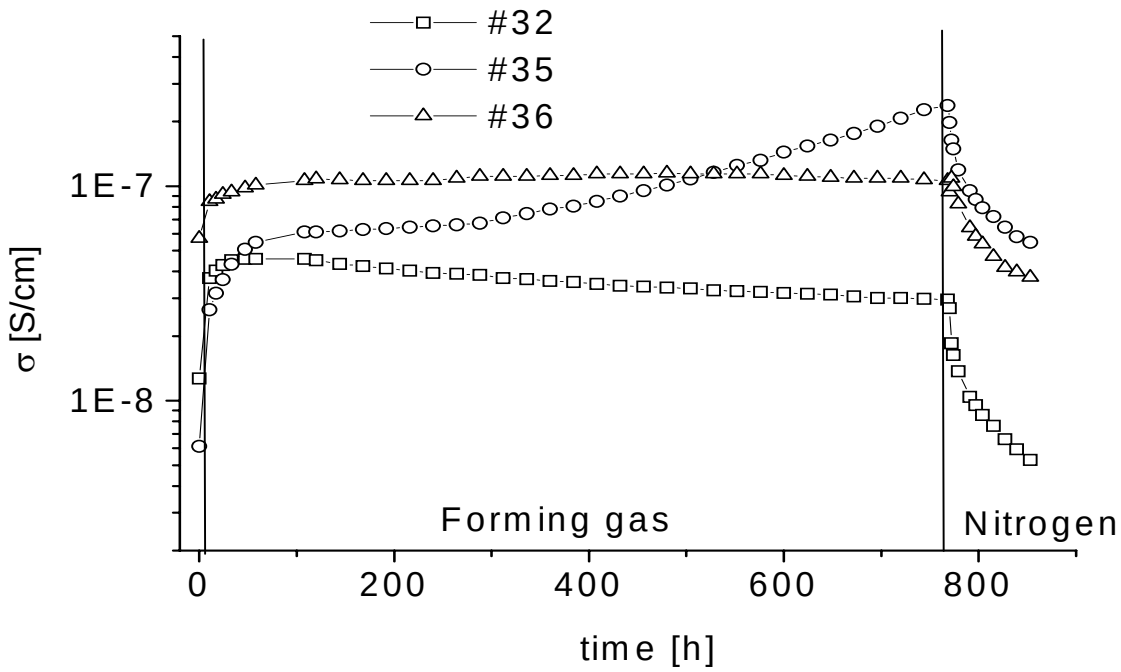

Figure 21: Electrical conductivity of reaction couples E-brite/glass/E-brite in forming gas and nitrogen at 750°C.

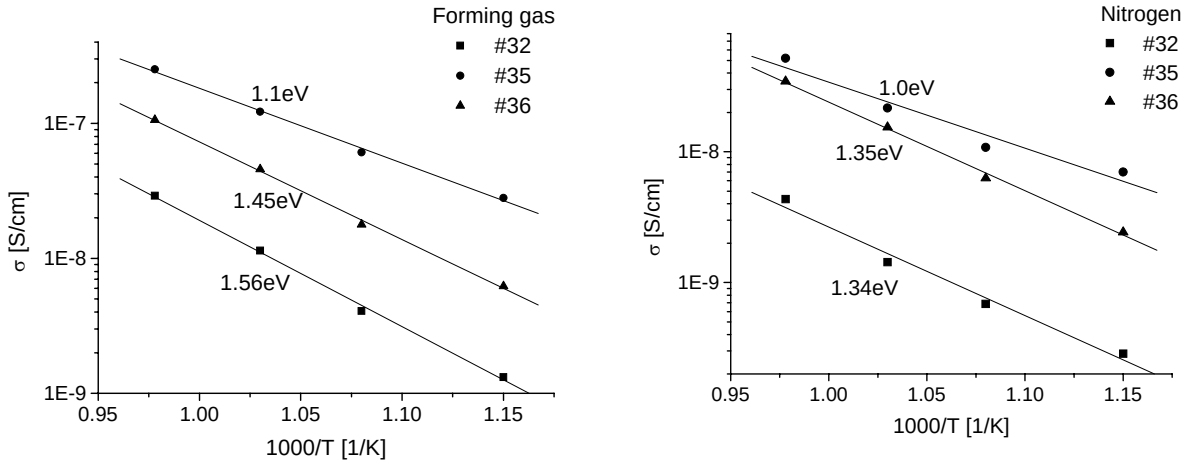

a.

b.

Figure 22: Ahrrenius plots of glass #32, #35 and #36 after 32 days of exposure to forming gas (a) and after 4 days of exposure to nitrogen (b).

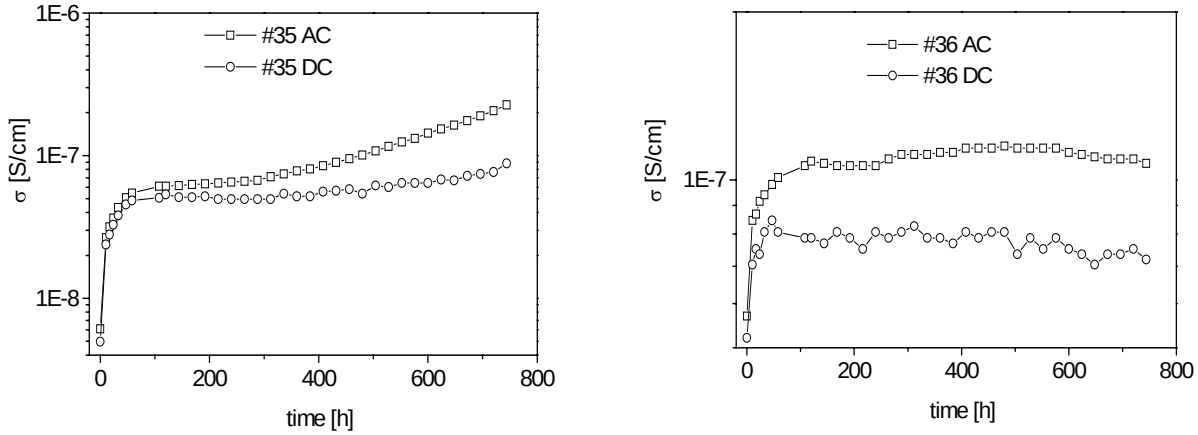

Figure 23 Comparison of conductivity retrieved from DC and AC measurements of glass (a) #35 and (b) #36.

4. CONCLUSIONS

- The "as sealed" glasses #27, #32, #36 and #42 possess desirable coefficients of thermal expansion in the range of ~ 100-116 x10^{-7}/°C, and are thermally stable under SOFC operational conditions. Each of these materials has excellent phase stability in reducing environments.
- Calcium-strontium alumino-pyrosilicate and calcium-zinc pyrosilicate phases are desirable crystalline phases which appear to stabilize the formation of higher CTE glass-ceramics in compositions like G#27 and G#42.
- Analytical SEM analyses of E-brite/Glass#27 and E-brite Glass#32 reaction couples held at 750°C in air for four days indicate that the reaction interfaces remain free of the extensive heterogeneities (reaction products) that are reported to form at other glass/metal interfaces.
- Glass systems #25, #27, #32, #35, and #36 are electrically insulating in oxidizing and reducing environments, and the relatively high conductivity in the 'as sealed' Glass #36 could be related to the high residual content of this sample after sealing.

6. REFERENCE

1. Trapp, H.J.L and J.M. Stevels, (1960), *Phys Chem Glasses* **1** 107
2. K.D. Meinhardt, et al., "Glass-ceramic material and method of making," US patent 6,430,966, Aug. 13, 2002; K.D. Meinhardt, et al., "Glass-ceramic joint and method of joining," US Patent 6,532,769, March 18, 2003.
3. P. Geasee et al., "Investigation of glasses from the system BaO-CaO-Al_2O_3-SiO_2 used as sealants for the SOFC," *Proc. Int. Congr. Glass*, Edinburgh, Scotland, Vol. 2 905 (2001).
4. Zhenguo Yang, Jeff W. Stevenson, Kerry D. Meinhardt, " Chemical interactions of barium-calcium-aluminosilicate- based sealing glass with oxidation resistant alloys" Solid State Ionics, Vol **160** pg. 213 (2003).
5. Keqin Huang, Peggy Y. Hou, John B. Goodenough, "Reduced area specific resistance for iron-based metallic interconnects by surface oxide coatings" Materials Research Bulletin, Vol. 36 pg.81 (2001).
6. Wolfram Höland and George Beall, "Glass Ceramic Technology" Published by American Ceramic Society, 735 Ceramic Place, Westerville, OH 43081.
7. Luisa Barbeeri et al., "The microstructure and mechanical properties of sintered celsian and strontium-celsian glass-ceramic" Materials Research Bulletin, Vol. 30 pg. 27 (1995).
8. I. V. Rozhdestvenskaya, I. I. Bannova, V. S. Barbanyagre, V. M. Shanmshurov, T. I. Timoshenko, Crystallography Reports, **40** (1995), 629.
9. T. Taniguchi, M. Okuno and T. Matsumoto, " X-ray diffraction and EXAFS studies of silicate glasses containing Mg, Ca and Ba atoms" Journal of Non-Crystalline Solids, Vol. 211 pg.56 (1997).

3.4.5) Fabrication of interconnects, manifolds and glass seals for the multi-cell SOFC stack

This task was never completed

3.4.6) Delivery of trilayer stack, a 2 layer planar stack and a multilayer SOFC stack for testing.

This task was never completed because flat oxide membranes were not produced.

4.0: Outcomes:

4.1) List of Publications Resulting from Program

I. Beologolovsky, X-D. Zhou, H. Kurokawa, P.Y. Hou, S.J. Visco and H.U. Anderson, "Effects of surface deposited nanocrystalline chromite thin films on the performance of a ferritic interconnect", submitted to J. Electrochem. Soc. (2007).

X.D. Zhou, L.R. Pederson, Q. Cai, J. Yang, B.J. Scarfino, M. Kim, W.B. Yelon, W.J. James, H.U. Anderson and C. Wang, "Structural and magnetic properties of $LaMn_{1-x}Fe_xO_3$ ($0<x<1.0$)", J. of Appl. Physics **99** 08M918 (2006).

X.D. Zhou, E. Thomsen, Q. Cai, J. Yang, B. Scarfino, W. James, W. Yelon, H.U. Anderson and L.R. Pederson, "Electrical, thermoelectric, and structural properties of $La(Fe,M)O_3$ (M = Mn, Ni and Cu)", J. of Electrochem. Soc. **153**, J133-J138 (2006).

X.D. Zhou, Q. Cai, J. Yang, B. Scarfino, W. James, W. Yelon, H.U. Anderson, Y. Shin and L.R. Pederson, "Electrical and structural properties of $La(Fe,M)O_3$ (M = Mn, Ni and Cu)", The Electrochem. Soc. Trans., **Vol. 1**, 211 (2006).

V.P. Kharem, A.R. Greenberg, S.S. Kelley, H. Pilath, I.J. Roh and J. Tyber, "Synthesis and Characterization of Dense and Porous Cellulose Films", J. of Appl. Polymer Science, (in press).

X.D. Zhou and H.U. Anderson, "Defect chemistry in ternary compounds", in "Materials for Energy Conversion Devices", C.C. Sorrell, J. Nowotny and S. Sugihara, Ed., Woodhead Publishing Ltd., p. 235-257 (2005).

J. Cheng, A. Navrotsky, X.D. Zhou and H.U. Anderson, "Enthalpies of formation of $LaMO_3$ perovskites (M = Cr, Fe, Co and Ni)", J. Mater. Res. **20**, 191-200 (2005).

J. Cheng, A. Navrotsky, X.D. Zhou and H.U. Anderson, "Thermochemistry of $La_{1-x}Sr_xFeO_{3-\delta}$ solid solutions ($0.0\leq x\leq 1.0$, $0.0\leq \delta\leq 0.5$)", Chemistry of Materials **17**, 2197-2207 (2005).

X.D. Zhou, J.B. Yang, Q. Cai, M. Kim, W.B. Yelon, W.J. James and H.U. Anderson, "Coupled electrical and magnetic properties in $(La,Sr)FeO_{3-\delta}$ by *in situ* studies", J. of Appl. Physics **97**, 10C314-316 (2005).

P. Jasinski, V. Petrovsky, T. Suzuki and H.U. Anderson, "Nanocomposite Nickel-Ceria Cermet with Low Nickel Content for Anode-Supported SOFCs", Electrochem. Solid-State Lett., 8 (4) A219-A221 (2005).

P. Jasinski, V. Petrovsky, T. Suzuki, T. Petrovsky and H.U. Anderson, "Electrical properties of yttria stabilized zirconia films prepared by net shape technology", J. Electrochem. Soc. **152** (2) A454-A458 (2005).

T. Suzuki, P. Jasinski, V. Petrovsky and H.U. Anderson, "The optical properties and band gap energy of nanocrystalline $La_{0.4}Sr_{0.6}TiO_3$ thin films", J. Am. Ceram. Soc. 88 (5) 1186-1189 (2005).

V. Petrovsky, T. Suzuki, P. Jasinski and H.U. Anderson, "Low Temperature Processed Anode for Solid Oxide Fuel Cells", Electrochemical Solid-State Lett., 8 (7) A341-A343 (2005).

X.D. Zhou, J.B. Yang, Q. Cai, M. Kim, W.B. Yelon, W.J. James and H.U. Anderson, "Role of Oxygen Deficiency on Electrical and Magnetic Properties of (La, Sr)$FeO_{3-\delta}$ by *in Situ* Studies", J. Appl. Phys. **97**, (2005) 10C314.

V. Petrovsky, T. Suzuki, P. Jasinski, T. Petrovsky and H.U. Anderson, "Low temperature processing of thin film electrolyte for electrochemical devices", Electrochem. Solid-State Lett., **7** (6) A138-A139 (2004).

T. Suzuki, P. Jasinski, F. Dogan and H.U. Anderson, "Role of composite cathodes in single chamber SOFC", J. Electrochem. Soc. **151** (10) A1678-A1682 (2004).

T. Suzuki, P. Jasinski, V. Petrovsky, F. Dogan and H.U. Anderson, "Anode supported single chamber solid oxide fuel cells in methane – air mixture", J. Electrochem Soc. **151** (9) A1473-A1476 (2004).

T. Suzuki, P. Jasinski, V. Petrovsky, F. Dogan and H.U. Anderson, "The microstructure effect on the electrical and optical properties of undoped and Sr-doped $SmCoO_3$ thin films", Solid State Ionics **175** p. 437-439 (2004).

X.D. Zhou, Q. Cai, Z. Chu, J. Yang, W.B. Yelon, W.J. James and H.U. Anderson, "Utilization of neutron diffraction and Mössbauer spectroscopy in the studies of the cathode for SOFCs", Solid State Ionics **175**, 83-86 (2004).

X.D. Zhou, B.J. Scarfino and H.U. Anderson, "Electrical conductivity and stability of CGO-YSZ solid solutions", Solid State Ionics **175**, 19-22 (2004).

R. Smith, X.D. Zhou, W. Huebner and H.U. Anderson, "Novel yttrium-stabilized zirconia polymeric precursor for the fabrication of thin films", J. Mater. Res., **19**, 2708-2713 (2004).

B.P. Gorman, V. Petrovsky, H.U. Anderson and T. Petrovsky, "Optical characterization of ceramic thin films: applications in low-temperature solid oxide fuel-cell materials research", Journal of Materials Research, **19**(2) 573-578 (2004).

T. Suzuki, P. Jasinski, V. Petrovsky, X.D. Zhou and H.U. Anderson, "Optical and electrical properties of $Pr_{0.8}Sr_{0.2}MnO_3$ thin films", J. Appl. Phys. **93** (10) 6223-6228 (2003).

J.B. Yang, X.D. Zhou, Q. Cai, W.B. Yelon, W.J. James and H.U. Anderson, "Charge ordering and disproportionation of $La_{1/3}Sr_{2/3}FeO_3$", J. Phys. Cond. Matt. **15**, 5093-5102 (2003).

X-D. Zhou, W. Huebner and H.U. Anderson, "Processing of nanometer-scale CeO_2 particles" Chem. Mater., **15**, 378 (2003).

Reviewed Proceedings/Book Chapters:

H. Kurokawa, P.Y. Hou, X. Chen, C.P. Jacobson, L.C. De Jonghe and S.J. Visco, "The effect of protective coatings for alloy interconnect on oxidation and Cr vaporization", in Proceedings of MS&T'06, Materials and Systems: Vol. I, pp. 245-253, 2006, Cincinnati, eds: P. Singh, D. Collins, G. Yang, P. Kumta, C. Legzdins, S.K. Sundaram and A. Manthiram, paper presented at Sym: Materials, Processing, Manufacturing and Power Management Technologies, Materials Science & Technology 2006, Cincinnati, OH, Oct. 15-19, 2006.

P.Y. Hou, H. Kurokawa, C.P. Jacobson, S.J. Visco and L.C. De Jonghe, "Interconnect performance in SOFC environments", Sym. Materials in Clean Power System: Applications, Corrosion, and Protection, 135th Annual TMS Meeting (TMS2006), San Antonio, TX, March 12-16, 2006.

X.D. Zhou and H.U. Anderson, "Some aspects of defect chemistry in p-type perovskite conductors", The Electrochem. Soc. Proceedings Series, **Vol. PV2005-07**, Solid Oxide Fuel Cells IX, Ed. S.C. Singhal and J. Mizusaki, 1479-1486 (2005).

V.P. Khare, A.R. Greenberg, S. Kelley and H. Pilath, "Synthesis of dense and porous films obtained from the cellulose polymer", International Congress on Membranes and Membrane Processes, August 2005, Seoul, South Korea.

X.D. Zhou and H.U. Anderson, "Defect chemistry of p-type perovskite conductor used in solid oxide fuel cells", Preprints of Symposia – American Chemical Society, Division of Fuel Chemistry, **49**, 749-750 (2004).

H.U. Anderson, X.D. Zhou and F. Dogan, "Defect chemistry of mixed ionic/electronic p type oxides", NATO Science Series, II: Mathematics, Physics and Chemistry, **173** (Mixed Ionic Electronic Conducting Perovskites for Advanced Energy Systems), 303-312 (2004).

X.D. Zhou, I. Belogolovsky, B.J. Scarfino, S.T. Reis, R.W. Brow, P. Hou and H.U. Anderson, "Oxidation protective coating onto ferritic interconnect by nanocrystalline thin films", Proc. Electrochem. Soc., **Vol. 2004-16**, pp. 159-169, ed. E. Opila, J. Fergus, T. Maruyama, J. Mizusaki, T. Narita, D. Shifler and E. Wuchina, The Electrochem. Soc., Inc., Pennington, NJ 2004.

V. Petrovsky, H.U. Anderson and T. Petrovsky, "Application of composite technology for SOFCs", Materials Research Society Symposium Proceedings, **822** (Nanostructured Materials in Alternative Energy Devices), 147-152 (2004).

V.P. Khare, A.R. Greenberg, H. Pilath and S.S. Kelley, "Synthesis and testing of dense and porous films obtained from the cellulose polymer", North American Membrane Society Annual Meeting, June 2004, Honolulu, Hawaii.

T. Suzuki, P. Jasinski and H.U. Anderson, "Electrical conductivity of nanocrystalline Sm-doped CeO_2 thin film", Ceramic Engineering and Science Proceedings, 24, 3 p. 323 (2003).

V. Petrovsky, H.U. Anderson, T. Petrovsky and E. Bohannan, "Structural behavior of zirconia thin films with different level of yttrium content", Materials Research Society Symposium Proceedings, **756** (Solid State Ionics—2002) 503-508 (2003).

H.U. Anderson, X.D. Zhou and F. Dogan, "Intermediate solid oxide fuel cells, challenges and opportunities for the materials scientists", Proc. of Electrochem. Soc. (Solid State Ionic Device III) **2002-26**, 16-17 (2003).

V. Petrovsky, H.U. Anderson and T. Petrovsky, "Low temperature technologies for SOFC", Proc. of Electrochem Soc., 2003-7 (Solid Oxide Fuel Cells VIII) 76-984 (2003).

I.J. Roh, H. Pilath, S. Kelley and A. Greenberg, "Formation of dense and microporous films from cellulose derivatives with a low degree of substitution", North American Membrane Society Meeting, May 2003, Jackson Hole, WY.

4.2) Copies of Selected Publications from Program

OXIDATION PROTECTIVE COATING ONTO FERRITIC INTERCONNECT BY NANOCRYSTALLINE PEROVSKITE THIN FILMS

Xiao-Dong Zhou[1], Inna Belogolovsky[2], Brett J. Scarfino[1], Signo T. Reis[1], Richard K. Brow[1], Peggy Hou[2], and Harlan U. Anderson[1]

1. Department of Materials Science and Engineering, University of Missouri-Rolla, Rolla, MO 65401
2. Lawrence Berkeley National Laboratory, One Cyclotron Rd., MS 62-203, Berkeley, CA 94720

ABSTRACT

Nanocrystalline chromite thin films were deposited on polished stainless steel (E-brite) substrates by spin coating suitable polymeric solutions onto the surface followed by annealing to develop the oxide film. These films had higher electrical conductivity as well as provide improved oxidation resistance compared to the normal Cr_2O_3 films, which occurred from oxidation of the alloy. This resulted in lower areal specific resistance (ASR) values for the chromite coated surfaces than those with the Cr_2O_3 scale.

INTRODUCTION

The interconnect in the solid oxide fuel cell (SOFC) systems provides the electrical connection between cells and gas separation within the cell stack.[1] The interconnect must be compatible with the other cell components and be stable in both oxidizing and reducing environments. In the high temperature regime (900-1000°C), perovskite type chromites ($LaCrO_3$ based) have been shown to be useful as interconnect materials.[2] The cost associated with the fabrication of these ceramic interconnect hinders the SOFC commercialization. Thus, in an effort to lower the overall cost of SOFCs, research is being done with the objective of lowering the operating temperature of the SOFCs to an intermediate temperature (IT) regime (500 – 700°C) so that metallic alloy can be used as the interconnect. The use of commercially available alloys not only offers the possibility of lower temperature interconnect materials, but also may improve the fabrication process. Thus, ferritic alloys are being considered as IT SOFC interconnect candidates. These alloys are protected from rapid oxidation by the formation of slow growing oxidation products of the alloy, such as Cr_2O_3. Unfortunately, these oxidation products tend to increase the interfacial resistance which increases the electrical losses in the cell. Thus a number of efforts have been made to develop films on the interconnect alloy which improve the oxidation resistance as well as increase the electrical conductivity.

Methods for preparing surface coatings to improve the oxidation resistance and electronic conductivity of ferritic alloys include pre-oxidation to form an oxide scale[3, 4], plasma spraying,[5] spray processing to form a perovskite coating,[6] spray deposition of a

Xiao-Dong Zhou, Inna Belogolovsky, Brett J. Scarfino, Signo T. Reis, Richard K. Brow, Peggy Hou and Harlan U. Anderson, Oxidation Protective Coating onto Ferritic Interconnect by Nanocrystalline Perovskite Thin Films, Proc. Electrochem. Soc. Vol. 2004-16, pp. 159-169, ed. E. Opila, J. Fergus, T. Maruyama, J. Mizusaki, T. Narita, D. Shifler and e. Wuchina, The Electrochem. Soc. Inc., Pennington, NJ, 2004.

perovskite coating onto the alloys [7] and wet-chemical methods [8]. Huang et al.[4] have extensively studied the effect of surface coatings of Y_2O_3 and NiO. They found that NiO in the Y/Ni double coating was necessary to improve the electrical conductivity of the resulting dense and strong oxide scale. The application of protective coatings prepared from plasma spraying processing was reported by Nie et al.[5] with $(La,Sr)MnO_3$ and Ni coatings sprayed onto Cr-based interconnects. The thickness of the dense LSM coating was about 20-25 μm. The electrical conductivity of the LSM coatings was nearly the same as that of bulk LSM ceramics. Zhu et al.[8] reported two methods for the fabrication of $LaCrO_3$-based coating on ferritic stainless steel, reactive formation and sol–gel process. Kirkendall voids were formed in the coating during the reactive formation process. *In situ* X-ray diffraction (XRD) studies showed that the chromites could be formed at 800°C. All these coating processes led to improved scale adhesion and electrical conductivity, while many of these publications reported reduced oxide growth rate and Cr volatility. Research, however, is still needed to study the formation and properties of chromite films. Moreover, the interaction between protective coatings and sealing glass has not been addressed. It is the intent of this article to report our work on chromite film fabrication, transport properties of thin films, and the role of the films as oxidation and reaction protective layers.

EXPERIMENTAL

Coating Process

Two types of substrates were employed in this study, single crystal Al_2O_3 [sapphire, (001) orientation] and a commercial ferritic stainless steel (E-brite) which has the nominal chemical composition (wt%) of 26.3Cr-0.15Ni-0.1Mn-0.21Si-1.01Mo-0.12Cd, with Fe being the balance. The alloy was cut into pieces of $10\times10\times1mm^3$, which were polished to a 10μm finish. Prior to coating, the samples were cleaned ultrasonically in distilled water and acetone.

The polymeric solution which was used as the thin film precursor, was prepared by dissolving the metal nitrates into distilled water with the appropriate concentration ratio of the cations.[9] Chelants, such as ethylene glycol and/or citric acid, were then mixed with the nitrate aqueous solutions, which were heated at 80°C for 72 hours. Thin films were deposited onto the substrates through a conventional spin-coating processing. The as-deposited thin films were then heated at 70°C for 30 min, followed by a treatment at 400°C in air for 5 min to form the oxides. Details on further annealing processing will be discussed later. The crystalline nature of the thin films was verified by XRD using a high-resolution four-circle diffractometer (Philips X'Pert MRD) with Cu Kα radiation. The typical scan parameters were: 2θ in the range of 5° – 90°, grazing of 1°, and step size of 0.03°. Micrographs of the deposited films were obtained with a Hitachi model S4700 cold field emission scanning electron microscope (SEM) coupled with energy dispersive spectroscopy (EDS).

Characterization of the coatings

Impedance spectroscopy (Solartron 1260 frequency analyzer with 1296 Interface, Solartron Group Co.) was employed to study the electrical conductivity of the oxide films. The substrate for conductivity measurements was single crystal Al_2O_3 and the electrodes were Ag paste. The electrical conductivity was measured in the plane of the films in the temperature range of 500-800°C and oxygen activity range of 10^{-6} atm to 0.2 atm. The measurements of the areal specific resistance of the coated E-brite were carried out over the temperature range of 600-800°C using a four-point DC arrangement with Pt electrodes. A comparison experiment was conducted on the alloy without coating using the same conditions. Oxidation studies were conducted in air on samples which were heated at 5°C/min to 750°C, held at 750°C for 50 hours, then cooled down at 5°C/min to room temperature. The experiments for cyclic oxidation studies (10 cycles) were performed at 750°C with each cycle of 24 hours.

RESULTS AND DISCUSSION

Thin Film Fabrication

The deposition of thin films by spin coating has been carried out for a variety of systems, such as ZrO_2, CeO_2, ferrites and manganites. It is somewhat surprising that few publications are on chromite thin films. The difficulties may be associated with the formation of chromates [10] ($LaCrO_4$, space group $P2_1/n$, a=0.7041nm, b=0.7237nm and c=0.6693nm) at low temperature. As was shown by Carter et al. [10], chromates can be transformed to the perovskite chromites ($LaCrO_3$, space group Pnma; note that space group of A site doping $LaCrO_3$ often is R3c) by heating in air at the elevated temperature (>1000°C). The phase transformation from chromate to chromite at the elevated temperature can result in two problems with respect to oxidation protective coatings, (1) at this condition, a Cr_2O_3 scale can be formed and (2) residual strain in the thin films can be induced during the transformation reaction which is not desirable for ferritic alloys. Thus, it is important to lower the temperature for perovskite phase formation. Initial research emphasized obtaining the perovskite structure at a low temperature. Fig. 1 illustrates grazing XRD of the films on the E-brite substrate. Sample I was annealed at 600°C in air for 1 hour after spin-coating, which possesses a structure similar to $LaCrO_4$ as shown in Fig. 1.

Since the transformation reaction between chromates and chromites evolves oxygen,

$$LaCrO_4 \rightarrow LaCrO_3 + 1/2\,O_2 \qquad [1]$$

it is very natural to place the films in reducing environment which in principle will favor chromite formation. This was done on sample 1 and as expected, the XRD of the resulting film, (sample II shown in Fig. 1) which was annealed at relatively low temperature (~600°C) in $10\%H_2/90\%N_2$ for four hours, does indicate the formation of the perovskite phase (chromites). Trace chromate phase, however, is still present. In addition to the phase formation, surface morphology is of importance to the thin films which function as protective layers. Fig. 2 shows SEM images of specimen II (Fig 1) which were reduced from the chromate to chromite at 600°C. The porosity shown in Fig. 2 may have resulted from the transformation reaction. Grain growth was not observed

after this annealing and reducing process. The pinholes shown in Fig. 2 may be resulted from either air bubbles during spin coating or roughness of the substrates.

Electrical Conductivity

$LaCrO_3$ based ceramics are of considerable interest largely due to their good electrical conductivity over a wide range of temperature and oxygen activities. Acceptor doped $LaCrO_3$ ceramics exhibit thermally activated electrical conductivity behavior which is due to the exponential temperature dependence of the mobility. The number of carriers is essentially constant with temperature (here electron holes) and is determined by the dopant level.[11, 12] Chromites, therefore, are considered as typical small polaron conductors, in which a strong electron-phonon interaction is exhibited. The electrical conductivity (σ, S/cm) can be represented in Eq. (2) as:

$$\sigma=\sigma_0 \frac{\mu}{T}\exp(-\frac{E_a}{kT}) \qquad [2]$$

Where σ_0 is the preexponential factor of conductivity (K C/cm^3), μ is the mobility (cm^2/(V s), T is the temperature (K), E_a is the activation energy (J), and k is the Boltzmann constant (J/K). The activation energy can be obtained by plotting $\ln(\sigma T)$ vs. 1/T. Shown in Fig. 3 are the plots of $\ln(\sigma T)$ versus inverse temperature for thin film $La_{0.80}Sr_{0.20}CrO_3$.[12] Conductivity of mixed chromates and chromites is ~ 2 orders of magnitude lower than bulk conductivities for $La_{0.84}Sr_{0.16}CrO_3$. In addition, the activation energy (~1 eV) is higher in the mixed phases than that of bulk chromites as shown in Fig. 3 (0.1 eV). Further experiments are being conduct to gain understanding of transport properties of chromite thin films.

Oxidation Protection

Surface Morphology and Electrical Properties. The sample used for oxidation testing was E-brite coated with chromite films which had been reduced for 4 hours at 600°C in H_2/N_2. Initially, the sample was oxidized in air at 750°C for two 24 hour cycles. The heating and cooling rate was controlled to be 5°C/min. Between each cycle, the specimen was taken out and its surface examined with XRD and SEM/EDS without any conductive coating. Fig. 2 shows the SEM observation of the sample surface before oxidation exposure. The cracks do not appear to penetrate through the coating. Large area EDS analysis showed rather uniform composition through out the film. On the micron scale, however, two slightly different morphologies were observed. The compositions (point 2 and point 3) were found to contain slightly different composition than that of point 1. The white particles on the film surface (point 1) are probably air dust or excess coating resulting from surface roughness during spin-coating process, which was not observed when a single crystal Al_2O_3 substrate was used. Microprobe study is under way to study the possible local composition variation.

After oxidation, in general, the coating remained adherent and appeared continuous. Compared to the average composition on the unoxidized sample, there seemed to be more Cr, which is an indication that Cr_2O_3 scale grew beneath the coating. Even places where most of the coating had spalled from the surface, the Cr_2O_3 layer underneath still contained some La and Sr, indicating possible reaction of the deposited coating with the thermally grown Cr_2O_3 scale. This kind of reaction is extremely

desirable for it will improve Cr_2O_3 conductivity and the adherence between the coating and the scale

As discussed in the previous section, conductivity of mixing chromites and chromates is lower than that of chromites. Areal specific resistance of the mixed phases, however, is still low because the coating is very thin (~100nm). Shown in Fig. 4 are the plots of ASR for E-brite and coated E-brite. The coated sample used for ASR measurements has been reduced for 4 hours at 600°C in H_2/N_2. Gold was used as the electrode. Samples were heated in a furnace to 500°C in 30min, and then were held for 10min. The V-I measurements were conducted with 20mA/step. The temperature was increased with an interval of 50°C to a maximum temperature. At 800°C, ASR of E-brite is ~0.03Ω cm^2, a very low value already, however ASR of the coated E-brite is ~ 0.004 Ω cm^2, which is nearly an order lower than that of E-brite. The coating developed in this study may be used as oxidation protective layer.

Effect of Thermal Cycling. The question remains as if the coating can remain adherent during thermal cycling. In this study, thermal cycling has been performed on the coated E-brite It was found that the coating remained protective after two oxidation cycle of 24 hours in air at 750°C. The EDS results show that some growth of the Cr_2O_3 scale under the coating takes place. Morphology of the surface chromite appeared similar, with only slight grain growth. Successive 24 hr oxidation runs for 10 cycles at 750°C. Fig. 5 shows a cross section SEM image of the coating after 10-thermal cycles at 750°C, which indicates an adhesive scale/alloy and the scale/coating interfaces. These results show strong adhesion and thermal stability of the coating.

CONCLUSIONS

Thin chromite films can be deposited onto ferritic stainless steel by spin coating process with control over grain size, film thickness and composition. Perovskite type chromite films can be formed at relatively low temperature (600°C). Coatings can minimize surface oxidation of stainless steel and thus decrease ASR ~ 10 times lower than that of uncoated alloy.

ACKNOWLEDGEMENTS

This work was supported by U.S. Department of Energy under the contract of: DE – FC36 – 01G011084.

REFERENCES:

[1] H. U. Anderson and F. Tietz, "Interconnects," in "High Temperature Solid Oxide Fuel Cells: Fundamentals, Design an Applications," Eds. S. C. Singhal and K. Kendall, Elsevier (2003).

[2] P. Singh and N. Q. Minh, "Solid Oxide Fuel Cells: Technology Status," *Int. J. Appl. Ceram. Technol.* **1**, 5 (2004).

[3] L. Mikkelsen, P. H. Larsen, and S. Linderoth, "High temperature oxidation of Fe22Cr-alloy," *J. Therm. Anal. Calorimetry*, **64**, 879 (2001)

[4] K. Huang, P. Y. Hou and J. B. Goodenough, "Reduced area specific resistance for iron-based metallic interconnects by surface oxide coatings," *Mater. Res. Bull.* **36**, 81 (2001).

[5] H. W. Nie, T.-L. Wen and H. Y. Tu, "Protection cotaings of planar solid oxide fuel cell interconnect prepared by plasma spraying," *Mater. Res. Bull.* **38**, 1531 (2003).

[6] S. Linderoth, "Controlled reactions between chromia and coating on alloy surface," *Surf. Coat. Technol.* **80**, 185 (1996).

[7] R. Ruckdäschel, R. Henne, G. Schiller, H. Greiner, in: Proc. 5th Int. Symp. Solid Oxide Fuel Cells (SOFC-V, eds.: U. Stimming, S. C. Singhal, H. Tagawa, W. Lehnert, **97-18**, 1273 (1997).

[8] J. H. Zhu, Y. Zhang, A. Basu, Z. G. Lu, M. Paranthaman, D. F. Lee, and E. A. Payzant, "$LaCrO_3$ based coatings on ferritic stainless steel for solid oxide fuel cell interconnect application," *Surf. Coating Technol*, **177-178**, 65 (2004).

[9] H. U. Anderson, C.-C. Chen and M. N. Nasrallah, U.S. Pat., No. 5,494,700, **1996**.

[10] J. D. Carter, H. U. Anderson and M. G. Shumsky, "Structure and phase transformation of lanthanum chromate," *J. Mater. Sci.* **31**, 551 (1996).

[11] D. P. Karim and A. T. Aldred, *Phys. Rev. B*, **20**, 2255 (1979)

[12] R. Raffaelle, H. U. Anderson, D. M. Sparlin and P. E. Parris, "Evidence for a crossover from multiple trapping to percolation in the high temperature electrical conductivity of Mn-doped $LaCrO_3$," *Phys. Rev. Lett.*, **65**, 1383 (1990).

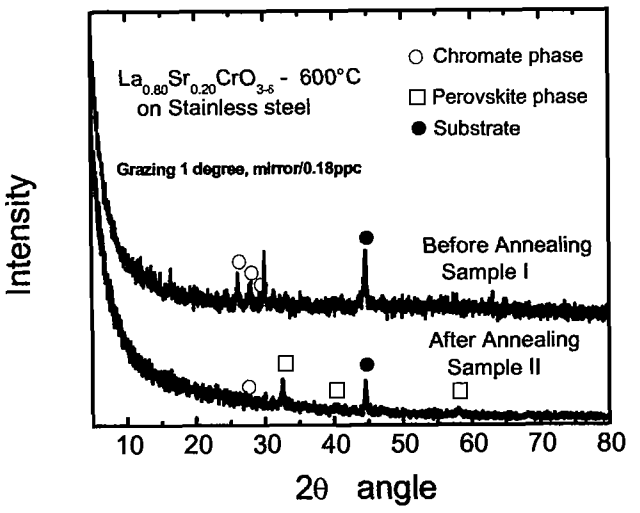

Fig. 1. XRD of thin films on stainless steel before and after reducing at 600°C with $10\%H_2/90\%N_2$ for 4 hours.

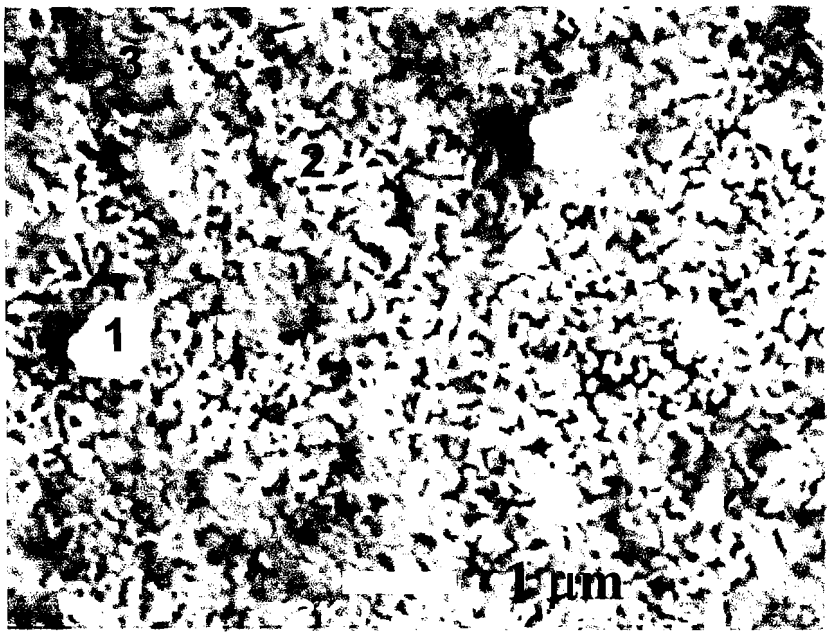

Fig. 2. Surface morphology of (La,Sr)CrO_3 films after reducing process

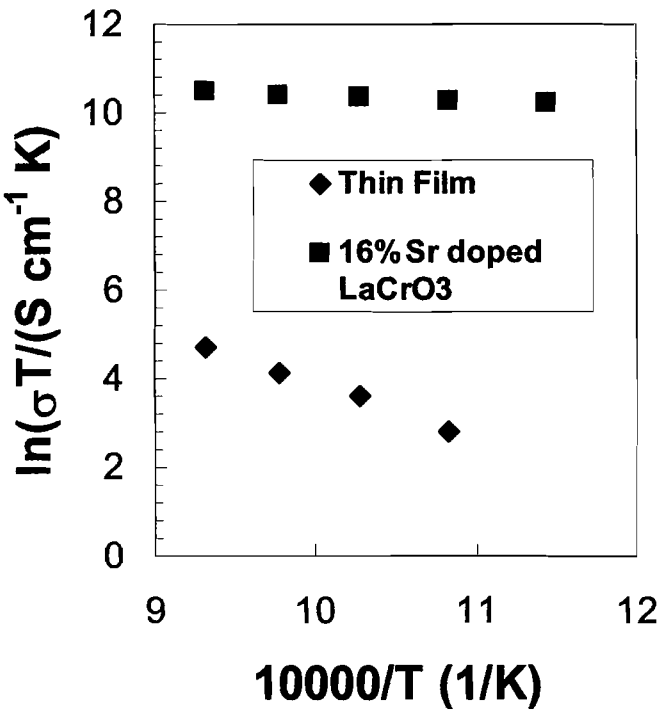

Fig. 3. A plot of ln(σT) and σ vs. 1/T for thin film of $La_{0.80}Sr_{0.20}CrO_3$ on single crystal Al_2O_3 substrate

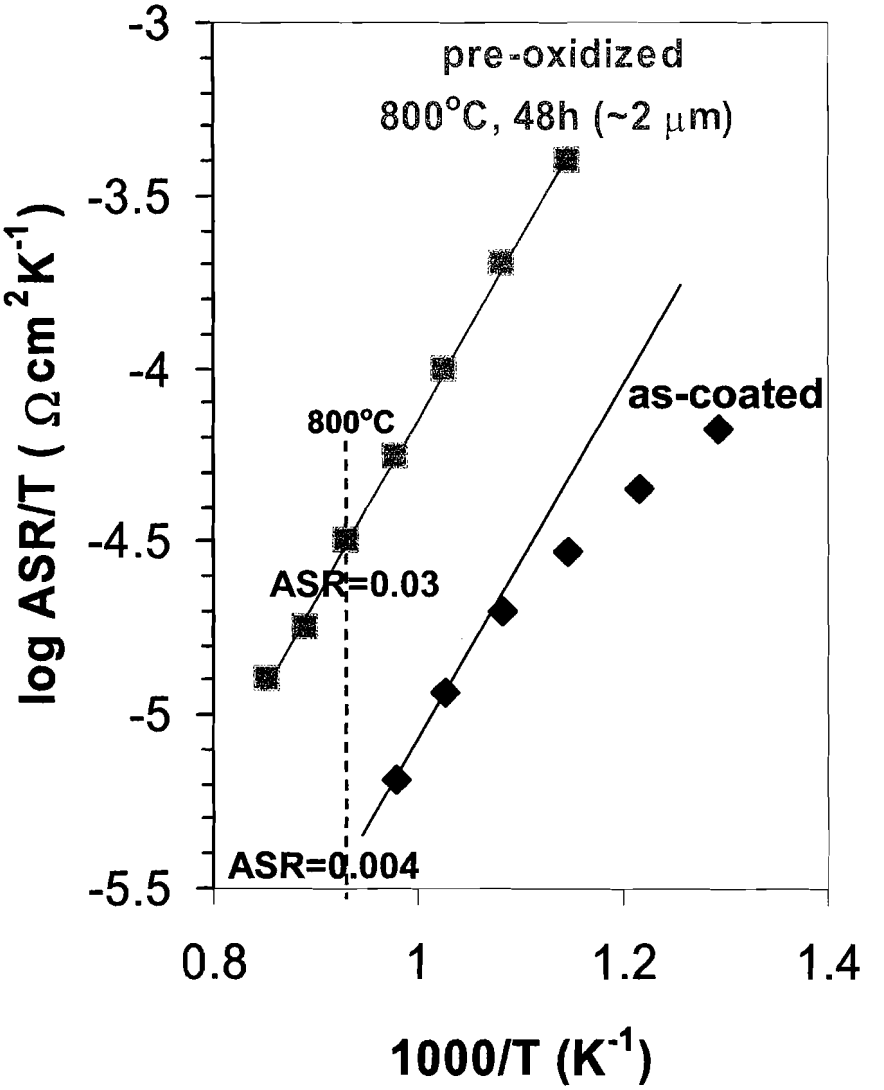

Fig. 4. A plot of ln(ASR/T) vs. 1/T for E-brite and of $La_{0.80}Sr_{0.20}CrO_3$ coated E-brite

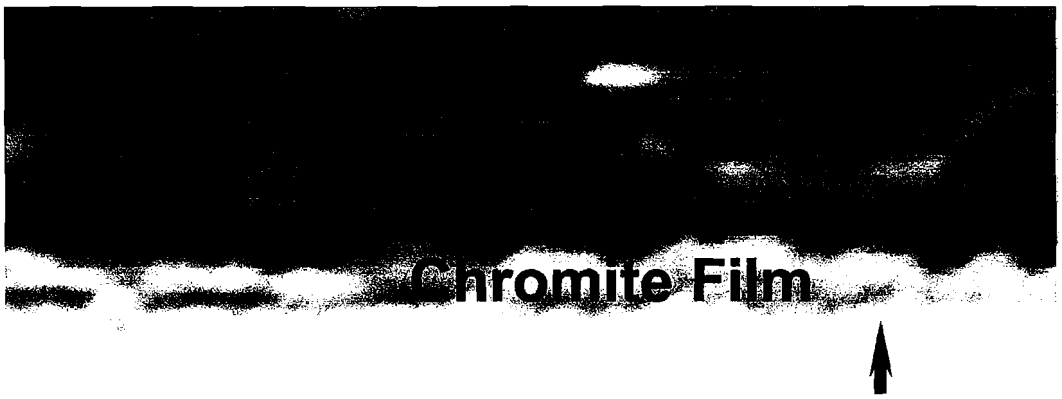

E-brite

After 10x24 RT-750°C cycling

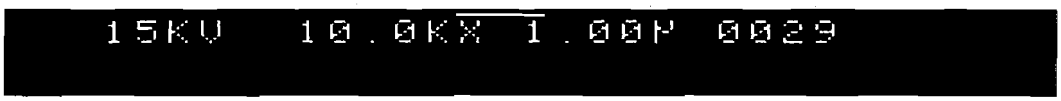

Fig. 5 Cross section image of $La_{0.80}Sr_{0.20}CrO_3$ coated E-brite after 10 times thermal cycling

Effect of Protective Coatings for Alloy Interconnect on Oxidation and Cr Vaporization

Hideto Kurokawa, Peggy Y. Hou, Xuan Chen, Craig P. Jacobson,
Lutgard C. DeJonghe and Steven J. Visco

Materials Sciences Division
Lawrence Berkeley National Laboratory
1 Cyclotron Road, 62R203, Berkeley, CA 94720

Abstract

Utilizing stainless steel as interconnect for solid oxide fuel cells (SOFCs), a promising high-efficiency energy conversion device, makes it possible to fabricate robust and low-cost cell stacks. However, there are important issues that must be addressed for practical applications. Oxidation rates of Fe-Cr alloys should be decreased to mitigate increasing of resistance due to scale growth. Cr vaporization from oxide scale formed on alloys should be suppressed. Otherwise, subsequent precipitation of chromium oxides on the electrodes and/or electrolyte can lead to rapid deterioration of cell performance. Ceramic coating for Fe-Cr alloys is a promising solution for these issues. The effect of $(Mn,Co)_3O_4$ and $(La,Sr)CrO_3$ coatings on oxidation rate was evaluated at 1023 and 1123 K and the effect of $(La,Sr)CrO_3$, $(Mn,Co)_3O_4$ and $(La,Sr)MnO_3$ coatings on chromium vaporization was evaluated at 873~1173 K. The results show ceramic coating has significant benefit for alloy interconnect at intermediate operating temperatures of SOFCs.

Introduction

The development of solid oxide fuel cells (SOFCs) have been received much attention because of its high electric efficiency, high power density, and high performance exhaust, which can be used for not only power generation and also co-generation. For practical application, cost reduction of materials is crucial factor to develop commercially viable SOFCs. The use of Fe-Cr stainless steels in SOFCs can reduce the cost of raw materials, and improve the mechanical strength of supported thin film fuel cell membranes. Fe-Cr alloys can be used as interconnect or support substrate of SOFCs operating at low-intermediate temperatures up to about 1000 K where chromia forming alloys show good oxidation resistance. Oxidation kinetics of several Fe-Cr alloys in the anode and cathode environments of SOFC has been studied by several authors[1-9]. Protective oxide layer consisting of Cr_2O_3, $(M,Cr)_3O_4$ (M=Fe, Mn) spinels[7-9] forms on the surface of Fe-Cr alloys at the operating temperatures.

In case of interconnects, oxidation rate is a important factor because the area specific resistance (ASR) has to be lower than acceptable limits to avoid increasing electrical resistance of the layers that can adversely affect contact resistances. And break away of scale should be prevented when alloys are exposed at high temperature for long time or severe thermal cycling conditions. To meet these requirements the

Part of the data (oxidation rates) were published in the following paper:
H. Kurokawa, P. Y. Hou, X. Chen, C. P. Jacobson, L. C. De Jonghe and S. J. Visco, The Effect of Protective Coatings for Alloy Interconnect on Oxidation and Cr Vaporization, in *Proceedings of MS&T'06, Materials and Systems: Volume I*, pp 245-253, 2006, Cincinnati, USA, eds: P. Singh, D. Collins, G. Yang, P. Kumta, C. Legzdins, S. K. Sundaram and A. Manthiram, paper presented at Sym: Materials, Processing, Manufacturing and Power Management Technologies, Materials Science & Technology 2006, Cincinnati, OH, Oct. 15-19, 2006.

oxidation rate of alloys should be decreased to reduce scale thickness. Metal and ceramic coating on Fe-Cr alloys has been studied to improve oxidation resistance. Zhu et al.[10] studied $LaCrO_3$-based coatings on 444 stainless steels by sol-gel method improved the oxidation resistance and scale adhesion of the alloy substrate at 1073 K, and coated samples showed much lower electrical resistance compared to the uncoated samples. Huang et al.[12] studied oxidation kinetics of Ebrite and 446 with coatings and reported that a significant and consistent reduction in oxidation rate at 973~1073 K by coating Y_2O_3 on the surface of alloys. The coating also reduced ASR values resulting from a smaller scale thickness and stronger metal/scale interface.

Volatile chromium gas species released from Cr_2O_3, particularly in the cathode environment of operating SOFCs, is another issue that should be addressed. The resulting deposition can reduce active electrode surface and deteriorate cell performance. $CrO_2(OH)_2(g)$ is known to the most abundant species in humid air, while CrO_3 (g) is the dominant species in dry flowing oxygen[6,13]. Jiang et al.[14] reported that preferential chromium deposition has been observed on YSZ electrolyte surface in alloy interconnect/LSM/YSZ cell and chromium deposition primarily occurred on $La_{0.6}Sr_{0.4}Co_{0.2}Fe_{0.8}O_3$ (LSCF) electrode surface in alloy interconnect/LSCF/SDC cell. Matsuzaki and Yasuda[15] reported that the typical chromium poisoning occurred near the Sr-doped $LaMnO_3$ (LSM) electrode and yttria-stabilized zirconia (YSZ) electrolyte interface to form dense Cr_2O_3 layer by reduction of $CrO_2(OH)_2(g)$, while uniform chromium distribution was observed in LSCF electrolyte on $Ce_{0.8}Sm_{0.2}O_{1.9}$ (SDC) electrode. Chromium deposition leads to rapid deterioration of the cathode's oxygen reduction reaction rate, and thus to a significant decline in cell performance[14-16]. Gindorf et al.[17] studied chromium vaporization rates of different interconnect alloys, revealing that ceramic coating such as $(La,Sr)MnO_3$ and $(La,Sr)CrO_3$, deposited on metallic substrates by vacuum plasma spraying (VPS), reduced chromium vaporization drastically by 93~99% at 1123~1223 K. Ceramic coating is effective in reducing Cr vaporization.

Reducing operating temperature is a recent trend of SOFC development due to severe requirement for materials at high temperature and finding of new materials working at lower temperatures. To clear the effect of ceramic coatings on oxidation and Cr vaporization at intermediate operating temperatures of SOFCs is needed. The present work reports the effect of ceramic coating for Fe-Cr alloys on oxidation rate and chromium vaporization at intermediate operating temperatures.

Experimental

Commercial 430 and Ebrite stainless steels (Allegheny Ludlum) with compositions shown in Table 1 were used. Specimens of these steels, 15x14x0.6 or 20x20x1.0 mm were cut from as-received sheet, ground with SiC abrasive paper and polished to 0.5~1 μm with diamond slurry. After polishing, the specimens were cleaned ultrasonically in distilled water and then acetone. Commercial LSM (Praxair $La_{0.65}Sr_{0.3}MnO_3$) and $MnCo_2O_4$ (MCO) synthesized by a glycine nitrate combustion synthesis (GNP)[18] and a co-precipitation with ammonium hydrogen carbonate (AHC), were prepared for 430 and $La_{0.8}Sr_{0.2}CrO_3$ (LSCrO) sol-gel coating was applied to Ebrite. Mn and Co nitrate hydrates were mixed with glycine in the appropriate ratio to make a

solution for GNP synthesis. After combustion, the MCO spinel powder was calcined at 1373 K in air, for 7.2 ks, to remove residual carbon. Another Mn and Co nitrate solution was prepared for co-precipitation with AHC. The mixed nitrate solution containing 0.05 M ($mol.dm^{-3}$) Mn ions and 0.10 M Co ions was dripped into 1.50 M AHC solution kept at 343 K with mild stirring, and the mixed solution was kept at the same temperature for 3.6 ks. The resulting solution was filtered, washed with distilled water, and dried slowly with a heating lamp. The resulting powder was calcined at 1073 K for 7.2 ks in air to remove residual carbon. Resulting LSM and MCO were mixed with isopropanol (IPA) and binders and milled in an attritor mill for 3.6 ks and coated on 430 by aerosol spraying. In the case of LSCrO coating for Ebrite, the coating was first applied by spin-coating a polymeric solution that was prepared by dissolving La, Sr and Cr nitrates in water using ethylene glycol and/or citric acid as chelates. The as-deposited thin films were heated at 343 K for 1.8 ks, and then at 673 K in air for 0.3 ks to convert the nitrates into oxides. Additional heat treatment for 14.4 ks at 873 K in H_2/N_2 converts the chromate rich oxide to mainly chromites.

Oxidation test was carried out to evaluate the effect of coatings. The MCO coating layer on 430 was mechanically compressed to 70 MPa prior to oxidation because as-sprayed layer was porous. Coated and uncoated samples were oxidized isothermally for 180~423 ks in a Cahn thermal gravimetric balance in air at 1023 or 1123 K. The parabolic rate constants of the samples were calculated from the gravimetric curves. The surfaces of the uncoated alloys were examined by X-ray diffraction (XRD) after oxidation at room temperature.

The coated 430 and Ebrite and uncoated alloys for Cr vaporization test were pre-oxidized at 1073 K in air for 172.8 ks to establish a common starting surface condition. After pre-oxidation, Cr transport rate was measured to evaluate Cr vaporization at 873~1173 K for 86.4~259.2 ks in humid air (P_{H2O} = 0.4~1.0x10^4 Pa) with a flow rate of 3.33x10^{-6} m^3s^{-1} (200 ml STP. min^{-1}). This flow rate was sufficient to have the sample's chromium loss independent of the gas flow rate in all circumstances. Details of this evaporation and collection apparatus have been described elsewhere[19]. The cross sections of the samples were examined with a scanning electron microscope (SEM), and elemental analysis was carried out by energy dispersive spectroscopy (EDS).

Table 1: Composition of Steels in wt%

	Fe	Cr	Ni	Mn	Si	Al	Ti	Mo	Cd	V	Co	N	Cu	S	P	C
430	Bal	16.3	0.20	0.45	0.40	-	-	-	-	-	-	-	-	-	-	0.04
Ebrite	Bal	26.3	0.15	0.1	0.21	0.05	0.05	1.01	0.12	0.07	0.05	0.011	0.05	0.013	0.01	0.0022

Results and Discussion

The samples for oxidation test were suspended in the thermal gravimetric balance in air and weight gains were recorded over time after the temperature of 1023 and 1123 K were reached. XRD showed that the oxides formed on 430 after oxidation at 1123 K were mainly Cr_2O_3 and $(Mn,Cr)_3O_4$, and oxides formed on Ebrite after oxidation at 1023 and 1123 K was mainly Cr_2O_3. The Mn concentration of 430 was 0.45 wt% while that of Ebrite was 0.1 wt%. The content of Mn influenced the formation of $(Mn,Cr)_3O_4$ spinel Wild[20] examined Fe-18Cr-8Ni alloy and reported that Mn ions diffuse two orders of magnitude faster than Cr ions in oxide layer. Formation of $(Mn,Cr)_3O_4$ spinel was due to the fast diffusion of Mn ions in oxide scales from alloy to the surface of scale. A rate constant, k_g, characterizing the rate of weight gain, $d\Delta W/dt$, as a result of oxidation can be defined by $(\Delta W)^2 = k_g t$. The oxidation kinetics of the uncoated and coated samples was nearly parabolic. The parabolic rate constants, k_g, of the coated and uncoated samples are plotted in Fig. 1. The oxidation rates of coated Ebrite with LSCrO at 1023 K were about an order of magnitude lower than that of uncoated Ebrite and even extrapolation line of Ebrite coated with thin layer of nitrate converted Y_2O_3[12], where the usual beneficial reactive element effect is expected. The rate constant of the coated sample, however, approached that of the uncoated Ebrite at 1123 K, indicating a loss of protection at higher temperature. Cross-sectional observation revealed that the thicknesses of as-coated MCO on 430 and LSCrO on Ebrite were about 10 μm and 0.15 μm respectively. Thin LSCrO coating layer decreased oxidation rate at lower temperature but cannot suppress oxidation rate at high temperature, 1123K, because the thin coating must have been disrupted from the fast initial oxide growth at the elevated temperature. The parabolic rate constant of MCO coated 430 was about 2 orders of magnitude lower than that of uncoated 430 at 1123 K. Thick coating layer decreased the rate constant drastically. A certain measure of thickness is probably needed at high temperature to suppress oxidation rate.

Comparison of the parabolic rate constant between coated and uncoated Fe-Cr alloys reveled that ceramic coating can decrease oxidation rate constant at lease an order of magnitude at low-intermediate operating temperatures as shown in Fig. 1. ASR of Fe-Cr alloy can be estimated with a reported Cr_2O_3 conductivity[21] and following equation.

$$\left(\frac{m}{A}\right)^2 = k_g t = \left(\frac{\frac{3}{2}M_{O_2}}{M_{Cr_2O_3}}\rho_{Cr_2O_3}\right)^2 k_p t \qquad (1)$$

where m is weight gain, A is the surface area of the sample, k_g and k_p are the rate constants for weight gain and thickness respectively, t is the time, and M_{O_2} and $M_{Cr_2O_3}$ are the molecular weights of oxygen and chromium oxide respectively, and $\rho_{Cr_2O_3}$ is the density of chromium oxide (5.21 gcm^{-3}). The obtained rate constant of LSCrO coated Ebrite at 1023 K, k_g =1.11x10^{-15} $g^2cm^{-4}s^{-1}$, yields the estimated ASR of 19 $m\Omega cm^2$ after 36 Ms (10000h) exposure to air at cathode side. The acceptable limit of interconnect ASR, including the contact resistance, is less than 50 $m\Omega cm^2$ over 36 Ms of operation[5]. Though this is a simple estimation with only Cr_2O_3 and the real scale includes other

oxides and impurities that may affect the ASR, the estimated value meets a requirement of acceptable limit for practical application. Taking rate constant and ASR into consideration, the maximum operating temperature for uncoated Fe-Cr alloys are about 923 K (650C) to meet the acceptable limit of ASR while that for coated alloys is increased to about 1023 K (750C). Ceramic coating can decrease oxidation rate and can also increase an acceptable temperature limit where the alloys can keep its conductivity during long-term operation.

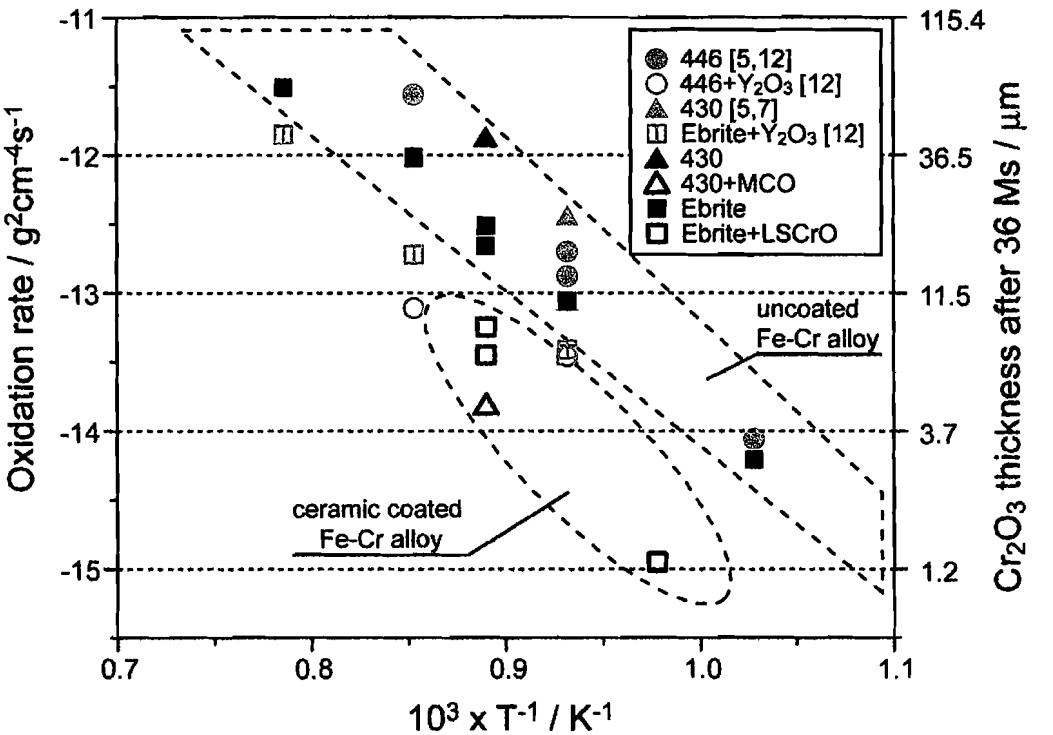

Fig. 1. Temperature dependence of oxidation rate of coated and uncoated Fe-Cr alloys

Several coated and uncoated alloys were tested for Cr vaporization at 873~1173K. The sample was placed in a set of glassware inside a furnace that was used to collect any evaporated chromium[19]. The Cr content, extracted through acid solution, was determined by inductively coupled plasma mass spectrometry (ICPMS). A unit of Cr transport rate ($CRT/ngm^{-2}s^{-1}$) was used to evaluate Cr vaporization of the samples. This value shows how much Cr is released from per unit surface of the sample per second. The Cr transport rates of the samples are shown in Table 2. The coatings of LSM and MCO deposited on 430 by aerosol spraying decreased Cr transport rate more than an order of magnitude at 873~1073 K compared with uncoated 430. Gindorf *et al.*[17] reported that LSM coating deposited on alloy X10CrAl18 by vacuum plasma spraying (VPS) yielded chromium retention of 97% (reduction factor is ~33) at 1123 K. The reduction factor of LSM coatings at 1073 K is 37 and this value is

in good agreement with this reported value of LSM coating by VPS. The thin LSCrO layer coated by sol-gel method decreased Cr transport of Ebrite about a half order of magnitude. The thickness of the thin LSCrO layer on Ebrite was about 0.15 μm while those of aerosol spray coatings were 10~20 μm. This data indicates that even vary thin oxide coating can suppress Cr vaporization to a certain degree. Cross-sectional SEM image and EDS data of uncoated 430 after Cr vaporization test at 1073 K are shown in Fig. 3. The surface of the uncoated 430 was covered with a dense oxide layer. The thickness of the layer observed with SEM was about 1 μm. The intensity of chromium is increasing at the interface of alloy/oxide layer and that of Mn is increasing at the surface of the oxide layer. These lines indicate that the surface of the 430 sample was covered with Cr_2O_3 and $(Mn,Cr)_3O_4$ spinel oxide. Cross-sectional SEM image and EDS data of 430+LSM after Cr vaporization test are shown in Fig. 4. The surface of the sample was rough and some particles were agglomerated but the cross section of the layer looked compacted. The coatings decreased the activity of Cr_2O_3 at the gas/oxide interface where Cr_2O_3 can evaporate. The vaporization reactions for the formation of the dominant gaseous chromium species, $CrO_2(OH)_2(g)$, can be expressed as

$$\frac{1}{2}Cr_2O_3(s)+\frac{3}{4}O_2(g)+H_2O\,(g)=CrO_2(OH)_2(g) \qquad (2)$$

This equation indicates that the partial pressure of volatile $CrO_2(OH)_2(g)$ is proportional to the partial pressure of water vapor, P_{H_2O}, oxygen partial pressure, $P_{O_2}^{3/4}$, and activity of Cr_2O_3 at the gas/oxide interface, $a_{Cr_2O_3}^{1/2}$. Cr transport rates measured in different water vapor condition can be compared since the partial pressure of $CrO_2(OH)_2(g)$ is proportional to P_{H_2O} theoretically. Figure 5 shows the Cr transport rate of coated and uncoated alloys assuming the samples were exposed to air with a water vapor pressure of P_{H2O} = 0.2x10^4 Pa (63% RH at 298 K). This figure revealed the effect of coatings on Fe-Cr alloy at high-intermediate operating temperatures. Differences of Cr transport rate between coated and uncoated alloy was 0.5~2 orders of magnitude in this temperature range. Fergus[6] calculated oxygen partial pressure dependence of the partial pressures of gaseous chromium species with the thermodynamic data from Ebbinghaus[22]. The calculation showed that most of gaseous chromium species decrease with decreasing temperature but the partial pressure of $CrO_2(OH)_2$, the predominant gas in cathode condition, does not decrease drastically. Even if the operating temperature is lowered from 1073 to 873 K, the chromium vaporization rate decreases by only an order of magnitude. The amount of evaporated chromium from bare alloy can be appreciable and chromium vaporization must be lowered. The present work demonstrated that ceramic coatings deposited on 430 and Ebrite by aerosol spraying and sol-gel method can decrease Cr vaporization and would prevent deterioration of cell performance due to chromium deposition at intermediate operating temperature of SOFCs.

Table 2: Cr transport rate of coated and uncoated 430 and Ebrite: log (CTR/ngm^{-2}s^{-1})

Sample	P_{H2O}/Pa in air	873 K	973 K	1073 K	1173 K
Uncoated 430	$1.0x10^4$	2.04	2.68	2.99	-
430 + LSM	$1.0x10^4$	0.61	1.04	1.39	-
430 + MCO	$1.0x10^4$	0.89	0.99	1.42	-
Ebrite	$0.4x10^4$	-	-	-	2.36
Ebrite + LSCrO	$0.4x10^4$	-	-	-	1.83

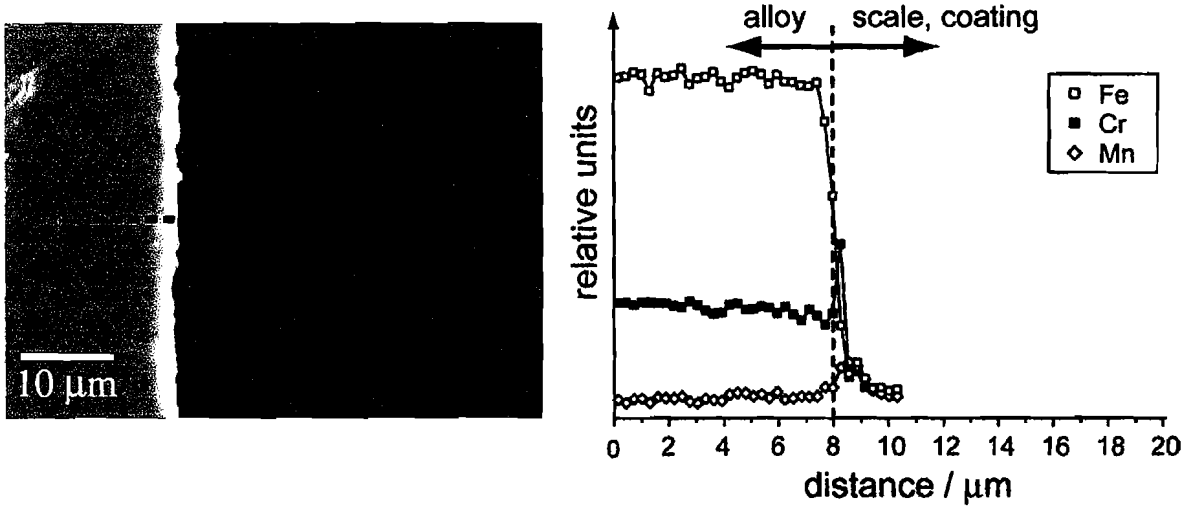

Fig. 3. Cross-sectional SEM image and EDS data (dotted lines) of 430 after chromium vaporization test at 1073 K.

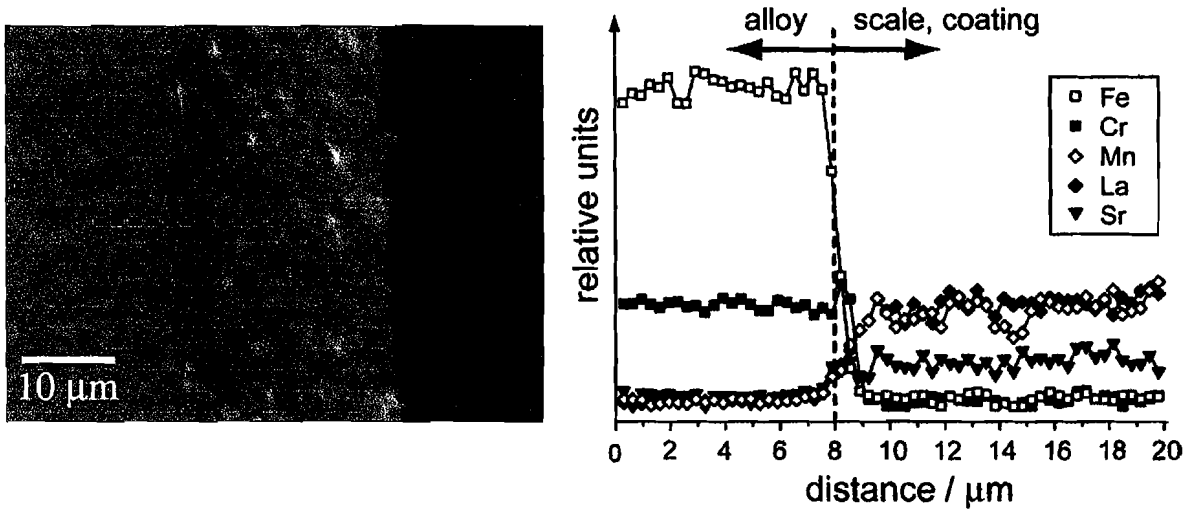

Fig. 4. Cross-sectional SEM image and EDS data (dotted lines) of 430+LSM after chromium vaporization test at 1073 K.

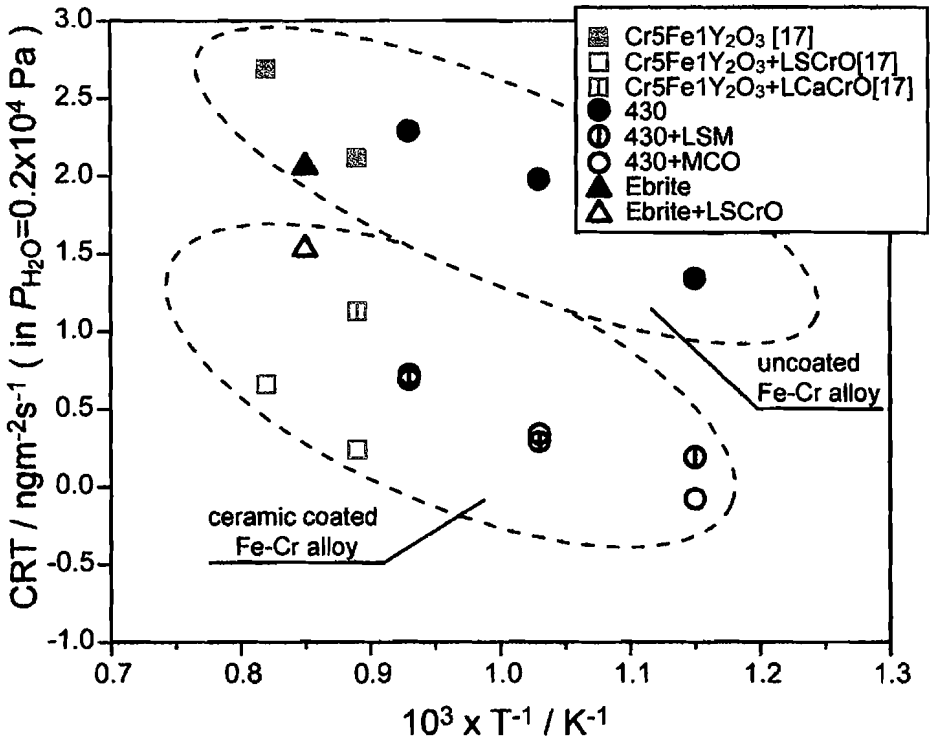

Fig. 5. Temperature dependence of Cr transport rate of coated and uncoated Fe-Cr alloys

Conclusion

The oxidation rate and chromium vaporization rate of coated and uncoated Fe-Cr alloys were measured to evaluate the effectiveness of ceramic coatings at intermediate operating temperatures of SOFCs. Ceramic coatings of MCO and LSCrO decreased oxidation rate of the coated alloys more than an order of magnitude compared with uncoated alloys. Decreasing oxidation rate by the coatings increases the acceptable temperature limit where the alloys can keep its conductivity during long-term operation. Ceramic coatings of MCO and LSM decreased Cr transport rate more than an order of magnitude at 873~1073 K. Even thin LSCrO coating is capable of reducing chromium vaporization a half order of magnitude. The comparison with other reported data revealed that ceramic coating could decrease oxidation rate more than an order of magnitude and can also decrease Cr vaporization up to two orders of magnitude. The present work demonstrated that ceramic coating for interconnect alloys gives an improvement in terms of oxidation rate and Cr vaporization. Ceramic coating has at least two significant benefits for interconnect alloys at intermediate operating temperatures.

References

1. P. Kofstad, and R. Bredesen, *Solid State Ionics*, **52** (1992) 69.
2. K. Huang, P.Y. Hou, J.B. Goodenough, *Solid State Ionics*, **129** (2000) 237.
3. S. Linderoth, and P. H. Larsen, *Mat. Res. Soc. Symp. Proc.*, **575** (2000) 325.
4. M.Hansel, W.J.Quadakkers, and D.J.Young, *Oxid. Met.*, **59** (2003) 285.
5. Z. Yang, K. S. Weil, D. M. Paxton, and J. W. Stevenson, *J. Electrochem. Soc.*, **150** (2003) A1188-A1201.
6. J. W. Fergus, *Mat. Sci. and Eng. A*, **397** (2005) 271-283.
7. T. Brylewski, M. Nanko, T. Maruyama, K. Przybylski, *Solid State Ionics*, **143** (2001) 131.
8. T. Horita, Y. Xiong, K. Yamaji, N. Sakai and H. Yokokawa, *J. Electrochem. Soc.*, **150** (2003) A243.
9. H. Kurokawa, Y. Oyama, K. Kawamura, and T. Maruyama, *Solid State Ionics,* **168** (2004) 13.
10. J. H. Zhu, Y. Zhang, A. Basu, Z. G. Lu, M. Paranthaman, D. F. Lee and E. A. Payzant, *Surface and Coatings Technology*, **177-178** (2004) 65.
11. Xuan Chen, Peggy Y. Hou, Craig P. Jacobson, Steven J. Visco, and Lutgard C. De Jonghe, *Solid State Ionics*, **176** (2004) 425
12. K. Huang, P. Y. Hou, J. B. Goodenough, *Mater. Res. Bul.*, **36** (2001) 81.
13. K. Hillpert, D. Das, M. Miller, D. H. Peck, and R. Weiβ, *J. Electrochem. Soc.*, **143** (1996) 11.
14. S. P. Jiang, J. P. Zhang and X. G. Zheng, *J. Europ. Ceram. Soc.*, **22** (2002) 361.
15. Y. Matsuzaki and I. Yasuda, *J. Electrochem. Soc.*, **148** (2001) A126.
16. S. P. S. Badwal, R. Deller, K. Foger, Y. Ramprakash and J. P. Zhang, *Solid State Ionics*, **99** (1997) 297.
17. C. Gindorf, K. Hilpert, and L. Singheiser, in Solid Oxide Fuel Cells VII (SOFC VII), H. Yokokawa and S. C. Singhal, Editors, PV 2001-16, p. 793, The Electrochemical Society Proceedings Series, Pennington, NJ (2001).
18. L.A. Chick, L.R. Pederson, G.D. Maupin, J.L. Bates, L.E. Thomas, and 1G.J. Exarhos, *Mater. Lett.* **10** (1990) 6.
19. H. Kurokawa, C. P. Jacobson, S. J. Visco and L. C. De Jonghe, Submitted to Solid State Ionics.
20. R.K. Wild, *Corros. Sci.*, **17** (1977) 87.
21. J. -H. Park, K. Natesan, *Oxid. Met.*, **33** (1990) 31.
22. B. B. Ebbinghaus, *Combus. Flame*, **93** (1993) 119.

Submitted to J. Electrochem. Soc., 1-18-07

LBNL-62320

Effects of surface deposited nanocrystalline chromite thin films on the performance of a ferritic interconnect

I. Belogolovsky[a], X.-D. Zhou[b,c], H. Kurokawa[a], P. Y. Hou[a,*], S. Visco[a], and H. U. Anderson[c]

a) Lawrence Berkeley National Laboratory, One Cyclotron Rd., MS 62-203, Berkeley, CA 94720

b) Pacific Northwest National Laboratory, Richland, WA 99352

c) Department of Materials Science and Engineering, University of Missouri-Rolla, Rolla, MO 65401

I. Belogolovsky, X-D. Zhou, H. Kurokawa, P. Y. Hou, S. J. Visco and H. U. Anderson, "Effects of surface deposited nanocrystalline chromite thin films on the performance of a ferritic interconnect", submitted to *J. Electrochem. Soc.*

ABSTRACT

$LaCrO_3$-based nanocrystalline thin films, substituted with Sr and Zn, and coated onto a Fe-26at%Cr Ebrite alloy were evaluated at 750-900°C as potential enhancers of oxide properties in ferritic interconnects of SOFC's. It was found that at 750°C the coatings provided (1) lower oxidation rates, (2) increased conductivity, (3) protection during 24-hour cycling and at least 2,375 hours of isothermal oxidation, as well as a (4) fine-grained and uniform microstructure. Although after oxidation at 850°C the grains grew substantially and the scale looks to be overgrowing the film, conductivity and oxidation rates still match that of the uncoated sample. Tensile tests showed that the coating improved scale adhesion after a 100-hour oxidation at 850°C. At 900°C, the film is still capable of blocking 70% of the Cr that evaporates from an uncoated Ebrite substrate.

INTRODUCTION

Ferritic steels have in recent years been widely studied as possible interconnect materials in solid oxide fuel cell (SOFC) systems, where they provide the electrical connection between single cells and allow gas separation within the cell stack [1,2] The choice of these steels is based on several factors, such as their low cost, compatible coefficient of thermal expansion (CTE) with the cell components and the relative slower growth rate and high conductivity of the oxide, namely Cr_2O_3, that forms on their surfaces during operation. Although Cr_2O_3 conductivity increases with temperature, these metallic

interconnects are limited to operating temperatures in an intermediate regime of 600°C to no more than 800°C, due to fast growth rates of the Cr_2O_3 [3] and of Cr evaporation at higher temperatures [4,5]. When water vapor is present, the evaporation problem becomes severe even within the 600-800°C temperature range [6]. On the cathode side, evaporated Cr species deposit on cold surfaces and poison the cathode for further catalytic reactions, thus greatly reducing cell performance [7-12]. The challenges of improving these steels as metal interconnects, therefore, involve reduction of the oxidation rate, enhancement of the oxide conductivity and elimination or significant reduction of Cr evaporation from the growing oxide. Any method that can at the same time improve oxide scale adhesion to the steel would also be very useful. In addition to these requirements, the chosen method should also be low-cost so as not to negate the advantage of selecting a low-cost steel in the first place, which is to lower the manufacturing costs for SOFCs and enable commercialization.

Alloy development [13-18] and coating applications [6,19-24] have been attempted to improve Cr_2O_3-forming alloys as interconnect materials. The former includes an earlier developed Plansee alloy [12,15,25] and a later Crofer alloy [12,13,26]. Although the Plansee has excellent CTE match with the cell components and forms stable and adherent Cr_2O_3 scales, it is expensive and Cr evaporation is expected to be a problem. The Crofer was tailored for slow Cr_2O_3 growth and adherence, and it makes use of the Mn in the alloy to develop a Mn-oxide rich surface layer above the Cr_2O_3 to help reduce Cr evaporation [12], but the amount of reduction is not yet sufficient. Many surface coating methods and materials have been examined [6,19-22,24,27-30], however, none have met

all the requirements for a successful SOFC interconnect material. The demand for improved coating materials and processes continues to motivate research in this area [5, 31-33]. The purpose of this work is to report a new type of thin coating, produced by a simple sol-gel method, and show how it affects a ferritic steel in terms of its oxide growth rate, adhesion, conductivity and the extent of Cr evaporation. The coating consists of nanocrystallites of perovskite type chromites ($LaCrO_3$ based). Since these oxides are known to have high conductivities at high temperatures [34] they are chosen not only as a protective layer for oxidation, but also to increase the conductivity of the Cr_2O_3 scale.

EXPERIMENTAL

Coating Procedure. – The base alloy used for this work was a commercial ferritic stainless steel (Ebrite from Allegheny Ludlum Steel, in the form of a 1 mm thick sheet) with compositions shown in Table 1. Specimens 10×10 or 20×20 mm^2 were cut from the as-received sheet, polished to a 1μm finish, and cleaned ultrasonically in distilled water and then acetone. The coating process (details published elsewhere [35]), involved deposition by spin-coating of a polymeric solution containing La, Sr (or Zn) and Cr nitrates, followed by several steps of subsequent heating. Electrical conductivity was measured on the thin films deposited on a single crystal Al_2O_3 substrate. The crystalline nature of the deposited thin films was verified by grazing x-ray diffraction (XRD) using a high-resolution four-circle diffractometer (Philips X'Pert MRD) with Cu Kα radiation. Since the effects caused by these two types of coatings, $La_{0.8}Sr_{0.2}CrO_3$ or $LaCr_{0.9}Zn_{0.1}O_3$,

were always indistinguishable, they will be treated as the same in this paper, where as results from one type of coating can be seen as applicable for the other.

Oxidation. – Coated and uncoated samples were oxidized isothermally for 50 hrs in a Cahn thermal gravimetric balance in air at 750°C or 850°C with a heating and cooling rate of 5°C/min. Cyclic oxidation was done in air at 5°C/min heating and cooling, and held for 24 hrs at 750°C during each cycle. A few specimens were held at 750°C or 850°C for 100 hrs to evaluate the effectiveness of the coatings after longer term oxidation. One coated sample oxidized at 750°C was held for 1 month (713 hours), removed for examination, and then placed back in the same furnace for another 2 months, for a total oxidation period of 2,375 hours.

Tensile Pull Test, ASR and Cr Evaporation. – Oxidized samples were characterized using scanning electron microscopy (SEM), energy dispersive spectroscopy (EDS), and XRD of the sample surface, plus Auger through oxide depth profiling and SEM analysis of sample cross-sections. A tensile pull test [36] was used to evaluate the fracture strength of the oxide, or that of the oxide/alloy interface, as an indication of scale adhesion. Measurements of the areal specific resistance (ASR) were carried out over the temperature range 500-750°C using a four-point DC arrangement with Au as electrodes and Pt mesh and leads as current collectors. With heating and cooling rates at 5°C/min, the test assembly was first heated to 500°C, then V-I measurements were conducted at each 50°C increment up to 750-850°C with 20 mA/step up to 1000 mA. Cr evaporation

was evaluated on a coated sample at 900°C for 24 hrs in humid air (P_{H2O} = 4.0x10^3 Pa). Details of this evaporation and collection apparatus has been described elsewhere [5].

RESULTS AND DISCUSSION

Fabrication and Electrical Conductivity of the Thin Films. – Spin coating has been used by a number of research groups to deposit thin films of zirconia, ceria and perovskite family oxides, but it has been rarely utilized to deposit chromite thin films on ferritic alloys [29]. The difficulty may be related to the formation of chromates ($LaCrO_4$) at low temperature, as shown by Carter et al. [37]. Chromates can be transformed to the perovskite chromites ($LaCrO_3$) by heating in air at the elevated temperature (>1000°C). Treatment at such a high temperature is not feasible for alloy interconnect. Recently, we reported a method to transform the chromate to chromite at relatively low temperature (600°C) in reducing conditions [35], where B site substituted $LaCrO_3$ thin films were reported for the first time. Initial research emphasized investigating the crystal structure of Zn substituted $LaCrO_3$ thin films. **Fig.** 1 illustrates grazing XRD of the films on a single crystal Al_2O_3 substrate, after annealing in air at 800°C. Included in **Fig.** 1 is the XRD result of a perovskite $La_{0.6}Sr_{0.4}FeO_{3-\delta}$ thin film for comparison. The strongest reflection of the chromate phase is at $2\theta \sim 30°$, which was not detected in the $LaCr_{0.9}Zn_{0.1}O_3$ after it was annealed in air.

Addtional experiments were carried out to investigate the electrical properties of $LaCr_{0.9}Zn_{0.1}O_3$ as a function of temperature and oxygen activity. $LaCrO_3$ based ceramics

are of interest in some particular applications, largely due to their good electrical conductivity (σ) over a wide range of temperature and oxygen activities. Low valence element substituted $LaCrO_3$ ceramics exhibit thermally activated electrical conductivity behavior which is due to the exponential temperature dependence of the mobility. Shown in **Fig.** 2 are the plots of $\ln(\sigma T)$ versus inverse temperature for thin films of $LaCr_{0.9}Zn_{0.1}O_3$. Bulk conductivity was included for comparison [38]. Previous studies [35] showed that the conductivity of $(La,Sr)CrO_3$ thin films was 2 orders of magnitude lower than bulk conductivities, which was attributed to the segregation of the dopant and the presence of the 2nd phase – chromate. At 750°C, the conductivity in $La(Cr,Zn)O_3$ thin films (~ 0.67 S/cm) was much lower than that of the bulk (~ 5.3 S/cm). When temperature was increased, the conductivity in the thin films increases more rapidly than that of the bulk, indicating a larger activation energy (~0.92 eV) for thin films than that (~ 0.14eV) in the bulk. Interestingly, at 1000°C, the conductivity in the thin film (~ 4.1 S/cm) is comparable with the bulk value (~ 5.9 S/cm). The conductivity was then measured upon decreasing temperature from 1000°C to 750°C. A lower activation energy was observed (~0.15 eV). This type of hysteresis in electrical properties of sol-gel films is fairly common and often attributed to incomplete crystallization of the amorphous precursor. Similar behavior was observed in $(Pr,Sr)MnO_3$ films [39], in which annealing temperature played an important role in the electrical conductivity of thin films.

Oxidation and Growth of Oxide Scale. – The oxidation kinetics of both the coated and uncoated Ebrite are nearly parabolic. XRD showed that the oxides formed above 750°C

on both samples are mainly Cr_2O_3. Parabolic rate constants obtained from these samples are plotted in **Figure** 3. Comparing the $(La,Sr)CrO_3$ and $La(Zn,Cr)O_3$ coatings at 750°C, one can see that they have very similar oxidation rates. These rates are about an order of magnitude lower than that of uncoated Ebrite and even Ebrite coated with a thin layer of nitrate-converted Y_2O_3 [19], where the usual beneficial reactive element effect is expected [40]. This slow rate demonstrates a strong effectiveness of the chromite coatings in reducing oxide growth rates. However, at higher temperature, namely 850°C, the rate constant of the coated sample approached that of the uncoated, signaling a loss of protection at higher temperatures.

Morphology of the as-coated $(La,Sr)CrO_3$ sample has been shown elsewhere [35]. SEM images in **Figs.** 4a and b depict the surface of a $La(Zn,Cr)O_3$-coated sample, where it is seen to be uniformly covered with a dense and adherent film, with the largest grain size no more than 100 nm. The film is about 150 nm thick, determined by AES depth profiling. Occasional non-uniform areas are present on the surface, as that marked by the arrow in **Fig.** 4a and the white particles seen in **Fig.** 4b, which are both richer in La. Particles higher in Zn content were also found distributed over the surface. After oxidation in air for 100 hrs at 750°C (**Fig.** 4c), the coated surface still appeared fine-grained and uniform. The average surface grain size is ~ 300 nm. EDS analysis showed similar overall concentrations of Zn and La, but increased Cr content, indicating that Zn and La most likely remained near the scale surface and Cr_2O_3, also verified by XRD, grew beneath the original coating. AES depth profiling of an oxidized La-chromite

coated sample verified that La was concentrated near the surface of the sample, within the outer 100 nm, while Cr and O were the major components of the oxide.

The same behavior of Cr_2O_3 growth beneath the deposited coating was also seen after extended cyclic oxidation at 750°C. **Fig.** 5b shows a scale cross section and its corresponding EDS line traces from a $(La,Sr)CrO_3$ coated sample, where it had undergone cyclic oxidation at 750°C for a total of 240 hrs (24 hr per cycle, 10 cycles total). Due to the lower oxidation temperature and probably mild heating and cooling rates, none of the cycled samples (coated or uncoated) showed any obvious spallation. The polished cross-sections in **Fig.** 5a and b showed an average scale thickness on the uncoated and coated samples to be ~1.2 and 0.6 μm respectively. Based on the EDS line scans of La and Sr in **Fig.** 5c, Cr_2O_3 is seen to have developed underneath the coating. The higher than expected Fe signal in the scale, which is known to be purely Cr_2O_3 from XRD and AES analyses, should be due to beam spreading of the X-ray probe, whose size was about 1 μm.

When a sample oxidized at 750°C for 100 hrs (**Fig.** 4c) was oxidized again for another 100 hours at 850°C, its surface appeared much different (**Fig.** 4d). Nodules of Cr_2O_3 grains, with grain sizes ranging from 1-2 μm, are seen to have grown through the original coating. Similar morphology was also observed when a coated sample was oxidized directly at 850°C for only 50 hrs, where the scale thickness, calculated by the oxidation rate constants, is 0.68 μm. However, under the same range of scale thickness at 750°C (0.64 μm, oxidized for 2,375 hours), the oxidized surface remained dense and smooth,

similar to the original coating, except the average grain size has increased to 0.6 μm. These results, along with oxidation rates shown in **Fig.** 3, indicate a strong temperature dependence on the protectiveness of these coatings. Overgrowth of Cr_2O_3, probably due to its faster growth rates at higher temperatures, disrupts and damages the original coating, hence reverts the alloy to its normal oxidation rate and reduces the coating's effectiveness as a protective layer. At 750°C, and most likely temperatures that are lower, Cr_2O_3 growth took place beneath the coating, with the coating acting like a protective layer. Even with thermal cycling, the coating remained undisrupted.

Adhesion of Oxide Scale. – Adhesive strength of the oxide film to its substrate was conducted on (1) the coated and uncoated Ebrite samples that were oxidized at 750°C and then 850°C for 100 hours each, and (2) the coated Ebrite sample oxidized for 2,375 hours at 750°C. The test made use of a commercial Quard Group pull tester that allowed tensile pulling of a 2.65mm diameter stub glued to the oxidized oxide surface, where the maximum strength of the glue was 101 MPa. Results are summarized in Table 2. After the first oxidation (750°C for 100hr), neither the coated or uncoated Ebrite showed any oxide or interface failure. Fracture only took place at the glue/oxide or the glue/stub interfaces. This indicates that the fracture strength of the scale exceeded that of the glue failure strength of 101 MPa.

Since failure of this type is dominated by internal defects, it is likely that the oxidation time is too short and the temperature too low for large enough defects to be established. The coated sample even remained adherent after a long-term 3-month oxidation (2,375

hrs) at 750°C. After a second 100-hour oxidation at 850°C, the uncoated sample failed at the scale/alloy interface, but the coated sample film remained intact. It appears that the coating increased adhesion of the oxide, most likely by a combination of slower oxide growth, hence reducing the rate of defect accumulation, and the incorporation of La, a reactive element that is known to improve Cr_2O_3 adhesion [40,41], into the growing Cr_2O_3.

Temperature Dependence of ASR – **Figure** 6 compares the ARS of the coated and the uncoated specimens at different temperatures during the heating cycle of a conductivity test. The uncoated sample was pre-oxidized at 800°C for 48 hrs, forming a Cr_2O_3 scale about 2 μm thick [42]. These data points fall on a straight line, giving an activation energy of 0.84 eV. The coated sample, on the other hand, was without a preformed oxide layer; its points deviate strongly from a linear relationship. Only after a sufficiently high temperature is achieved (~650°C) and time elapsed (~2.5hrs), the points transition into a linear behavior, where a line parallel to that of the uncoated specimen can be drawn. Since the conductivity test proceeds at increasing temperatures, oxidation rate will also increase to eventually allow an appreciable oxide layer to develop on the sample surface. At the end of the test, the oxide scale that formed on the coated surface was about 0.2 μm. The fact that the presence of this oxide layer causes the coated surface to conduct with similar activation energy as the uncoated sample suggests that the same conductivity mechanism is at play and the most resistant constituent is the thermally grown oxide layer. According to **Figure** 6, at 800°C, the ASR of the uncoated alloy is 0.03 Ωcm^2, but an order of magnitude lower on the coated, at 0.0043 Ωcm^2. This reduction should be

mainly due to the difference in oxide thickness, which agrees with prior results on the effect of Cr_2O_3 scale thickness on conductivity [42]. Therefore, it seems that thin film chromite coating by itself did not significantly affect conductivity (even though these films have lower conductivity than its bulk phase), but the effect comes from a reduced Cr_2O_3 growth rate.

Evaporation of Cr Species. – Two 20x20x1 mm^3 samples, one uncoated (A) and one coated on one side (B) were tested for Cr evaporation at 900°C for 24 hours. The sample was placed in a set of glassware inside a furnace that was used to collect any evaporated chromium [5]. The Cr content, extracted through acid solution, was determined by inductively coupled plasma mass spectrometry (ICPMS). The chromium transport rates from the uncoated and coated samples were 0.228 and 0.067 mg m^{-2} s^{-1} respectively. Using the uncoated sample A as a reference, and the relative coated vs. uncoated areas on sample B (not taken into account sample edges), it was found that the coated film is capable of blocking ~ 70% of the evaporated chromium.

This initial result, although promising, is rather surprising, since the coated film is thin and kinetics and morphological studies presented above indicated that it can be overgrown by Cr_2O_3 at higher temperatures or longer times. Therefore, any reduction in Cr_2O_3 evaporation must not be due to a physical blocking effect. A possible explanation may be that the coatings are not exactly stoichiometric, but contain excess oxides, such as La_2O_3. These oxides are known to reduce the Cr_2O_3 activity [6], hence can reduce its evaporation rates.

CONCLUSION

For consideration of chromite films as protective coatings for metallic interconnects, the following were studied: film cycling and long term oxidation behavior, oxidation kinetics, oxide adhesion, conductivity, and relative amounts of Cr evaporation. Ferritic, Fe-26at%Cr Ebrite alloy was used as the substrate. Deposited thin $(La,Sr)CrO_3$ and $La(Zn,Cr)O_3$ films behaved very similarly under the testing conditions. In comparison to the uncoated Ebrite, the coated specimen exhibited an oxidation rate constant that was 10 times lower at 750°C, due to the film's protective properties and minimization of Cr transport while the chromia grew underneath it. The film remained protective even after extended thermal cycling and long term exposures at 750°C. However, at 850°C, the chromia has overgrown the film, its grains coarsened, and the oxidation rate constant approached that of the uncoated Ebrite. The oxides formed on a coated sample proved to have higher adhesion strength and conductivity than its uncoated counterpart. Cr evaporation testing showed that the film is capable of blocking ~70% of the Cr that evaporates from an uncoated sample, even at 900°C. These chromite films, therefore, are worthy candidates as protective coatings for metallic interconnects in SOFC's, especially at temperature below 750°C.

Acknowledgement

Research sponsored by the U. S. Department of Energy, Office of Energy Efficiency and Renewable Energy under contract DE – FC36 – 01G011084.

REFERENCES

1. H. U. Anderson and F. Tietz, "Interconnects," in "High Temperature Solid Oxide Fuel Cells: Fundamentals, Design an Applications," Eds. S. C. Singhal and K. Kendall, Elsevier (2003).

2. J.W. Fergus, "Metallic interconnects for solid oxide fuel cells", Materials Science and Engineering, **397**, 271-83 (2005).

3. P.Y. Hou, K.Huang, W.T.Bakker, "Promises and problems with metallic interconnects for reduced temperature solid oxide fuel cells", Proc. 6th International Symposium on solid oxide fuel cells, ed. S.C.Sighal et. al, Honolulu, Hawaii, 1999.

4. M.C.Tucker, H. Kurokawa, C.P.Jacobson, L.C.DeJonghe, S.J.Visco, "A fundamental study of chromium deposition on solid oxide fuel cell cathode materials", Journal of Power Sources, **160**, 130-138 (2006).

5. H. Kurokawa, C.P.Jacobson, L.C.DeJonghe, S.J.Visco, "Chromium vaporization of uncoated and of coated iron-chromium alloys at 1073K", submitted to Solid State Ionics (2006).

6. K. Hilpert, D.Das, M..Miller, D.H.Peck, R.Weiß, "Chromium vapor species over solid oxide fuel cell interconnect materials and their potential for degradation processes", J. Electrochem. Soc., **143**, 3642-3647 (1996).

7. S.P.S. Badwal, R. Deller, K. Foger, Y. Ramprakash, J.P. Zhang, "Interaction between chromia forming alloy interconnects and air electrode of solid oxide fuel cells", **99**, 297-310 (1997).

8. S.C. Paulson, V.I. Birss, "Chromium poisoning of LSM-YSZ SOFC cathodes", J. Electrochem. Soc., **151**, A1961-8 (2004).

9. Y. Matsuzaki, I. Yasuda, "Dependence of SOFC cathode degradation by chromium-containing alloy on compositions of electrodes and electrolytes", J. Electrochem. Soc., **148**, A126-31 (2001).

10. S.P. Jiang, J.P. Zhang, X.G. Zheng, "A comparative investigation of chromium deposition at air electrodes of solid oxide fuel cells", J. European Ceram. Soc., **22**, 361-73 (2002).

11. S. Taniguchi, M. Kadowaki, H. Kawamura, T. Yasuo, Y. Akiyama, Y. Miyake, T. Saitoh, "Degradation phenomena in the cathode of a solid oxide fuel cell with an alloy separator", Journal of Power Sources, **55**, 73-9 (1995).

12. E. Konysheva, H. Penkalla, E. Wessel, J. Mertens, U. Seeling, L. Singheiser, K. Hilpert, "Chromium poisoning of perovskite cathodes by the ODS alloy Cr5FeY_2O_3 and the high chromium ferritic steel Crofer22APU", J. Electrochem. Soc., **153**, A765-73 (2006).

13. W.J. Quadakkers, J. Piron-Abellan, V. Shemet, L. Singheiser, "Metallic interconnectors for solid oxide fuel cells – a review", Materials at High Temperatures, **20**, 115-27 (2003).

14. T. Kadowaki, T. Shiomitsu, E. Matsuda, H. Nakagawa, H. Tsuneizumi, T. Maruyama, "Applicability of heat resisting alloys to the separator of planar type solid oxide fuel cell", Solid State Ionics, **67**, 65-69 (1993).

15. S. Linderoth, P.V. Hendricksen, M. Mogensen, N. Langvad, "Investigations of metallic alloys for use as interconnects in solid oxide fuel cell stacks", J. Materials Science, **31**, 5077-82 (1996).

16. T. Brylewski, M. Nanko, T. Maruyama, K. Przybylski, "Application of Fe-16Cr ferritic alloy to interconnector for a solid oxide fuel cell", Solid State Ionics, **143**, 131-150 (2001).

17. J.H. Zhu, S.J. Geng, Z.G. Lu, "Evaluation of Haynes 242 alloy as SOFC interconnect material", Solid State Ionics, **177**, 559-68 (2006).

18. L. Mikkelsen, P. H. Larsen, and S. Linderoth, "High temperature oxidation of Fe22Cr-alloy," *J. Therm. Anal. Calorimetry*, **64**, 879 (2001)

19. K. Huang, P. Y. Hou and J. B. Goodenough, "Reduced area specific resistance for iron-based metallic interconnects by surface oxide coatings," *Mater. Res. Bull.* **36**, 81 (2001).

20. W.J. Quaddakkers, H. Greiner, M. Haensel, A. Pattanaik, A.S. Khanna, W. Mallener, "Compatibility of perovskite contact layers between cathode and metallic interconnector plates of SOFC", Solid State Ionics, **91**, 55-67 (1996).

21. T. Brylewski, K. Przybylski, J. Morgiel, "Microstructure of Fe-25Cr/(La,Ca)CrO3 composite interconnector in solid oxide fuel cell operating conditions", Materials Chemistry and Physics, **81**, 434-437 (2003).

22. N. Oishi, T. Namikawa, Y. Yamazaki, "Oxidation behavior of an La-coated chromia-forming alloy and the electrical property of oxide scales", Surface and Coatings Technology, **132**, 58-64 (2000).

23. Y. Larring, T. Norby, "Spinel and perovskite functional layers between Plansee metallic interconnect (Cr-5wt%Fe-1wt% Y_2O_3) and ceramic $(La_{0.85}Sr_{0.15})_{0.91}MnO_3$ cathode materials for solid oxide fuel cells", J. Electrochem. Soc., **147**, 3251-6 (2000).

24. S. Linderoth, "Controlled reactions between chromia and coating on alloy surface", Surface Coating and Technology, **80**, 185-189 (1996).

25. Y. Larring, R. Haugsrud, T. Norby, "HT corrosion of a Cr-5wt%Fe-1wt% Y_2O_3 alloy and conductivity of the oxide scale", J. Electrochem. Soc., **150**, B374-9 (2003).

26. S.P. Simner, M.D.Anderson, G-G. Xia, Z. Yang, L.R. Pederson, J.W. Stevenson, "SOFC performance with Fe-Cr-Mn alloy interconnect", J. Electrochem. Soc., **152**, A740-5 (2005).

27. E. Batawi, A. Plas, W. Straub, K. Honegger, R. Diethelm, "New cost-effective ceramic oxide phases used as protective coatings for chromium-based interconnects", Proc. 6th International SOFC Symposium, 767-73, Pennington, NJ, USA (1999).

28. T. Brylewski, K. Przybylski, J. Morgiel, "Microstructure of Fe-25Cr/(La, Ca)CrO_3 composite interconnector in solid oxide fuel cell operating conditions", Materials Chemistry and Physics, **81**, 434-437 (2003).

29. J.H. Zhu, Y. Zhang, A. Basu, Z.G. Lu, M. Paranthaman, D.F. Lee, E.A. Payzant, "$LaCrO_3$-based coatings on ferritic stainless steel for solid oxide fuel cell interconnect applications", Surface and Coating Technology **177-178**, 65-72 (2004).

30. H.W. Nie, T.-L. Wen, H.Y. Tu, "Protection coatings for planar solid oxide fuel cell interconnect prepared by plasma spraying", Materials Research Bulletin, **38**, 1531-1536 (2003).

31. X. Chen, P.Y.Hou, C.P.Jacobson, L.C.DeJonghe, S.J.Visco, "Protective coating on stainless steel interconnect for solid oxide fuel cells: oxidation kinetics and electrical properties", Solid State Ionics, **176**, 425-433, (2005).

32. W. Qu, L. Jian, D.G. Ivey, J. M. Hill, "Yttrium, cobalt, and yttrium/cobalt oxide coatings on ferritic stainless steels for SOFC interconnects", Journal of Power Sources, **157**, 335-350, (2006).

33. G. Cabouro, G. Gabouche, S. Chevalier, P. Piccardo, "Opportunity of metallic interconnects for ITSOFC: Reactivity and electrical property", Journal of Power Sources, **156**, 39-44 (2006).

34. P. Singh and N. Q. Minh, "Solid Oxide Fuel Cells: Technology Status," *Int. J. Appl. Ceram. Technol.* **1**, 5 (2004).

35. X-D. Zhou, I. Belogolovsky, B.J.Scarfino, S.T.Reis, R.K.Brow, P.Y.Hou, H.U.Anderson, "Oxidation protective coating onto ferritic interconnect by nanocrystalline perovskite thin films", Electrochemical Society Proceedings, **16**, 159-163, (2004).

36 P. Y. Hou and K. Priimak, "Interfacial segregation, pore formation and scale adhesion on NiAl alloys", *Oxid. Metals*, **63**, 113-130, (2005).

37 J. D. Carter, H. U. Anderson and M. G. Shumsky, "Structure and phase transformation of lanthanum chromate," *J. Mater. Sci.* **31**, 551 (1996).

38 V. L. Sprenkle, "Sintering and Electrical Properties of the $LaCr_{1-x-y}Mg_xZn_yO_3$ System," Ph.D. Dissertation, University of Missouri-Rolla (1996).

39 T. Suzuki, P. Jasenski, V. Petrovski, X.-D. Zhou, and H. U. Anderson, "Electrical and Optical Properties of $Pr_{0.8}Sr_{0.2}MnO_3$ Thin Films," J. Appl. Phys. **93**, 6223-6228 (2003).

40. S.M.C. Fernandes, L.V. Ramanathan, "Influence of rare earth oxide coatings on oxidation behavior or Fe-20Cr alloys", Surface Engineering, **16**, 327-32 (2000).

41. P.Y.Hou, J.Stringer, "Effect of reactive element additions on the selective oxidation, growth and adhesion of chromia scales", Materials Science and Engineering, **A202**, 1-10 (1995).

42. K. Huang, P.Y.Hou, J.B.Goodenough, "Characterization of iron-based alloy interconnects for reducted temperature solid oxide fuel cells", Solid State Ionics, **129**, 237-250, (2000).

TABLES

Table 1: Composition of Ebrite Alloy (wt%).

Cr	Ni	Mn	Si	Mo	Cd	V	Co	N	Ti	Cu	Al	S	P	C	Fe
26.3	0.15	0.1	0.21	1.01	0.12	0.07	0.05	0.011	0.05	0.05	0.05	0.013	0.01	0.0022	bal

Table 2. Strength Testing after long-term oxidation on Ebrite alloy uncoated and coated with a $LaCr_{0.9}Zn_{0.1}O_3$ film.

Load (MPa)	**Oxidation Condition**		
	750°C/100hrs (scale thickness)	750°C/2,375hrs (scale thickness)	750°C/100hrs+ 850°C/100hrs (scale thickness)
Uncoated	97.5* (0.43 μm)	-----	90.3 ± 0.24** (1.56 μm)
Coated	>101* (0.12 μm)	>101* (0.58 μm)	>101* (1.05 μm)

Glue strength = 101 MPa; scale thickness estimated from kinetics data.

* No scale or interface failure

**Failed at the scale/alloy interface

FIGURE CAPTIONS:

Figure 1. XRD of thin films deposited on single crystal Al_2O_3. The films were annealed in air at 800°C for 1 hour.

Figure 2. A plot of ln(σT) vs. 10000/T for $LaCr_{0.9}Zn_{0.1}O_3$ thin films measured in air as the temperature increases and decreases. Conductivity of the bulk, from the work of Sprenkle (ref. 38), is included as a comparison.

Figure 3. Oxidation rate constants for various coated and uncoated alloys.

Figure 4. SEM images of $LaCr_{0.90}Zn_{0.10}O_3$ coated Ebrite surface (a);

(b) as coated surface at different magnifications;

(c) after oxidation at 750°C for 100 hours;

(d) after oxidation at 750°C for 100 hours, then at 850°C for another 100 hours;

(e) after oxidation at 750°C for 3 months (2,375 hours).

Figure 5. SEM images of polished cross-section of

(a) uncoated Ebrite after ten 24-hr cycles at 750°C;

(b) $LaSrCrO_3$ –coated sample after cycling under the same conditions;

(c) EDS line scans across the coated sample at the location marked by the vertical arrow on (b).

Figure 6. A plot of log(ASR) vs. 1000/T for uncoated pre-oxidized and coated Ebrite samples.

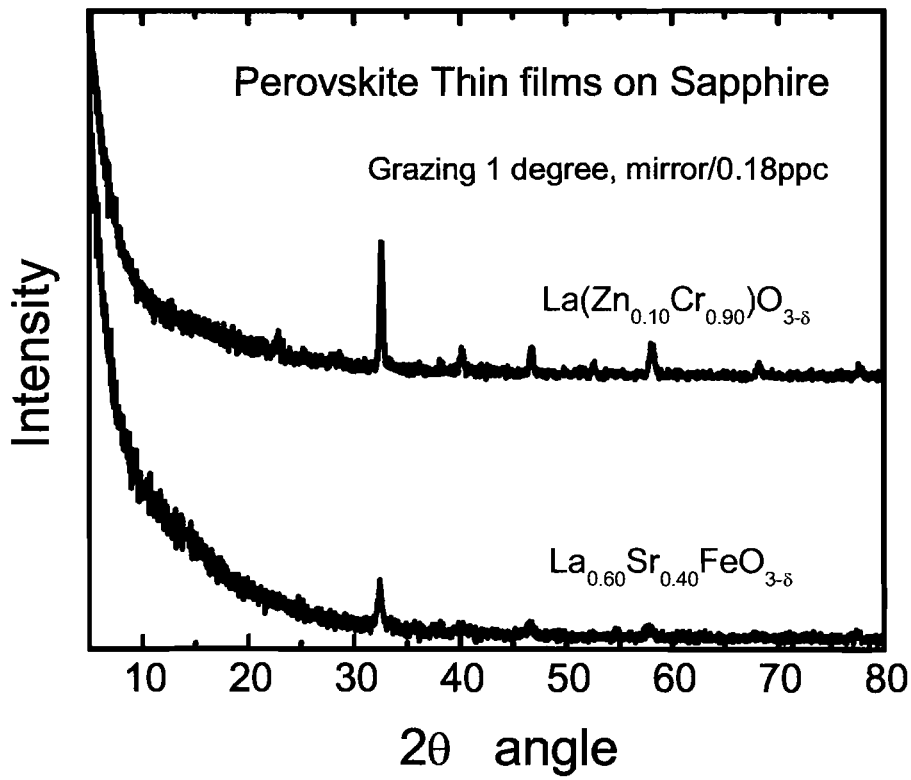
Perovskite Thin films on Sapphire
Grazing 1 degree, mirror/0.18ppc
La(Zn0.10Cr0.90)O3-δ
La0.60Sr0.40FeO3-δ
Intensity
10
20
30
40
50
60
70
80
2θ angle

Figure 1

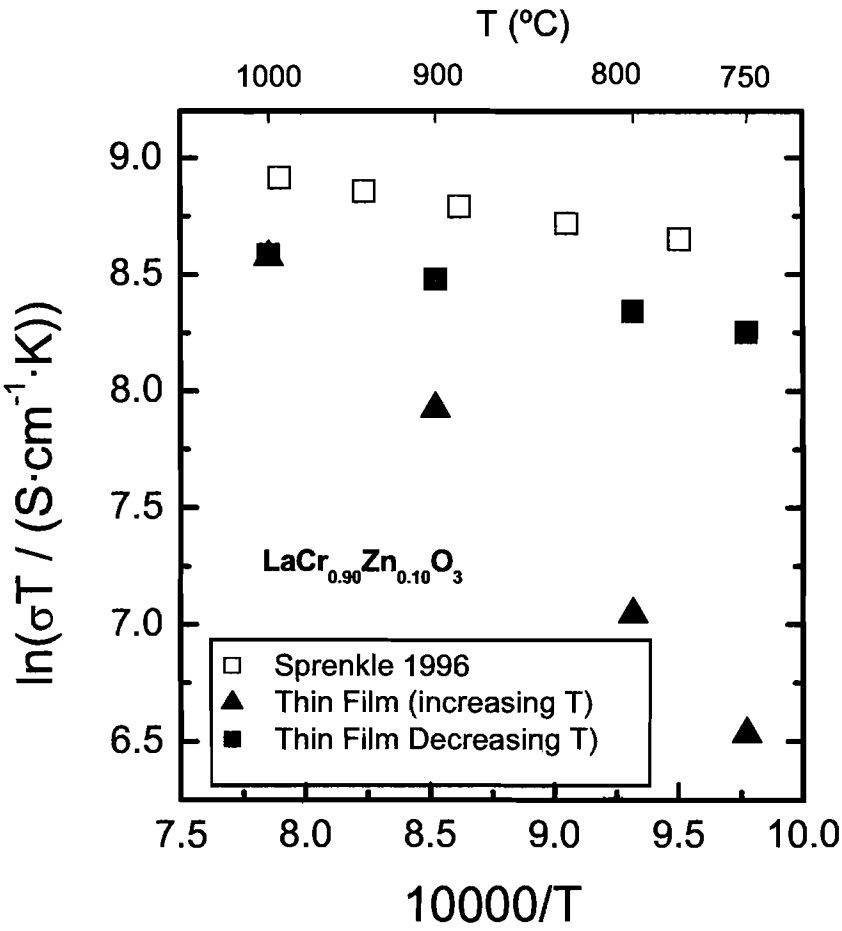
T (°C)
1000
900
800
750
9.0
8.5
8.0
7.5
7.0
6.5
ln(σT / (S·cm⁻¹·K))
LaCr0.90Zn0.10O3
Sprenkle 1996
Thin Film (increasing T)
Thin Film Decreasing T)
7.5
8.0
8.5
9.0
9.5
10.0
10000/T

Figure 2

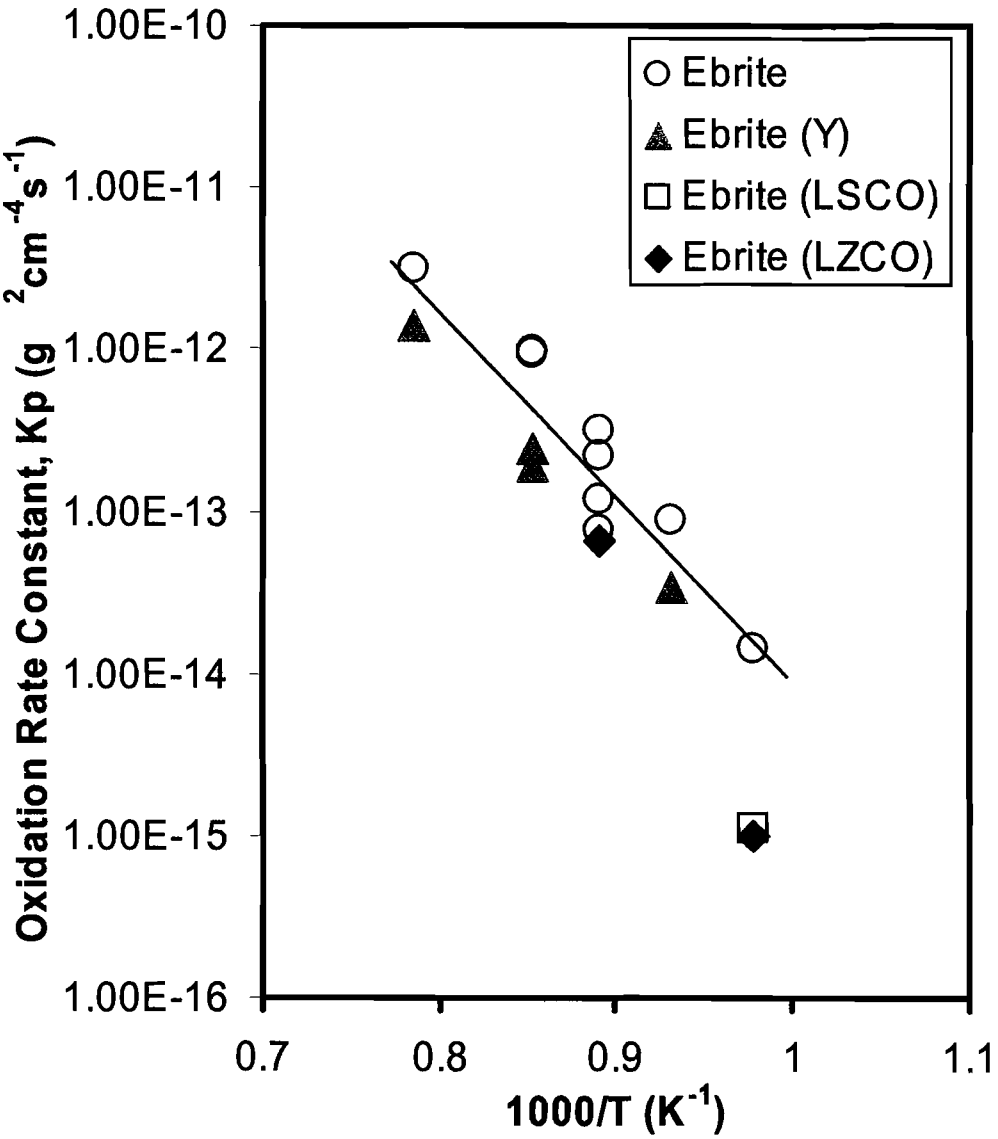
1.00E-10
1.00E-11
1.00E-12
1.00E-13
1.00E-14
1.00E-15
1.00E-16
Oxidation Rate Constant, Kp (g ^{2}cm^{-4}s^{-1})
0.7
0.8
0.9
1
1.1
1000/T (K^{-1})
Ebrite
Ebrite (Y)
Ebrite (LSCO)
Ebrite (LZCO)

Figure 3

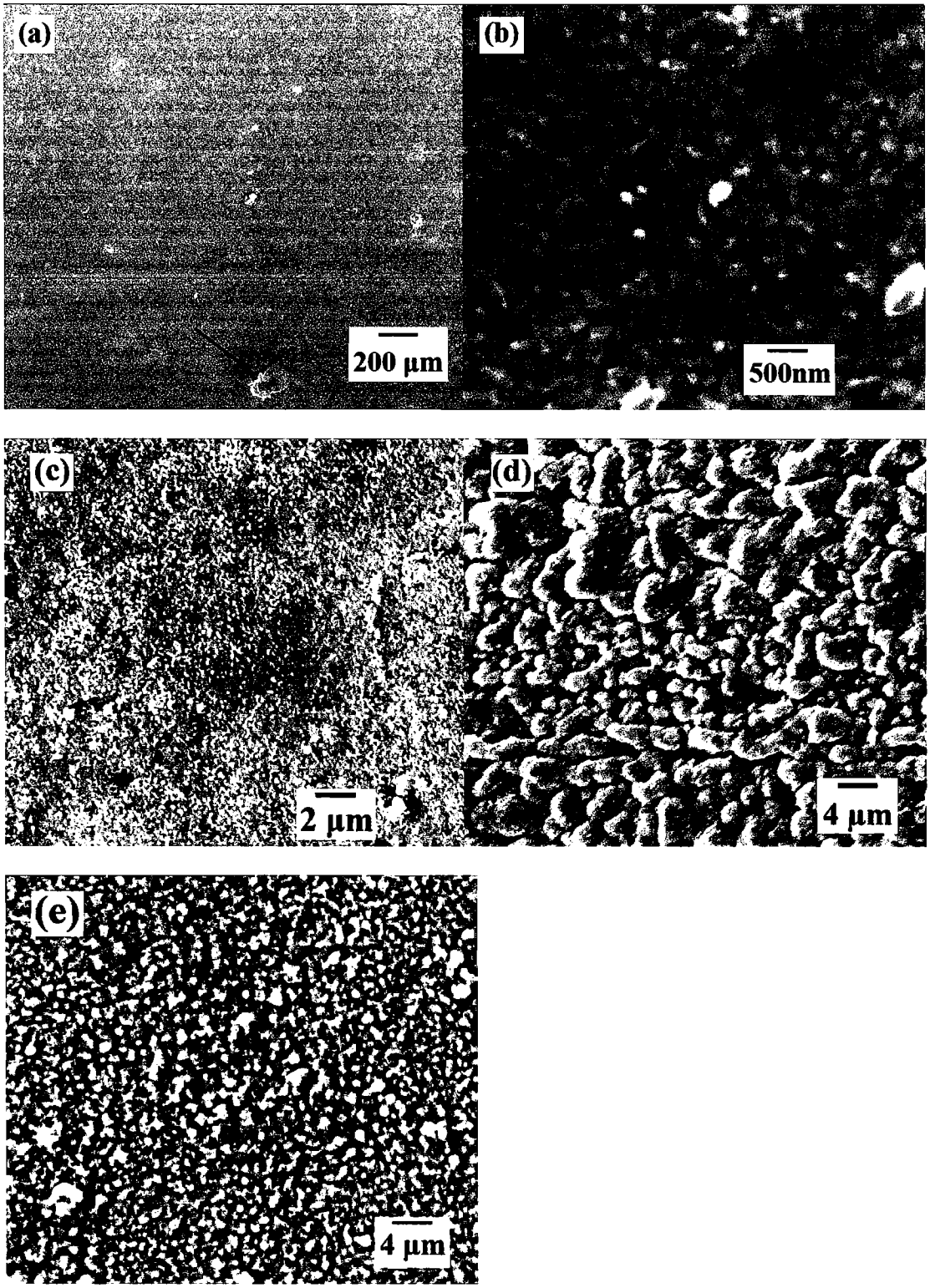

Figure 4

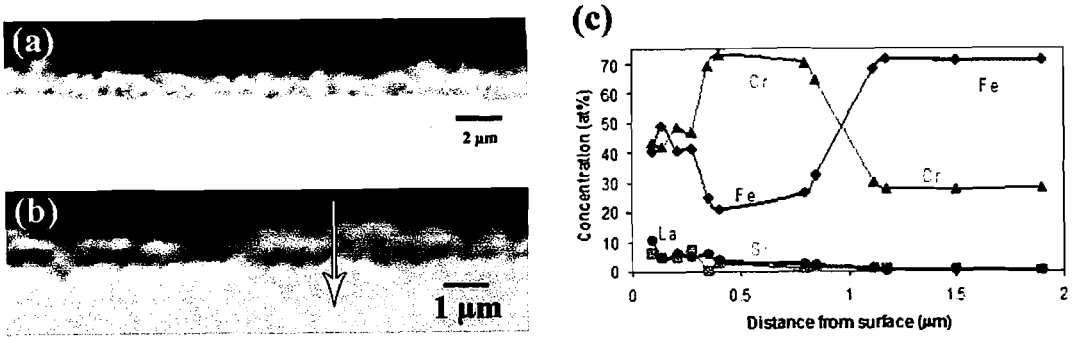
(a)
2 µm
(b)
1 µm
(c)
Concentration (at%)
Distance from surface (µm)
Cr
Fe
Cr
Fe
La
S
0
10
20
30
40
50
60
70
0
0.5
1
1.5
2

Figure 5

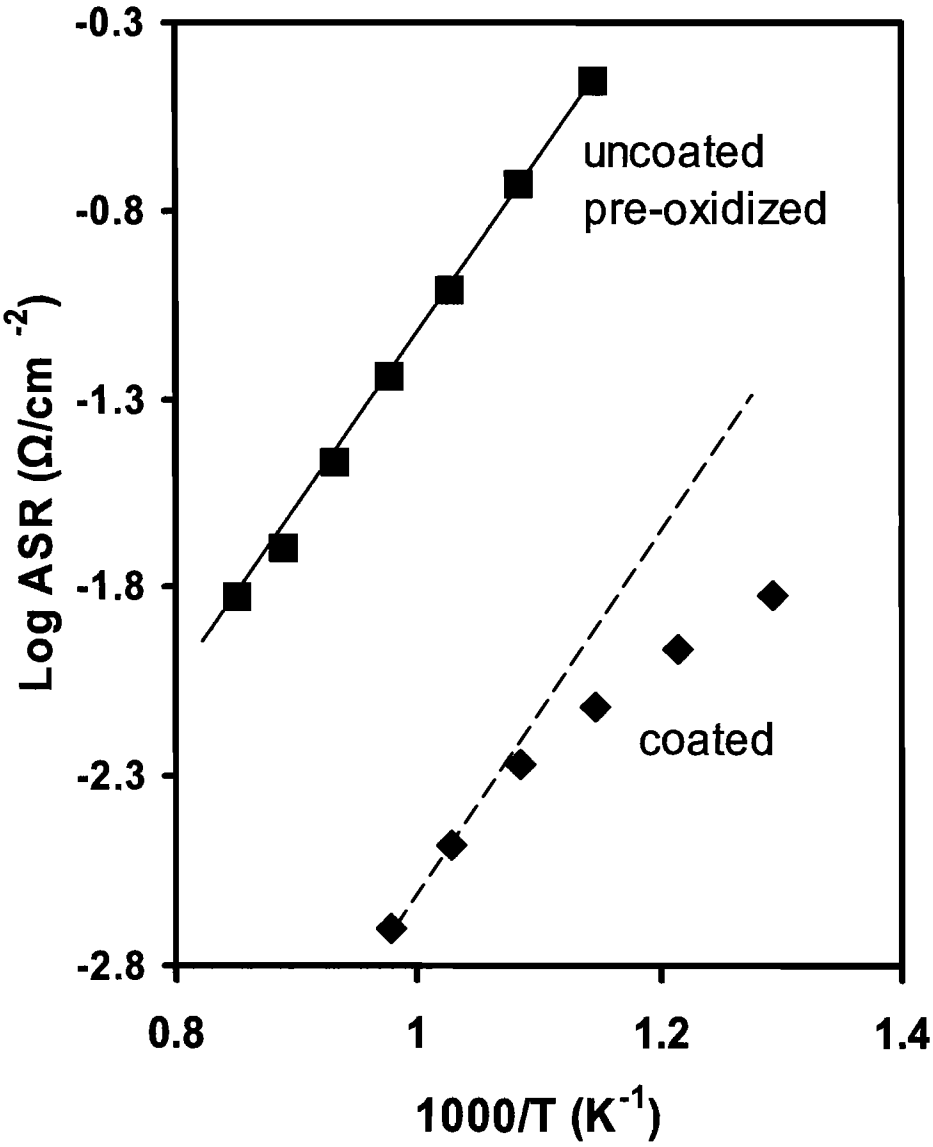
-0.3
-0.8
-1.3
-1.8
-2.3
-2.8
Log ASR (Ω/cm -2)
uncoated
pre-oxidized
coated
0.8
1
1.2
1.4
1000/T (K-1)

Figure 6

Synthesis and Characterization of Dense and Porous Cellulose Films

Vivek P. Khare[1,*], Alan R. Greenberg[1], Stephen S. Kelley[2], Heidi Pilath[2], Il Juhn Roh[3], and Jeff Tyber[1]

[1]*Department of Mechanical Engineering*
NSF Membrane Applied Science and Technology Center
University of Colorado at Boulder, Boulder CO 80309-0427.

[2]*National Renewable Energy Laboratory*
Golden CO 80401-3393.

[3]*Hydranautics, Inc.*
401 Jones Road, Oceanside CA 92054.

*Corresponding author, Tel: +1 303-492-5009; fax: +1-303-492-3498
E-mail address: vivek.khare@colorado.edu

Abstract

Cellulose derivate polymers such as cellulose acetate, cellulose triacetate, and cellulose nitrate are routinely used as membrane materials for applications involving microfiltration, ultrafiltration and gas separation. However, the cellulose polymer itself is not directly used to synthesize dense or porous films for membrane applications. Recently, N-methylmorpholine N-oxide (NMMO) and dimethylacetamide (DMAc)/lithium chloride (LiCl) have been successfully employed for dissolution of unmodified cellulose. There is thus a strong rationale for re-examining the possibility of cellulose membrane fabrication using these solvents.

By a judicious selection of solvents, casting conditions, solution composition, and solvent exchange steps, we have successfully cast dense as well as skinned asymmetric porous cellulose films. The porous films were obtained from a range of cellulose solution concentrations. The pore size and porosity decreased systematically with increasing cellulose concentration. SEM analysis of the cross sections revealed an asymmetric skinned structure with a monotonically increasing pore size away from the skin. Quantitative image analysis techniques revealed that the measured pore diameters are in the range 1.8–4.8 μm. Mechanical testing indicated that the dense cellulose films possessed tensile properties comparable to those of cellulose acetate (CA) films. Transport measurements indicated that whereas the nitrogen permeability values were comparable for cellulose and CA dense films, the cellulose permeability depended upon the type of drying protocol employed. These results demonstrate that processability need not be a constraint in the use of cellulose polymer for membrane fabrication. In selected applications, cellulose membranes could become a cost-effective, environmentally friendly alternative to other more commonly employed membrane polymers.

Keywords: membranes; cellulose; morphology; phase separation; natural polymers;

Introduction

Cellulose derivatives – cellulose acetate (CA), cellulose triacetate (CTA), and cellulose nitrate (CN) are routinely and extensively used as membrane materials. For example, CA membranes are used in gas separation, reverse osmosis (RO), ultrafiltration (UF), and microfiltration (MF) [1–3]; CTA membranes are used in RO and UF [1,2]; and CN membranes are used in MF applications [1]. These membranes are typically made using phase inversion techniques whereby a solution containing the polymer is cast in the desired shape, and phase inversion is effected by incorporation of a nonsolvent, removal of the solvent, or by changing the temperature of the polymer solution. The ability to obtain a moderately viscous homogeneous polymer solution is an important precondition to such membrane formation techniques. CA, CTA, and CN readily dissolve in numerous ketone and ester solvents such as acetone, methyl acetate, and polar aprotic solvents such as dimethyl acetamide (DMAc), n-methyl pyrrolidone (NMP), and dimethyl sulfoxide (DMSO) [4]. As is well recognized, a variety of membrane microstructures can be prepared from these cellulose derivatives.

Unlike cellulose derivatives, the cellulose polymer itself is not viewed as a good membrane material because its unique structure (Figure 1) severely limits the processability of the cellulose polymer. Cellulose is a polysaccharide composed of glucosidic rings linked through oxygen bridges with a repeat unit having three hydroxyl groups and an acetal linkage. Strong hydrogen bonding between the hydroxyl groups make cellulose a highly crystalline, insoluble polymer that degrades before melting [5,6]. Since cellulose is not soluble in common solvents, casting by standard methods is not possible and the relatively low degradation temperature precludes melt processing [6].

From a broader perspective, cellulose is a relatively inexpensive, biodegradable, and sustainable polymer. Hence, there is a strong rationale to use the cellulose polymer itself as a raw material for making porous and dense membranes. Since the early 1990s, new processes based on organic solvents – N-methylmorpholine N-oxide (NMMO) and dimethylacetamide (DMAc)/lithium chloride (LiCl) – and more recently ionic liquids such as 1-butyl-3-methylimidazolium chloride have been explored to produce regenerated cellulose films [7,8]. The use of such solvents for making cellulose films and fibers has several important advantages. Since cellulose dissolution involves purely physical unit operations, no chemical bi-products requiring disposal as waste products are formed. Moreover, the solvents can be recycled completely, which makes the cellulose-dissolution-based processes environmentally friendly. Not surprisingly, the dissolution-based processes are increasingly being adopted to obtain cellulose products. For example, the Lyocell process utilizes the NMMO solvent to obtain regenerated cellulose fibers [9]. The Lyocell process is receiving considerable interest because of its environmentally friendly characteristics, simplicity, and the special properties of the resulting fibers. Compared to viscose fibers, the Lyocell fibers have higher tenacity, higher modulus, lower shrinkage in the dry state, and lower tenacity and modulus reduction in the wet state [10].

While there has been considerable effort in obtaining fibers using cellulose solutions, reports describing the preparation of cellulose films are relatively scarce. Wu and Yuan [6] measured the gas permeability of dry as well as water-swollen cellulose films obtained by precipitating films of NMMO-cellulose solution in a water bath. The water-swollen films showed high CO_2/N_2, CO_2/CH_4, and CO_2/H_2 separation factors. Zhang and coworkers [11] measured the permeation of bovine serum albumin (BSA) through cellulose membranes prepared by coagulating films of NMMO-cellulose solution in aqueous NMMO-water baths. The scanning electron micrographs

(SEMs) as well as pore size calculations indicate either dense films or films possessing extremely small pores (pore size ~ 15-40 nm). The researchers determined that BSA permeability decreased and BSA rejection increased with increasing solution cellulose concentration. Abe and Mochizuki [12] investigated the water permeation and sieving of dextran in flat hemodialysis membranes prepared from films of NMMO-cellulose solution coagulated in NMMO-water baths. While no morphological characteristics of the membranes were reported, our experience suggests that their casting protocols generated dense cellulose films. The authors indicate that water permeation increased with temperature and decreased with increasing cellulose concentration in the solution. In addition, they determined that the sieving coefficient (SC) for dextran (defined as the ratio of dextran concentration in the permeate to that in the feed solution) decreased with increasing temperature. However, the SC decrease was much less for smaller cellulose concentrations in the solution.

In contrast to the use of NMMO as a solvent, Zhou and Zhang [11] utilized an aqueous solution of urea and sodium hydroxide (NaOH) for dissolving regenerated cellulose. They prepared cellulose solutions by dissolving approximately 4.3 wt% cellulose polymer in a 6 wt% NaOH/4 wt% urea solution. Phase inversion was achieved by using aqueous H_2SO_4 solutions of varying concentrations as the coagulation bath. SEM analysis indicated that the films had an isotropic structure with very small pores (< 1μm).

This literature review indicates that research has focused on dense films or films with very small pore sizes. Even for the dense films, the information available in the open literature is rather meager compared to that for cellulose derivatives such as CA. If native cellulose is to be treated as a more common starting material for membrane formation, then protocols and methods to obtain porous cellulose films of specified pore size, porosity, and morphology need to be

established. Clearly, the cellulose membrane morphologies reported to date do not seem suitable for NF, UF or MF separations.

In this work we have focused our attention on fabrication of porous cellulose films with morphologies suitable for NF/UF applications. By a judicious selection of solvents, casting conditions, solution composition, and solvent exchange steps, we have successfully cast dense as well as skinned asymmetric porous cellulose films. In this paper, we present details of the casting process and the resulting film characteristics including mechanical properties, N_2 permeability, and pore size/porosity.

Materials and Methods

Materials and casing solution preparation

All membranes were prepared from a hardwood acetate grade dissolving cellulose supplied by Rayonier Performance Fibers, Inc in the form of flat sheets. After vacuum drying at 80°C, small pieces (~ 1 mm × 3 mm) cut from the sheets were used to prepare the cellulose solution. Solid NMMO (97%) obtained from Sigma-Aldrich was used as the starting material for preparation of the cellulose solvent. Since NMMO is hygroscopic and forms a stable complex with water, it was stored in a desiccator in a refrigerator. Whenever the NMMO bottle was opened, the space within the bottle was purged with dry N_2 prior to closing. DMSO (analytical grade, Fisher) was the cosolvent, and was used as received; deionized (DI) water was used as a cosolvent for the NMMO. The polymer content (x) was varied in the range 4–12 wt%, and the casting solution composition was x wt% cellulose, 45 wt% NMMO, (100-x) wt% DMSO, and 5 wt% water. The water content of 5 wt% in the casting solution was chosen empirically, recognizing the fact that NMMO-water complexes (water:NMMO molecular ratio < 1) are direct solvents for cellulose [13].

A clear homogeneous cellulose solution was obtained by adding the above components to a glass conical flask, and heating the flask in a silicone oil bath at 135°C under constant stirring for 20 min. At such a high temperature, degradation reactions occur that form several byproducts that, in turn, can provoke severe effects such as the degradation of cellulose, and accelerated decomposition of NMMO [13]. To prevent these side reactions and to stabilize NMMO, a small quantity of propyl gallate (PG, Sigma-Aldrich, 97%, 0.005g/g of cellulose) was added to the cellulose solution. Water evaporation from the casting solution during heating can change the composition of the casting solution and seemed to adversely affect film morphology. Hence, evaporation of water was limited by piercing a Pasteur pipette through the septum that sealed the conical flask; the evaporated water condensed in the pipette and dripped back into the casting solution.

Dense Film casting

To obtain dense cellulose films, the cellulose solution was poured on a clean glass plate between 200-μm steel shims, and a film was cast using a casting knife. The glass plate was then immersed in a DI water bath. Generally, the cellulose films peeled off the glass plate within 5 minutes of immersion. The films were washed by successively transferring them to two additional water baths for 30 minutes each, and finally stored in a third water bath overnight. The dense films so obtained were significantly swollen with water, and underwent significant shrinking and deformation upon drying. The dried films were extremely brittle, greatly distorted, and unsuitable for analytical testing. The shrinkage-induced deformation was prevented/minimized by using two different drying protocols:

(1) After cutting off all the edges, the films were placed on glass plates and exposed to ambient conditions. Since the films adhered to glass strongly, they retained their flat shape even after

the water had evaporated. When the corners started peeling, the glass plates were immersed in a water bath, and the films peeled-off. These films were placed on paper towels, and after wiping off the excess water, kept in a vacuum oven at room temperature for 24 hr. The residual stresses were relieved by placing the films in a vacuum oven at 110°C for 24 hr. The dry film thickness was 14 ± 0.5 μm.

(2) The films were transferred and stored in an isopropyl alcohol (IPA) bath for 24 hr. Subsequently, slow drying was conducted by placing the films in a 1 mm gap between two glass plates and keeping them in a vacuum oven for 48 hours at room temperature. Again the residual stresses were relieved by keeping the films in the vacuum oven at 110°C for 24 hours. The dry film thickness was 14 ± 0.5 μm.

Porous Film Casting

To obtain porous films, the glass plate was immersed in an acetone bath. Acetone is a nonsolvent for cellulose, and the ensuing mass transfer involving acetone, NMMO, DMSO, and water led to the formation of porous films. Due to the high surface energy of water, the pores invariably collapsed when the films were simply air-dried. In order to preserve the morphology, solvent exchange steps were incorporated into the protocol. After immersing the films in acetone for 20 minutes, the films were placed in an isopropyl alcohol bath for 20 minutes. Subsequently, they were stored in a heptane bath for 24 hours. The films were then dried by placing them on glass plates and exposing to dry ambient conditions. In order to ensure complete removal of residual solvent, the films were finally stored in a vacuum oven at 80°C.

Cellulose Film Characterization

SEM analysis (Aspex Instruments, Tungsten filament with a 15 keV beam energy), tensile testing (Instron 8500 with a 5000 N load cell), and N_2 permeability measurements were utilized

to characterize the dense films. Cross sections of the dense films for SEM analysis were obtained by standard freeze-fracturing. For tensile testing, small strips (50 mm × 3 mm) of the dense films were attached to a specially designed fixture and extended under a constant rate of 0.1 mm/sec. The force-elongation data were converted to corresponding engineering stress-strain values using the initial specimen dimensions, and the tensile modulus, failure stress, and failure strain were determined. N_2 permeability was obtained via the permeate pressure-rise technique. Small circular samples (diameter 25 mm) were placed in a permeation cell that was pressurized to 552 kPa (80 psi), and the rise in permeate pressure with time was recorded.

The effect of the polymer concentration on the porous film morphology was studied by casting porous films from 4, 7, and 11 wt% cellulose in the casting solution. The morphology was characterized in terms of the skin layer thickness, pore-size distribution, and total porosity. Commercial image analysis software (Sigmascan) was used to obtain these three parameters from SEM micrographs of the film cross sections.

Results and Discussion

Dense film studies

Microscopy

The dense films obtained by the aforementioned procedure were transparent and had a thickness of 14 ± 0.3 μm. Figure 2 shows SEM micrographs of typical dense film cross sections. The micrographs indicate the expected unremarkable film structure with no pores apparent within the resolution limit of the SEM (~ 0.1 μm). However, the films might still possess small pores of the order of a few nanometers. No evidence of significant differences in microstructure or thickness was obtained among the dense films obtained via the two drying protocols. We

obtained good control over the final thickness of the films, which could be easily varied by using shims of different dimensions.

Mechanical property measurements

The tensile properties of the dense films were measured using a mechanical test system in order to ascertain the processability of the films in conventional fabrication equipment. For comparison, CA films fabricated in our laboratory via dry casting from a binary 15/85 wt% CA/Acetone solution were also tested. The measurements were conducted on 14 samples of cellulose films dried via protocol 1, four samples of cellulose films dried via protocol 2, and 10 CA film specimens. Table 1 summarizes the mechanical properties obtained including the tensile modulus (E) and the stress (σ_f) and strain (ε_f) at failure. The cellulose films dried via protocol 2, *i.e.*, initial immersion in an IPA bath followed by slow drying between two glass plates, evidenced higher ductility than those dried via protocol 1. Since the films had been thoroughly dried to remove all of the volatile IPA, it is unlikely that residual solvent plasticized the films. We believe that the higher ductility of these films is caused by IPA conditioning. Since cellulose-water interactions are stronger than cellulose-IPA interactions (as reflected in the liquid retention values [5]), differences in the drying process likely produce differences in the inter- and intramolecular hydrogen bonding patterns for the cellulose hydroxyl group. A lower degree of intermolecular hydrogen bonding between the cellulose chains for the IPA-dried films could account for the higher ductility.

In general, the only significant difference in mechanical response of the specimens was the more brittle nature of cellulose as compared to the CA films. This is expected, since cellulose films will have a significant degree of crystallinity, while CA has only limited crystallinity. The failure strain values in the range 5–10% agree with those reported in the literature for

regenerated cellulose fibers [5]. The larger variability in the failure strain of the cellulose films appears to be caused by residual non-uniformity in the cellulose film samples. Despite the rigorous drying protocols employed, some of the films still contained small folds and creases. We observed that the more uniform cellulose samples evidenced somewhat greater failure stress and smaller failure strain values. Nonetheless, the mechanical property values obtained suggest that the dry cellulose films compare favorably to the CA films, and most likely possess sufficient mechanical integrity to enable processing on conventional fabrication equipment after casting and drying.

Gas permeability measurements

Prior to conducting nitrogen permeability measurements, the cellulose dense films were placed in the permeation cell and both sides of the films were exposed to nitrogen pressurized to 552 kPa (80 psi) for 12 hours. Permeability testing was initiated after the films had been equilibriated with nitrogen in this fashion. Multiple permeability measurements were performed on each cellulose film sample, since the film permeability was found to decrease with each progressive measurement. This suggests collapse of nanopores or the presence of residual solvent. Typical permeability values obtained on a single cellulose film are shown in Figure 4. Whereas the initial values were high, film permeability seemed to attain a constant value after six consecutive runs. Consequently, 10 successive measurements were conducted on each cellulose film sample. Figure 5 shows the consolidated nitrogen permeability data obtained from three films dried via protocol 1 and protocol 2, respectively, as well as three CA films. The data indicate that the film permeability depends upon the drying protocol. Films that were immersed in isopropyl alcohol prior to slow drying evidenced lower permeability values than the films that

were simply air-dried (protocol 1). The relatively modest difference may reflect small differences in the nanostructure or in the degree of crystallinity.

Porous film studies

Effect of the presence of water on film morphology

Subtle variations in the composition of the ternary cellulose solvent system can have a significant effect on the morphology of the resulting cellulose films. Figure 6a shows the structure of a porous film that was cast from a cellulose solution in which the evaporated water was not recycled, *i.e.* returned to the solution. These films had a dense structure with small pores, in which the larger pores likely have collapsed. In contrast, when the evaporated water was returned to the casting solution, the films (Figure 6b) had a well-defined pore structure. While the exact mechanism for this behavior is unclear, we believe that the pore collapse is related to the kinetics of the phase inversion process. The solutions with slightly lower water content are in a "poorer" solvent for the cellulose polymer and thus precipitate more rapidly when immersed in the non-solvent bath. Pore collapse is generally associated with rapid phase inversion during the coagulation step [15-17], whereas slow mass transfer in the solutions with high water content leads to the formation of a more spongy porous structure (Figure 6b).

Effect of cellulose concentration on film morphology

Having established the importance of controlling the water concentration in the cellulose solvent system to prevent pore collapse, we cast several porous films using water recycle during cellulose dissolution and studied the influence of cellulose solution concentration on the porous film morphology. As expected, the pore size as well as the porosity decreased with an increase in the casting solution cellulose concentration (Figures 7 and 8). The lowest cellulose concentration of 4 wt% yielded films with large pores having a mean diameter of 4.8 μm. The pore diameter

monotonically decreased to 2.9 μm and 1.8 μm when the cellulose concentration was increased to 7 wt% and 10 wt%, respectively. Figure 9 shows the pore-size distribution obtained from image analysis of multiple films at each cellulose concentration. The distribution was wide at a 4 wt% cellulose concentration due to the presence of large pores with diameters greater than 10 μm. The distribution progressively became narrower with increasing cellulose concentration, indicating much smaller differences in the pore sizes. The similarity of the pore-size distributions of multiple samples at the same solution cellulose concentration indicates the reproducibility of the porous film formation protocols. Thus, films with a mean pore diameter in the range 1.8–4.8 μm can be produced by simply using a solution with the appropriate cellulose concentration.

Figure 10 shows the morphology of films made from the three cellulose solution concentrations. The cross-section micrographs (Figures 10b, 10e, 10h) reveal that the porous films possess a skinned asymmetric structure, with small pores immediately beneath the skin, and pore size increasing away from the skin. Even though all of the films possessed a skin, the top surface of films made from 4 wt% cellulose concentration evidenced isolated small pores, probably formed because the thin skin layer is not strong enough to withstand the large interfacial stresses created during skin formation.

Conclusions

The availability of new solvents such as NMMO, DMAc/LiCl, and 1-butyl-3-methylimidazolium chloride provides potential new routes for the synthesis of membranes directly from unmodified cellulose polymer. By using a judicious selection of solvents, cosolvents, non-solvents and casting solution composition we were able to reproducibly cast dense films as well as porous cellulose films with mean pore diameters in the range 1.8–4.8 μm. Compared to dense CA films, the dense cellulose films were somewhat more brittle with similar

N_2 permeability values. Interestingly, the mechanical behavior depended upon the drying protocol employed, with films undergoing an IPA exchange step evidencing a slightly more ductile response. This dependence is most likely due to changes occurring in the hydrogen bonding at the intra- and inter-molecular level during the drying process.

Subtle changes in the composition of the ternary cellulose solvent system significantly affected the porous structure. Porous films with a skinned asymmetric structure, and anisotropic porosity, i.e., small pores beneath the top skin and pore size increasing away from the skin, could easily be obtained. The mean pore size of these films can be altered by appropriate variation in the cellulose concentration of the casting solution.

Although the porous morphologies obtained would be suitable for ultrafiltration applications, some significant limitations for water-based uses exist since cellulose swells significantly in the presence of water and is especially susceptible to biological fouling. However, given the advantages of low cost and an environmentally friendly material, porous cellulose films might well find a niche in non-aqueous separation applications.

Acknowledgements

The authors gratefully acknowledge support of this research by the US Department of Energy through award DE-FC01G011084 and the technical support provided by the NSF Industry/University Cooperative Research Center for Membrane Applied Science and Technology (MAST) at the University of Colorado.

References

[1] Lloyd, D.R.; Meluch, T.B. In Materials science of synthetic membranes, D.R. Lloyd, Ed.; ACS Symposium Series, 269, 1985.

[2] Cardew, P.T.; Le, M.S. Membrane processes: A technology guide; The Royal Society of Chemistry: Cambridge, 1998.

[3] Koros, W.J.; Fleming, G.K. J Membrane Sci 1993, 83, 1.

[4] Baker, R.W. Membrane technology and applications, 2nd ed.; John Wiley: West Sussex, UK, 2004.

[5] Klemm, D.; Philipp, B.; Heinze, T.; Heinze, U.; Wagenknecht, W. Comprehensive cellulose chemistry, Vol 1. Fundamentals and analytical methods; Wiley VCH: Germany, 1998.

[6] Wu, J.; Yuan, Q. J Membrane Sci 2002, 204, 185.

[7] Fink, H.P.; Weigel, P.; Purz, H.P.; Ganster, J. Prog Polym Sci 2001, 26, 1473.

[8] Swatloski, R.P.; Spear, S.K.; Holbrey, J.D.; Rogers, R.D. JACS 2002, 124, 4974.

[9] Liu, R.; Shen, Y.; Shao, H.; Wu, C.; Hu, X. Cellulose 2001, 8, 13.

[10] Peng, S.; Shao, H.; Hu, Z. J Appl Polym Sci 2003, 90, 1941.

[11] Zhang, Y.; Shao, H.; Wu, C.; Hu, Z. Macromol Biosci 2001, 1, 141.

[12] Zhou, J.; Zhang, L.; Shu, H.; Chen, F. J Macromol Sci – Physics 2001, B41, 1.

[13] Biganska, O.; Navard, P. Polymer 2003, 44, 1035.

[14] Rosenau, T.; Potthast, A.; Adorjan, I.; Hofinger, A.; Sixta, H.; Firgo, H.; Kosma, P. Cellulose 2002, 9, 283.

[15] Machado, P.S.T.; Habert, A.C.; Borges, C.P. J Membrane Sci 1999, 155, 171.

[16] Kang, Y.S.; Kim, H.J.; Kim, U.Y. J Membrane Sci 1991, 60, 219.

[17] Vandenburg, G.B.; Smolders, C.A. J. Membrane Sci 1992, 73, 103.

Table 1: Mechanical Properties of Porous Cellulose and CA Films.

Polymer	Tensile Modulus (GPa)	Failure Stress (MPa)	Failure Strain (%)
Cellulose	1.6 ± 0.6	64.9 ± 18.3	6.5 ± 1.5
CA	2.0 ± 0.6	60.1 ± 11.6	13.1 ± 8.0

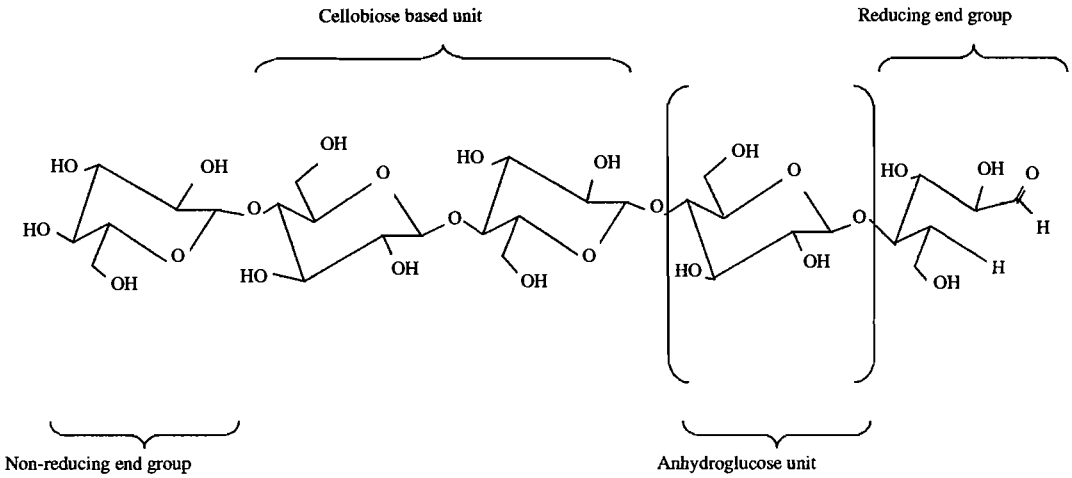

Figure 1: Molecular structure of cellulose. Cellulose is a linear syndiotactic homopolymer composed of D-anhydroglucopyranose units (AGU) linked together by β-(1→4)-glycosidic bonds. If the dimer cellobiose is considered as the basic unit, then cellulose can be considered as an isotactic polymer of cellobiose.

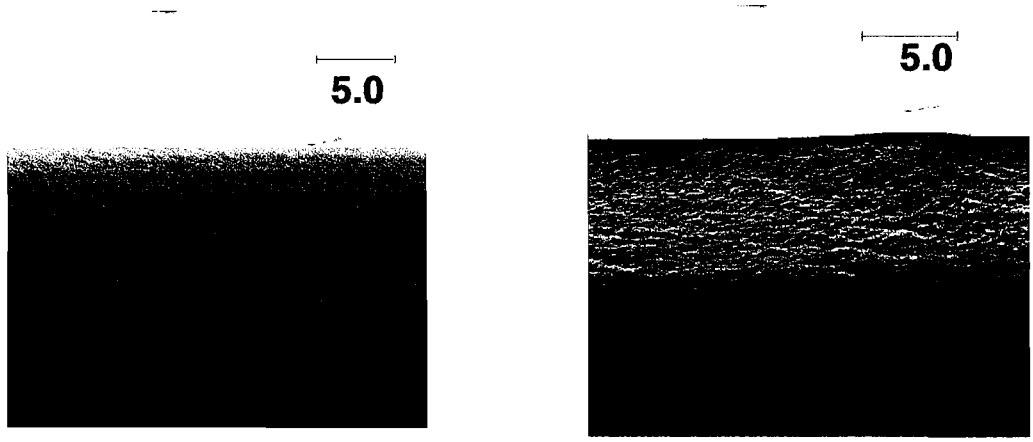

(a) (b)

Figure 2: SEM micrographs of the cross-sections of two identical dense films obtained using a 4 wt% cellulose solution concentration and the following drying protocols: slow constrained air-drying (a) and IPA exchange followed by slow air-drying (b). Films of thickness 14 ± 0.3 μm could be reproducibly obtained, and no pores could be observed in the cross section within the resolution limit of the SEM (~ 0.1 μm). However, nitrogen permeation measurements suggested that the films might contain smaller pores, i.e., on the order of a few nanometers.

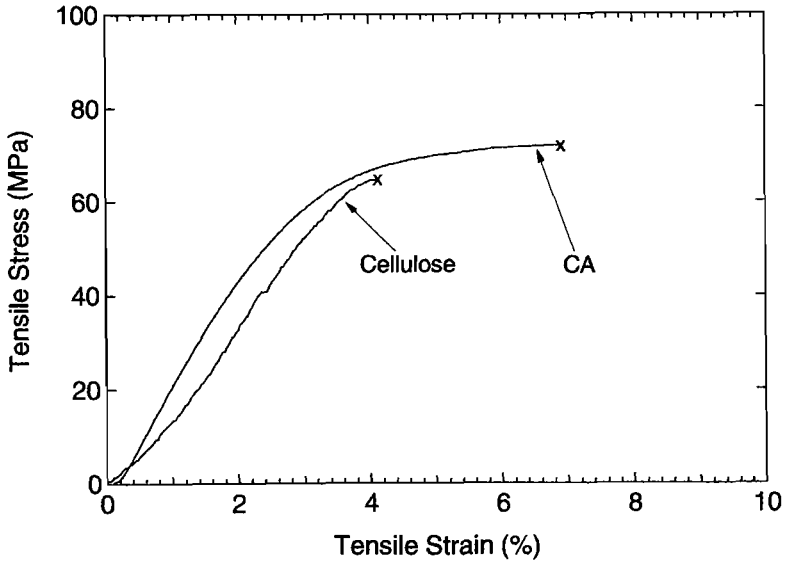

Figure 3: Representative stress-strain responses of a cellulose and CA film: X indicates failure.

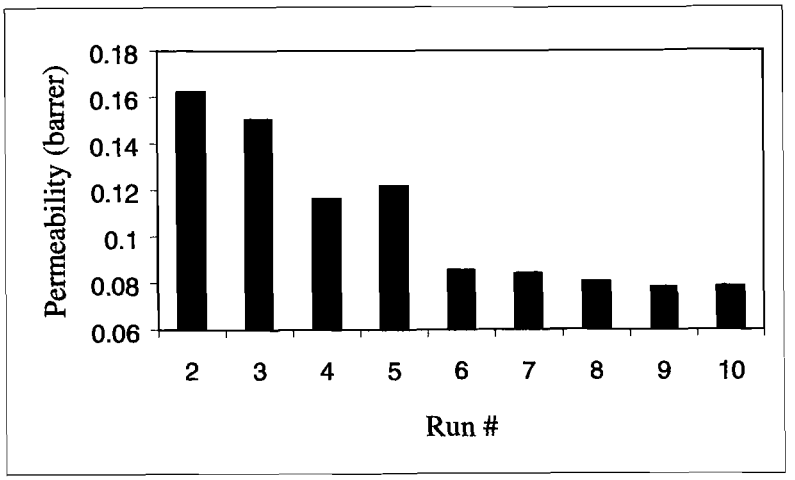

Figure 4: Results of permeability measurements conducted on a single cellulose film sample. Successive measurements yielded progressively decreasing permeability values. However, film permeability attained a relative constant value after six successive runs. Consequently, 10 runs were conducted on each sample, and the mean of the final four runs was taken as the sample permeability.

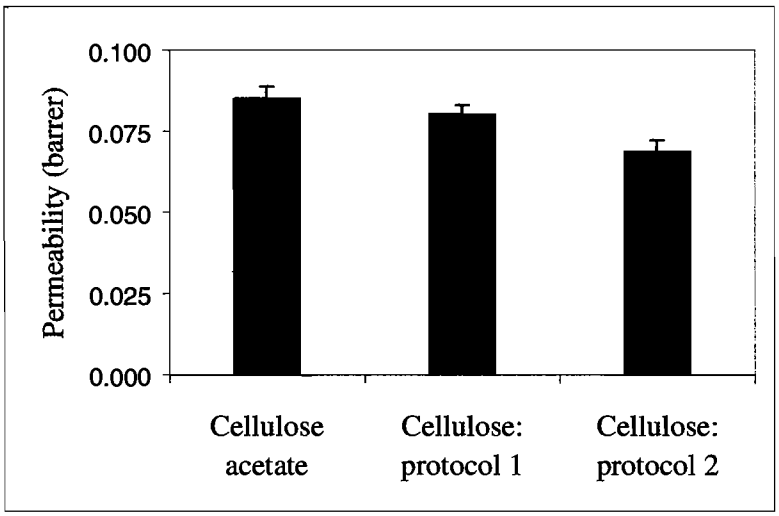

Figure 5: Consolidated nitrogen permeability data obtained from three samples each of cellulose films dried via protocols 1 and 2, as well as CA dense films. Cellulose films dried via protocol 2 (isopropyl alcohol immersion prior to slow drying) evidence the lowest permeability values.

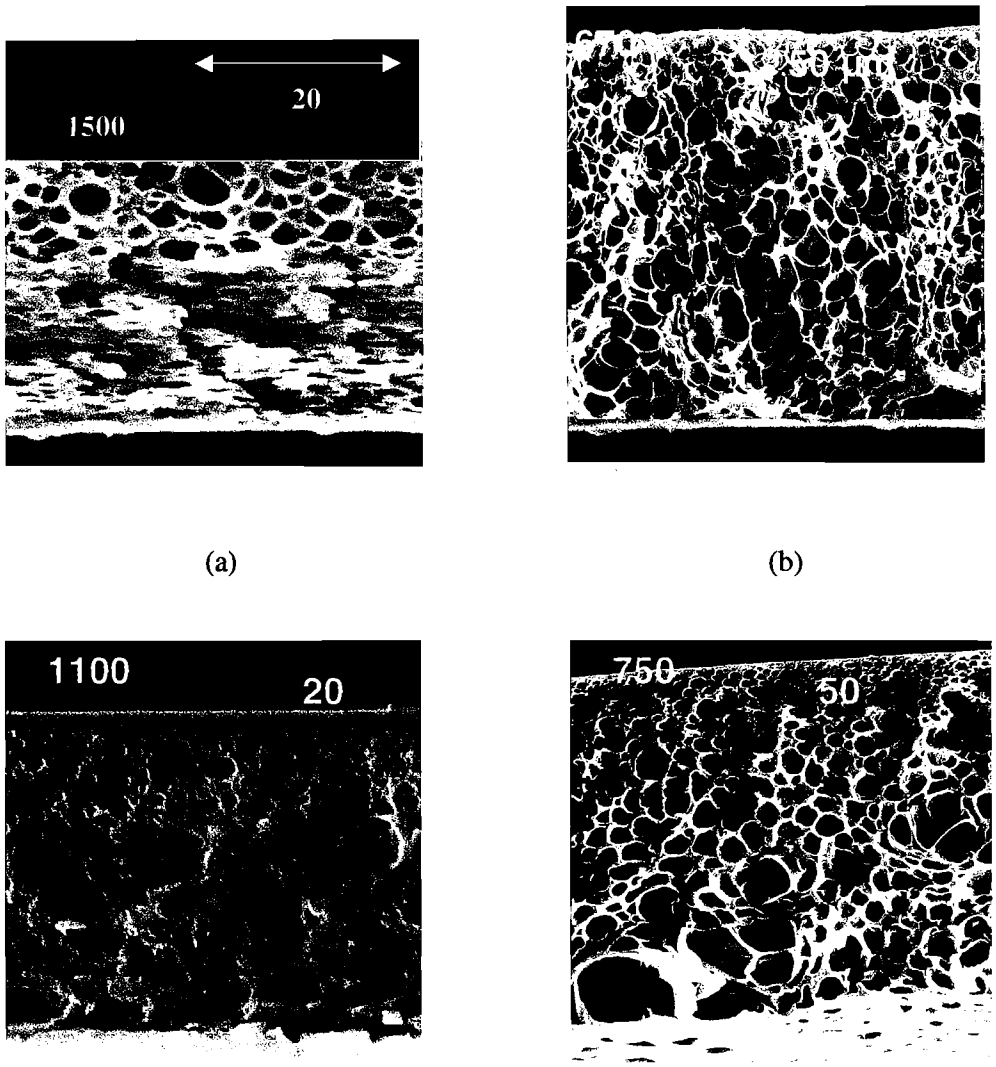

Figure 6: SEM micrographs of porous film cross-sections with (a and c) and without (b and d) water recycle during dissolution. For the films in (a) and (b), the solution contained 7 wt% cellulose, while for (c) and (d), the solution contained 10 wt% cellulose. The morphologies shown in (a) and (c) indicate that the loss of water via evaporation leads to pore collapse during drying.

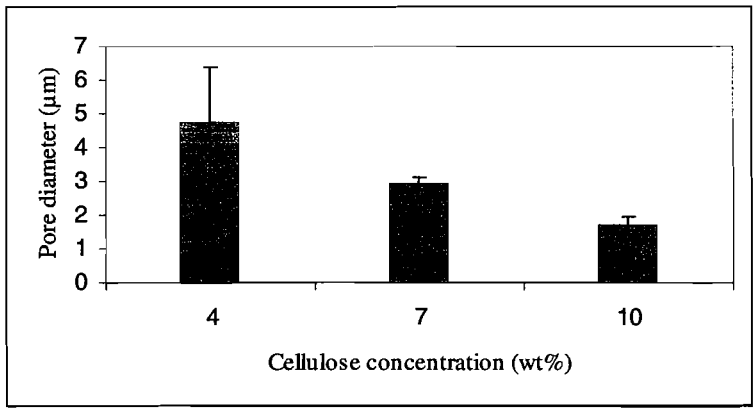

Figure 7: Influence of the cellulose concentration in the solution on the mean pore diameter.

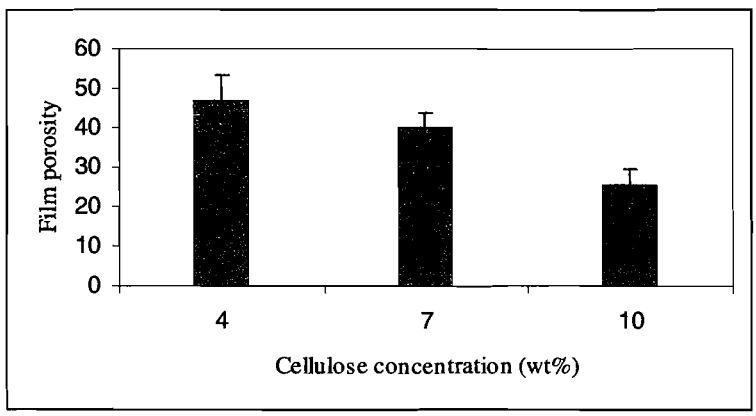

Figure 8: Influence of the cellulose solution concentration on film porosity.

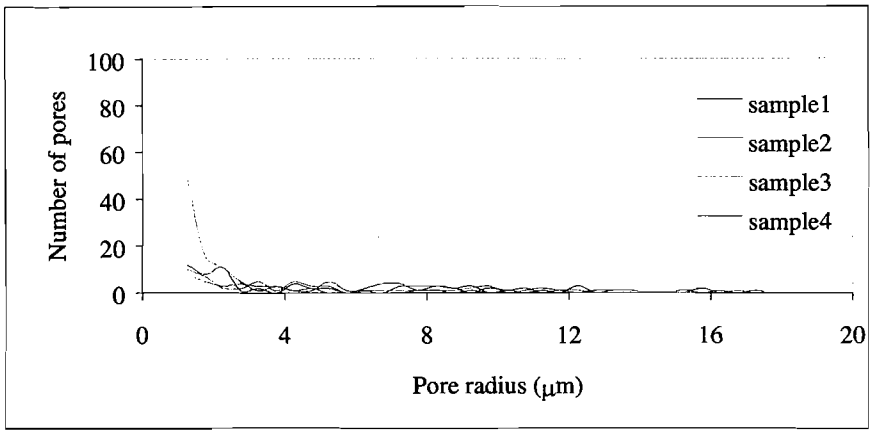

(a)

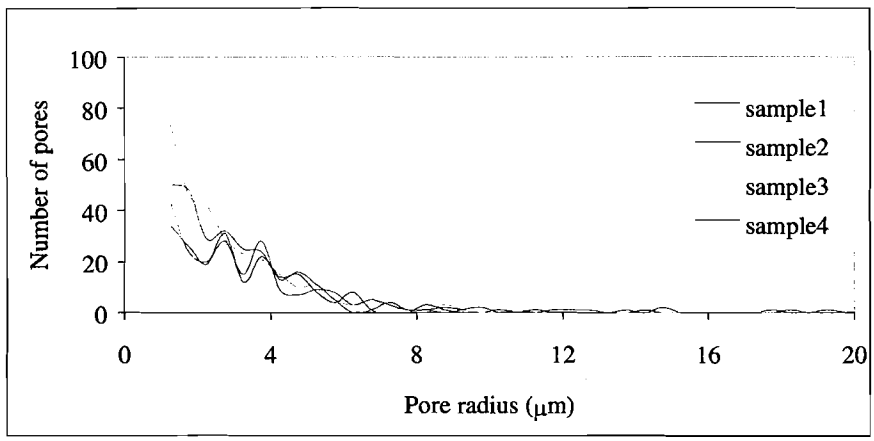

(b)

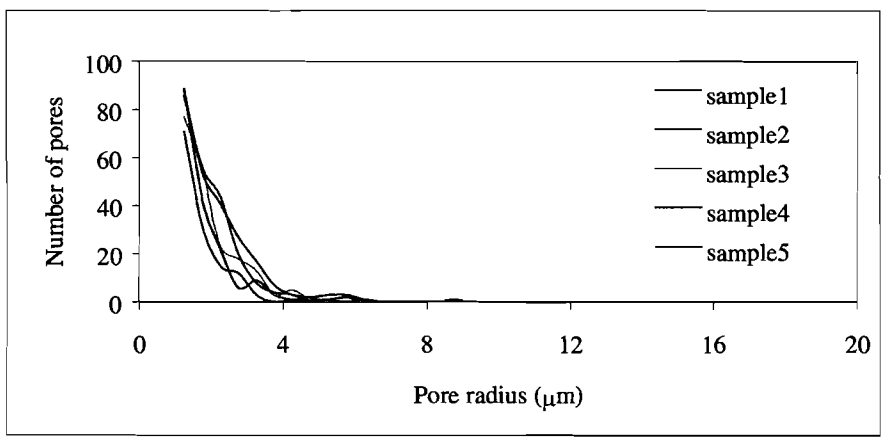

(c)

Figure 9: Pore-size distribution graphs for porous films made from 4 wt% (a), 7 wt% (b), and 10 wt% (c) cellulose concentrations. The figures show a systematic decrease in the pore size with an increase in the cellulose concentration in the solution. At each

concentration, tests were conducted on multiple films so that the reproducibility of the porous film formation protocol could be established.

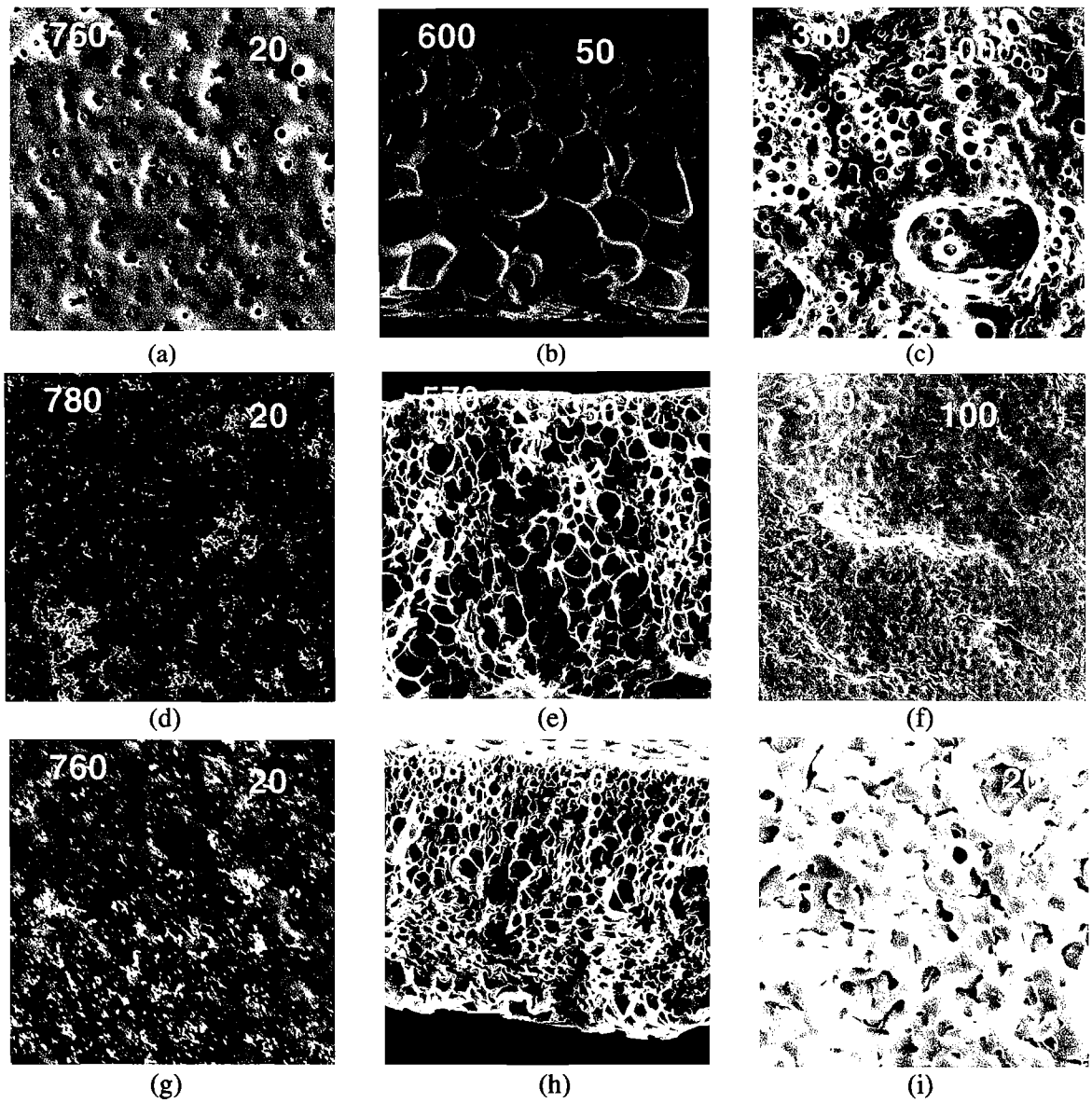

Figure 10:SEM micrographs showing the morphology of cellulose films prepared from solutions with different cellulose concentrations. Figures (a), (d), and (g) correspond to the top surface of films cast using 4, 7, and 10 wt% cellulose in the solution, respectively. Likewise, figures (b), (e), and (h) correspond to the cross-section, and figures (c), (f), and (i) correspond to the bottom surface at the three cellulose concentrations. The skin at the top surface is non-porous, and the micrographs indicate the precipitation of some polymer at the higher (7 and 10 wt%) cellulose concentration. The cross sections reveal a skinned asymmetric structure.

Journal of The Electrochemical Society, **152** (3) 1-0 (2005)
0013-4651/2005/152(3)/1/5/$7.00 © The Electrochemical Society, Inc.

Performance of a Porous Electrolyte in Single-Chamber SOFCs

Toshio Suzuki,*z Piotr Jasinski,* Vladimir Petrovsky, Harlan U. Anderson,* and Fatih Dogan

Electronic Materials Applied Research Center and Department of Materials Science and Engineering, University of Missouri-Rolla, Rolla, Missouri 65401, USA

A cell which consists of a porous 18 μm thick Y-doped ZrO_2 (YSZ) electrolyte (23 ± 3 vol % open porosity) on a NiO-YSZ anode substrate and a cathode using $(La, Sr)(Co, Fe)O_3$ has been investigated in the single-chamber configuration. The cell performance and catalytic activity of the anode was measured in a flowing air-methane gas mixture with various flow rates. The results showed that the open-circuit voltage and the power density increased as the gas flow rate increased. The cell generated an open-circuit voltage of about 0.78 V, which was only about 0.1 V lower than that observed with dense electrolyte specimens. A maximum power density of 660 mW cm^{-2} (0.44 V) was obtained at set temperature = 606°C (cell temperature = 744°C) in the flow rate of 900 cm^3 min^{-1}, where the current efficiency was about 5% determined from fuel consumption.

Manuscript submitted June 25, 2004; revised manuscript received August 23, 2004.

A single-chamber solid oxide fuel cell (SC-SOFC),[1-3] which is operated using a mixture of fuel and oxidant gas, provides several advantages over the conventional double-chamber SOFC, such as simplified cell structure (no sealing required) and direct use of hydrocarbon fuel. In addition, the SC-SOFC is not affected by the problems associated with carbon deposition, which is a significant drawback for double-chamber SOFCs when Ni-cermet is used as anode material.[4] Several studies reported a promising performance of SC-SOFCs using a mixture of air and hydrocarbon fuel. A typical SC-SOFC consists of Sm-doped ceria (SDC) as electrolyte, Ni-SDC cermet as anode, and $(Sm, Sr)CoO_3$ as cathode as well as several other electrode materials.[5,6] So far, using a Pd-Ni-cermet anode, a power density of 644 mW cm^{-2} has been obtained with the methane-air mixture at 550°C operating temperature.[7]

The oxygen activity at the electrodes in SC-SOFCs is not fixed and one electrode has a higher electrocatalytic activity for the oxidation of the fuel than the other. Typical oxidation reactions using methane are

$$CH_4 + 1/2\ O_2 \rightarrow CO + 2H_2 \quad [1]$$

$$H_2 + O^{2-} \rightarrow H_2O + 2e^- \quad [2]$$

$$CO + O^{2-} \rightarrow CO_2 + 2e^- \quad [3]$$

The other electrode has a higher electrocatalytic activity for the reduction of oxygen according to the following reaction

$$1/2\ O_2 + 2e^- \rightarrow O^{2-} \quad [4]$$

As a result, an electromotive force (emf) between two electrodes is generated even in a uniform gas composition. Because the oxygen activity difference occurs only in the region of electrodes, it may allow the oxygen potential to be maintained between electrodes without requiring gas tightness in the electrolyte. This fact allows using simple and conventional processing methods to prepare the electrolyte with relatively lower temperatures. For example, screen-printing can be utilized to prepare thin electrolyte on the substrates (anode), because it is not necessary to obtain a dense electrolyte when it is used in the SC configuration.

In this study, a cell with a porous electrolyte was examined in an air-fuel mixture. The cell consists of a yttria-doped ZrO_2 (YSZ) porous electrolyte on a NiO-YSZ anode substrate and a $(La, Sr)(Co, Fe)O_3$ cathode. The catalytic activity of anode was also investigated by measuring fuel conversion rate (conversion rate of Eq. 1) of the anode. From the results of catalytic activity and SC-SOFC measurements, fuel utilization of the current fuel cell design is discussed.

Experimental

Commercially available Y-doped ZrO_2 (YSZ, 16% Y-doped ZrO_2, Daiichiki Genso Co., Japan) powder was used to prepare porous electrolyte by screen printing YSZ ink onto a 0.7 mm thick NiO-YSZ (NiO/YSZ = 80/20 weight ratio) anode substrate and sintered at 1300°C for 1 h. The thickness of the electrolyte was about 18 μm with the relative density of 66 ± 3% (open porosity ~23 ± 3 vol % and close porosity ~10%). The cell was completed by screen-printing $La_{0.8}Sr_{0.2}Co_{0.2}Fe_{0.8}O_3$ (LSCF; SSI Technologies, Inc., Janesville, WI) ink as cathode material onto the electrolyte followed by annealing at 1000°C for 1 h. Typical size of the cell tested in this study was 0.48 cm^2 for the anode substrate with an electrolyte and 0.18 cm^2 for the cathode, respectively. The microstructural development of the materials was observed by scanning electron microscopy (SEM; Hitachi S4700).

Figure 1 shows the experimental setup for this study. The properties of the cells were measured using a tube furnace in which a mixed gas flowed consisting of methane (17 vol %) and air (83 vol %), avoiding the explosion limits of the gas mixture (5-15 vol % of methane in air). The fuel and air was premixed before entering the furnace. The fuel:oxygen ratio of the gas mixture was 1:1, which was oxidant rich according to Eq. 1 (fuel-oxygen ratio, 1:0.5). Using the oxidant-rich gas mixture prevents possible carbon deposition on the electrodes. Note that the reaction in Eq. 1 is a heterogeneous reaction occurring on the surface of catalytic materials. Therefore, the optimum fuel-to-oxygen ratio could vary depending upon the type of catalyst and experimental conditions. The furnace temperature was set at 556-606°C in the absence of the gas flow while the cell temperature was simultaneously monitored using a thermocouple attached to the cell. The flow rate of the mixed gas was controlled with gas flow controllers in a range of 300-900 cm^3 min^{-1}. Pt and Au mesh were used as current collectors for the anode and cathode, respectively, with size similar to the cathode electrode area of 0.18 cm^2. Ag paste was used to improve the contact between the mesh current collector and cathode. The cell performance was investigated by impedance spectroscopy using a Solartron 1470 Battery Tester and a 1255B Impedance Gain Phase Analyzer. The data for impedance spectra were collected at a current of 1 mA. Current and power density were calculated using the area of the cathode. The effect of electrode area difference on the performance of the cell was studied previously,[8] and the area ratio used in this study should not bring significant error to the estimation of the current and power density.

Methane reaction rates were studied using a Dycor Dymaxion quadrupole mass spectrometer and software (Dycor system 2000) by

* Electrochemical Society Active Member.
z E-mail: toshio@umr.edu

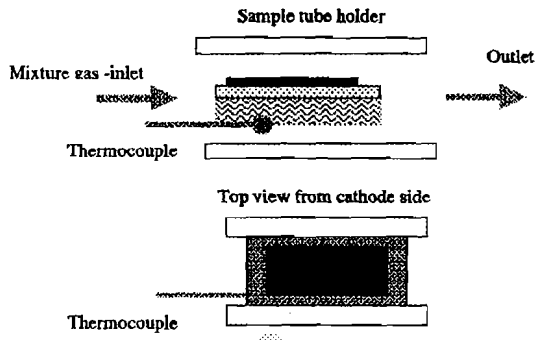

Figure 1. Sample configuration for SC-SOFC measurement.

measuring the inlet and outlet gas composition (Fig. 1). The ratio of inlet and outlet fuel concentration gives the conversion rate (r_c) of methane as follows

$$r_c(\%) = \frac{C_i - C_o}{C_i} \times 100 \quad [5]$$

where C_o (vol %) and C_i (vol %) are outlet and inlet fuel volume fraction in the mixture, respectively. The reaction rate (r) can be obtained by the following expression

$$r\ (\mathrm{cm^3\ min^{-1}}) = fC_i r_c/10^4 \quad [6]$$

where f is the gas flow rate ($\mathrm{cm^3\ min^{-1}}$) of air-fuel mixture. Typically, the reaction rate follows the Arrhenius relation

$$r = A \exp\left(-\frac{E_a}{kT}\right) \quad [7]$$

where A, E_a, k, and T are temperature-independent constant, activation energy for this reaction, Boltzmann's constant, and temperature in Kelvin, respectively. Note that the catalytic activity of materials can also be influenced by the surface area, microstructure, and the composition of catalytic materials (*i.e.*, Ni content in anode).

Results

Due to the electrode reactions, expressed by Eq. 1-3, the cell temperature is higher than the furnace set temperature during operation of the fuel cell. The cell temperatures were measured using a thermocouple directly attached to the cell, as shown in Fig. 2. By varying the gas flow rates the cell temperatures changed simultaneously, so that the performance of the cell can be controlled to a certain extent by adjusting the flow rate of reactant gases.

Figure 3 shows the fracture surface of YSZ porous electrolyte. It shows that the particles of YSZ are well connected and form open channels in the electrolyte, which allow gas permeation through the electrolyte.

Open-circuit voltages (OCVs) of the fuel cell with the porous electrolyte are shown in Fig. 4, along with the results of a dense YSZ electrolyte using the same anode and cathode materials.[8] The results showed that the OCV attained by the porous electrolyte cell, 0.68-0.78 V, was affected by the gas flow rate. Under the same conditions the cell with a dense YSZ showed an OCV of >0.8 V. The difference is probably due to the permeability of porous electrolyte by H_2 and/or CO may diffuse from anode to cathode through the porous electrolyte so that oxygen can be consumed at the cathode side and lower the oxygen partial pressure, which leads to a decrease in the OCV. This explanation is supported by the fact that the OCV increases with increasing gas flow rate, which gives rise to faster gas diffusion. These results indicate that a porous electrolyte can provide a sufficient barrier to separate the oxygen activities at the electrodes by optimizing the gas flow rate.

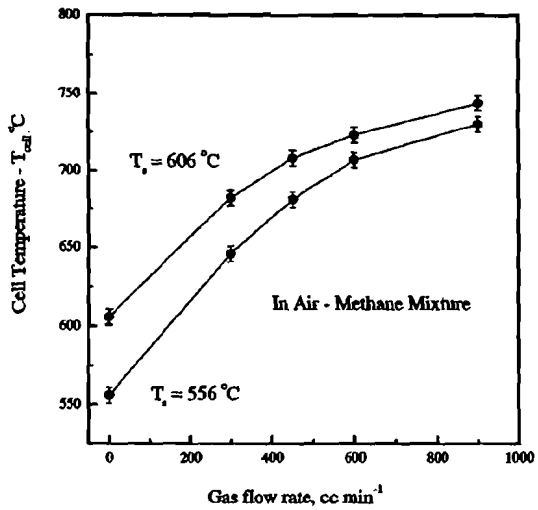

Figure 2. Cell temperatures as a function of gas flow rate with different set temperatures.

Figure 5a and b shows the discharge profile of a cell with different gas flow rates, heated to 556 and 606°C (furnace set temperature), respectively. The performance of the cell strongly depends upon the gas flow rate, mainly due to increased cell temperature. A maximum power density of about 660 mW $\mathrm{cm^{-2}}$ (0.44 V) was obtained at a cell temperature of 744°C (set temperature 606°C), and a power density of 560 mW $\mathrm{cm^{-2}}$ (0.44 V) was obtained at 730°C cell temperature (set temperature 556°C) both at the gas flow rate of 900 $\mathrm{cm^3\ min^{-1}}$. Note that a drop in cell performance was observed with decreasing cell temperature at gas flow rates above 900 $\mathrm{cm^3\ min^{-1}}$.

Impedance spectra for the porous electrolyte SC-SOFC in Fig. 6 show relatively large electrode overpotentials due to gas diffusion and charge transfer[9] compared to electrolyte resistances (high-frequency resistance, R_1). Note that the results in Fig. 6 are actual impedance data obtained using a cathode electrode with an area of 0.18 $\mathrm{cm^2}$. It is shown that not only the overpotential resistances, which are given by the size of semicircles in Fig. 6, but also the electrolyte resistances (high-frequency resistance) decreased as the gas flow rate increased. As shown in Fig. 2, an increase of the cell temperature is the main cause for the improvement of the cell performance, which was affected by the gas flow rate.

Figure 7 shows the area specific resistances (ASRs) for the overpotential as a function of the gas flow rate and reciprocal cell tem-

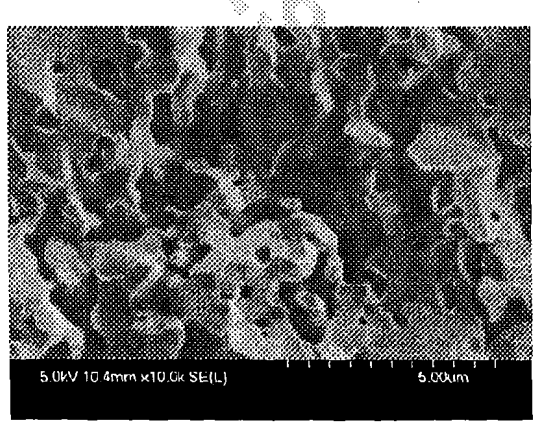

Figure 3. Fracture surface SEM image of porous YSZ electrolyte.

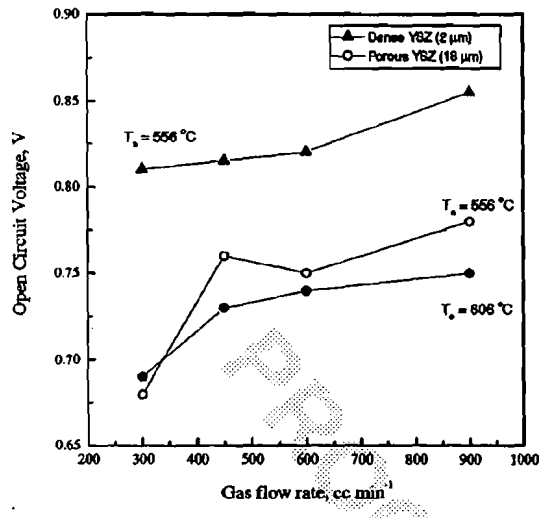

Figure 4. OCV as a function of gas linear velocity obtained in SC configuration at 556 and 606°C set temperature.

perature. Lower ASRs were observed for higher gas flow rates at the same cell temperature. An increase of the gas flow rate (or linear velocity) usually results in an improvement of gas diffusion in the vicinity of electrodes and therefore, overpotential resistances could be effectively reduced. The results showed that the electrolyte resistance had little effect on the performance of the cell, with the performance being limited by the electrode overpotential.[10]

Figure 8 shows the reaction rates of methane as a function of reciprocal cell temperature, obtained at different gas flow rates and furnace set temperature. The results follow the Arrhenius relation (Eq. 7), which shows an increase of the reaction rates (catalytic activity) due to an increase of the cell temperatures. Thus, it appears that the effect of gas flow rates on the reaction rates may be less significant than that of the cell temperatures.

Discussion

Surface migration of ions/molecules.—Earlier studies by van Gool[11] on new fuel cell concepts led to the development of the SC-SOFC. The anode and cathode were arranged on the same surface of the electrolyte so that migration of fuel and oxygen occur on the surface of electrolyte between two electrodes. It was suggested that the surface migration of ions, which might lead to increased surface conductivity, could be significant in the development of SOFCs.[11] Hibino *et al.* showed a good cell performance using a butane-air mixture for a cell with two electrodes arranged on the same surface of an SDC electrolyte.[12] The results showed the power density of ~200 and ~250 mW cm^{-2} using Ni-SDC anode and Pd-Ni-SDC anode, respectively, at 600°C with 0.5 mm gap between electrodes. In this configuration, the cell performance was strongly limited by the distance between the electrodes. Van Gool extended the idea of surface migration to the use of porous, gas-permeable electrolyte in fuel cells, which can increase the effective surface area. Therefore, the use of an electrolyte with optimum porosity may lead to an improved performance of the fuel cell.

Figure 9 shows the area specific resistances (ASRs) for the porous electrolyte as a function of the cell temperature. The gas flow rate had a slight effect on the electrolyte ASRs. The ASRs of the porous electrolyte were lower than those estimated from the values in the literature,[13] which were calculated using the equation ASR = (electrolyte thickness,18 μm)/(electrical conductivity of YSZ). The results showed increased conductivity in porous YSZ, which may be attributed to the surface migration effect. Further studies are

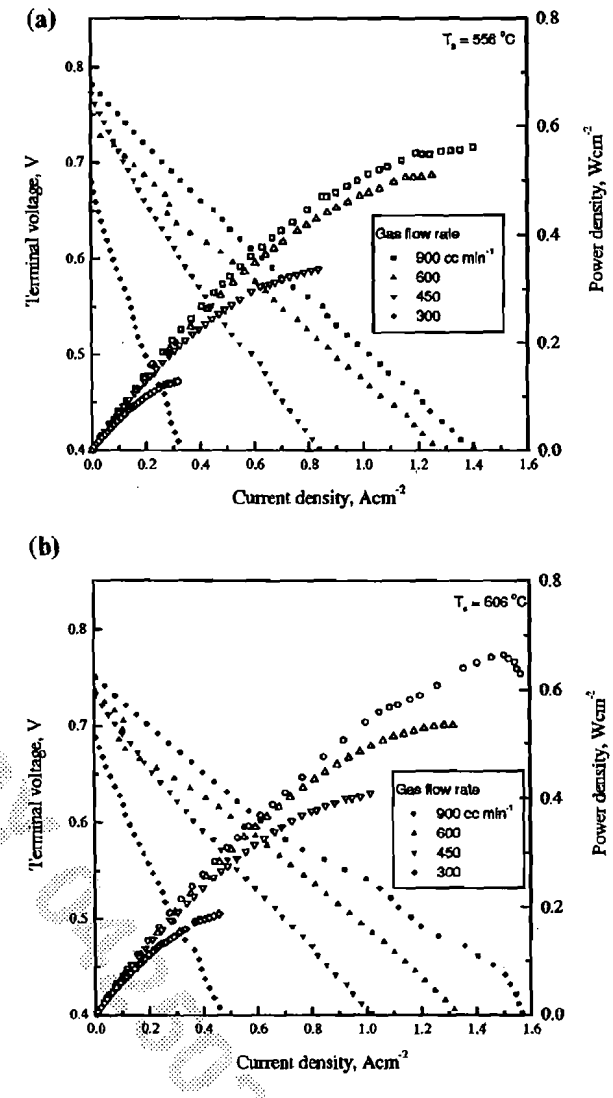

Figure 5. (●,▲,▼,◆) I-V discharge profile and (O,△,∇,◇) power density of the porous electrolyte SC-SOFC. Data collected at (a) 556 and (b) 606°C set temperature.

underway to determine the effect of surface migration on the performance of the porous electrolyte SC-SOFC.

Fuel utilization.—Fuel utilization during fuel cell operation is discussed by estimating the current efficiency.[14] The following relation was used to estimate the current efficiency: current efficiency = (current density where maximum power density was obtained) / (theoretical current determined from the consumption of the fuel according to Eq. 1-3). The consumption of the fuel was determined from the results in Fig. 8, which were normalized to the area of the anode for this calculation. Figure 10 shows the current efficiency as a function of the gas flow rate where a maximum power density was obtained. The current efficiency was determined to be 4-8%, depending upon the set temperature and gas flow rate. The results, obtained at the furnace set temperature of 556°C, led to higher current efficiency. Terminal voltage and overpotential of the cell were effectively improved at 556°C furnace set temperature compared to

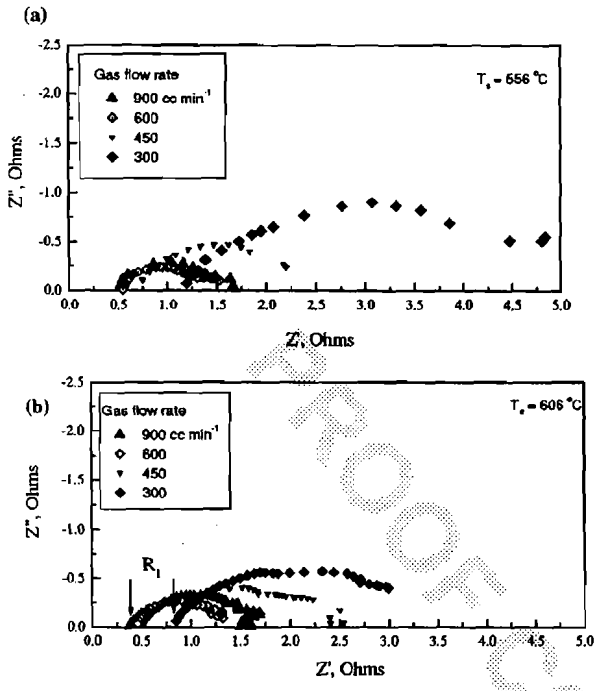

Figure 6. Impedance spectra of the porous electrolyte SC-SOFC. Data collected at (a) 556 and (b) 606°C set temperature. The electrode area of the cell is 0.18 cm^2.

606°C furnace set temperature. Further improvement of fuel utilization depends upon improvement of electrode materials, for example, by optimizing their porosity and catalytic activity.

Effect of gas flow rate.—An increase of the gas flow rate leads to higher cell temperatures due to the increasing oxidation of methane, which results in a decrease of cell resistance (electrolyte and overpotential). The gas flow rate affected the OCV of the cells and the overpotential resistance. OCV increased as the gas flow rate increased and as the furnace set temperature decreased. The increase

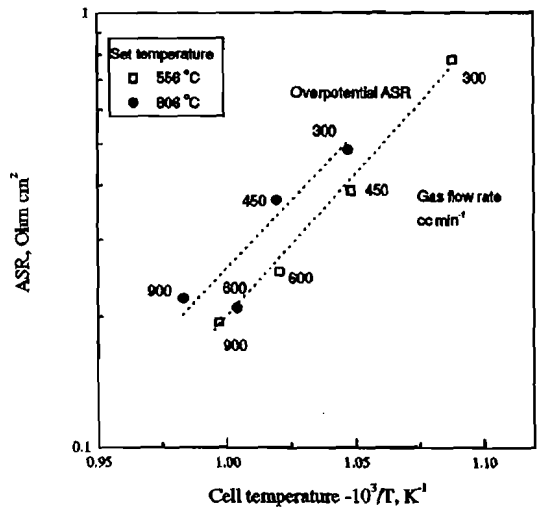

Figure 7. ASRs of the overpotential in Fig. 6. Numbers in the figure indicate the value of gas flow rate where data were acquired.

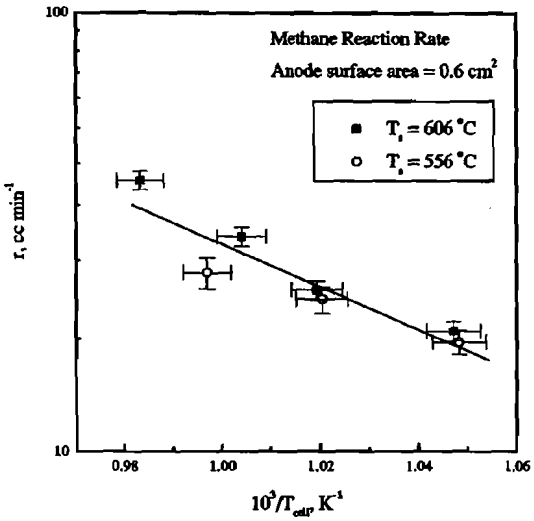

Figure 8. Methane reaction rate as a function of reciprocal cell temperature.

of gas flow rate (or linear velocity) enhances interfacial gas diffusion through the electrode. The same effect can be expected by increasing the gas linear velocity, instead of increasing the gas flow rate. The gas linear velocity can be increased by reducing the diameter of sample holder tube. Thus, the design of cell configuration is an important factor for obtaining an improved fuel cell performance.

Conclusion

The effect of mixed gas flow rates on the performance of SC-SOFCs has been investigated using a cell which consists of a 18 μm thick YSZ porous electrolyte on a NiO-YSZ anode substrate with a $(La, Sr)(Co, Fe)O_3$ cathode. Higher gas flow rates led to an increase of cell temperature due to increasing methane reaction rate, which resulted in improved cell performance. It was shown that optimiza-

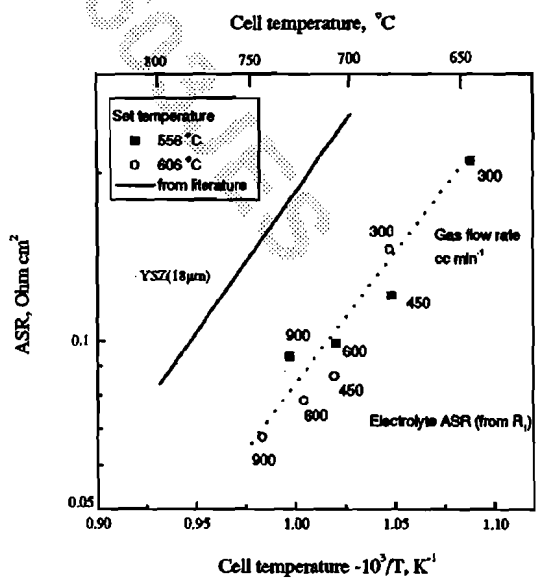

Figure 9. ASRs of the electrolyte in Fig. 6. The ASRs of YSZ were calculated from literature[13] using 18 μm thick. Numbers in the figure indicate the value of gas flow rate where data were acquired.

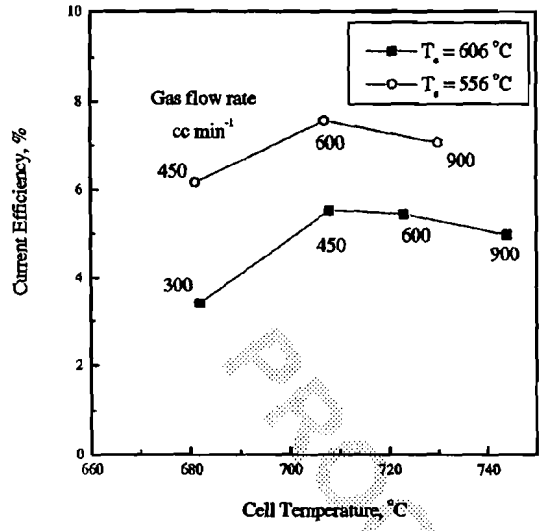

Figure 10. Current efficiency (0.44 V) as a function of cell temperature.

tion of gas flow rate (linear velocity) lead to a decrease of the operating temperature effectively and increased cell performance as well as fuel efficiency.

At a cell temperature of 744°C, an OCV of ~0.78 V and a maximum power density of ~660 mW cm^{-2} (0.44 V) were obtained. The results indicated that a porous ion-conducting membrane provides sufficient separation of oxygen activity at the electrodes by selection of optimum operation temperature and gas flow rate. Thus, it appears that SC-SOFCs with porous electrolyte provides opportunities to design thermally and mechanically more robust stacks by utilizing hydrocarbon fuels. It also allows processing the cells at lower temperatures using conventional processing techniques such as screen printing because densification of the electrolyte is unnecessary.

Acknowledgment

The authors thank Professor Virkar, University of Utah, for supplying anode substrates and the University of Missouri Research Board for financial support of this research.

The University of Missouri-Rolla assisted in meeting the publication costs of this article.

References

1. T. Hibino and H. Iwahara, *Chem. Lett.*, **7**, 1131 (1993).
2. T. Hibino, A. Hashimoto, T. Inoue, J. Tokuno, S. Yoshida, and M. Sano, *J. Electrochem. Soc.*, **148**, A544 (2001).
3. T. Hibino, A. Hashimoto, T. Inoue, J. Tokuno, S. Yoshida, and M. Sano, *Science*, **288**, 2031 (2000).
4. B. C. H. Steele, *Solid State Ionics*, **86-88**, 1223 (1996).
5. P. Jasinski, T. Suzuki, F. Dogan, and H. U. Anderson, *Solid State Ionics, to be published* ■, ■■■ (2003).
6. T. Suzuki, P. Jasinski, F. Dogan, and H. U. Anderson, *J. Electrochem. Soc.*, **151**, A1678 (2004).
7. T. Hibino, A. Hashimoto, M. Suzuki, M. Yano, S. Yoshida, and M. Sano, *J. Electrochem. Soc.*, **149**, A133 (2002).
8. T. Suzuki, P. Jasinski, V. Petrovsky, F. Dogan, and H. U. Anderson, *J. Electrochem. Soc.*, **151**, A1473 (2004).
9. S. B. Adler, *Solid State Ionics*, **111**, 125 (1998).
10. R. E. Williford, L. A. Chick, G. D. Maupin, S. P. Simner, and J. W. Stevenson, *J. Electrochem. Soc.*, **150**, A1067 (2003).
11. W. van Gool, *Philips Res. Rep.*, **20**, 81 (1965).
12. T. Hibino, A. Hashimoto, M. Suzuki, M. Yano, S. Yoshida, and M. Sano, *J. Electrochem. Soc.*, **149**, A195 (2002).
13. T. H. Etsell and S. N. Flengas, *Chem. Rev. (Washington, D.C.)*, **70**, 339 (1970).
14. N. Q. Minh and T. Takahashi, *Science and Technology of Ceramic Fuel Cells*, Elsevier, The Netherlands (1995).

Available online at www.sciencedirect.com
SCIENCE DIRECT
Solid State Ionics 175 (2004) 35–38
SOLID STATE IONICS
www.elsevier.com/locate/ssi

Impedance spectroscopy of single chamber SOFC

P. Jasinski*, T. Suzuki, F. Dogan, H.U. Anderson

Electronic Materials Applied Research Center, University of Missouri-Rolla, 303 MRC, Rolla, 65401 Missouri, USA

Abstract

The mechanism of operation of a single chamber solid oxide fuel cell (SOFC), where a mixture of fuel and oxidant is utilized, is not completely understood. In this study, electrolyte supported single chamber SOFCs consisting of lanthanum strontium cobalt ferrite cathode, yttria stabilized zirconia (YSZ) electrolyte and nickel cermet anode have been fabricated and investigated in the intermediate temperature range (500–700 °C) using propane–air mixtures as fuel. An attempt has been made to separate the cathode and anode overpotentials on the fuel cell performance using impedance spectroscopy and utilizing different anode compositions. Low and high frequency relaxations of impedance data were attributed to the anode and cathode overpotentials, respectively.

PACS: 84.60.D; 66.30.H
Keywords: Impedance spectroscopy; Single chamber fuel cell; Solid oxide fuel cell; Propane fuel

1. Introduction

In contrast to conventional solid oxide fuel cell (SOFC), single chamber fuel cells operate in a mixture of fuel and oxidant gas, and therefore, cell structure can be significantly simplified [1,2]. Recently, relatively high current and power densities were obtained in single chamber SOFCs at moderate operating temperatures (300–600 °C) [3,4]. However, little information is available on the mechanism of power generation in single chamber SOFCs. This knowledge may help in optimizing the cell structure and improving the cell performance. Although the SOFC configuration is significantly simplified in a single chamber cell, the reactions between the SOFC materials and gas mixtures become more complex. The oxygen partial pressures at the anode and cathode sides are not fixed and do depend on the catalytic activity of the electrodes, temperature, fuel and oxidant ratio and its flow rate. Ideally, the fuel reaction should take place only at the anode. For the fuel used in current investigation (mixture of 10% propane and 90% air), the most favorable reaction can be described by Eq. (1):

$$C_3H_8 + 2O_2 \rightarrow 2CO + CO_2 + 4H_2 \quad (1)$$

Reaction (1) leads to a decrease of oxygen partial pressure in the vicinity of the anode and consequently to an increase of the voltage according to the Nernst relation. Once the load is connected to the cell, the current starts to flow due to reactions (2) and (3) occurring at the anode and (4) cathode:

$$H_2 + O^{2-} \rightarrow H_2O + 2e^- \quad (2)$$

$$CO + O^{2-} \rightarrow CO_2 + 2e^- \quad (3)$$

$$1/2O_2 + 2e^- \rightarrow O^{2-} \quad (4)$$

As a consequence of the reaction (2) the following reaction (5) may also occur:

$$C_3H_8 + 3H_2O \rightarrow 3CO + 7H_2 \quad (5)$$

Since reaction (1) is exothermic (ΔG=−903 kJ at 600 °C) and reaction (5) is endothermic (ΔG=4 kJ at 600 °C), the cell temperature is influenced by reaction kinetics. The reactions become even more complex when the cathode becomes catalytically active as well. In this case, cathode

* Corresponding author. On Post Doctoral Fellowship from Gdansk University of Technology, Poland. Tel:. +1 573 3414858; fax: +1 573 3416151.
E-mail address: piotrj@umr.edu (P. Jasinski).

0167-2738/$ - see front matter © 2004 Elsevier B.V. All rights reserved.
doi:10.1016/j.ssi.2004.09.041

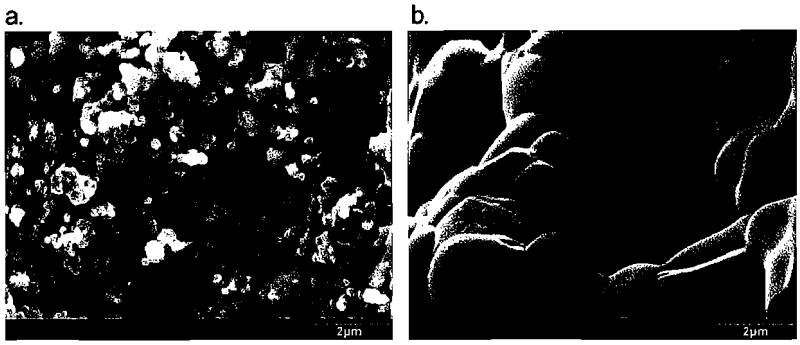

Fig. 1. SEM images of the anodes; (a) Ni+CGO, (b) Ni+YSZ.

reactions affect the cell voltage, temperature and overall SOFC performance [5].

Yttria stabilized zirconia (YSZ) electrolyte has been widely used in the single chamber SOFC studies [6–8] using a methane–air mixture as a typical fuel at relatively higher operating temperatures. Previously we have shown that $La_{0.8}Sr_{0.2}Co_{0.2}Fe_{0.8}O_3$ (LSCF) performs well as a cathode with YSZ electrolyte in both electrolyte and anode supported single chamber cells [5,9]. In this paper, YSZ electrolyte supported cells with LSCF cathode and different Ni cermet anodes are investigated. An attempt is made to separate the influence of the cathode and anode on single chamber SOFC performance using impedance spectroscopy.

2. Experimental

Electrolyte supported cells were prepared by conventional tape casting and screen printing techniques. YSZ and LSCF were used as electrolyte and cathode, respectively. Three different Ni cermet anode compositions were prepared: (i) 70 wt.% Ni/30 wt.% YSZ (Ni+YSZ), (ii) 70 wt.% Ni/30 wt.% $Sm_{0.2}Ce_{0.8}O_x$ (Ni+CSO), and (iii) 60 wt.% Ni/40 wt.% $Gd_{0.1}Ce_{0.9}O_x$ (Ni+CGO). Preparation of YSZ electrolyte and LSCF cathode was described previously [9]. Commercially available CGO powder (Praxair Specialty Ceramics) was used to prepare the Ni+CGO anode. The Ni+CSO powder was obtained by mixing and drying CSO powder (Praxair Specialty Ceramics) in Ni nitrate solution, while the Ni+YSZ powder was prepared by mixing YSZ powder (Zirconia Sales of America) with Ni oxide powder (Aldrich-particle size <10 μm). Printable inks were obtained by mixing of anode powders with BX-016 binder (Ferro). After sintering of the YSZ electrolyte (1450 °C), the anode pastes were screen printed and sintered at 1200 °C for Ni+CGO, 1300 °C for Ni+CSO and 1450 °C for Ni+YSZ. These were the lowest sintering temperatures, which provided a good bonding of the anode to the electrolyte. Finally LSCF cathode was screen printed and sintered at 1000 °C. The YSZ electrolyte was 0.1 mm thick, while the electrodes were about 10–20 μm thick and about 0.18 cm^2 in area. Fig. 1 shows the SEM images of Ni+YSZ and Ni+CGO anodes. The Ni+YSZ anode exhibits much larger NiO particles than the Ni+CGO anode, as expected by the use of NiO powder for anode preparation and the higher sintering temperature. The microstructure of the Ni+CSO anode is very similar to that of the Ni+CGO cermet.

The properties of the cells were measured in a tube furnace using a flowing gas mixture with a composition of 10% propane and 90% air. Mass flow controllers were used to maintain the gas flow rate at 300 ml/min. The furnace temperature was adjusted with an electronic controller, while the temperature a few millimeters from the sample was monitored using a S type thermocouple. The direct measurement of the sample temperature was not possible. The data were presented using the temperature of the

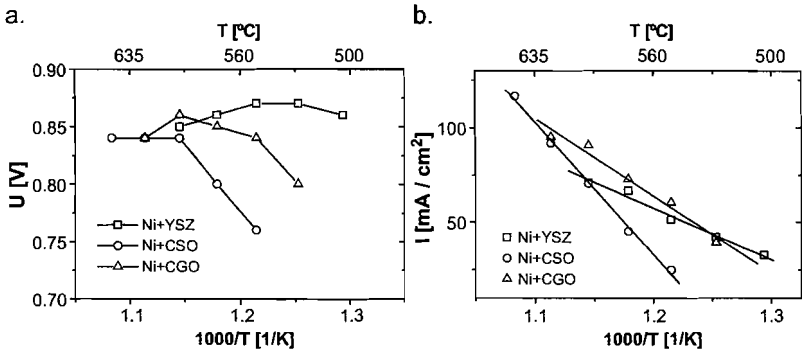

Fig. 2. The temperature dependence of open circuit voltage (a) and short circuit current (b).

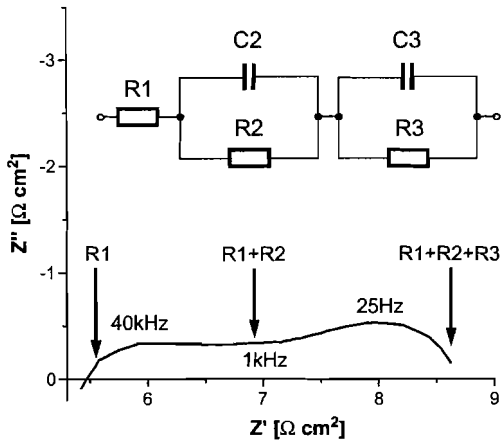

Fig. 3. Typical impedance spectra of the cell (Ni+CGO anode under 50 mA/cm^2 load at 630 °C).

furnace. The actual sample temperature is expected to be higher because of the combustion reaction in the vicinity of the anode.

Current–voltage dependence was measured using a Solartron 1470 Battery Tester, while for impedance measurements a 1255B Impedance Gain Phase Analyzer was employed.

3. Results and discussion

Fig. 2 shows comparison of open circuit voltage and short circuit current of all examined samples as a function of temperature. In the low temperature range (<550 °C) the highest open circuit voltage is obtained for Ni+YSZ anode, which is attributed to the highest catalytic activity among the investigated anodes. The lowest voltage is obtained for the cell with Ni+CSO anode. Above 570 °C, the difference in the voltage for different anode materials become insignificant and in all cases open circuit voltage is higher than 0.8 V.

Fig. 2b shows that the cell with the Ni+CGO anode exhibits the highest short circuit current in the temperature range from 500 to 625 °C. At the furnace temperature 650 °C, the cell with Ni+CSO anode reaches 120 mA/cm^2. The difference in the current level may be at least partially related to the difference of open circuit voltage of these cells. The short circuit current of the cell with Ni+YSZ anode shows lower temperature dependence then ceria based anodes.

Impedance spectroscopy was employed in order to investigate the differences of the fuel cell performance. Measurements were conducted with the load applied to the cells, which was equivalent to the half of the short circuit current. A typical impedance spectra of a single chamber SOFC are presented in Fig. 3. The spectra consist of two depressed semicircles, which can be attributed to the response from the electrodes. The spectra were fitted to the equivalent circuit shown in the Fig. 3. Typically, in a simple attempt of analysis, one would consider the resistance R1 as the resistance of the electrolyte and resistance R2 and R3 as the overpotential of the electrodes. With this approach, resistance R1 shows a much larger value than one would expect from the cell. However, in this particular system, the relaxation frequency of the elements R2 and C2 tends to respond in a relatively high frequency range (above 10 kHz), which in addition to the inductance from the cables and sample holder introduce errors in the determination of the resistance R1. Therefore, the resistance R1 is not analyzed separately, but together with the resistance R2. In Fig. 4a, the temperature dependence of the area specific resistance R1+R2 is presented. For all anodes, a similar resistance with an average activation energy of 0.5 eV is obtained, that allows to attribute it to the resistance of the electrolyte and the cathode overpotential.

Fig. 4b shows the temperature dependence of the area specific resistance R3. For the resistance R3, each cell shows a different response, which may be attributed to the anode overpotential. The highest resistance (between 5 and 10 Ω cm^2) and the lowest activation energy (0.43 eV) were obtained for the cell with the Ni+YSZ anode. This may result from the larger size of NiO particles as compared to other cermets as shown in Fig. 1. The cell with the Ni+CGO anode shows the lowest resistance (between 2 and 4 Ω cm^2) but a similar activation energy (0.38 eV) in comparison to the Ni+YSZ anode. The largest change of

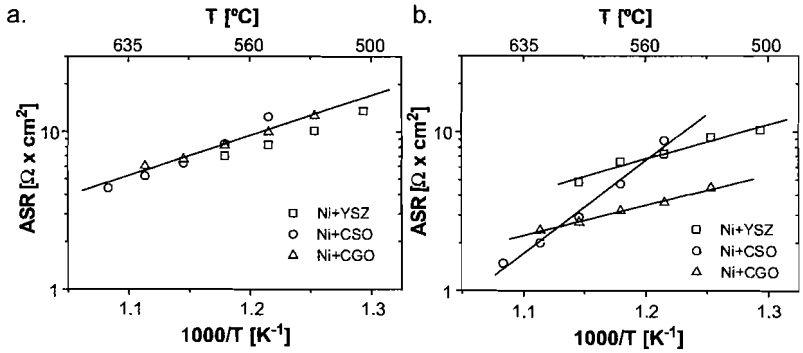

Fig. 4. Temperature dependence of the area specific resistance; (a) sum of high and middle frequency R1+R2; (b) low frequency R3.

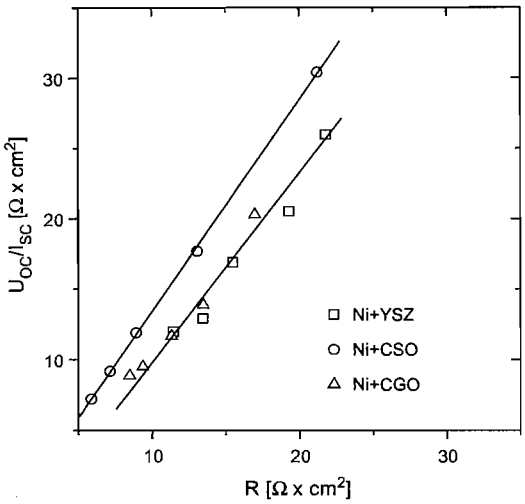

Fig. 5. Correlation graph of total resistance and ratio of open circuit voltage and short circuit current.

the resistance (between 1.5 and 10 Ω cm^2) as a function of temperature is obtained for the cell with the Ni+CSO anode, which has an activation energy of 1.1 eV. The differences in the activation energies are not understood at this time.

Comparison of the data obtained by AC and DC measurements is shown in Fig. 5. The AC measurements are represented by a total area specific resistance R1+R2+R3, while DC measurements as a ratio of open circuit voltage (Fig. 2a) and short circuit current (Fig. 2b). These data indicate a good correlation between the AC and DC measurements for all investigated cells. However, the resistance, calculated from the DC short circuit current and open circuit voltage, is higher than the AC total resistance. This is particularly pronounced for the cell with Ni+CSO anode, which may be attributed to the activation polarization effect [10].

Based on the preliminary studies of the single chamber fuel cell, long-term stability of the cells is yet to be investigated. However, a relatively stable cell performance (several hours of operation) was observed in the low temperature range (500–625 °C). Slow but permanent degradation of the cell performance took place at temperatures above 625 °C. This was manifested by the detachment of the anode from the electrolyte, probably due to the severe combustion reactions. Further investigations are necessary to fully understand the electrode effects on the cell performance of a single chamber SOFC.

4. Summary

The single chamber SOFC, consisting of LSCF as the cathode, YSZ as the electrolyte and Ni cermets as the anodes, have been investigated. For all the cells, the open circuit voltage was above 0.8 V at 600 °C, while short circuit current at this temperature exceeded 70 mA/cm^2. Impedance spectroscopy has been employed to investigate the cell performance. All investigated cells showed similar values of the resistance R1+R2, which allowed attributing of the high frequency and low frequency semicircles to the cathode and anode response, respectively. Both electrodes had significant effect on the cell performance. Namely, the influence of the Ohmic resistance together with the cathode overpotential (R1+R2=5–10 Ω cm^2) on the total resistance of the cell was comparable with that of the Ni+YSZ anode (R3=5–10 Ω cm^2). However, the influence of R1+R2 was higher in case of the Ni+CGO anode (R3=2–5 Ω cm^2). The data obtained by DC and AC measurements showed a good correlation.

Acknowledgement

The authors would like to thank the Department of Energy, Contracts No. DE-FC36-01G011084, DE-FC26-02NT41563 and University of Missouri Research Board for the financial support of this research.

References

[1] T. Hibino, H. Iwahara, Chem. Lett. 7 (1993) 1131.
[2] T. Hibino, K. Ushiki, T. Sato, Y. Kuwahara, Solid State Ionics 81 (1995) 1.
[3] T. Hibino, A. Hashimoto, T. Inoue, J. Tokuno, S. Yoshida, M. Sano, J. Electrochem. Soc. 148 (2001) A554.
[4] T. Hibino, A. Hashimoto, M. Yano, M. Suzuki, S. Yoshida, M. Sano, J. Electrochem. Soc. 149 (2002) A133.
[5] P. Jasinski, T. Suzuki, X.D. Zhou, F. Dogan, H.U. Anderson, Ceram. Eng. Sci. Proc. 24 (2003) 293–298.
[6] T. Hibino, S. Wang, S. Kakimoto, M. Sano, J. Electrochem. Solid-State Lett. 2 (1999) 317.
[7] S. Wang, M. Awano, K. Maeda, Electrochemical Society Proc. "Power Sources for the New Millennium" PV 2000–22, 2000, p. 134.
[8] A. Demin, F. Gulbis, Solid Sate Ionics 135 (2000) 451.
[9] P. Jasinski, T. Suzuki, Z. Byars, F. Dogan, H.U. Anderson, Electrochemical Society Proc. "Solid Oxide Fuel Cells VIII" PV 2003–07, p. 1101.
[10] N.Q. Ming, T. Takahashi, Science and Technology of Ceramic Fuel Cells, Elsevier, Amsterdam, 1995, p. 22.

Defect chemistry of p-type perovskite conductor used in solid oxide fuel cells

Xiao-Dong Zhou and Harlan U. Anderson

Department of Ceramic Engineering, Electronic Materials Applied Research Center, University of Missouri-Rolla, Rolla, MO 65409

Introduction

The development of solid oxide fuel cells (SOFCs) has been driven by both industry and academy for the purpose of searching for the alternative energy sources. Over last several years, operation of SOFCs in the intermediate temperature regime (500 – 700°C) is of particular interest, which seems mandatory for SOFC commercialization. Strict materials requirements are of great importance for the electrode of SOFCs operated over the intermediate temperature region. Therefore, it is necessary to study the electrode materials by understanding the mechanisms for the conductive and catalytic behavior and developing reliable and stable experimental methods to measure defect density and catalytic ability. Perovskite type oxides are of great interest for use as the electrodes in SOFCs because (1) site occupancy is determined mainly by ionic radius so lattice site location of a particular cation is fairly certain; (2) electronic conductivity (σ) is determined by B site ion; and (3) ionic conductivity results from the presence of oxygen vacancies. Thus, this family of oxides was tailored to use as mixed ionic and electronic conductors, superionic conductors, and superconductors. Defect chemistry is a particularly powerful technique in understanding the mass and charge transfer properties by determining defect type, density, association and mobility. In this article, it is our intent to report the global solutions to defect chemistry models, with an emphasis on the p-type perovskite conductors which are being considered as the electrodes of SOFCs. The global defect chemistry models allow us to better understand and predict the electrochemical properties of perovskite type p-type conductors.

Defect Chemistry Modeling

The procedure is to write the defect formation reactions: 1) list the basic defect types and reactions which can occur: intrinsic, stoichiometric, oxygen excess and oxygen deficient; 2) write the overall neutrality relation and 3) combine the resulting equations to yield a relationship which can be solved for particular temperature and oxygen activity regimes. Considering a general type perovskite type oxide (ABO_3), the occupants at A site can be (Kroger-Vink notation is used) A_A^x , $V_A^{'''}$ and $Sr_A^{'}$ (for simplicity, assume Sr is the low valence element substituting at the A site). The occupants at the B site are B_B^x, $B_B^{'}$, $B_B^{\bullet}$ and $V_B^{'''}$, where B_B^x indicates a majority of B cations which are in valence of 3+, $B_B^{'}$ represents that some B site cations are in 2+ state and $B_B^{\bullet}$ shows some B site cations are in 4+ valence state. The oxygen site can have two type of occupants, $V_O^{\bullet\bullet}$ and O_O^x.

Since there exist nine variables, nine equations are needed to obtain these values. Two methods can be used to solve the resulting equations: 1) divide into regions of particular neutrality conditions and solve for that particular region or 2) do not use limiting conditions, but allow a computer to make a numerical solution to the overall equation using the total neutrality condition. More detailed equations and solutions can be found elsewhere. [1] A global solution will be discussed in this article, in which the overall electron neutrality expression is used results in a term named as the ability for oxygen vacancy generation (AOG). This method is considered as a model based on delocalized electron holes.

The total electrical conductivity, σ, is given by

$$\sigma = N\mu q \tag{1}$$

where μ is the mobility, q is the carrier charge and N is the carrier concentration. Because of the mobility of either the electrons or holes is much higher than that of oxygen ions, the total conductivity in ferrites is dominated by hole conduction. The carrier concentration, N is:

$$N = [Sr_{La}^{'}] - 2[V_O^{\bullet\bullet}] \tag{2}$$

where $[Sr_{La}^{'}]$ is the acceptor level and $[V_O^{\bullet\bullet}]$ is the oxygen vacancy concentration. For simple analysis, it is assumed that all doping centers are dissociated. Generation of oxygen vacancy, $V_O^{\bullet\bullet}$, follows:

$$O_O^x \rightarrow V_O^{\bullet\bullet} + \frac{1}{2}O_2 + 2e^{'} \cdot \tag{3}$$

The reaction constant (K_1) of reaction in Eq. (3) is:

$$K_{V_O^{\bullet\bullet}} = [V_O^{\bullet\bullet}]\, pO_2^{1/2}\, n^2 \tag{4}$$

where, pO_2 is the oxygen partial pressure and n is the electron concentration. Assuming this reaction follows the Ahrennius law:

$$K_{V_O^{\bullet\bullet}} = K_{V_O^{\bullet\bullet},0}\exp(-\frac{E_{V_O^{\bullet\bullet}}}{kT}), \tag{5}$$

where $E_{V_O^{\bullet\bullet}}$ is the activation energy for oxygen vacancy generation and k is Planck's constant. Considering $np = K_i$, then the expression can be rearranged to yield

$$\ln(\frac{[V_O^{\bullet\bullet}]}{([Sr_{La}^{'}] - 2[V_O^{\bullet\bullet}])^2}) = \ln(\frac{K_{V_O^{\bullet\bullet},0}}{K_i^2}) - \frac{1}{2}\ln(pO_2) - \frac{E_{V_O^{\bullet\bullet}}}{kT} \cdot \tag{6}$$

From this expression the oxygen vacancy concentration can be derived as a function of substitution level ($[Sr_A^{'}]$), temperature, and materials properties:

$$[V_O^{\bullet\bullet}] = \frac{(4MN+1) - \sqrt{1+8MN}}{8A} \text{ where} \tag{7}$$

$$M = \frac{K_{V_O^{\bullet\bullet},0}}{K_i^2} \cdot \exp(-\frac{E_{V_O}}{kT}) \cdot P_{O_2}^{-1/2} \text{ and } N = [Sr_{La}^{'}] \cdot$$

The term M can be expressed as $AOG*pO_2^{-1/2}$, where AOG stands for the ability for oxygen vacancy generation, which is a function of temperature and intrinsic materials properties. Fig. 1 shows a plot of carrier concentration calculated from Eqs. (2), (6) and (7). The ability for oxygen vacancy generation as a function of temperature and oxygen activity can be determined by simulating experimental conductivity data with the current defect chemistry. Fig. 2 shows a plot of the experimental and simulated conductivity of LSM, LSF and LSCF. Table 1 lists the AOG values of these compounds. It is worthwhile to note again that the B site cation can be easily driven from 4+ to 3+ for the perovskites which possess high values of AOG, such as $(La,Sr)FeO_{3-\delta}$. For instance, $\delta \sim 0.2$ takes place at ~1500°C for $La_{0.60}Sr_{0.40}FeO_{3-\delta}$ in air, which indicates that all of the Fe ions are in the 3+ valence state. If the temperature is lowered to 1000°C, the oxygen activity has to be lowered to $\sim 10^{-14}$ atm to observe this state. Activation energy values for AOG of manganites and chromites are larger than those of ferrites, hence, it is expected that Cr and Mn cations can be reduced to 3+ in air only if the temperature is sufficiently high.

X.D. Zhou and H.U. Anderson, "Defect chemistry of p-type perovskite conductor used in solid oxide fuel cells", Preprints of Symposia – American Chemical Society, Division of Fuel Chemistry, **49**, 749-750 (2004).

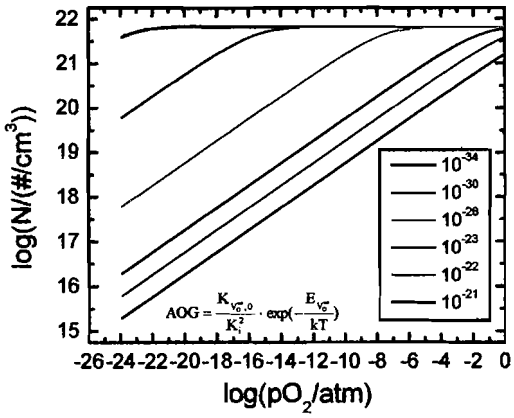

Figure 1: A plot of carrier concentration as a function of oxygen activity with various AOG values

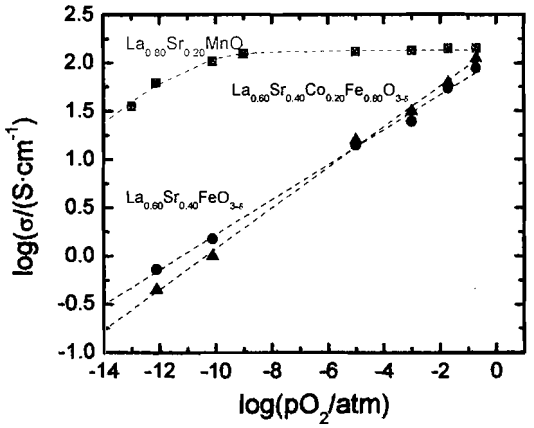

Figure 2. Plot of log(σ) vs. log(pO_2) for LSM, LSF and LSCF. The solid points are experimental data. The dash lines are fitting results from the global defect chemistry model. [2-4]

The knowledge of the values for the AOG terms can enable us to understand the maximum conductivity of many p type conductors. For example, from the previous results, we know that at temperatures < 600°C in air LSF possesses nearly stoichiometric oxygen occupancy. Thus it can be expected that the oxygen vacancy concentration is extremely low at relatively low temperature (~ room temperature), therefore conductivity should increase with increasing temperature because of the increasing mobility. At elevated temperature, more oxygen vacancies are generated which will decrease the total carrier numbers because of the increasing oxygen vacancy concentration. The mobility, however, continuously increases with increasing temperature. Hence, a maximum conductivity at a specific temperature is expected due to an increasing mobility and decreasing carrier concentration. A shift of the temperature corresponding to the maximum conductivity is observed as shown in Table 1. As discussed previously this maximum in conductivity represents the temperature at which the oxygen vacancy concentration starts to influence the carrier concentration. It does not mean that the oxygen vacancy concentration is negligible at this temperature, but on the other hand, the influence of oxygen vacancy concentration on total carrier concentration is negligible below this temperature and the concentration of oxygen vacancies is so small that their contribution to transport processes becomes minimal.

The values of AOG and understanding of the maximum conductivity are of particular importance in the search for materials for energy conversion devices. Since oxygen vacancies are required for lower cathodic overpotentials, this temperature also represents the temperature below which a cathode can be expected to have high overpotentials. Therefore, when pure LSM is used as the cathode, it will be expect to work well when the operation temperature is ~ 1000°C because the oxygen vacancy concentrations are sufficiently high to support the required transport processes of the cathode. Below this temperature range, overpotential problems are commonly encountered. It has been found that the addition of a second ionic conducting phase to the cathode enhances the ionic transport processes, which allows lower temperature operation. Thus the use of cathodes consisting of mixtures of LSM and YSZ or LSM and CGO has become common practice in the SOFC industry, but these mixtures will not extend the temperature much below 750-800°C before cathodic overpotentials become too large because the concentration of oxygen vacancies is insufficient to support the transport processes which are required for oxygen reduction and transport of the oxygen ions to the electrolyte.

Conclusions

The understanding of the defect chemistry in the perovskite family p type conductors allows us to search for the novel materials for use in fossil energy conversion system, which requires a sufficient vacancy density, a mixed ionic and electronic conductance, high catalytic ability and stability. Examples include the electrodes used in SOFCs where the cathode component which requires high oxygen vacancy density and electronic conductance and the anode requires stability in a very reducing atmosphere, electronic conductance, and oxygen vacancy density.

Acknowledgement. This work was supported by contracts DE-FC26-02NT41563 and DE – FC36 – 01G011084.

References

(1) Zhou X D and Anderson H U. unpublished.
(2) Kuo J H, Anderson H U, Sparlin D M, "Oxidation-reduction behavior of undoped and strontium-doped lanthanum manganese oxide ($LaMnO_3$): defect structure, electrical conductivity, and thermoelectric power," *J. Solid State Chem.* (1990) **87**, 55-63.
(3) Tai L W, Nasrallah M M, Anderson H U, Sparlin D M, Sehlin S R, "Structure and electrical properties of $La_{1-x}Sr_xCo_{1-y}Fe_yO_3$, part 2. The system of $La_{1-x}Sr_xCo_{0.2}Fe_{0.8}O_3$," *Solid State Ionics* (1995), **76**(3,4), 273-83.
(4) Kaus I, Anderson H U, "Electrical and thermal properties of $La_{0.2}Sr_{0.8}Cu_{0.1}Fe_{0.9}O_{3-d}$ and $La_{0.2}Sr_{0.8}Cu_{0.2}Fe_{0.8}O_{3-\delta}$," *Solid State Ionics* (2000), **129**(1-4), 189-200.

Table 1 AOG and T_{max} for four p type conductors

	LSM	LSF	LSCF	LSFCu
AOG	2.9×10^{-27}	3×10^{-21}	3×10^{-20}	
T_{max} (°C)	900	600	550	400

ECS

Low Temperature Processed Cathode for Solid Oxide Fuel Cells

Toshio Suzuki, Vladimir Petrovsky, Piotr Jasinski, and Harlan U. Anderson.

Electronic Materials Applied Research Center

University of Missouri-Rolla, Rolla MO 65401 USA

Abstract

Composite (La, Sr)MnO_3 (LSM) -Y doped ZrO_2 (YSZ) was prepared by coating YSZ colloidal suspension (initial YSZ particle size ~ 100 nm) and YSZ and LSM polymer precursors on dense substrates at 800 °C annealing temperature. The results of a symmetrical LSM-YSZ cell test showed that the area specific resistance for overpotential of 0.14 Ωcm^2 at 800 °C, which indicated that the composite LSM-YSZ could be a potential candidate for cathode in SOFCs. The performance of the cell with the composite LSM-YSZ and Ni-YSZ anode was investigated and the power density of about 0.26 Wcm^{-2} was obtained at 850 °C using hydrogen fuel.

"Low Temperature Processing of Thin Film Electrolyte for Electrochemical Devices", V. Petrovsky, T. Suzuki, P. Jasinski, T. Petrovsky and H. U. Anderson. *Electrochem. Solid-State Letters*, 7 (6) p. 2004

Introduction

Solid oxide fuel cells (SOFCs) have been paid a lot of attention as an environmental friendly energy source due to their high fuel utilization [1-3]. Recent studies focus on lowering operation temperature of SOFCs (intermediate temperature (IT) SOFCs) under 800 °C to open opportunities to see SOFCs in variety of application use, on which numbers of research groups worldwide are currently working. For the development of IT-SOFCs, new materials and cell configurations have been proposed to reduce operating temperatures[4, 5]. Several successful results have been shown for cells with Ni-cermet anode support to reduce the thickness of an electrolyte (anode supported SOFC) for IT-SOFCs [6,7].

Reducing a cell processing temperature is another challenge for the development of SOFCs because it could (i) reduce processing cost, (ii) avoid interfacial reactions between an electrode and an electrolyte, which may cause degradation of cell performance, (iii) avoid sample damages due to thermal expansion mismatch at high processing temperature and (iv) provide variety of material selection. Several low temperature ceramic processing techniques have been proposed such as chemical vapour phase deposition, polymeric precursor spin coating and radio frequency sputtering. Among these techniques, the polymer precursor technique has been proven to be one of the suitable methods for the preparation of oxide in low temperature under 800 °C [8]. Our group previously showed that a dense YSZ electrolyte could be prepared on porous substrates with 400 °C annealing temperature to receive as same conductivity as bulk YSZ has by using the YSZ polymer precursor and YSZ colloidal suspension (YSZ particle size ~ 100 nm) [9]. The process of this technique is as follows; first, a YSZ skeleton layer is prepared by the colloidal suspension, then, densified the layer by filling

the YSZ polymer precursor. This technique can be applied for the process of not only an electrolyte but also electrodes by choosing suitable polymer precursor and controlling concentration of materials inside the polymer precursor.

In this study, a new type of composite cathode has been prepared using (La, Sr)MnO_3 (LSM) polymer precursor and Y doped ZrO_2 (YSZ) colloidal suspension under 800 °C processing temperature. The composite LSM-YSZ was examined the performance as a cathode for SOFCs in different conditions including overpotential measurement using a symmetrical composite LSM-YSZ cell and a fuel cell measurement.

Experimental

Composite $(La_{0.8}Sr_{0.2})_{0.9}MnO_3$–Y doped ZrO_2 (LSM-YSZ) was prepared by coating YSZ colloidal suspension (initial YSZ particle size ~ 100 nm) and LSM polymer precursor on dense YSZ substrate (0.4 mm thick). Commercially available YSZ powder (16% Y doped ZrO_2, Daiichiki Genso Co, Japan) was used for processing colloidal suspension. For the preparation of polymer precursors, the details were discussed elsewhere [10]. Figure 1 shows a scheme of the composite technology, which was used in this study. Preparation process is as follows;

(i) Preparation of YSZ colloidal suspension

(ii) Preparation of polymer precursors (YSZ and target cathode materials)

(iii) Coating the colloidal suspension on the substrate to prepare YSZ porous layer.

(iv) Application of YSZ polymer precursor to a porous layer to connect particles.

(v) Impregnation process - impregnate LSM polymer precursor to a porous layer by spin coating multiple times. Every coating, the polymer coatings are converted to the oxide by heating to 380°C to remove the hydrocarbons.

(vi) Annealing at 800 °C.

For the preparation of a symmetrical cell, the composite LSM-YSZ was prepared for both sides of a 0.4 mm thick YSZ substrate, which was used as an electrolyte. For a fuel cell preparation, Ni-YSZ powder ink (Ni 45 wt%) was screen printed on the YSZ substrate and sintered at 1400 °C for 1h. Then, the composite LSM -YSZ was prepared on the other side. The microstructures of the resulting cells were analyzed using a Hitachi S4700. Impedance spectroscopy techniques were utilized to investigate the performance of the composite LSM-YSZ symmetrical cell using Solartron 1470 Battery Tester and 1255B Impedance Gain Phase Analyzer with 4-probe configuration.

The fuel cell performance was evaluated in the double chamber configuration (Fig. 2) using a forming gas (10 vol% H_2 in N_2) at an anode side and air at a cathode side. A mixture of Ag paste and YSZ powder was used as a current collector, which was applied to the area of electrodes, 0.28 cm^2.

Results and Discussion

Figure 3 shows an SEM image of LSM-YSZ composite cathode. As can be seen, a 2 μm thick LSM-YSZ cathode was obtained using this method. The YSZ particles are well covered with the LSM layer. Porosity of the composite layer can be controlled by the number of application of the polymer precursor.

Figure 4 shows the electrical conductivity of the composite LSM-YSZ as a function of reciprocal temperature along with the conductivity of YSZ [11] and LSM [12]. Compared to the literature, composite LSM-YSZ showed lower conductivity simply due to lower concentration of LSM in the composite. However, it was observed high conductivity of the composite LSM-YSZ that made it attractive to use as a cathode.

Figure 5 shows the impedance spectra of the symmetrical cell obtained in air at 700-800 °C. Two semi-circles were observed in the impedance spectra, which are typically interpreted as the charge transfer and gas diffusion process [13], namely R_2 and R_3, respectively (Fig. 5). High frequency resistance, R_1, is corresponding to the resistance of the YSZ substrate.

Figure 6 shows the area specific resistance for LSM-YSZ symmetrical cell determined from the impedance spectra in Fig. 5. Overpotential resistances, R_2 and R_3, are low compared to the electrolyte resistance, which are corresponding to the charge transfer and the gas diffusion processes, respectively. Relatively large overpotential from the gas diffusion process was observed probably due to dense structure of the composite LSM-YSZ. Total over potential resistance for the LSM-YSZ composite cathode can be estimated as 0.14Ωcm^2 at 800°C and 0.3 Ωcm^2 at 700°C for single electrode.

Fuel cell performance of the composite LSM-YSZ (cathode)/ YSZ/ Ni-YSZ (anode) cell was investigated using a forming gas (10 vol% H_2 in N_2) (Fig.2). Figure 7 shows the discharge profile of the cell at the temperature range from 650 to 850 °C. The results showed that a maximum power density of about 0.26 Wcm^{-2} was obtained at a temperature of 850 °C with a current density of 0.65 Acm^{-2}. The impedance spectra for this cell were shown in Fig. 8. The spectra showed distorted semi circles with relatively

higher high frequency resistance corresponding to thick YSZ electrolyte. The area specific resistances of the cell were shown in Fig. 9. The overpotential ASR of the cell was estimated as 0.3 Ωcm^2 at 800°C, which are the total of anode and cathode overpotential. It appeared to be good correlation between symmetrical cell and fuel cell test, since the overpotentiual ASR of the composite cathode determienrd from symmetrical cell test was estiamted as 0.14 Ωcm^2 at 800°C. The performance of the cell was mainly limited by the electrolyte resistance, which can be easily improved by reducing the thickness of an electrolyte. Further investigation is undergoing to improve microstructure of the composite to decrease the overpotential from gas diffusion process, as well as searching for new materials for a cathode.

Summary

Composite LSM-YSZ was prepared by combining YSZ colloidal suspension (initial YSZ particle size ~ 100 nm) and, YSZ and LSM polymer precursor coatings. This composite technique allows preparing fuel cell components under 800 °C, which makes it possible to use variety of materials and cell configurations. The composite LSM-YSZ prepared under 800 °C showed high conductivity enough to be used as a electrode. The results of the symmetrical cell test showed that the area specific resistances (ASR) for overpotential were 0.14 and 0.3 Ωcm^2 at 800 and 700 °C, respectively, mainly due to the gas diffusion process.

The performance of the composite LSM-YSZ as a cathode for SOFC was investigated. It was obtained a maximum power density of about 0.26 W cm^{-2} at 850 °C

using 0.4 mm thick YSZ electrolyte and Ni-YSZ as an anode, with the ASR for total overpotential was about as 0.17 Ωcm^2 at 850°C.

References

1. N.Q. Minh and T. Takahashi, *Science and technology of ceramic fuel cell*, Elsevier, The Netherlands (1995)
2. B.C.H. Steele, *J. Mater. Sci.*, 36 p.1053-1068 (2001)
3. S.C. Singhal, *MRS Bulletin*, p.16-21 March (2000)
4. B.C.H. Steele, *Solid State Ionics*, 86-88, p.1223-1234 (1996)
5. S. Park, R.J. Gorte and J.M. Vohs, *J. Electrochem. Soc.*, 148 (5) A443-A447 (2001) direct hydrocarbon
6. B.C.H. Steele, *Solid State Ionics*, 94 p.239-248 (1997)
7. R.E. Williford, L.A. Chick, G.D. Maupin, S.P. Simner and J.W. Stevenson, *J. Electrochem. Soc.*, 150 (8) A1067-A1072 (2003).
8. T. Suzuki, I. Kosacki and H. U. Anderson. *J. Am. Ceram. Soc.* 85(6) p.1492-98, (2002).
9. V. Petrovsky, T. Suzuki, P. Jasinski, T. Petrovsky and H. U. Anderson, *Electrochem. Solid-State Letters*, 7 (6) A138-A139 (2004)
10. H. U. Anderson, M. M. Nasrallah, and C. C. Chen, *U.S. Patent*, 5494700 (1996).
11. T.H. Etsell and S.N. Flengas, Chem. Rev., 70 p.339 (1970)
12. J.H. Kuo, H.U. Anderson, and D.M. Sparlin, *J. Solid State Chem.*, 87 p.55 (1990)
13. S.B. Adler, *Solid State Ionics*, 111 p.125 (1998)

Figure Caption

Figure 1: The schematic diagram of composite technique.

Figure 2: Fuel cell test configuration

Figure 3: SEM image of $(La_{0.8}Sr_{0.2})_{0.9}MnO_3$ -YSZ composite cathode

Figure 4: Electrical conductivity of the composite LSM-YSZ along with the conductivity of bulk YSZ and $La_{0.8}Sr_{0.2}MnO_{3-\delta}$

Figure 5: Impedance spectra of $(La_{0.8}Sr_{0.2})_{0.9}MnO_3$ -YSZ composite cathode (symmetrical double sided cell, electrode area = $0.28cm^2$).

Figure 6: Area specific resistance of $(La_{0.8}Sr_{0.2})_{0.9}MnO_3$ -YSZ composite symmetrical cell

Figure 7: I-V discharge profile and I-P characterization for a cell with LSM compoiste chathode.

Figure 8: Impedance spectra for LSMcompoiste chathode cell.

Figure 9: Area specific resistance of $(La_{0.8}Sr_{0.2})_{0.9}MnO_3$ -YSZ composite cathode-YSZ-Ni-YSZ cell.

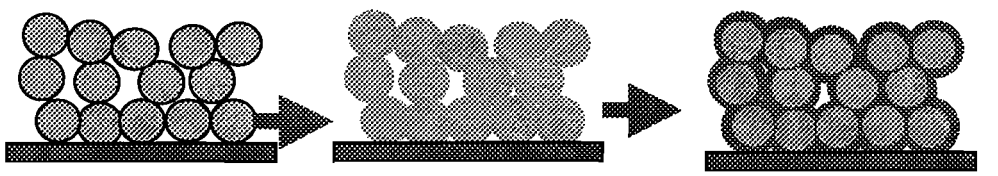

YSZ skeleton from YSZ slurry YSZ polymer precursor coating LSM polymer precursor coating

Figure 1

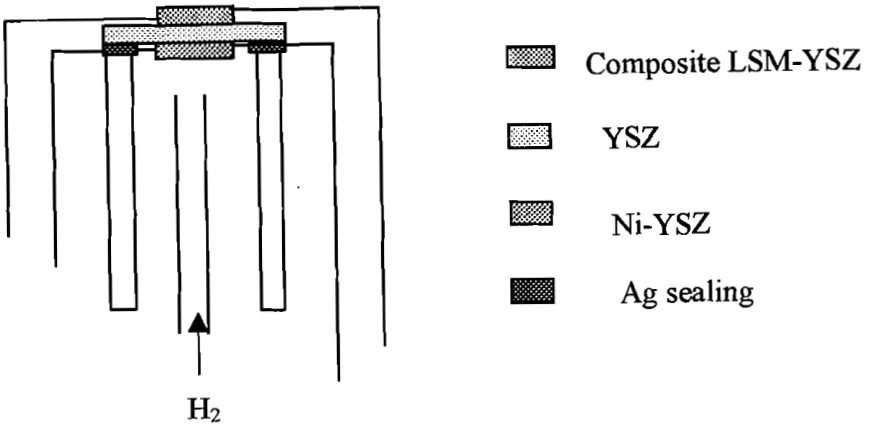

Figure 2

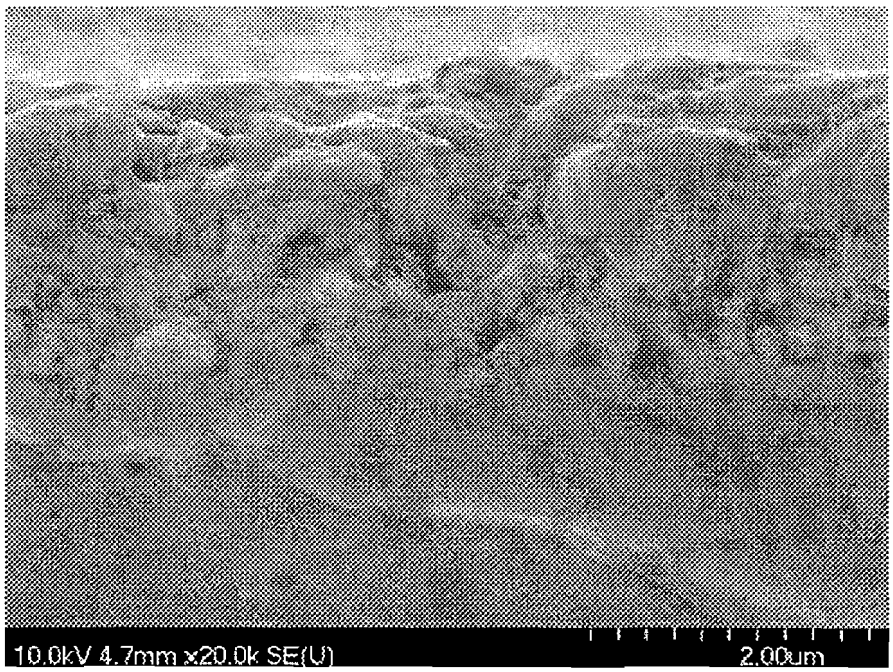

Figure 3

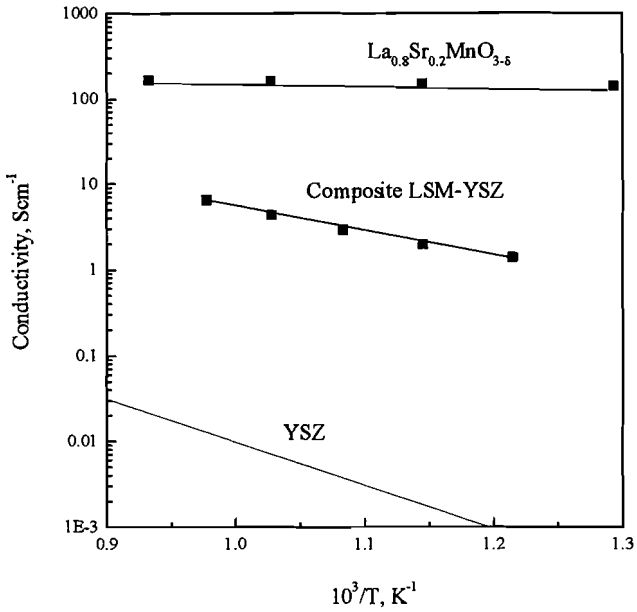
1000
100
10
1
0.1
0.01
1E-3
0.9
1.0
1.1
1.2
1.3
Conductivity, Scm-1
10³/T, K-1
La0.8Sr0.2MnO3-δ
Composite LSM-YSZ
YSZ

Figure 4

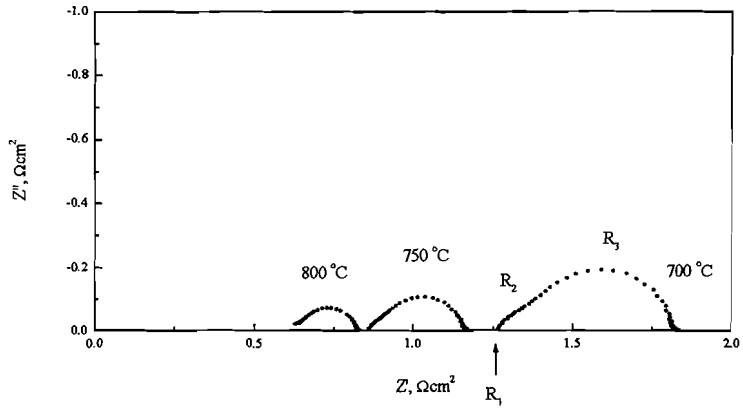
-1.0
-0.8
-0.6
-0.4
-0.2
0.0
Z'', Ωcm²
0.0
0.5
1.0
1.5
2.0
Z, Ωcm²
800 °C
750 °C
700 °C
R1
R2
R3

Figure 5

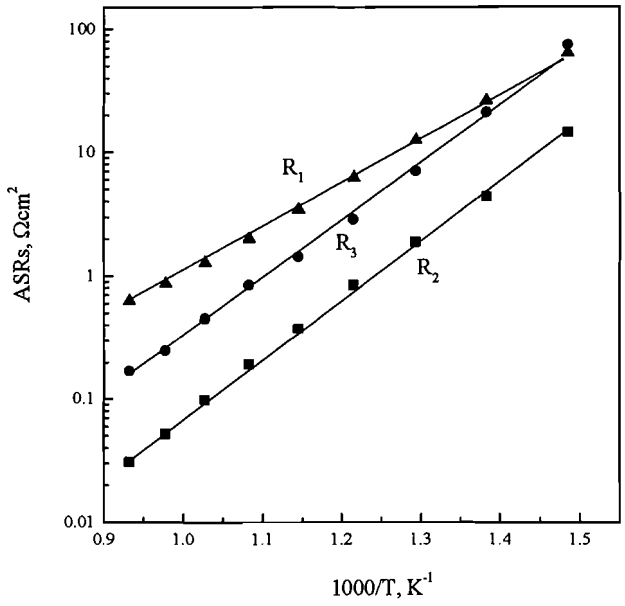

Figure 6

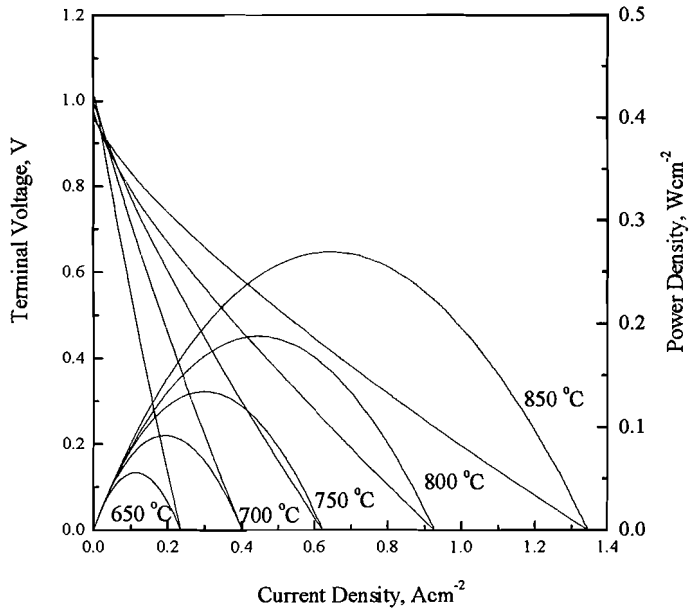
Terminal Voltage, V
Power Density, Wcm^{-2}
Current Density, Acm^{-2}
650 °C
700 °C
750 °C
800 °C
850 °C
0.0
0.2
0.4
0.6
0.8
1.0
1.2
1.4
0.1
0.3
0.5

Figure 7

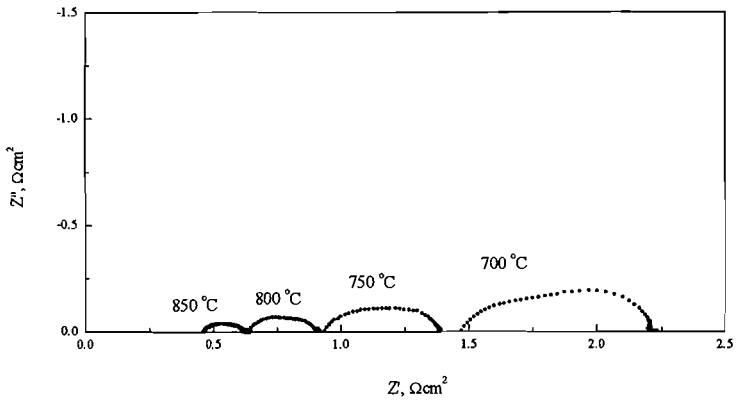

Figure 8

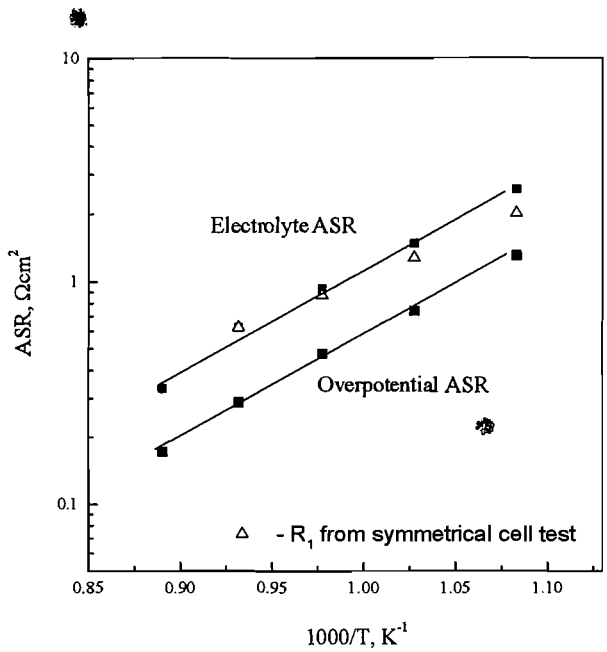
10
1
0.1
ASR, Ωcm²
Electrolyte ASR
Overpotential ASR
△ - R1 from symmetrical cell test
0.85
0.90
0.95
1.00
1.05
1.10
1000/T, K⁻¹

Figure 9

SOFC IX Quebec City May 15-20, 2005

SOME ASPECTS OF DEFECT CHEMISTRY IN P TYPE PEROVSKITE CONDUCTORS

Xiao-Dong Zhou and Harlan U. Anderson

Electronic Materials Applied Research Center, Department of Ceramic Engineering, University of Missouri-Rolla, Rolla, MO 65401, USA

ABSTRACT

This paper is aimed at addressing some fundamental aspects of defect chemistry in p type perovskite conductors, including determination of different oxidation states, contribution of various oxidations states to electronic conduction (p type and n type) and magnetic interaction, origin of nonstoichiometry and defect chemistry modeling. Studies on doped and undoped $LaMnO_{3+\delta}$, $LaCrO_3$, $LaFeO_3$ and $La(Ni,Fe)O_3$ indicate that the electron hole conduction in perovskite MIECs results from high oxidation state of B site cations, in which the electron holes are localized. The magnetic interaction, on the other hand, is attributed to the superexchange between B^{3+} and oxygen ions. The electron conduction in these systems is due to B^{2+}, however some of the perovskites can not hold the structural integrity before B^{2+} cations are generated.

INTRODUCTION

Mixed conduction in ceramic oxides is of particular interest because of the simultaneous transport phenomena of ions and electrons (or electron holes). Research on the p type perovskite mixed ionic and electronic conductors (MIECs) has been stimulated by a variety of electrochemical applications during past decades, such as gas separation membranes, fuel cell electrodes, sensors and catalysts. In addition, some of these materials are being considered as candidates for superconductors or components in giant magneto resistance devices. The most extensive studies materials are the perovskite family oxides with a general formula of ABO_3, in which A, the large cation site, may be an alkali, alkaline earth, or rare earth ion, and B, the small cation site, a transition metal cation. The most important unit in the perovskite structure is the BO_6 octahedral, which repeats in space to form a large crystal through the fully cornered sharing. The larger cation A will fill the cavity. Since A and B sites are very different in size, the occupancy of these sites is determined primarily by ionic size rather than valency, so it is possible to substitute selectively for either the A or B ion by introducing isovalent or aliovalent cations. The oxygen octahedral is the most important group in perovskites because it can tolerate a variety of local chemical and structural changes, such as distortion, rotation, or redox reaction. This provides the materials scientist an opportunity to alter the properties of a given oxide by choosing hosts and substitutes of either the A or B site to meet the requirements of electrochemical applications by assuming that (1) the electronic conductivity (σ) is determined by the B site ion; and (2) the ionic conductivity results

from the motion of oxygen vacancies. When a perovskite which contains transition metal ions on the B site is heated to a sufficiently high temperature that it can equilibrate with the ambient oxygen activity, reversible changes in the oxygen content occur as the oxygen activity is varied. The holes generated through element substitution or changes in oxygen activity are localized on B site cations, thus altering the oxidation states of B site ions. Fluctuation of oxidation states has two primary consequences, (1) influencing the electron-electron interaction between B-O-B, thus magnetic properties and (2) influencing the carrier density, thus electrical properties. This paper is aimed at understanding the oxidation states in several typical p type perovskite conductors, including doped $LaCrO_3$, $LaMnO_3$, $LaFeO_3$ and $La(Ni,Fe)O_3$.

BASIC DEFECT NOTATIONS AND EQUATIONS

The occupants at the A site can be $A_A^{\times}$, $V_A^{'''}$ and $Sr_A^{'}$ (for simplicity, assume Sr is the low valence element substituting at the A site). The occupants at the B site are $B_B^{\times}$, $B_B^{'}$, $B_B^{\bullet}$ and $V_B^{'''}$, where $B_B^{\times}$ indicates a majority of B cations are in valence of 3+, $B_B^{'}$ represents that some B site cations are in 2+ state and $B_B^{\bullet}$ shows some B site cations are in 4+ valence state. The oxygen site can have two types of occupants, $V_O^{\bullet\bullet}$ and $O_O^{\times}$. Nine equations plus the electron neutrality expression are therefore needed in order to determine these nine defect concentrations. The simple solution which was previously presented [1] in the literature solved for the defect concentrations by restricting the electron neutrality conditions to specific oxygen activity and temperature regimes. This limitation can be removed by making digital solutions to yield the defect concentrations using an electron neutrality expression, which covers the entire oxygen activity and temperature range. Moreover, the universal solution can be obtained independent of chemical composition. Details have been published elsewhere. [2,3,4]

OXIDATION STATES

The accuracy for determination of oxidation states and nonstoichiometry lies in the heart in understanding the defect chemistry.[4] Exact oxygen occupancy and valence state of B site cation are key parameters that allow a possibility to develop the right defect chemistry model and then to tailor the materials properties.

$LaCrO_3$ and $LaFeO_3$:

Oxidation states in Fe containing systems (Ferrites) are particularly preferable for the use of Mössbauer spectrometry because of the immediate availability of isotope sources, ^{57}Co, which also can reveals information on chemical bonding and magnetic properties of the ferrites.[5] The isomer shift of Mössbauer spectra provides unequivocal information on the oxidation states of Fe ions. The average isomer shift and hyperfine field values were used to study the valence states and hyperfine interaction in these compounds, from which the average Fe valence was achieved for each specimen. In addition, neutron diffraction is a powerful tool to characterize these oxides because it

resolves not only the crystal structure, but also the magnetic properties and the oxygen vacancy concentration. Compared to x-ray diffraction, neutron diffraction possesses several significant advantages, including: (1) the sensitivity of neutron scattering to light atoms such as oxygen is far greater than that of x-ray scattering because the coherent scattering of neutrons is only determined by the nucleus and is independent of the number of electrons and (2) the neutron has a magnetic moment so it can probe the magnetic structures and excitations through a strong interaction.

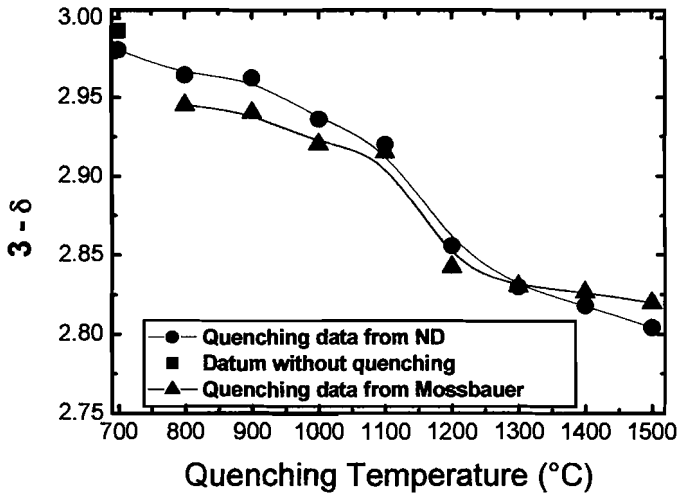

Figure 1 3-δ vs. quenching temperature for LSF, determined from Mössbauer measurements and refinement of neutron diffraction

Based on the charge neutrality, the oxygen occupancy (3-δ) can be calculated from the oxidation states of the cations, which is plotted in Figure 1 as a function of quenching temperature for $La_{0.60}Sr_{0.40}FeO_{3-\delta}$. A datum of ~3 for the specimen without quenching is shown in Figure 1 as well. The relative ratio of Fe^{3+} and Fe^{4+} ions for $La_{0.60}Sr_{0.40}FeO_{3-\delta}$ without quenching obtained from relative areas of the Mössbauer spectra is 64:36, indicating a nearly zero oxygen vacancy concentration in these compounds. This ratio changes to 70:30 for the specimen quenched from 800°C, showing an increase of oxygen vacancy concentration. Shown in Figure 1 also includes oxygen content, which was directly determined from refinements of neutron diffraction results. A value around 2.8 was observed for $La_{0.60}Sr_{0.40}FeO_{3-\delta}$ quenched from 1500°C, whereas full stoichiometry ($\delta \sim 0$) was determined for $La_{0.60}Sr_{0.40}FeO_{3-\delta}$ without quenching. From charge neutrality, it is evident that Fe is in the valence state of 3+ for $La_{0.60}Sr_{0.40}FeO_{2.8}$ and exhibits an average valence state of 3.4 for $La_{0.60}Sr_{0.40}FeO_{3.0}$. Therefore, the magnetic moments for $La_{0.60}Sr_{0.40}FeO_{3-\delta}$ are expected to be a function of δ. The magnetic moment and oxygen content can be determined independently by Rietveld refinement of neutron diffraction data. A strong correlation between oxygen deficiency and magnetic moment has been observed, which indicates that this technique can be used to resolve the oxygen content in perovskite type ferrites. In this study, the highest deficiency ($\delta = 0.2$) corresponds to a nearly pure Fe^{3+} state with a stoichiometric ($\delta = 0$) composition, the fraction Fe^{3+} is 60% and that of Fe^{4+} is 40%. The magnetic moment for $La_{0.60}Sr_{0.40}FeO_{2.8}$ is ~ 3.8μB, which is a typical moment for Fe^{3+} in $LaFeO_3$ system. The magnetic moment for $La_{0.60}Sr_{0.40}FeO_{3.0}$ is ~ 2.3μB (~ 3.8μB × 60%). The magnetic moment is as expected, linear with vacancy concentration and can be used to determine oxygen content by direct

crystallographic refinement. The use of the magnetic moment as a measure of the vacancy concentration has the advantage that it is quite precise and the uncertainty in magnetic moment is 2% at low vacancy concentration, decreasing to less than 1% when the moment is large.

Questions still remain as to the behavior of electrons in Fe^{4+} ions. Information on multivalent Fe site cations and valency distribution can contribute to understanding conduction mechanisms in p type perovskite family oxides. At high temperature, LSF will lose oxygen to form oxygen vacancies, at the cost of decreasing hole concentration. This reaction can be represented in Kröger-Vink notations:

$$2Fe_{Fe}^{\bullet} + O_O^x \rightarrow \frac{1}{2}O_2 + 2Fe_{Fe}^{\times} + V_O^{\bullet\bullet},$$

where $Fe_{Fe}^{\bullet}$ represents Fe ions in the 4+ valence state (similar to holes), $Fe_{Fe}^{\times}$ indicates Fe cations in 3+, and $V_O^{\bullet\bullet}$ represents the oxygen vacancy. Thus, the hole conductivity (σ) follows $\sigma = N\mu q$, where μ is the mobility, q is the carrier charge and N is the hole concentration (Fe4+). Because of the much higher mobility of the electrons or holes than that of oxygen ions, the total conductivity in ferrites is dominated by hole conduction. The carrier concentration can be directly determined from the measurements of Seebeck coefficient (Q). Figure 2 shows the plots of carrier density calculated from Fe4+ concentration, which is determined from the Seebeck coefficient and Fe4+ fraction in the system.

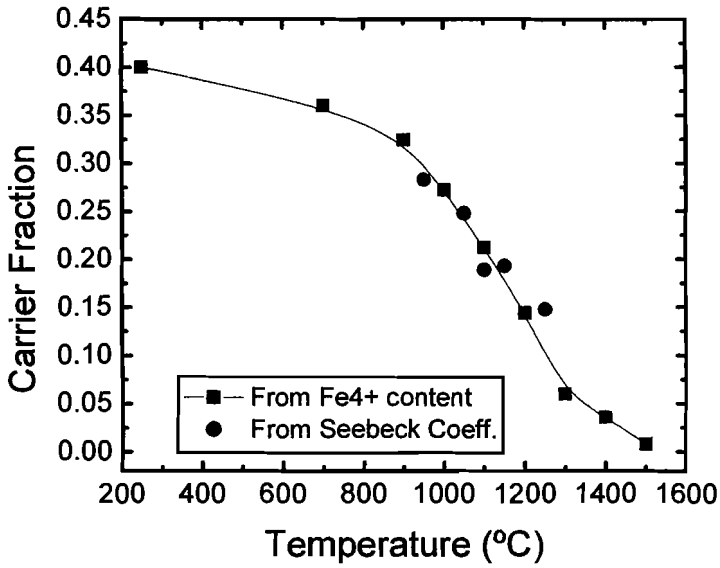

Figure 2: A plot of carrier density calculated from Fe^{4+} concentration and measured carrier density from Seebeck coefficient. [6]

One would expect that a p-n transition occurs when the $Fe_{Fe}^{\bullet}$ concentration (functioning as holes) further decreases, and the average Fe valence drops below 3+, generating electron carriers.. Theoretically, both increasing temperature and decreasing oxygen activity can drive this transition. However, resistivity measurements at 1600°C are extremely difficult to perform. Therefore, we studied this phenomenon by decreasing oxygen activity (from 10^{-13} Pa to 10^{5} Pa) at 1000°C. Figure 3 illustrates this transition.

In the pO_2 region from 10^{-9} Pa to 10^5 Pa, the total isothermal conductivity decreases due to decrease of $Fe^{\bullet}_{Fe}$ (hole) concentration as a result of generation of oxygen vacancies. At the minimum conductivity, Mössbauer data on quenched samples show nearly all Fe cations are in 3+ valence state and oxygen occupancy ~ 2.8, in agreement with the neutron results. Further decreasing oxygen activity increases the Fe^{2+} concentration, which functions as electrons. Thus, conductivity (n type) increases when $pO_2 < 10^{-9}$ Pa (shown in Figure 3).

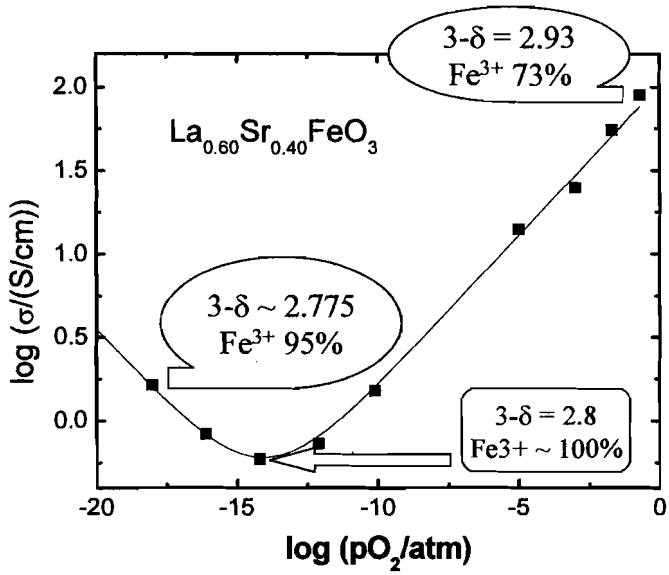

Figure 3: A p-n transition in LSF due to changing of oxygen activity [6]

There exist difficulties in directly determining the oxidation states of Cr ions in chromites, however, extensive work has been performed to indirectly study the Cr oxidation states in A site and/or B site doped $(La,Y)CrO_3$. For example, Flandermeyer et al.[7] showed that the existence of Cr^{4+} in $La(Mg,Cr)O_3$, from which the conductivity and oxygen nonstoichiometry could be fit with a simplified defect chemistry model quite well.

<u>$(La,A)MnO_3$ (where A = Sr or Ca)</u>

Oxidation states of Mn ions in manganites are far more complicated that those of chromites or ferrites. The reasons may have two aspects (1) manganites often have oxygen excess and (2) carrier density is anomalously high in undoped $LaMnO_3$. These two reasons may be correlated. An extensive study was done in the early 1990s by Raffaelle et al.,[8,9] who designed a unique compounds as $La_{1-x}Sr_xCr_{1-y}Mn_yO_{3+\delta}$ ($x = 0$ and 0.1; $0 \leq y \leq 1.0$). A nearly constant carrier density was observed at $T > 1000°C$ when the Mn fraction was higher than 60%, which seemed to be independent of either Sr dopant or Mn contents. They argued that the lack of change in carrier density was due to charge disproportionation from Mn^{3+} to Mn^{2+} and Mn^{4+}, which preserved Mn^{4+} density through the conversion of Mn^{2+} to Mn^{3+}. Additionally, the charge disproportionation reaction successfully explained the carrier density at low Mn concentration through a so-called "trapping to percolation" theory. The charge disproportionation reaction may be very trivial, if there exists, in ferrite systems, as aforementioned magnetic discussion. Mizusaki et al. [10] recently reported that p type conduction changed to n type in the system

of $La_{1-x}Sr_xMnO_{3+\delta}$ when $x > 0.5$, which was deduced from Seebeck coefficient with a value close to zero for $x = 0.5$ and less than zero for $x = 0.7$. Complexity in manganites necessitates the similar studies on coupled magnetic and electrical properties.

La(Ni,Fe)O_3

The Fe^{4+} was argued to be favorable in $La(Ni_{1-x}Fe_x)O_3$, based on the Goodenough-Kanamori superexchange rules, when Ni content (x) is small (<0.5).[11] Mössbauer measurements were performed by Goeta et al. [12] on $x = 0.25$. They obtained Fe^{4+} to Fe^{3+} populations as 52(3)% and 48(3)%, which indicates that a large fraction of Ni cations (~52%) have been pushed from Ni^{3+} to Ni^{2+}. The anomalous Fe^{4+} density leads us to postulate that the carrier density is very high in $La(Ni,Fe)O_3$, in particular when $x > 0.5$. Electrical conductivity measurements were performed on the sintered bars of $x = 0.4$.

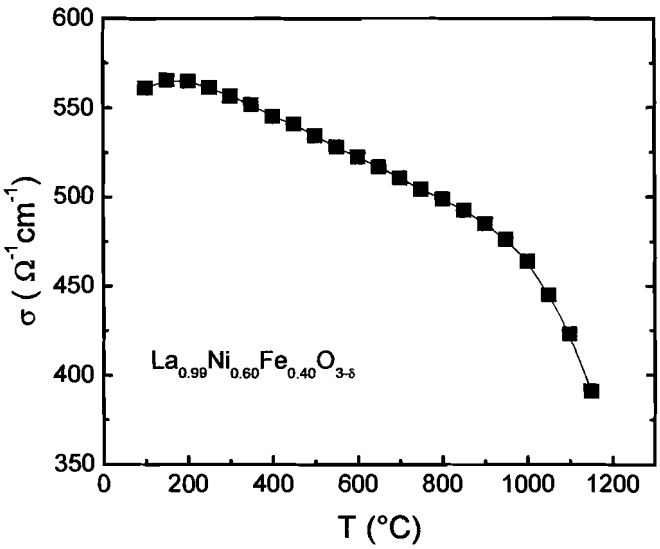

Figure 4: A plot of σ vs. temperature for LNF measured in air

Figure 4 shows the plots of σ vs. temperature (°C) for LNF measured in air from 200°C to 1200°C. A maximum conductivity around 250°C was observed for all gas atmospheres with $\sigma \sim 540$ S/cm in air. A maximum conductivity has been observed in many p-type conductors, which was explained from defect chemistry analysis. The electroneutrality condition is given in the Kröger-Vink notation as $[A'_{Fe}]=2[V_O^{\circ\circ}]+[h^{\circ}]$, where $[A'_{Fe}]$ is the acceptor dopant concentration, $[V_O^{\circ\circ}]$ is the oxygen vacancy concentration and $[h^{\circ}]$ is the hole concentration. The oxygen vacancies are generated at high temperature due to loss of oxygen, which results in a higher $[V_O^{\circ\circ}]$ and a lower $[h^{\circ}]$, assuming $[A'_{Fe}]$ is constant. Therefore, since $\sigma = \mu\ n\ q$, where n is the carrier concentration and q is the carrier charge, at elevated temperature, the mobility increases whereas the carrier concentration, n, decreases, which results in the maximum conductivity. This was found to be valid in most of A site substituted ferrites, manganites and chromites, such as $La_{1-x}Sr_xFeO_3$, $La_{1-x}Sr_xMnO_3$ and $La_{1-x}Sr_xCrO_3$. Both the thermogravimetric analysis and refinements of neutron diffraction showed that oxygen vacancy density was around 1% for LNF quenched from 1100°C, therefore the

decrease in conductivity at T > 1100°C in Figure 4 can be contributed to generation of oxygen vacancies. Oxygen content in LNF, however, was determined to be ~3.0 for the sample quenched from T < 1000°C. Thus, the decreasing conductivity in LNF from 300 to 1000°C may not be attributed to generation of oxygen vacancies. This behavior is not well understood. Chainani et al. [13] has studied low temperature electrical conductivity of $LaNi_{1-x}Fe_xO_3$ and observed an increase of conductivity in the temperature range from 2 to 300K for x > 0.3. They explained this behavior in terms of a metal-insulator transition and therefore, the negative temperature coefficient for conductivity was the result of scattering. This explanation seems reasonable, however, the conductivity value in their system was much lower (~10X) than that measured in this study, which could be because the sintering temperature (800°C) was too low and thus the final density was too low and the specimens were porous.

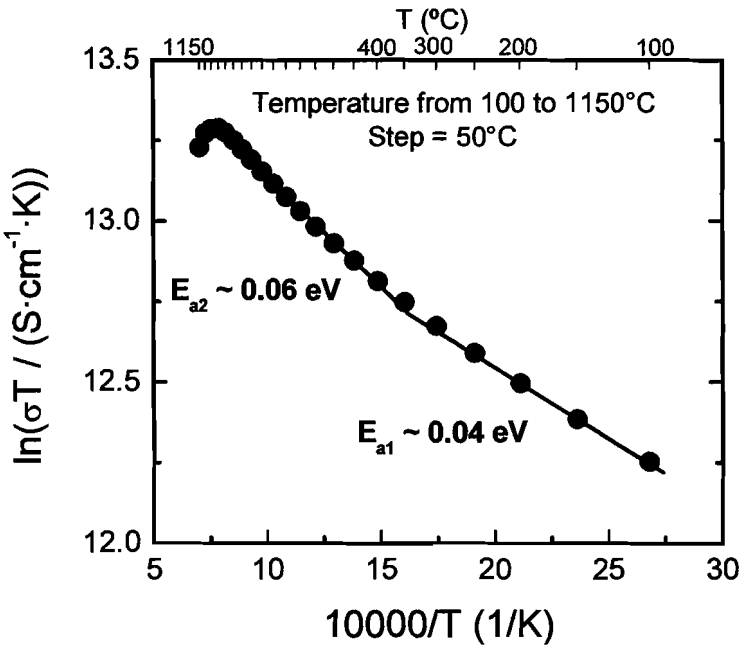

Figure 5: A plot of ln(σT) vs. 1/T for LNF measured in air

A plot of ln(σT) vs. 1/T (Figure 5) may enable us to understand the conduction mechanism by assuming a small polaron conduction in LNF system and mobility following non-adiabatic condition as $\mu \propto \frac{\mu_0}{T}\exp(-\frac{E_a}{kT})$. A maximum of ln(σT) was observed at T = 1000°C, at which oxygen vacancies started to play a role in the total carrier concentration. Two separate regions at T < 1000°C with activation of 0.06eV and 0.04eV indicate the possibility of different conduction mechanisms for temperature less than 1000°C. A comparison of LNF with LSF, LSM and LSCr suggests that the LNF redox reaction takes place in two cations, Ni and Fe, whereas the redox reaction only occurs for a single cation in LSF, LSM and LSCr system. This may be the reason that the nonlinearity is observed. The very low activation energy may very well represent small polaron conduction; however more work has to be performed in order to resolve the conduction mechanism.

CONCLUSIONS

In summary, oxidation states of the B site ions in p type perovskite conductors has been discussed in ferrites, chromites, manganites and nickelates. The low valence element substitution into ferrites and chromites was compensated by higher oxidation state Fe and Cr, both in 4+ states. Charge disproportionation was assumed in manganites, which was successfully explained the origin of higher carrier density in undoped $LaMnO_{3+\delta}$. The disproportionation reaction is trivial in $LaFeO_3$ and $LaCrO_3$ systems. A large fraction of high oxidation Fe ions (4+) were observed in the $La(Ni,Fe)O_3$ system. Complexity of oxidation states in manganites and nickelates necessitates further studies on coupled electrical and magnetic properties.

ACKNOWLEDGEMENTS

The authors wish to thank the Department of Energy, the Gas Research Institute and Praxair, Inc who provided financial support for part of this research.

REFERENCES:

[1] H. U. Anderson, "Review of p-type doped perovskite materials for SOFC and other applications," *Solid State Ionics* 52, 33-41 (1992).

[2] J. Nowotny and M. Rekas, "Defect chemistry of (La,Sr)MnO_3" *J. Am. Ceram. Soc.* **81**, 67-80 (1998).

[3] F. W. Poulsen, "Defect chemistry modeling of oxygen-stoichiometry, vacancy concentrations, and conductivity of $La_{1-x}Sr_xMnO_{3\pm\delta}$" *Solid State Ionics* 129, 145-162 (2000).

[4] X.-D. Zhou and H. U. Anderson, "Defect Chemistry in Ternary Compounds," in "Materials for Energy Conversion Devices," C. C. Sorrell, J. Nowotny, and S. Sugihara, Ed., Woodhead Publishing Ltd., (2004) (In press)

[5] X.-D Zhou, Q. Cai, Z. Chu, J. Yang, W. B. Yelon, W. J. James and H. U. Anderson, "Utilization of Neutron Diffraction and Mössbauer Spectroscopy in the Studies of the Cathode for SOFCs," *Solid State Ionics* **175**, 83-86 (2004).

[6] X.-D. Zhou, J. B. Yang, Q. Cai, M. Kim, W. B. Yelon, W. J. James and H. U. Anderson, "Coupled Electrical and Magnetic Properties in (La,Sr)$FeO_{3-\delta}$ by *in Situ* Studies," *J. Appl. Phys.* (In press)

[7] B. K. Flandermeyer, "Thermogravimetric and Electrical Conductivity Studies of Mg-doped $LaCrO_3$ and La Doped $SrTiO_3$," University of Missouri-Rolla, Dissertation (1984).

[8] R. Raffaelle, H. U. Anderson, D. M. Sparlin, and P. E. Parris, "Transport anomalies in the high-temperature hopping conductivity and thermopower of Sr-doped La(Cr,Mn)O_3," *Phys. Rev. B* **43**, 7991–7999 (1991).

[9] Raffaelle, H. U. Anderson, D. M. Sparlin, and P. E. Parris, "Evidence for a crossover from multiple trapping to percolation in the high-temperature electrical conductivity of Mn-doped $LaCrO_3$," *Phys. Rev. Lett.* **65**, 1383–1386 (1990)

[10] J. Mizusaki, Y. Yonemura, H. Kamata, K. Ohyama, N. Mori, H. Takai, H. Tagawa, M. Dokiya, K. Naraya, T. Sasamoto, H. Inaba, and T. Hashimoto, "Electronic conductivity, Seebeck coefficient, defect and electronic structure of nonstoichiometric $La_{1-x}Sr_xMnO_3$," *Solid State Ionics* **132**, 167-180 (2000).

[11] N. Y. Vasanthacharya, P. Ganguly, and C. N. R. Rao, "Magnetic Interactions in the Oxide Systems $LaNi_{1-x}M_xO_3$ (M = Cr, Fe, or Co)," *J. Solid state Chem.* **53**, 140-143 (1984).

[12] A. E. Goeta, G. F. Goya, R. C. Mercader, and G. Punte, "Oxidation States of Fe in $LaNi_{1-x}Fe_xO_3$," *Hyperfine Interactions* **90**, 371-375 (1994)

[13] A. Chainani, D. D. Sarmayk, I. Dasz and E. V. Sampathkumaranz, "Low-temperature electrical conductivity of $LaNi_{1-x}Fe_xO_3$," *J. Phys. Cond. Matt.* **8**, L631-L636 (1996).

Electrochemical and Solid-State Letters, 7 (11) A391-A393 (2004)
1099-0062/2004/7(11)/A391/3/$7.00 © The Electrochemical Society, Inc.

Single Chamber Electrolyte Supported SOFC Module

Toshio Suzuki,*,z Piotr Jasinski,* Harlan U. Anderson* and Fatih Dogan

Electronic Materials Applied Research Center and Department of Ceramic Engineering, University of Missouri-Rolla, Rolla, Missouri 65401, USA

An electrolyte supported single chamber solid oxide fuel cell (SOFC) module consisting of two cells has been proposed. The module consists of one Sm-doped CeO_2 (SDC) electrolyte substrate (0.5 mm thick with the size of 5 × 10 mm), two Ni-SDC anodes on one side, and two SDC-$(La,Sr)(Co,Fe)O_3$ cathodes on the other side. Two modules with different electrode areas were prepared and tested using an air-propane mixture. The electrode area had a strong influence on the performance of the module. It was shown that the two-cell module generated 1.5 V open-circuit voltage and about 17 mW maximum power at 550°C.
 [DOI: 10.1149/1.1799952]

Manuscript submitted February 13, 2004; revised manuscript received March 11, 2004. Available electronically September 28, 2004.

Single chamber solid oxide fuel cells (SC-SOFCs) operate in a mixture of fuel and oxidant gas with both anode and cathode exposed to the same gas environment.[1] The oxygen activity at the anode and cathode is not fixed. The anode has a higher electrocatalytic activity for the partial oxidation of the fuel and the cathode has a higher electrocatalytic activity for the reduction of oxygen. As a result, an electromagnetic field (EMF) between the two electrodes will be generated even in a mixed-gas atmosphere. Direct use of hydrocarbon fuel is a challenging issue in the conventional (double chamber) SOFC and a number of studies have been reported, especially focused on Ni-free anodes.[2] For SC-SOFC with Ni-cermet anode, carbon deposition is less of a problem due to the presence of oxygen, which leads to partial oxidation of the fuel rather than coking (carbon deposition). However, an optimum fuel-oxygen ratio must be sought even in SC-SOFC to avoid carbon depositions. Several studies have been reported on this, showing that the optimum fuel-oxygen ratio was also affected by the type of fuel and catalyst.[3] Recent studies have shown that relatively high power densities in the range of 250-650 mW cm^{-2} were obtained in SC-SOFCs at operating temperatures in the 400-550°C range using hydrocarbon fuel.[4,5]

Because of the simplified cell structure of SC-SOFC, a miniature cell module can be utilized for devices with low power demand. In this study, a design of electrolyte supported SOFC module is proposed. The module was prepared using conventional ceramic processing techniques and tested using an air-propane mixture as fuel. Two cells were processed on an electrolyte (0.5 mm thick with the size of 5 × 10 mm), which consisted of a Ni-SDC anode and SDC-$(La,Sr)(Co,Fe)O_3$ (LSCF) cathode as illustrated in Fig. 1. Sm-doped ceria (SDC) was selected as an electrolyte due to its relatively high ionic conductivity. The SDC-LSCF cathode was studied by the authors and served as an excellent cathode material for SC-SOFC.[6]

Sm-doped ceria (SDC) electrolyte was prepared by pressing commercial powder at 2 × 10^3 kg cm^{-2} (20% samarium-doped ceria, Daiichiki Genso, Co., Japan) and sintering at 1500°C for 10 h. The anode consisting of 70 wt % Ni-SDC ink (anode) was painted on the electrolyte and sintered at 1450°C for 1 h. Subsequently, a cathode consisting of $La_{0.8}Sr_{0.2}Co_{0.2}Fe_{0.8}O_3$ (LSCF) and SDC powder (10 vol % SDC in LSCF) ink was painted on the electrolyte and sintered at 1000°C for 1 h.[4] A cell and two modules with difference electrode areas were prepared on the 5 × 10 mm SDC electrolyte using the same anode and cathode materials; a single cell with a 3 × 6 mm electrode and double cell modules with two 2 × 2 mm (module A) and 3 × 3 mm (module B) electrodes. The cells on the SDC were connected in series using Au paste (Fig. 1). Pt and Au mesh were used as current collectors for the anode and cathode, respectively. Minimum amounts of Pt paste for anode and Ag paste for cathode were used to improve the attachment of mesh to the electrodes.

The cell and the modules were placed in an alumina tube (~5 mm diam) with a flowing gas mixture of propane (10%) and air (90%). The ratio of gas mixture is off-stoichiometric of the partial oxidation reaction. However this oxygen-rich region showed better prevention of carbon deposition which lowers the performance of the cell. The flow rate of mixed gas was adjusted to 300 cm^3 min^{-1} by a gas flow controller. The alumina tube was placed in a furnace and heated between 500 and 575°C. The temperature of the furnace and the sample were monitored simultaneously. Impedance spectroscopy was used to investigate the cell performance using a Solartron 1470 battery tester and 1255B impedance gain phase analyzer. The impedance spectra were obtained using a 1 mA load.

Figure 2 shows the discharge profile of the single cell. The open-circuit voltage (OCV) of the cell was stable and showed ~0.8 V within the test temperature range. The power of about 17 mW was obtained at 550°C. The impedance spectra in Fig. 3 show a relatively small overpotential for the higher furnace temperatures. Considering that the high frequency intersection with Z′ axis (Fig. 3) was the electrolyte resistance, the sample (cell) temperatures should be 60-80°C higher than the furnace temperature. However, the actual measured cell temperature was only 15-20°C higher than the

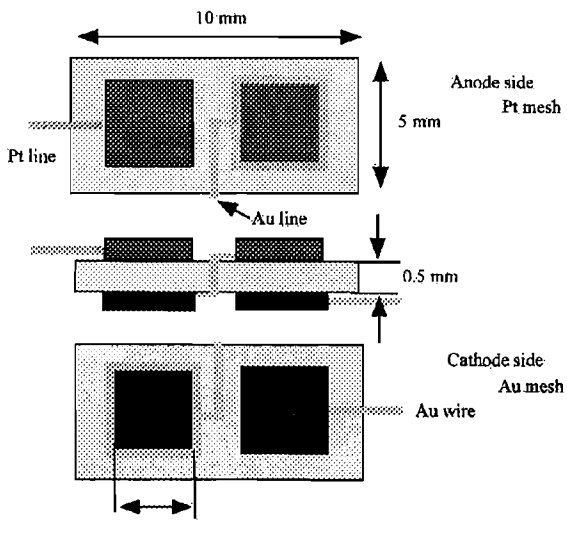

Figure 1. Schematic diagram of SC-SOFC module.

* Electrochemical Society Active Member.
z E-mail: toshio@umr.edu

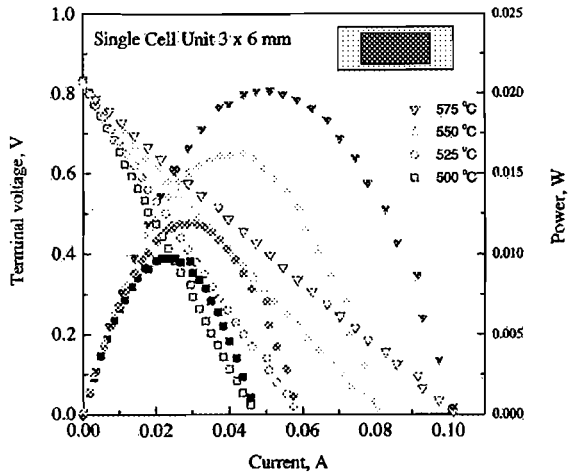

Figure 2. Temperature dependence of discharge profile (I-V open symbols and P-I closed symbols) for single cell (3 × 6 mm).

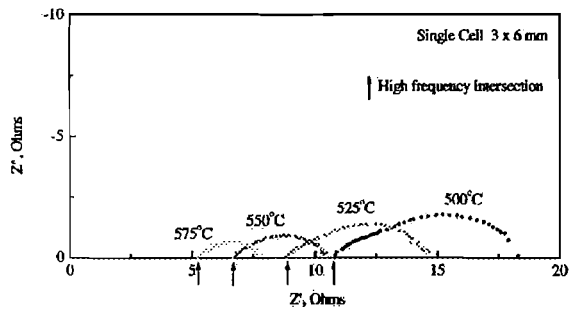

Figure 3. Impedance spectra for single cell test (3 × 6 mm).

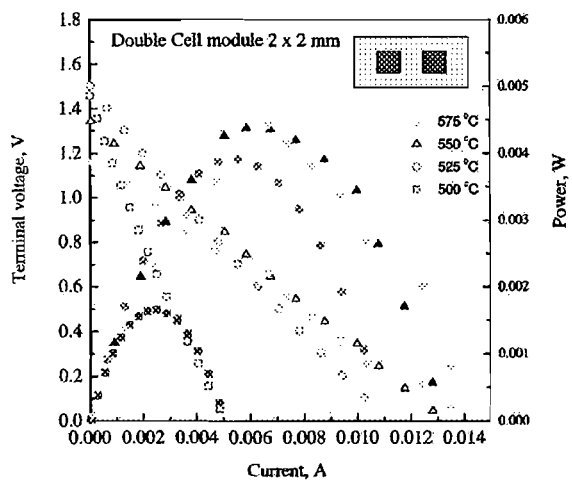

Figure 4. Temperature dependence of discharge profile (I-V open symbols and P-I closed symbols) for double cell module SC-SOFC (2 × 2 mm cell).

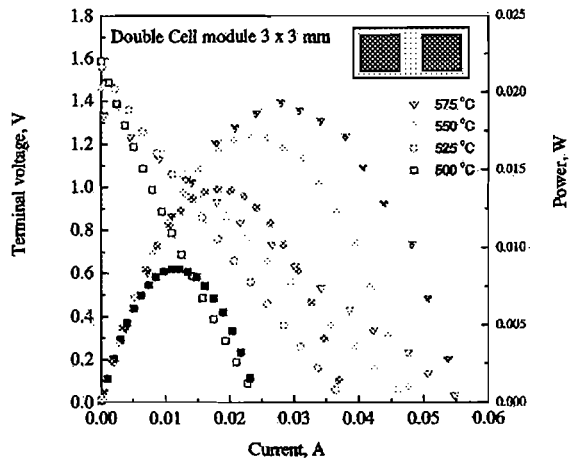

Figure 5. Temperature dependence of discharge profile (I-V open symbols and P-I closed symbols) for double cell module SC-SOFC (3 × 3 mm cell).

furnace temperature, which is probably due to inaccuracy of the temperature measurement with the thermocouple. As can be seen, the electrolyte resistance appeared to be of great influence on the performance of the cell. This implies that the cell performance can be improved by reducing the electrolyte thickness.[2]

Figures 4 and 5 show the discharge profile of the double cell configurations with 2 × 2 mm (module A) and 3 × 3 mm (module B) electrodes, respectively. Module A with the smaller electrode area showed terminal voltage as high as 1.5 V, but a lower maximum current than that expected from the results in Fig. 2. This may be attributed to the small electrode area, which results in lower cell temperature due to the catalytic reaction occurring over a smaller area. The voltage of module B reached as high as 1.6 V OCV with a maximum power of 8 mW at 500°C, and 1.5 V OCV with a maximum power of 17 mW at 550°C furnace temperature.

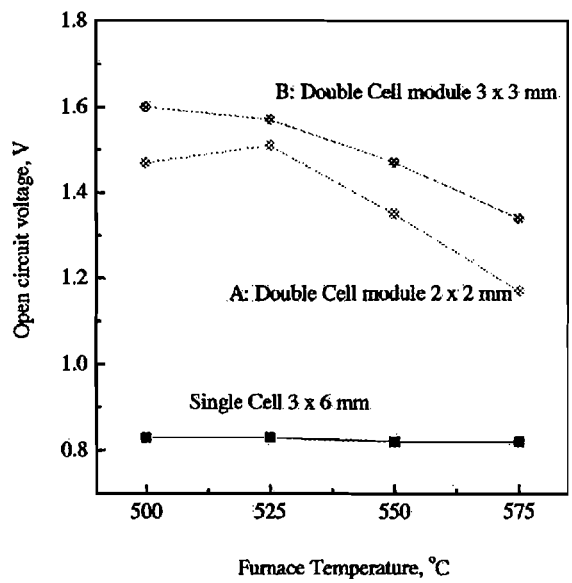

Figure 6. OCV as a function of furnace temperature.

Figure 6 shows the OCV of the cells as a function of furnace temperature. While the single cell with 3 × 6 mm electrode showed a stable voltage with respect to the temperature variations, the voltage of double cell modules decreased as the furnace temperature increased. Such a dependence may be attributed to local temperature variations, gas flows in the measuring system, etc.; however, the OCV of the cell would not be influenced by current collector or geometry of electrodes. This could be simply related to the change of the oxygen activity on the electrodes and/or electron leakage from Au interconnect, which was attached on the electrolyte. Because the voltage drop became significant as electrode area decreased, these results suggest that the electrode size may be the limitation for this module geometry. As mentioned above, a Au interconnect was attached to the electrolyte and, therefore, there is a possibility of electron leakage through the electrolyte thereby lowering the OCV.

In summary, module B (electrode area 3 × 3 mm) showed stable performance below 550°C furnace temperature. Based on these results, one would expect that a ceramic tube (10 cm long and 5 mm diam) containing a 20 cell module with a single electrode area 3 × 3 mm would result in an OCV of 15 V and ~0.18 W maximum power at 550°C. As discussed above, the power density of the cell can be increased by reducing the thickness of the electrolyte.

Acknowledgments

The authors thank the Research Board of University of Missouri for financial support of this research.

The University of Missouri-Rolla assisted in meeting the publication costs of this article.

References

1. T. Hibino, A. Hashimoto, T. Inoue, J. Tokuno, S. Yoshida, and M. Sano, *Science*, **288**, 2031 (2000).
2. S. Park, J. M. Vohs, and R. J. Gorte, *Nature (London)*, **404**, 265 (2000).
3. T. Hibino, S. Wang, S. Kakimoto, and M. Sano, *Solid State Ionics*, **127**, 89 (2000).
4. T. Hibino, A. Hashimoto, T. Inoue, J. Tokuno, S. Yoshida, and M. Sano, *J. Electrochem. Soc.*, **148**, A544 (2001).
5. T. Hibino, A. Hashimoto, M. Yano, M. Suzuki, S. Yoshida, and M. Sano, *J. Electrochem. Soc.*, **149**, A133 (2002).
6. T. Suzuki, P. Jasinski, F. Dogan, and H. U. Anderson, *J. Electrochem. Soc.*, **151**, 021410 (2004).

Journal of The Electrochemical Society, **151** (10) A1678-A1682 (2004)
0013-4651/2004/151(10)/A1678/5/$7.00 © The Electrochemical Society, Inc.

Role of Composite Cathodes in Single Chamber SOFC

Toshio Suzuki,[a,*,z] Piotr Jasinski,[a,*] Harlan U. Anderson[a,*] and Fatih Dogan[b]

[a]Electronic Materials Applied Research Center, [b]Department of Materials Science and Engineering, University of Missouri-Rolla, Rolla, Missouri 65401, USA

The influence of cathode composition on the open-circuit voltage (OCV) and the performance of a single chamber solid oxide fuel cell (SC-SOFC) was investigated. Because the SC-SOFC is operated using a mixture of air and fuel, the OCV of the cell is determined by the difference of catalytic activity between the cathode and anode. Due to its catalytic activity with fuel, Ni-cermet has proven to be an excellent anode. Typical cathode materials such as perovskite oxides also have catalytic activity with fuel, which can influence the OCV. In this study, cells with composite cathode materials (a mixture of Sm-doped ceria (SDC) and (La, Sr)(Co, Fe)O_3 (LSCF)) and reference electrode (Ag) on SDC electrolyte were prepared and tested in a mixture of propane and air. Several cathode compositions yielded a voltage as high as 0.1 V against the Ag reference electrode and the voltage decreased as the SDC content in the LSCF increased. These cathodes were also tested in the SC-SOFC configuration with Ni-cermet anode on an SDC electrolyte (0.5 mm thick). A cell using a cathode composition of 30 vol % SDC-LSCF showed the lowest overpotential among those tested.
 [DOI: 10.1149/1.1786071]

Manuscript submitted February 20, 2004; revised manuscript received March 3, 2004. Available electronically September 27, 2004.

Single chamber solid oxide fuel cells (SC-SOFCs) whose anode and cathode are exposed to the same mixture of fuel and oxidant gas have been proposed and successfully demonstrated by Hibino *et al.*[1-3] These studies have shown that a relatively high power density can be obtained in operating temperatures as low as 550°C using hydrocarbon fuel. These cells typically consist of Sm-doped ceria (SDC) as the electrolyte, Ni-SDC cermet as the anode, and (Sm, Sr)CoO_3 as the cathode.

Because this cell operates in a mixture of fuel and oxidant gas, it has several advantages: (*i*) a simplified cell (module/stack) structure can be made because sealing is not required, (*ii*) there are fewer problems with thermal and mechanical stress compared to double chamber SOFCs, and (*iii*) due to the fuel oxidation reaction, the cell temperature can effectively be increased; consequently, the cell resistance can be reduced.[3]

The oxygen activity at the electrodes is not fixed, and one electrode has a higher electrocatalytic activity for the oxidation of the fuel (propane as an example), as given possibly by the following reactions

$$C_3H_8 + 3/2\ O_2 \rightarrow 3CO + 4H_2 \quad [1]$$

$$H_2 + O^{2-} \rightarrow H_2O + 2e^- \quad [2]$$

and

$$CO + O^{2-} \rightarrow CO_2 + 2e^- \quad [3]$$

The other electrode has a higher electrocatalytic activity for the reduction of oxygen as follows

$$1/2\ O_2 + 2e^- \rightarrow O^{2-} \quad [4]$$

As a result, an electromotive force (emf) between two electrodes is generated even in a uniform gas composition due to the high catalytic activity of anode materials such as Ni-cermet. However, studies have shown that typical cathode materials such as perovskite oxides also exhibit catalytic activity for hydrocarbon oxidation[4] and may affect the emf of the cell.

In this study, cells were prepared using SDC as an electrolyte, Ni-SDC cermet as an anode, and several composite mixtures of SDC and (La, Sr)(Co, Fe)O_3 as cathodes. The influence of cathode materials on the cell voltage has been investigated using an Ag reference electrode in a propane/air mixture.

* Electrochemical Society Active Member.
[z] E-mail: toshio@umr.edu

Experimental

The electrolyte, which consisted of 0.5 mm thick SDC, was prepared by dry pressing commercial powder, 20% SDC (Daiichiki Genso, Co, Japan) at 2×10^3 kg cm^{-2} and sintering at 1500°C for 10 h. Subsequently, the anode material (70 wt % Ni-SDC) was screen printed onto the electrolyte and sintered at 1450°C for 1 h. The cathode, a mixture of $La_{0.8}Sr_{0.2}Co_{0.2}Fe_{0.8}O_3$ (LSCF) and SDC powder (0, 10, 30 vol % SDC) was then screen printed onto the electrolyte and sintered at 1000°C for 1 h. The cathode and anode were each about 20 μm thick. Typical specimen sizes are 0.18 cm^2 electrode area. The microstructures of different SDC content cathodes were analyzed by scanning electron microscopy (SEM) (Hitachi S4700).

As illustrated in Fig. 1, the properties of the cells were measured using a tube furnace in which a mixed gas with a composition consisting of propane (10 vol %) and air (90 vol %) was flowing at a rate of 300 cc min^{-1}, avoiding the explosion limits (2.1-9.5 vol % of propane in air). The fuel-oxygen ratio of 1:1.8 in this mixture, which is oxidant rich compared to the conditions in Reaction 1 (1:1.5), can prevent possible problems with the carbon deposition. Note that Reaction 1 is a heterogeneous reaction occurring on the surface of the catalyst. Therefore, the optimum ratio of fuel-oxygen could vary, depending on the type of fuel gas and catalyst.[5] The furnace temperature was controlled between 500 to 650°C while the sample temperature was simultaneously monitored. Pt and Au mesh, whose sizes were adjusted to the electrode size, were used as current collectors for the anode and cathode, respectively.[1-3] Minimum amounts of Pt and Ag paste for the anode and cathode, respectively, were used to improve the attachment between mesh and electrodes.

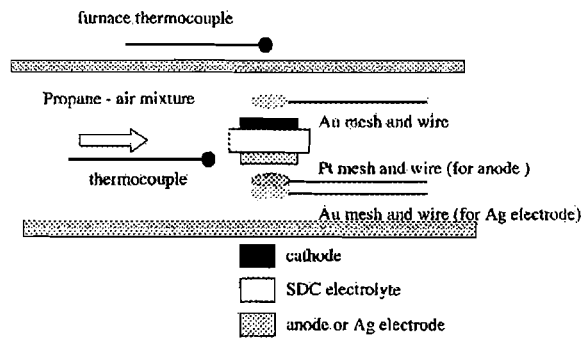

Figure 1. Experimental setup for SC-SOFC test.

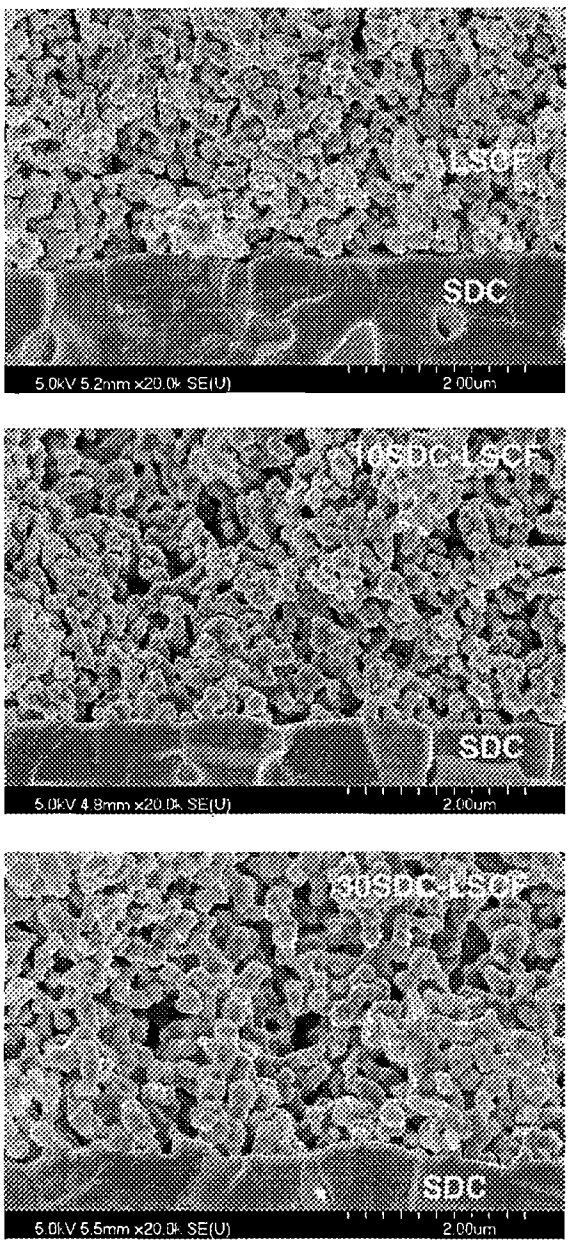

Figure 2. SEM images of cathode materials on electrolyte: (top) LSCF, (middle) 10SDC-LSCF, and (bottom) 30SDC-LSCF.

Ag paste (Electro-Science Laboratories, King of Prussia, PA) was used as a reference electrode. The cell performance was investigated by impedance spectroscopy using a Solartron 1470 battery tester and a 1255B impedance gain phase analyzer. The impedance spectra were collected under a 1 mA current load.

Results and Discussion

Figure 2 shows SEM images of SDC-LSCF cathodes prepared on the SDC electrolyte: (top) LSCF, (middle) 10 vol % SDC (10SDC-LSCF), and (bottom) 30 vol % SDC (30SDC-LSCF). As can be seen, both the porosity and the bonding of particles at the electrolyte interface improved as the SDC content increased. These changes in microstructure can be expected to influence the performance of the cells.

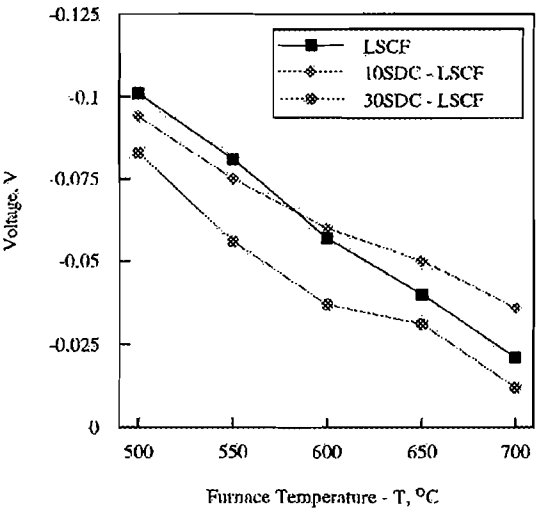

Figure 3. Voltage occurring between varying SDC content LSCF electrodes and Ag electrode as a function of furnace temperature.

Figure 3 shows the voltage occurring between cathodes with different SDC contents in LSCF and the Ag reference electrode as a function of furnace temperature. The minus sign in the voltage means that the SDC-LSCF composites act as an anode relative to the Ag reference electrode. These results show that the voltage over the temperature range 500-650°C reached as high as 0.1 V, which implies that LSCF also exhibits catalytic activity for hydrocarbon oxidation (Reaction 1). As can be seen, the voltage decreased as the SDC content in LSCF increased. An increase of SDC content in LSCF may cause a decrease in the number of catalytically active sites, leading to a decrease in the reaction rate. As a result, the voltage decreases as the SDC content increases in LSCF. Figure 3 also shows that the negative potential of the cathode against the

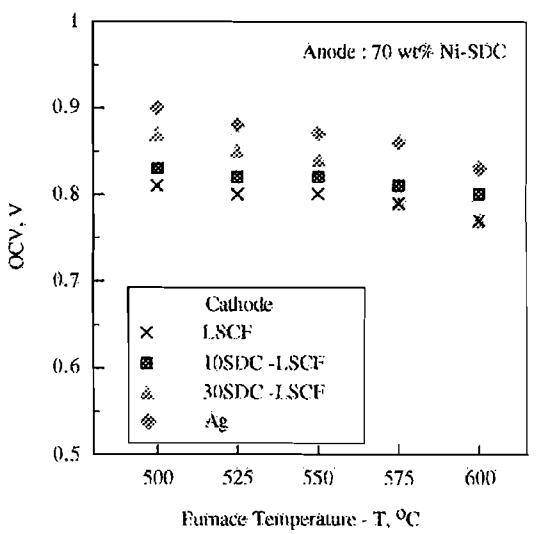

Figure 4. OCV for SC-SOFC with several electrodes *vs.* Ni-cermet anode.

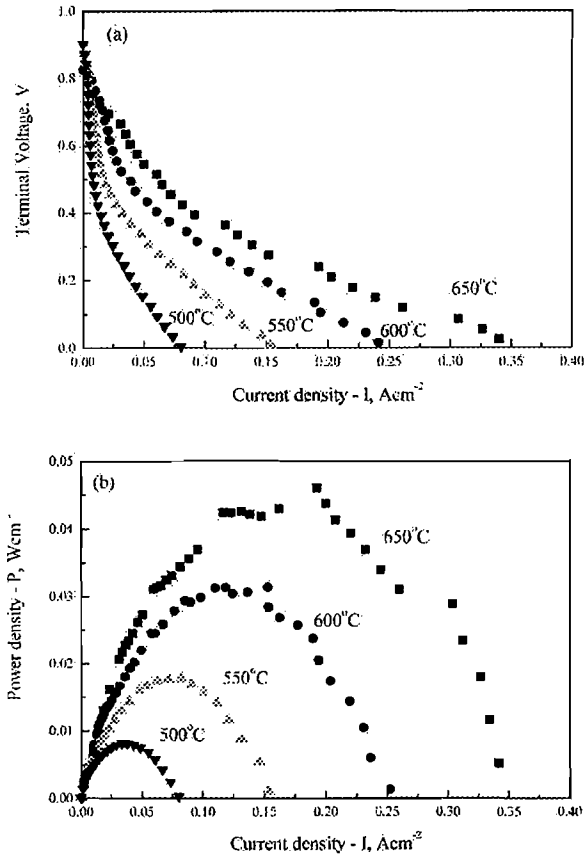

Figure 5. Cell performance of Ag/SDC/Ni-SDC cell in SC-SOFC condition. (a) Current-voltage (I-V) discharge profile, (b) the power density. Electrolyte thickness = 0.5 mm.

reference electrode decreased with increasing temperature, which suggests that the catalytic activity of the cathode decreases as the temperature increases. This contradicts the general behavior of catalysts for hydrocarbon oxidation. A possible explanation for this contradiction is that both the reference electrode and the cathode show

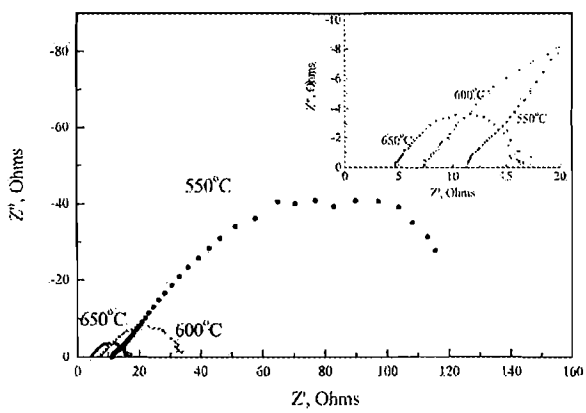

Figure 6. Impedance spectra for Ag/SDC/Ni-SDC cell.

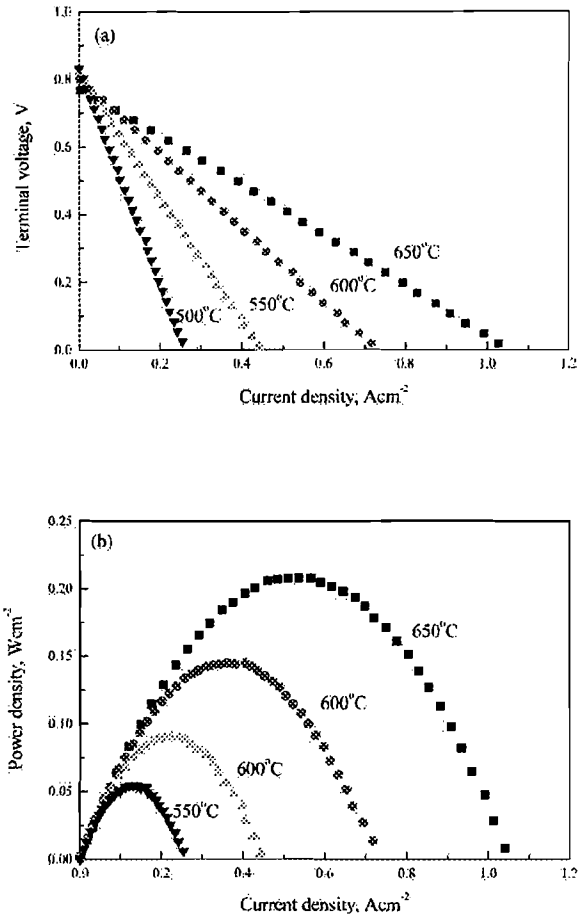

Figure 7. Cell performance of 10SDC-LSCF/SDC/Ni-SDC cell in SC-SOFC condition. (a) I-V discharge profile, (b) the power density. Electrolyte thickness = 0.5 mm.

an increasing catalytic activity for the hydrocarbon oxidation with increasing temperature. Therefore, the difference in catalytic activity between the two electrodes is reduced at high temperatures, thus resulting in a small voltage between them. Further studies are required before this behavior can fully be understood.

Figure 4 shows the open-circuit voltage (OCV) of the cell using 70 wt % Ni-SDC anode for different cathode compositions as a function of furnace temperature. As can be seen, the OCV showed higher values as the SDC content increased over the temperature range 500-650°C. These results are consistent with those shown in Fig. 3, showing that the use of catalytic active materials in the cathode lowers the OCV of the cell. The drop of OCV in the 30SDC-LSCF for the furnace temperature above 550°C is not understood, but it may be due to cracking of the sample during measurements, which has been observed in some specimens.

The discharge profile and the power density for the Ag/SDC/Ni-SDC cell are shown in Fig. 5. Although the cell showed the highest OCV, its performance was lower than that obtained using other cathode materials. The lower performance can be explained by the impedance spectra shown in Fig. 6. As can be seen, large overpotentials were observed, which may be related to the gas diffusion process[6] due to the lack of porosity in the Ag electrode.

As shown in Fig. 7, the best cell performance was obtained using a cell with the 10SDC-LSCF cathode, which had a maximum power

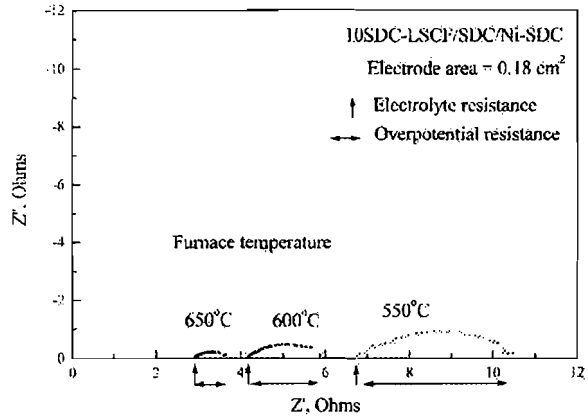

Figure 8. Impedance spectra for 10SDC-LSCF/SDC/Ni-SDC cell.

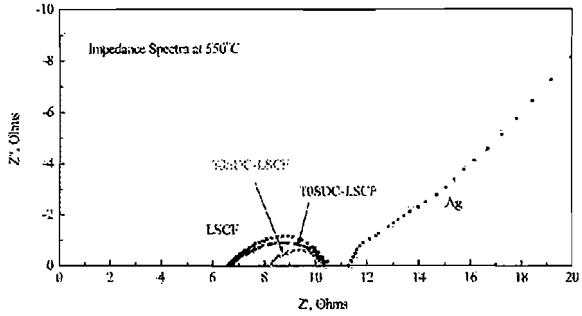

Figure 10. Impedance spectra of SC-SOFC with different cathode materials at 550°C furnace temperature.

density of 210 mW cm^{-2} at about 0.4 V at 650°C. Figure 8 displays the impedance spectra of this cell showing relatively small overpotentials. The intersection of the semicircle at high frequency with the Z′ axis was taken as the electrolyte resistance. The electrolyte resistance obtained from the impedance spectra was less than that reported in the literature,[7] which is probably due to an increase in temperature resulting from Reaction 1. The electrolyte resistance of the cell can be estimated as 16 Ω at 600°C,[7] as compared to 7.5 Ω determined from the impedance spectrum in Fig. 6, which implies that the cell temperature increases about 60-80°C. The area specific resistance (ASR) as a function of reciprocal furnace temperature for the electrolyte and the overpotential are shown in Fig. 9. As can be seen, the ASR of the electrolyte limits the performance of the cell, which can be improved by reducing the electrolyte thickness.[2]

Figure 10 shows the influence of cathode composition on the impedance spectra determined at 550°C furnace temperature. As can be seen, the high-frequency intercepts of the semicircle (electrolyte resistances) shifted to lower resistance as the SDC content decreased. This can be explained by the increase of cell temperatures due to the increase of catalytic activity by reducing SDC content in the LSCF. This is consistent with the results shown in Fig. 3; a higher OCV (higher catalytic activity) was observed when the SDC content in LSCF decreased. The ASR of the cell as a function of reciprocal furnace temperature is plotted in Fig. 11, showing the lowest overpotential for the cell with the 30SDC-LSCF cathode composition. The lower performance of the cell with the 30SDC-LSCF cathode composition is probably related to lower cell temperature, resulting from lower catalytic activity of the cathode.

Among the specimens tested, the cell with the 10SDC-LSCF cathode achieved the highest power density of 210 mW cm^{-2} at 650°C. As discussed previously, the cell performance is not only affected by the OCV and the overpotential of electrodes, but also by the catalytic effect of cathode materials. Further improvement of cell

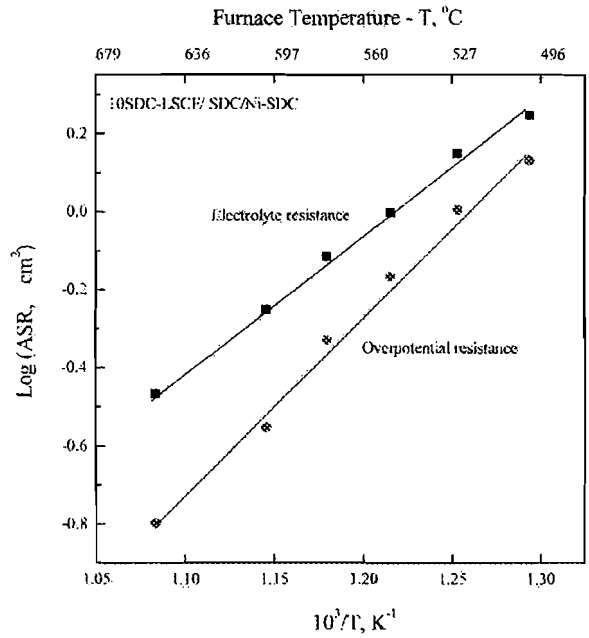

Figure 9. ASR of electrolyte and overpotential for SDC-LSCF/SDC/Ni-SDC cell.

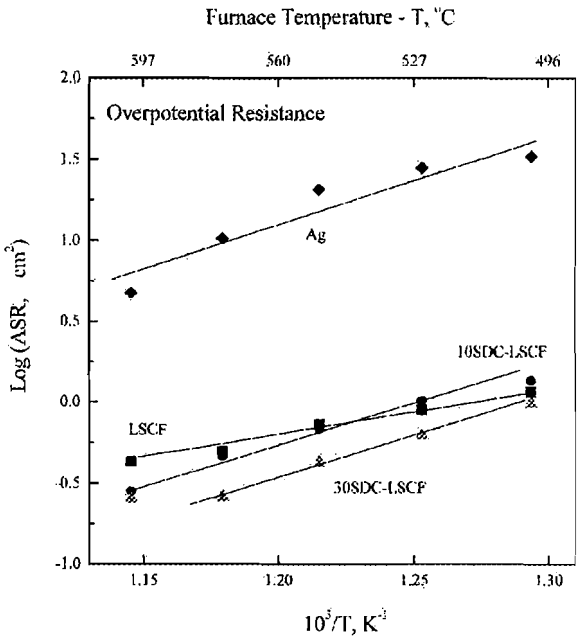

Figure 11. ASR of overpotential for SC-SOFCs with different cathode materials.

performance requires thinner electrolytes as well as the development of cathode and anode materials with lower and higher catalytic activity for fuel oxidation, respectively.

Conclusion

The influence of cathode composition on the OCV of SC-SOFCs was investigated. Because an SC-SOFC is operated using a mixture of air and fuel, the OCV of the cell is determined by the difference of catalytic activity between cathode and anode. In this study, cells with several cathode composites [mixtures of SDC and (La, Sr)(Co, Fe)O_3 (LSCF)] and reference electrode (Ag) on SDC electrolyte were prepared and tested in the single chamber arrangement. The voltage occurring between the SDC-LSCF cathode materials and Ag was observed as high as 0.1 V, which decreased as the SDC content in LSCF increased. This indicated that LSCF also exhibits catalytic activity toward fuel oxidation, which may lower the performance of the cell.

Single chamber fuel cell tests for these cathodes with Ni-cermet anodes on SDC electrolyte showed that the OCV increased as SDC in the LSCF increased, which was consistent with the results obtained from the voltage measurement of the cathode materials. The SDC in the LSCF affected the cell overpotential so that the cell with the 30SDC-LSCF cathode showed the lowest overpotential. However, the best performance (the power density of 210 mW cm^{-2} at 650°C) was obtained using a 10SDC-LSCF cathode with a 0.5 mm thick electrolyte. It was suggested that a decrease of catalytic activity in the cathode would lower the effective cell temperatures.

Acknowledgments

This work was supported by grants from the Research Board of the University of Missouri and Motorola Advanced Technology Center.

The University of Missouri-Rolla assisted in meeting the publication costs of this article.

References

1. T. Hibino, A. Hashimoto, M. Yano, M. Suzuki, S. Yoshida, and M. Sano, *J. Electrochem. Soc.*, **149**, A133 (2002).
2. T. Hibino, A. Hashimoto, T. Inoue, J. Tokumo, S. Yoshida, and M. Sano, *J. Electrochem. Soc.*, **148**, A544 (2001).
3. T. Hibino, A. Hashimoto, T. Inoue, J. Tokuno, S. Yoshida, and M. Sano, *Science*, **288**, 2031 (2000).
4. R. J. H. Voorhoeve, in *Advanced Materials in Catalysis*, J. J. Burton and R. L. Garten, Editors, p. 129, Academic Press, New York (1977).
5. T. Hibino, S. Wang, S. Kakimoto, and M. Sano, *Solid State Ionics*, **127**, 89 (2000).
6. S. B. Adler, *Solid State Ionics*, **111**, 125 (1998).
7. M. Mogensen, N. M. Sammes, and G. A. Tompsett, *Solid State Ionics*, **129**, 63 (2000).

Available online at www.sciencedirect.com
SCIENCE DIRECT®
Thin Solid Films 457 (2004) 258–263
thin solid films
www.elsevier.com/locate/tsf

Processing and characterization of yttrium-stabilized zirconia thin films on polyimide from aqueous polymeric precursors

B.P. Gorman*, H.U. Anderson

Electronic Materials Applied Research Center, University of Missouri – Rolla, Rolla, MO 65409, USA

Received 3 July 2003; received in revised form 29 September 2003; accepted 20 October 2003

Abstract

Low-temperature deposition of dense, nanocrystalline yttrium-stabilized zirconia (YSZ) thin films on polyimide (PI) substrates is illustrated using an aqueous polymeric precursor spin-coating technique. The polymeric precursor uses low-cost materials, is water-soluble and the viscosity and cation concentrations can be easily adjusted in order to vary the film thickness from 0.02 to 0.3 μm. Due to the use of water as the solvent in the YSZ precursor and the hydrophobic nature of the PI surface, surface modification processes were utilized in order to improve the wetting characteristics. Surface modification of PI substrates using wet chemical and oxygen plasma techniques led to a decrease in the precursor contact angle, and ultimately allowed for uniform film formation on both bulk and thin film PI substrates. Scanning electron microscopy, transmission electron microscopy and UV/Vis absorption illustrate that near full-density nanocrystalline thin films of YSZ can be produced at temperatures as low as 350 °C. Thermogravimetric analyses illustrate that the PI substrate does not undergo any weight loss up to these temperatures.

Keywords: Polyimide; Yttrium-stabilized zirconia; Polymeric precursor

1. Introduction

Polyimides (PI) are frequently used in microelectronic applications due to their high thermal stability, good mechanical properties and ease of processing. They are frequently used in circuit boards and multichip modules as well as insulators for pulsed power applications. Polymers coated with thin film materials are being used more frequently in capacitors, thermal barrier protection [1], ferroelectric liquid crystals, solar cells [2,3], flexible and transparent electronic conducting substrates [4], as well as in nonlinear optical applications. Processing of thin films on polymeric substrates can be difficult due to the temperatures needed in order to achieve the desired properties of the film. These processing temperatures can exceed the glass transition temperature or result in pyrolysis of the polymer substrate. PI has a glass transition temperature of approximately 400 °C, and thus increases the range of available processing temperatures.

PI surfaces are inherently hydrophobic and also have low adhesion strength with metallic and ceramic films. Thus, several surface modification techniques have been developed in order to improve the wetting characteristics and adhesion strength between PI and inorganic films. Chromic and perchloric acids were used [5] in order to increase the bonding strength between PI and epoxy and PI and copper thin films. The wetting angle of water on the PI surface changed from 82° to 55° and the adhesion strength was increased approximately twofold.

Deposition of other organic groups onto PI substrates also has been shown to increase the wetting characteristics and adhesion strength to inorganic films. Amino and cyano compounds have shown a large increase in the adhesion strength between PI and inorganic films [6–8]. In particular, plasma polymer deposition of acrylonitrile onto PI increases the adhesion strength of copper films by 4.3 times as compared with untreated PI. ArF laser and high fluence UV irradiation of a PI thin film in air have also been shown to greatly improve

*Corresponding author. Department of Physics, University of North Texas, Denton, TX 76203, USA. Tel.: +1-940-5654187; fax: +1-940-5652515.
E-mail address: bgorman@unt.edu (B.P. Gorman).

0040-6090/04/$ - see front matter © 2003 Elsevier B.V. All rights reserved.
doi:10.1016/j.tsf.2003.10.034

the wetting characteristics of water on PI [9]. The water contact angle changed from 45° to less than 10° following exposure to an ArF laser fluence of 40 mJ/cm^2 and subsequently treating with water.

Radio frequency oxygen plasma surface modification of PIs has been studied extensively [10–13]. It was shown [11] that the water contact angle of plasma-treated PI changes contact angle from 70° to less than 10° after a treatment time of 15 s. Surface modification has also been illustrated using a wet chemical technique utilizing strong bases such as NH_4OH, NaOH or KOH [14,15]. The strong bases react with an imide functional group to open the imide ring, resulting in amides and carboxylate salts. It has been shown that the water contact angle changes from 38° to 5° upon reaction of the PI with the strong bases.

After modification of the PI surfaces, many different techniques have been used in order to form ceramic films on these substrates. SiO_2 thin films were produced on PI using a sol–gel dip coating technique [16]. Reactive evaporation has been used to produce ITO films on modified PI [4]. Magnetron sputtering has been used in order to produce thin ZrO_2 films on RF oxygen plasma modified PI substrates [1]. Unfortunately, none of these techniques are highly cost-effective in a manufacturing environment.

A polymeric precursor spin-coating technique has been developed in our laboratory for the production of thin (0.02–3 μm thickness) oxide films on a variety of substrates [17–19]. These precursors have many advantages compared with other techniques such as the low cost of the starting materials, high water solubility of the polymer and low processing temperatures (typically <300 °C). In this study, the polymeric precursor technique has been applied to the processing of dense oxide thin films on PI substrates.

2. Experimental procedures

Polymeric precursors for depositing ZrO_2:16%Y (yttrium-stabilized zirconia, YSZ) thin films were prepared using a solution chemistry outlined previously [17]. Reagent grade $ZrOCl_2$ and $Y(NO_3)_3$ were used as the cation sources. These cation salts were dissolved in distilled water and thermogravimetrically standardized to obtain the exact cation contents in the solutions. The cation solutions were weighed according to the appropriate molar ratio, and mixed with tartaric acid and ethylene glycol. The resulting solution was heated and stirred at 70 °C for approximately 40 h, resulting in a polymeric solution that was homogeneous, precipitate-free and had a viscosity of 90 cps (as measured with a Brookfield viscometer at 25 °C). Filtering the precursor through a 0.45-μm glass fiber filter (Whatman, Inc.) removed any foreign material from the precursor.

Surface modifications of Kapton (DuPont, Inc.) PI substrates were accomplished using a wet chemical technique. Substrates approximately 10 cm^2 were trimmed from a large sheet and placed in hot ammonium hydroxide diluted to various concentrations with distilled water. Treatment temperatures, time and the ammonium hydroxide concentration were varied and the precursor wetting angles qualitatively measured in order to achieve good wetting characteristics.

Thin films of PI were produced on glass substrates using a spin-coating technique. PI precursor resin (PiRL III, Brewer Science, Inc.) was spun on cleaned glass substrates at 3000 rpm for 45 s, followed by drying the resin at 170 °C on a hot plate for approximately 5 min. The films were then fully polymerized at 350 °C for 10 min. Surface modifications of the PI thin films were accomplished using an RF oxygen plasma system. The RF power and exposure time were varied and the precursor wetting angles qualitatively measured in order to achieve the best wetting characteristics.

Thin films of YSZ on the modified PI substrates were produced by spin-coating the polymeric precursor on both the Kapton substrates as well as the PI thin film/glass substrates following surface modification. The YSZ precursor solution was applied to the surface and spun at 4000 rpm for 30 s. The wet polymeric precursor was then dried at 70 °C for 1 h followed by pyrolization and oxide formation at 350 °C for 5 min.

A vacuum-chuck hotplate (CEE, Brewer Science, Inc.) was used during the initial 70 °C precursor drying on the Kapton substrates to prevent curling of the flexible substrate. Curling occurs when the wet precursor film evolves its solvent (water in this precursor system) and thus undergoes a large volume change. This large shrinkage of a continuous thin film induces a strain on the coated side of the substrate, which causes the flexible substrate to deform.

Cross-sectional SEM (Hitachi S4700 and JEOL S570) of YSZ/PI structures was done in order to find the film thickness as well as any defects such as delamination. A Cary 5 UV/Vis/NIR spectrophotometer was used to characterize as-deposited films of YSZ on the PI/glass composites. The YSZ film refractive index was modeled from these data over the wavelength range 300–700 nm. Using the Lorentz–Lorenz relationship, the density of the film was determined as a function of annealing temperature.

TEM (Philips EM430) of the YSZ/Kapton composites was done to determine the film morphology and grain size. Selected area electron diffraction was done during the TEM investigation to find the crystallographic phase of the YSZ film. Cross-sectional TEM samples of the YSZ/Kapton films were prepared using a freeze-fracture technique. Samples were placed in liquid nitrogen and fractured into small slivers and mounted on slotted copper grids using silver epoxy.

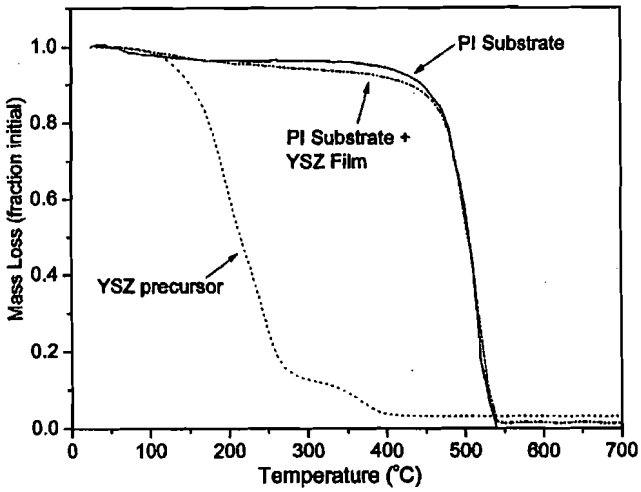

Fig. 1. TGA of the YSZ precursor, Kapton substrate and YSZ/Kapton composite.

Fig. 2. Cross-sectional SEM image of a YSZ thin film on modified Kapton substrate. YSZ thickness is approximately 0.5 μm.

Thermogravimetric analysis (TGA, Cahn TG-1) was done on the YSZ precursor, the Kapton substrate and a 70 °C dried YSZ film on Kapton over the temperature range 25–800 °C. TGA data reveal information about the amount of solvent in the precursor, the wt.% of the oxide in the precursor, the oxide formation temperature, the Kapton decomposition temperature, as well as the wt.% of YSZ on the Kapton substrate. Planar TEM and electron diffraction of YSZ films after pyrolizing the PI substrate at 800 °C was also accomplished in order to determine the YSZ crystallographic phase, grain size and grain morphology.

Auger electron spectroscopy and sputter depth profiling were also utilized in the characterization of these films. A Physical Electronics Model 545 Auger electron spectrometer was used in the capturing of the spectra. An electron beam accelerated at 3 kV with a current of 1 mA was used in the generation of the electrons. The films were sputtered using a 3-kV Ar beam using a gun current of 15 mA. The sputtering depth was calibrated using a standard 100-nm-thick Ta_2O_3 film on Ta metal. These standard samples were alternately sputtered and spectra taken every 2 nm, until the oxygen signal was minimized. The total YSZ film thickness achieved using Auger depth profiling was compared with SEM images, and the differences were found to be negligible.

3. Results and discussion

Heating and stirring the YSZ precursor at 70 °C for approximately 40 h resulted in a viscosity of approximately 90 cps, which was subsequently cooled before spin-coating. Fig. 1 is a TGA curve (heating rate=2 °C/min) for the precursor over the temperature range 25–800 °C. Initially, excess water as well as polyethylene glycol (PEG) are pyrolized, and the sample loses mass until approximately 250 °C. A slight plateau is evident from 250 to 300 °C, indicating that the film has pyrolized the entire PEG and only the 3-d network of tartaric acid cross-linked with the ethylene glycol and metal cations are still present in the film. Above 300 °C, another weight loss is observed, which is the tartaric polymer backbone pyrolizing and giving way to the oxide. All of the organic material is removed from the precursor above 400 °C, leaving only the oxide behind. From the masses of the final oxide and starting precursor, a weight loss of 95% has been observed. As also seen in Fig. 1, the Kapton substrates begin to lose mass at temperatures greater than 450 °C. Thus, processing temperatures greater than approximately 400 °C (near the polymer glass transition temperature) should not be used.

Surface modification of the Kapton substrates using 1 M NH_4OH in distilled water was done at 70 and 90 °C, as outlined previously. It was found that continuous films of the YSZ precursor could be formed on surface-modified substrates after reacting for 55 and 30 min, respectively. Similarly, the PI thin film on glass structure exhibited good precursor wetting characteristics following oxygen plasma treatments for 15 s at 300 W or 40 s at 150 W. Both surface treatment techniques illustrate similar results to previous investigations of wetting by water on PI following strong base and oxygen plasma surface treatments [11,14].

After a continuous film of YSZ precursor was formed on the modified substrates, the structures were allowed to dry. After the film had fully dried, the YSZ/Kapton structure was pyrolyzed thermogravimetrically in order to determine the difference between the burnout temperatures of the film and the substrate. The TGA curve of

(a)

(b)

Fig. 3. TEM image (a) of a YSZ thin film on modified Kapton substrate annealed at 350 °C (YSZ grain size is ≈5 nm) and selected area diffraction pattern (b) illustrating the fluorite structure. Diffraction rings are diffuse due to broadening from the nanocrystalline grain size.

the YSZ/Kapton composite (Fig. 1) illustrates that the YSZ film pyrolizes at temperatures lower than the substrate, thus allowing for processing of these films on PI substrates.

Although the YSZ precursor formed a continuous film on the surface of the PI and pyrolyzed before the substrate, the microstructural integrity of the structure should be characterized. Fig. 2 is a cross-sectional SEM image of a YSZ/Kapton composite fracture section. The composite was produced after modifying the substrate with 0.5 M NH_4OH at 70 °C for 30 min, depositing two layers of YSZ and annealing at 350 °C for 2 min after each deposition. As can be seen from this image, the YSZ film is 0.5 μm thick and there is no significant delamination between the YSZ and the Kapton.

Fig. 3a is a cross-sectional TEM image of a YSZ film on a Kapton substrate after annealing at 350 °C. As can be seen from this image, the film appears dense and has an average grain size of approximately 5 nm. Fig. 3b is a selected area diffraction pattern of the YSZ film cross-section. Indexing of the diffraction pattern rings near the transmitted spot is difficult due to the diffuse rings. Indexing the outer rings, however, matches well with fluorite-structured YSZ. These diffuse rings are due to the broadening associated with the nanocrystalline grain size of the YSZ film, a phenomenon which has been observed in both X-ray and electron diffraction [17].

In order to determine more exactly the crystallographic phase of the film, the YSZ remaining in the TGA crucible after annealing at 800 °C was placed on a 200 mesh copper TEM grid. Fig. 4a is a bright-field TEM image of the YSZ film after annealing at 800 °C. As can be seen, the YSZ grains grow from 5 nm at 350 °C

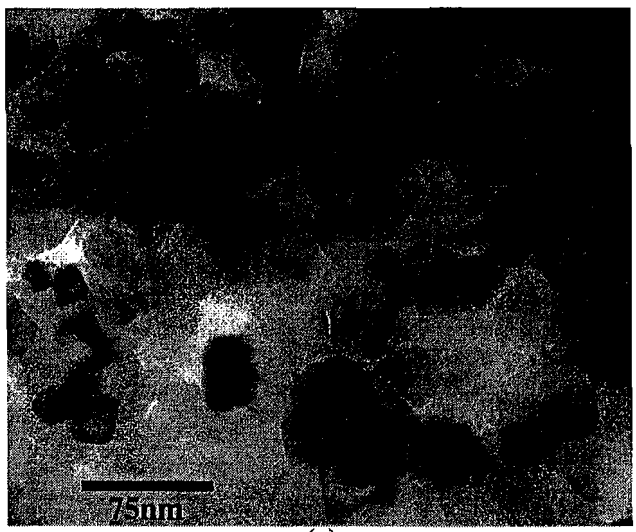

(a)

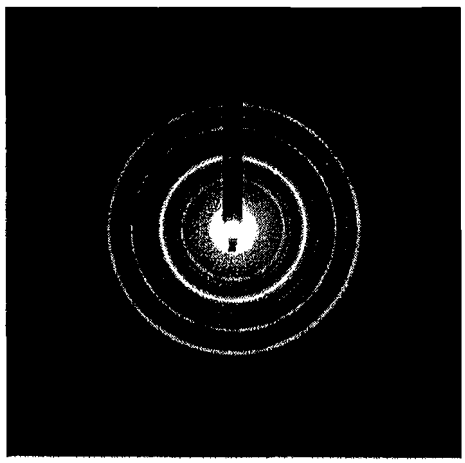

(b)

Fig. 4. Bright-field TEM image (a) of a YSZ thin film produced on a Kapton substrate after pyrolizing at 800 °C and its corresponding selected area diffraction pattern (b). YSZ grains are approximately 50 nm in diameter.

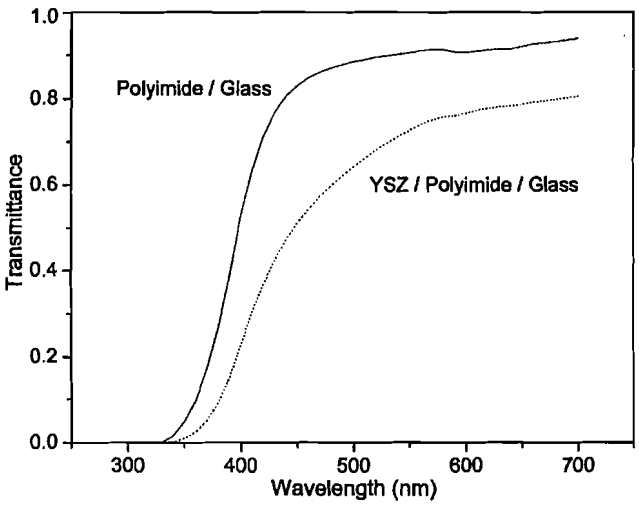

Fig. 5. UV/Vis transmittance spectrum of as-deposited PI/glass and 0.5-μm YSZ/PI/glass composites. Both structures are highly transparent.

(Fig. 3a) to approximately 35 nm at 800 °C. The film does not appear fully dense due to the thermal shock of the film upon imaging with a 300-kV electron beam in the TEM. Fig. 4b is a selected area diffraction pattern of the film in Fig. 4a. The pattern lines are much less diffuse than that in Fig. 3b, again illustrating the grain size impact on the diffraction characteristics.

UV/Vis transmittance spectra of the PI film/glass and YSZ/PI film/glass are shown in Fig. 5. The composite transmits greater than 90% from 500 to 700 nm, followed by absorption due to the PI at approximately 450 nm. The YSZ/PI film/glass transmittance spectra shows transmittance in the 80% range at 700 nm. The difference in the transmittance between the PI and the YSZ/PI is due to the reflection losses at the air/YSZ and YSZ/PI interfaces. Using the method described in detail by Heavens [20], the refractive index of the YSZ film can be calculated, given the refractive indices of the glass and PI materials, and assuming near zero extinction coefficient at the measured wavelength (633 nm in this case).

This is a good approximation due to the negligible absorption by the PI and YSZ (bandgap 5.9 eV) at this wavelength. Scattering due to the grain size of the YSZ film is highly unlikely because, according to Rayleigh scattering statistics, the loss in intensity is calculated to be 10^{-9}, and does not nearly account for the observed change in intensity. In order to account for the change in intensity due to scattering, the defect size must be on the order of 0.5 μm. As is evidenced in the field-emission SEM micrograph in Fig. 6a, there are no significant scattering sites of this size in the YSZ film. No delamination defects that may contribute to scattering losses are evident in the fracture cross-sectional FESEM image of the YSZ/PI/glass structures (Fig. 6b).

Ultimately, using the thickness of the YSZ film obtained from this SEM micrograph, the YSZ refractive index was calculated to be 2.12. The density of the YSZ film could then be calculated from the theoretical refractive index (zirconia=2.2 [21]) and using the Lorentz–Lorenz relationship [22,23]. The optical density of the YSZ film is thus calculated to be 95% theoretical after processing at 350 °C.

Fig. 7 shows the results of the Auger electron spectroscopy depth profiling study for a single YSZ film deposited on the PI substrate, followed by annealing at 350 °C. A small amount of carbon is present in the YSZ film. This can be due to either incomplete pyrolization of the polymer compound, which is unlikely from the TGA data, or due to contamination within the Auger system. The depth profile shows the change in Zr/C

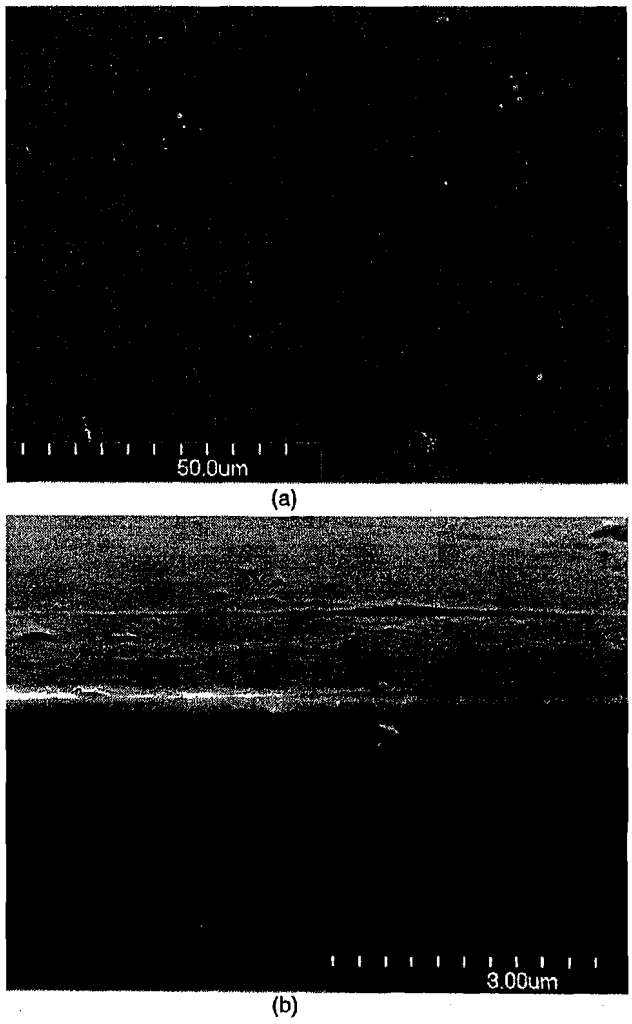

Fig. 6. Field emission SEM images of a YSZ/PI/glass structure (a) as-deposited surface and (b) cross-sectional fracture surface annealed at 350 °C. The YSZ film is approximately 0.3 μm thick and no delamination or cracking is observable.

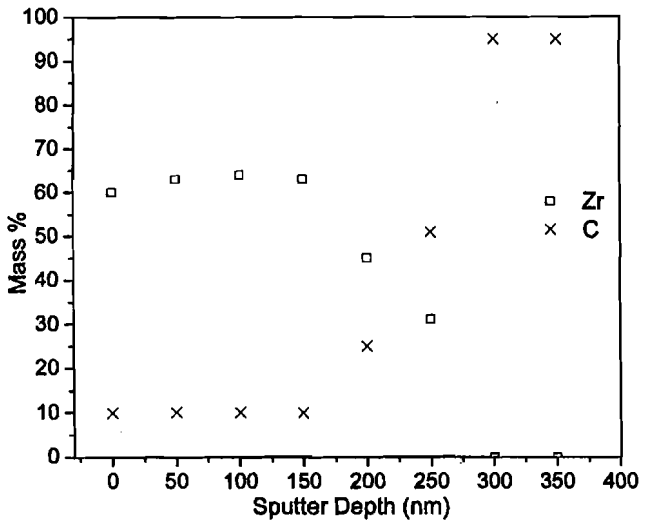

Fig. 7. Auger electron spectroscopy depth profile for the YSZ film processed on a PI substrate. The single YSZ layer is approximately 250 nm thick, which corresponds well to Fig. 2.

ratio as the film is sputtered past the initial surface layer, resulting in a solid YSZ film until the PI substrate is reached.

4. Conclusions

A simple technique for producing dense, nanocrystalline YSZ thin films from a polymeric precursor spin-coating technique was illustrated on a variety of PI substrates. Both wet chemical and oxygen plasma surface treatments were found to greatly improve the wetting characteristics of the water-soluble precursor on the substrates. Film thickness can be varied up to 0.3 μm per deposition with no significant defects present. Processing temperatures can be kept low enough (350 °C) such that no deformation of the polymeric substrate occurs. Films are near full-density after annealing at 350 °C, as determined from the film optical properties. The structures are highly transparent (>80% in the visible range) and do not exhibit delamination between the YSZ and the PI substrate. This technique should be applicable to virtually any other oxide system and have a wide range of applications.

Acknowledgments

Special thanks go to Jeff Wight of the University of Missouri, Rolla Materials Research Center, for his assistance with the Auger depth profiling measurements.

References

[1] B. Rogier, G. Nanse, M. Nardin, G. Baud, M. Jacquet, J. Schultz, J. Adhesion Sci. Tech. 14 (2000) 339–350.
[2] B.M. Basol, V.K. Kapur, C.R. Leidholm, A. Halani, In Conference Record of the 25th Photovoltaics Specialists Conference, May 13–16, 1996, IEEE, Washington, DC, 1996, p. 157.
[3] V. Chariar, A.K. Tripathi, T.C. Goel, R.G. Mendriatta, P.K.C. Pillai, K. Dutta, Ferroelectrics 184 (1996) 117.
[4] J. Ma, D. Zhang, J. Zhao, C. Tan, T. Yang, H. Ma, Appl. Surf. Sci. 151 (1999) 239.
[5] I. Ghosh, J. Konar, A.K. Bhowmick, J. Adhesion Sci. Technol. 11 (1997) 877.
[6] L.P. Buchwalter, T.S. Oh, J. Kim, J. Adhesion Sci. Technol. 5 (1991) 333.
[7] H.K. Yun, K. Cho, C.E. Park, S.M. Sim, S.Y. Oh, J.M. Park, Polymer 38 (1997) 827.
[8] N. Inagaki, S. Tasaka, H. Ohmori, S. Mibu, J. Adhesion Sci. Technol. 10 (1996) 243.
[9] H. Hiraoka, S. Lazare, Appl. Surf. Sci. 46 (1990) 264.
[10] S. Mukkavilli, R.W. Pasco, M.S. Farooq, M.J. Griffin, In Proceedings of the 40th Electronic Components and Technology Conference, IEEE, 1990, p. 737.
[11] A.D. Katnani, A. Knoll, M.A. Mycek, J. Adhesion Sci. Technol. 3 (1989) 441.
[12] F.D. Egitto, L.J. Matienzo, K.J. Blackwell, A.R. Knoll, J. Adhesion Sci. Technol. 8 (1994) 411.
[13] A. Ermolieff, S. Marthon, H. Granges, J. Piaguet, F. Pierre, Thin Solid Films 239 (1994) 220.
[14] K.-W. Lee, A. Viehbeck, IBM J. Res. Dev. 38 (1994) 457.
[15] M.M. Plechaty, R.R. Thomas, J. Electrochem. Soc. 139 (1992) 810.
[16] N. Tohge, K. Tadanaga, H. Sakatani, T. Minami, J. Am. Ceram. Soc. 79 (1996) 1517.
[17] B.P. Gorman, H.U. Anderson, J. Am. Ceram. Soc. 85 (2002) 981.
[18] H.U. Anderson, M.M. Nasrallah, C.C. Chen, US Patent No. 5494700, February 1996.
[19] C.C. Chen, M.M. Nasrallah, H.U. Anderson, J. Electrochem. Soc. 140 (1993) 3555.
[20] O.S. Heavens, Optical Properties of Thin Solid Films, second ed., Dover Press, NY, 1992.
[21] D.R. Lide, H.P.R. Frederikse (Eds.), CRC Handbook of Chemistry and Physics, 75th ed., CRC Press, 1994.
[22] V. Petrovsky, B.P. Gorman, H.U. Anderson, T. Petrovsky, in: C.B. Carter, X. Pan, K. Sickafus, H.L. Tuller, T. Wood (Eds.), Structure–property relationships of oxide surfaces and interfaces, Mater. Res. Soc. Symp. Proc. 654 (2001) AA7.6.
[23] V. Petrovsky, B.P. Gorman, H.U. Anderson, T. Petrovsky, J. Appl. Phys. 90 (2001) 2517.

INTERMEDIATE SOLID OXIDE FUEL CELLS, CHALLENGES AND OPPORTUNITIES FOR THE MATERIALS SCIENTIST

H. U. Anderson, X.-D. Zhou and F. Dogan
Electronic Materials Applied Research Center, 303 MRC, University of Missouri-Rolla, Rolla, MO 65401

The awareness of environmental factors and limited energy resources has driven the search for the new energy supply even though the fossil and nuclear sources can remain adequate for the next few decades. The new energy technologies have to be cleaner, cheaper, smaller and more efficient, such as fuel cells or solar cells. The development of solid oxide fuel cells (SOFC's) has been carried out over the period of several decades by both industry and academia. This has led to SOFC's, which operate in the 850 to 1000°C range, but economics have curtailed their development. Over the past few years, in an effort to address the costs and reliability issues, work has been focused on the SOFC'S that can operate in an intermediate temperature regime (500 – 700°C), which seems mandatory if they are to be commercialized. Compared to the conventional high temperature cell operation (>800°C), the intermediate temperature operation requires (1) an extremely strict material selection, which allows the similar electrode kinetics and internal resistance as those at high temperature; (2) feasible techniques to build those devices so that each component in the SOFC can function efficiently. It is the intent of this presentation to give an overview of the challenges and opportunities that the intermediate temperature SOFC's present to materials scientists, but will focus on the cathode and electrolyte since in the reviewers' opinion, for both the anode and interconnect there exists adequate materials at least for the first generation of SOFC's, so the cathode and electrolyte present the most significant challenges to the development of SOFC's.

Currently, $La_{0.80}Sr_{0.20}MnO_3$ is being used as the cathode, but due to unacceptably high area specific resistance (ASR >0.3ohms/cm2), it has proven to be unsuitable for use at or below 800°C. Three ways have been tried to solve this problem: (1) replacing La with Pr, Nd, Sm or Gd; (2) partial or complete substituting of Mn by Fe, Co and/or Ni; (3) combination of (1) and (2). This review mainly deals with ferrites and cobaltites, with an emphasis on the determination of oxygen vacancy level, ionic and electronic conductivity, kinetics for oxygen transfer reaction and thin film techniques for fabrication of cathode component.

Yittrium or scandium substituted zirconia (YSZ, SSZ respectively) and gadalinium or samarium substituted ceria (CGO, CSO respectively) are the prime candidates for the electrolyte. Both of these electrolytes require thickness of <10micrometers in order to operate with ASR <0.1 at temperatures in the 500 to 700°C range. This means when we consider the electrolyte, the main challenge has to be related to the processing of dense electrolyte layers using either the anode or cathode as the supporting structure. Several of the processes which are being evaluated to economically achieve this required electrolyte/electrode structure will be described. A particular emphasis will be placed on the development of an electrolyte/electrode composite structure which involves the deposition of dense thin electrolyte layers onto sintered porous anode/cathode structures at processing temperatures below 800°C.

H.U. Anderson, X.D. Zhou and F. Dogan "Intermediate solid oxide fuel cells, challenges and opportunities for the materials scientists", Proc. of Electroche Soc. (Solid State Ionic Device III) **2002-26**, 16-17 (2003).

INTERMEDIATE SOLID OXIDE FUEL CELLS, CHALLENGES AND OPPORTUNITIES FOR THE MATERIALS SCIENTIST

H. U. Anderson, X.-D. Zhou and F. Dogan

Electronic Materials Applied Research Center, 303 MRC, University of Missouri-Rolla, Rolla, MO 65401

ABSTRACT

In an effort to address the cost and reliability issues, over the past few years, the development of Solid Oxide Fuel Cells (SOFCs), has been towards the reduction of operation temperature into the intermediate temperature (IT) regime (500 – 700°C). The intermediate temperature operation requires (1) an extremely strict material selection, which allows electrode kinetics and internal resistance similar to those occurring in the high temperature regime (900 – 1000°C); (2) feasible techniques to build devices so that each component in the SOFC can function efficiently. It is the intent of this review to give an overview of the challenges and opportunities that the intermediate temperature SOFCs presents to the materials scientists.

INTRODUCTION

The awareness of environmental factors and limited energy resources has driven the search for improved utilization of our fossil energy resources. These new energy technologies have to be cleaner, cheaper, smaller and more efficient than those currently being employed. Fuel cells are considered an excellent alternative energy resource because of their very unique advantages, including (1) Environmentally sound: Fuel cells convert fossil energy sources directly to electricity, without combustion, so that they have the potential of reducing pollutant emissions by orders of magnitude below those for conventional combustion generating equipment; (2) Excellent energy conversion efficiency: Fuel cells offer significant improvements in energy efficiency as they remove the intermediate step of combustion and mechanical devices such as turbines and pistons. Unlike conventional systems their high efficiency is not compromised by small sizes; (3) Energy security: Fuel versatility promotes energy security as they can use fuels derived from a variety of sources (natural gas, propane, coal and renewable sources). Moreover, Fuel cell cogeneration plants have the potential of unprecedented reliability and durability that is significantly better than conventional competitive equipment because of the absence of combustion and moving parts.[1-3]

The development of solid oxide fuel cells (SOFCs) has been carried out over the period of several decades by both industry and academia. This has led to SOFCs, which operate successfully in the 900 to 1000°C range, but economics have curtailed their development. Over the past few years, in an effort to address the costs and reliability issues, work has been focused on the SOFCs that can operate in an intermediate temperature regime (500 – 700°C). The recent formation of the Solid State Energy

Conversion Alliance (SECA) program within the Department of Energy (DOE), where the goals are to lower the operating temperatures into the 500 – 700°C range and to deliver electrical energy at $400/KW or lower before the year of 2010, is evidence of this high level of interest.[4] Compared to the conventional high temperature cell operation (>900°C), the intermediate temperature operation requires (1) an extremely strict material selection, which allows electrode kinetics and internal resistance similar to those obtained at high temperature; (2) fabrication techniques to build those devices so that each component in the SOFC can function efficiently. It is the intent of this article to give an overview of the challenges and opportunities that the intermediate temperature SOFCs present to materials scientists, but will focus on the cathode and electrolyte since in the reviewers' opinion there exists adequate materials for both the anode and interconnect at least for the first generation of SOFCs, so the cathode and electrolyte present the most significant challenges to the development of SOFCs.

ELECTROLYTE

The electrolyte in SOFCs function as an oxygen ion conductor and an electronic insulator, therefore the open circuit voltage (EMF) of the cell can be determined from the chemical potential of oxygen (i.e. oxygen activity) which is expressed by Nernst Equation as [5]:

$$EMF = \Gamma \frac{RT}{4F} \ln\left(\frac{(pO_2)_a}{(pO_2)_b}\right) \quad (1)$$

where Γ is the transference number (ionic conductivity/total conductivity), T is operation temperature, F is Faraday constant, $(pO_2)_a$ is oxygen activity in cathode side and $(pO_2)_b$ is oxygen activity in anode side.

Requirements:

The requirements for the electrolyte used in IT SOFCs include:

(1) The materials must be gas tight and have an ionic transference number close to unity. Gas leakage and/or electrical current between the electrodes through the electrolyte represent energy losses and reduce the operating efficiency.

(2) In order to produce maximum power density, Electrical losses in the electrolyte must be minimized. In order to produce maximum power density, SOFCs generally operated at about 0.7V and at current density in the 0.5 to 2 amps/cm^2 range. This requires the Areal Specific Resistance (ASR) of the cell to be $<0.2\Omega cm^2$. Figure 1 illustrates the ASR of the electrolyte as a function of electrolyte thickness at 500 and 600°C. In the IT regime, the electrode overpotential, particularly cathode overpotential, is in the order of the ASR of the electrolyte. Therefore, a maximum allowed electrolyte thickness is directly determined by cell design. For example, if the electrolyte contributes to half of the ASR, at 600°C, if YSZ is the electrolyte, the thickness must less than 5μm.

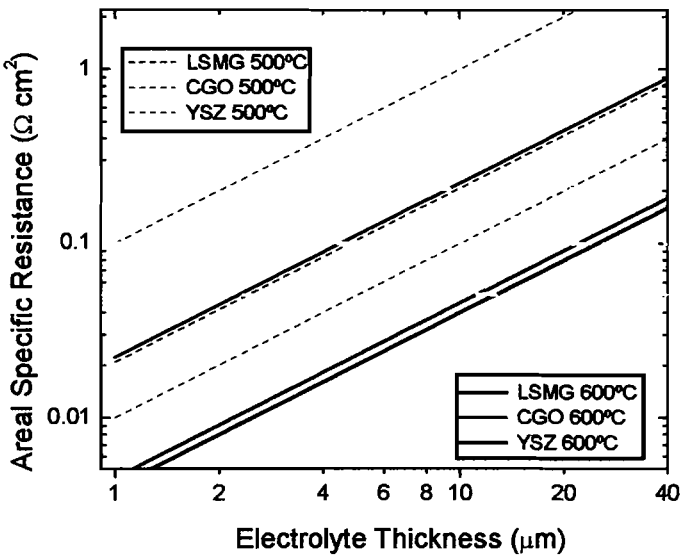

Figure 1. Areal Specific Resistance vs. Electrolyte Thickness for YSZ, CGO and LSMG at 600°C and 500°C.

This means when we consider the electrolyte, the main challenge has to be related to the processing of dense electrolyte layers using either the anode or cathode as the supporting structure. Several of the processes that are being evaluated to economically achieve this required electrolyte/electrode structure are described here. A particular emphasis is placed on the development of an electrolyte/electrode composite structure, which involves the deposition of dense thin electrolyte layers onto sintered porous anode/cathode structures at processing temperatures below 800°C.

(3) Thermal, Chemical and Mechanical Compatibility

The operation of SOFCs requires the cathode and the anode to be porous; therefore, the electrolyte is exposed to the oxidant (such as air) and the fuel at elevated temperature. Since the electrolyte and electrodes must function as one unit, thermal and mechanical stability must be such that cell must be able to survive thermal circling. This means that the thermal expansion coefficient must match as the interface. Chemical reaction between the components must be minimized if the cells are to produce the required stability. (Stable operation for 40,000 hours)

Materials:

The challenge for the materials scientists is to design a chemical composition and/or to tailor a structure of a solid-state material that can function as the super oxide ion conductors in the IT regimes. At this time, only one electrolyte material can satisfy these requirements, which is Y stabilized ZrO_2 (YSZ), with acceptor substituted CeO_2 and (La, Sr)(Mg, Ga)O_3 being investigated as potential primary candidates. Several review articles have detailed the progress of fast oxide ion conductors.[6-8]

ZrO_2 based materials: The application of stabilized ZrO_2 was first initiated by Nernst, particularly in his patent in early 1900s[9] and in 1937 YSZ was the first material to be used as an electrolyte in SOFCs. Since that time, extensive studies on stabilized ZrO_2

have been performed,[6, 10] however YSZ is still the most interesting and practical materials currently being used.

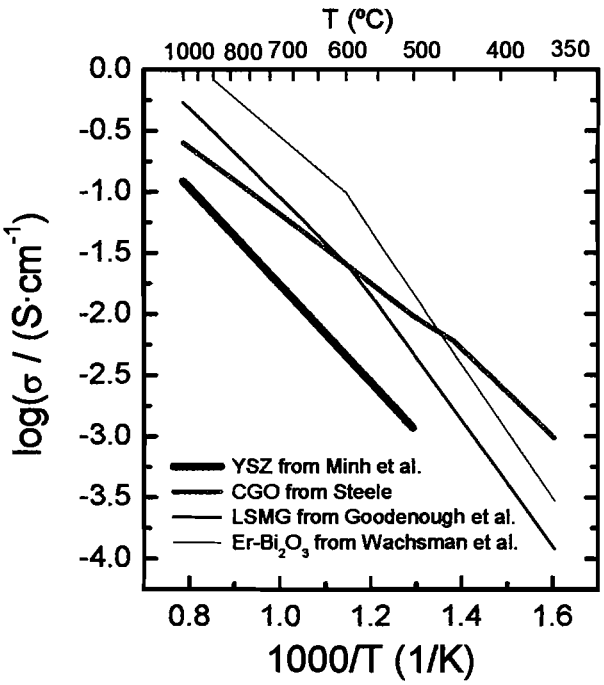

Figure 2: Log(σ) vs. 1/T for YSZ, CGO, LSMG and Er-Bi_2O_3. (Ref. YSZ [11], CGO [12] LSMG [13], Bi_2O_3 [14])

The only drawback of stabilized ZrO_2 is the low ionic conductivity in the IT regime. Figure 2 shows a combination of the possible electrolyte materials in IT SOFCs, in which YSZ shows the lowest ionic conductivity. Two solutions have been tried to resolve this problem are: (1) to decrease the thickness of YSZ electrolyte and (2) to find other acceptors to replace Y. The first solution seems to be only valid when the operation temperature is higher than 600°C, at which the maximum electrolyte thickness is about 5μm assuming the electrolyte ASR ~ 0.1 Ω cm^2, which currently is a high value. Scandium substituted zirconia (SSZ) is a promising candidate because SSZ has a conductivity similar to doped CeO_2 and is a good candidate if the cost of scandium oxide decreases.[15]

CeO_2 based materials: Acceptor substituted CeO_2 materials are being considered as intermediate temperature (500 to 700°C) solid electrolytes for solid oxide fuel cells (SOFC) [12, 16, 17]. This is due to their higher oxygen ion conductivity compared to YSZ, particularly in the IT regime. The principle problem with CeO_2 is the stability under reducing conditions. This results in significant electronic conductivity and dimensional instability due to the formation of oxygen vacancies and the associated reaction of Ce^{4+} to Ce^{3+}. Thus if it is to be used as an electrolyte, it either has to be protected from the reducing conditions or perhaps be operated at temperatures below 600°C.

LSMG: Oxide in the perovskite structure ,(ABO_3) have the potential of a wide range of geometrical and chemical flexibility, which allows the formation of high oxygen vacancy concentrations. This is borne out by LSMG [13, 18-19], so it certainly is a viable

candidate for an alternative electrolyte in the IT SOFC. Thus a number of studies are currently being made on this material. . Two of the primary issues related to the use of LSMG is the uncertainty of the cost of Ga sources and the mechanical strength.

Regarding the applicability of perovskite structure oxides as electrolytes in general, one must remember that the presence of oxygen vacancies alone may not be sufficient for an oxide to function well as an electrolyte. The oxygen vacancies must remain disordered for the oxygen ionic conductivity to be high enough to be useful. It is apparent that ordering occurs (sometimes at specific temperatures) which significantly decreases the oxygen ionic conductivity because of lower defect mobility and reduced effective vacancy concentration

Search for the new materials:

Search for the new materials with much higher ionic conductivity than YSZ or CeO_2 based materials is a worthy endeavor, but the operating requirements for the electrolyte severely limits choices. Currently, most of these efforts are centered on two possibilities, namely designing nanocomposites or tailoring crystal structure. The ionic conductivity was observed to increase with increasing content x of $(1-x)Li_2O : xB_2O_3$ up to a maximum at $x \sim 0.5$ for nanocrystalline samples [20], which was interpreted as an enhanced conductivity at the interface between conducting and insulating components. This behavior presents an interesting possibility that has been rarely observed or studied, which is that in two-component composites the ionic conductivity can also be size dependent. This has been observed in CeO_2 systems where enhanced electronic conductivity has been found.[21-22] The materials currently being used are those with extrinsic defects, which are acceptor-doped materials. A challenge for materials science is to see if is possible to find an oxide ion conductor with a sufficient intrinsic vacancy concentration. Studies of $La_2Mo_2O_9$ showed that partial substitution of oxygen for vacancies occupied by lone pairs may be an excellent design strategy for finding new intrinsic vacancy oxide ion conductors.[23-25]

Device

As discussed in the previous section, when we consider the electrolyte, the main challenge has been related to the processing of dense electrolyte layers using a supporting structure, either the anode, cathode or other possible supports. Several of the processes that are being evaluated to economically achieve this required electrolyte/electrode structure are described here. A particular emphasis is placed on the development of an electrolyte/electrode composite structure, which involves the deposition of dense thin electrolyte layers onto sintered porous anode/cathode structures at processing temperatures below 800°C with a targeted electrolyte thickness below 10μm, preferably below 5μm.

Obviously, it is not trivial to process dense electrolyte with a thickness less than 5μm because of the mechanical requirements to maintain the electrolyte structure. The feasible techniques to achieve the dense thin electrolyte structure include tape-casting, , colloidal coating, plasma or vapor deposition and chemical deposition process, such as sol-gel or polymer coating. Each of these processes has its own unique advantages, thus choosing one of them to fabricate dense electrolyte films actually depends on the problems to be solved and the technique that is accessible. Several overview articles have covered the film processing.[26, 27]

The usual methods to achieve this structure are:

Tape Casting: Tape casting[28, 29] is the most widely used technique to fabricate the electrolyte structure, in particular the sintering of laminated tapes of the electrode and the electrolyte. Green tapes are produced from slurry of solvents, binders, plasticizer and ceramic powders, followed by lamination of the tapes of substrate and the electrolyte. Tape casting has been developed to produce large-thin, flat ceramic layers for the monolithic and planar SOFC. Van Berkel et al. [30] have explored a multi-layer tape casting technique, with which an electrode layer is tape-cast on top of a green thin electrode layer. Ihringer et al.[31] utilized a water-based slurry to fabricate 0.6 – 10 μm YSZ layers on NiO/YSZ anode substrates. A power density 0.58 W/cm^2 was achieved at 760°C (cell diameter ~ 31mm). Cast thin tape of the electrolyte and laminate it to tape of the electrode, followed by co-sintering to obtain the dense electrolyte/porous electrode structure. Most of these electrolytes are > 5 micrometer in thickness.

Vapor Deposition: Electrochemical Vapor Deposition (EVD) is a modified Chemical Vapor Deposition (CVD), which was originally developed at Westinghouse to fabricate dense electrolyte onto a porous cathode substrate (LSM) [32].

Liquid Precursors: Spin coating[33-36], colloidal, spray processes and dip-coating[37] have been utilized to fabricate thin electrolyte. Some of these processes have importance because of high deposition rates which range from 2nm to 20,000nm/h. The spin coating technique for fabricate thin films is the Pechini process that utilizes a polymeric precursor containing the chelated cations. The polymeric solutions require a suitable surface tension that allows a low wetting angle with the substrate and a sufficient viscosity in order to achieve of variable grain size polymer film. These two requirements are adjusted by control over the polymeric solution chemistry, such as the chelant type, concentration and the ratio of the chelant over the cations.

Future Work

1. *Fabrication of the thin electrolyte on various substrates:* The materials for use as electrolytes for the first generator of IT SOFCs are YSZ for T > 600°C and doped CeO_2 for T < 600°C. For doped CeO_2 materials, work still has be performed to study the mechanical stability over the temperature and oxygen partial pressure cycling and reaction between CeO_2 and electrode materials. Cost effective thin electrolyte processing is of significant importance in developing the second generation SOFCs, which requires a low temperature deposition and liquid precursor selection.

2. *Grain boundary role:* Lower temperature operation does pose a problem due to the higher activation energy of the grain boundary resistivity, ρ_{gb}. A high ρ_{gb} can be due to many factors, including (1) amorphous phases, (2) dopant segregation, (3) an altered local defect chemistry due to space charge effects, and (4) intergranular porosity (small effect). These effects are all strongly related to grain size and the associated grain boundary area. Some recent reports show that some Si containing compounds have been found to possess sufficient oxide ion conductivity to alter the influence of the grain boundary phase in $Ce_{0.80}Gd_{0.20}O_{1.90}$. However, since there appears to be some controversy regarding this issue further study has to be employed to examine this behavior [3, 17, 38, 39].

3. *Low densification temperature:* The impurities could be induced during high temperature calcining or sintering (>1350°C). A fine particle size of the raw materials and a high green density can lower the densification temperature.

CATHODE

Requirements:

The cathode for IT SOFCs must have high electronic conductivity and high activity for oxygen reduction. In addition, the cathode has to maintain a stable chemical composition and porous microstructure at high temperature in air or oxygen; and have a thermal expansion compatible with the SOFC electrolyte. The cathode for IT SOFCs must be mixed ionic and electronic conductor (MIEC), which in principle can be achieved by two ways: (1) Single chemical composition, mostly perovskite type oxide that possesses reasonable electronic and oxygen ion conductivities. (2) Composites with electronic and ionic conductors, for example, perovskite type oxides and oxygen ion conductors. However, for single phase cathodes, difficulties have been encountered with the optimization of both the ionic and electronic conductivities in the IT temperature regime.

Materials:

1. Materials chemical composition

In order for a cathode to operate successfully in the IT SOFC temperature regime, the electrode kinetics have to be at least as fast as those observed at high temperature. $La_{0.80}Sr_{0.20}MnO_3$, the currently preferred cathode material, has proven to be unsuitable for use below 800°C due to very low oxygen vacancy concentration. Therefore, research work is required if a cathode is to be developed which will be suitable for use in the intermediate temperature range. Current studies have tried three ways to address this problem: (1) replacing La with Pr, Nd, Sm or Gd; (2) partial or complete substitution of Mn by Fe, Co and/or Ni; (3) combination of (1) and (2). From these studies, ferrites and cobaltites have shown reasonably good, stable performance, and in addition have displayed lower activation energy, smaller areal resistance, higher oxygen vacancy level and faster kinetics for interfacial oxygen transfer reaction, compared to the manganites. Thus it appears that there may be solutions to the cathode problem, but in order to develop the fundamental knowledge required to resolve a number of the practical and fundamental problems, experiments have to be conducted from the viewpoints of materials selection, defect chemistry, and electric, magnetic and catalytic properties.

2. Materials defect structure and properties

The perovskite-type oxides encompass a large variety of chemical compositions that contribute to their diverse and unique properties. An example is (La, Sr)$FeO_{3-\delta}$, (LSF) which is particularly interesting for oxygen membranes and for the cathode for IT SOFCs. In particular, LSF has shown excellent cathode performance at 750°C.[40] Structure and defect properties of LSM are of importance to understand why ferrites functions better than LSM and to search for new cathode materials. Initial studies on ferrite materials have shown that structure plays an important role in the electrical and magnetic properties and that the electrical, catalytic and magnetic properties have an inter-relationship that is commonly related to the electronic structure and oxygen vacancy concentration.[41] Therefore, it is important to study the ferrite materials from the atomic structure point of view. For example, the hybridization of transitional metal and oxygen orbitals plays a dominant role in the properties such as the generation of oxygen vacancies, holes, and spin state of the transitional metals.[42]

This interrelationship is shown in the (La, Sr)(Fe, Co)$O_{3-\delta}$ system. For the 20% Co composition, electrons (holes) move indirectly between Co ions via an O ion rather than directly between Co ions, i.e., the fluctuation of the charges on the O ions as well as Co ion causes electrons (holes) to move with a complicated interaction between the generated holes and electrons. The effects of Fe doping in $La_{0.67}Sr_{0.33}CoO_{3-\delta}$ showed that

no apparent structure change was introduced by Fe doping up to x = 0.3, but the Curie temperature T_C, magnetization M and electrical resistivity are lowered by Fe substitution. A smaller localization length and a more severe disorder in the lattice due to Fe doping were observed. Previous research showed that two transitional metals, Fe and Co, in the B site of ABO_3 allowed a better performance compared to only Co or Fe located at B site. For example, cobaltites exhibit a significant weight loss when the annealing temperature is higher 1000°C (in some cases 800°C) and a higher resistivity and oxygen diffusivity were observed in ferrites.[43, 44]

Further study was then performed on the electrical conductivity of $La_{0.60}Sr_{0.40}FeO_3$ at the low pO_2, in which oxygen vacancy concentrations were increased. Figure 3 shows the plot of $\log(\sigma)$ vs. $\log(pO_2)$ at 1000°C with a control over the oxygen activity being made by using a mixture of CO/CO_2, from which the pO_2 can be determined thermodynamically. In addition to the conductivity, oxygen vacancy concentration also plays a key role in the function of cathodes, in particular in the catalytic properties. Determination of the oxygen vacancy level has been performed by thermogravimetric analysis (TGA) and neutron diffraction. TGA simply measures the weight changes with the variable being time, gas environment and temperatures. Neutron diffraction was performed on the samples which were quenched at 1000°C from different oxygen activities. A large decrease in 3-δ was observed when the gas was changed from 90%CO to 99%CO. XRD results showed that $La_{0.60}Sr_{0.40}FeO_{3-\delta}$ decomposed in the 99% CO atmosphere. The consistence results between TGA and neutron diffraction confirmed that the quenching experiment could be used to study the ferrites under reducing conditions. Figure 3 shows a reasonable high oxygen vacancy level in Ferrites in a wide oxygen activity, however, compared to ferrites, oxygen vacancy level in LSM is rather low.[45]

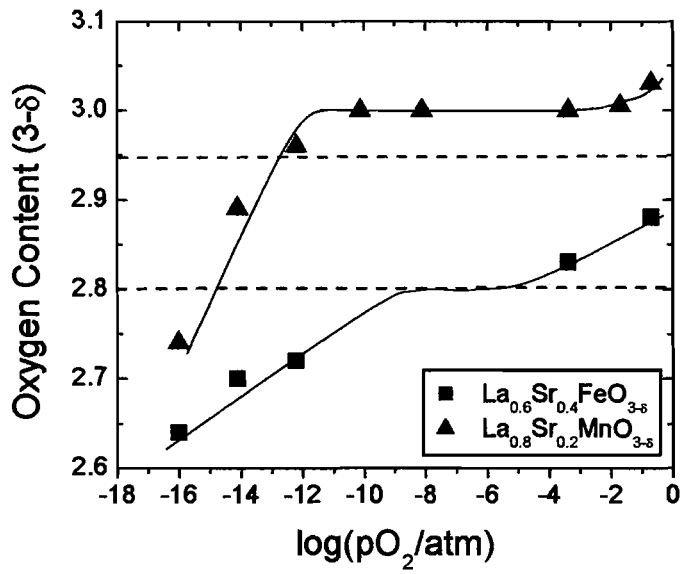

Figure 3: Oxygen content (3-δ) vs. $\log(pO_2)$ for $La_{0.6}Sr_{0.4}FeO_{3-\delta}$ [41] and $La_{0.8}Sr_{0.2}MnO_{3-\delta}$ [45] at 1000°C.

Figure 4 shows the Nèel Temperature and Fe-O-Fe angles as a function of pO_2, at the oxygen partial pressure from which the specimen was quenched. The bonding angles of Fe-O-Fe were increased with decreasing oxygen partial pressures. Because the bonding lengths were nearly constant, the increasing of the bonding angle increases the overlap between Fe and O atomic states that results in an increase in the superexchange interaction between Fe and Fe.[42] The Fe-Fe super-exchange interaction is highly dependent on the Fe-O-Fe bond angle and the superexchange through the oxygen atoms that is more effective when the Fe-O-Fe paths are close to linear. It is also found that the increase in the superexchange interaction results in an increase in Nèel temperature, as shown in Figure 4. The Fe moments for the three reduced samples refine between 3.72 and 3.82 μ_B while the moments for the other two samples are much smaller (1.4 μ_B and 1.2 μ_B for the air- and N_2- quenched samples, respectively).

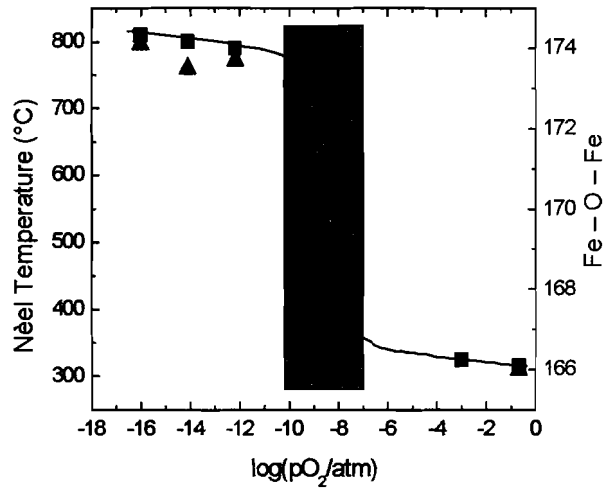

Figure 4: Nèel temperature and Fe – O – Fe angle vs. log(pO_2) for $La_{0.6}Sr_{0.4}FeO_{3-\delta}$ at 1000°C.[41]

3. Cathode microstructure

A large group of chemical compositions has been investigated as the candidate for IT SOFC cathode. A recent article by Skinner overviewed the progress of perovskite type oxides for SOFCs cathode, with an emphasis on the role of chemical compositions.[46] On the other hand, microstructure plays a major role in the cathode function as well. This is particularly true when the composite cathode is used, which shows a better performance compared to a single composition cathode. Several authors have shown that electrode microstructure and transport properties have a profound effect on polarization. Tanner et al. [47] have shown that polarization resistance (R_p) depends upon the grain size, d, of the ionic conductor in the composite electrode and the volume fraction porosity, which was further derived as in equation 2 by considering the monolayer gas adsorption:

$$R_p \approx \left(\sqrt{\rho_i \rho_{ct}}\right) \times \left(\sqrt{\frac{d}{(1-V_v)l_{TPB}}}\right) \times \left(\frac{1}{\sqrt{\theta_{O_2}}}\right) \quad (2)$$

In equation (2), the first part consists of the ionic resistivity, ρ_i, and the intrinsic charge transfer resistivity, ρ_{ct}; the second part represents the microstructual factor and the last

part oxygen coverage at the triple phase boundary (TPB) sites. A similar relation has been proposed as [48]:

$$R_{Chem} = A\frac{1}{T}\sqrt{\frac{\tau}{(1-\varepsilon)aC_O^2 D^* k}} \quad (3)$$

where, R_{chem}: chemical reaction induced R; D^*: oxygen self-diffusion coefficient (cm^2 s^{-1}); k: oxygen surface exchange coefficient (cm s^{-1}); C_O: concentration (mol cm^{-3}) τ: tortuosity; ε: fractional porosity; a: surface area/unit volume. This equation explicitly shows the resistance induced by chemical reaction between the cathode and the electrolyte as a function of microstructure and reaction parameters, which can reveal some criteria for the search of the new cathode materials.

Interfacial Layer:

Perovskite type oxides, particularly (La, Sr)MO_3 (M = Co, Fe, and/or Ni) which are being considered as the cathode candidates for IT SOFCs, are very reactive towards YSZ.[49] Therefore, a thin layer, mostly CeO_2 based materials, has been to reduce the chemical reaction between the cathode and YSZ. However, the reaction between CeO_2 and $LaMnO_3$ was overlook n the field of SOFCs, whereas a solid solution of CeO_2 with $LaMnO_3$ has been observed, which was later questioned by Ganguly et al. [50-52].

CONCLUSIONS

The major intent of reducing the operation temperature for SOFCs is to lower the overall cost. The strict requirements for the electrolyte materials results in YSZ remaining the candidate when T>600°C with doped CeO_2 a possible choice for T < 600°C. A composite structure consisting YSZ and doped CeO_2 with a controllable layer thickness seems feasible to further lower the electrolyte thickness less than 5μm. However, it is important to remember that a thin film electrolyte requires a supporting structure, either cathode or anode composites, and that the cost of these composites may become an important cost item in the SOFC. Therefore, it is of great importance to search for new materials or structures for IT SOFCs to both improve cell performance as well as lower the overall materials costs.

Currently there are no single phase or composite materials which will adequately function as the cathode of the IT SOFC. Further research is required for the development of a material and/ or microstructure adequate to perform as a cathode for the 40,000 h time duration required for the commercialization of the IT SOFC.

ACKNOWLEDGEMENT

This research was supported by the Department of Energy under the Contracts DE-AC26-99FT40710 and DE-FC36-01G011084

REFERENCES

1. D. A. Berry, W. A. Surdoval and M. C. Williams, 222nd ACS National Meeting, Chicago, IL, United States, (2001)
2. http://www.fe.doe.gov/coal_power/fuelcells/
3. B. C. H. Steele, *Solid State Ionics,* **134**, 3 (2000).
4. M. C. Williams, *Fuel Cells,* **1**, 87 (2001).
5. J. Koryta, *Principles of Electrochemistry*, Wiley (1993).
6. J. C. Boivin and G. Mairesse, *Chem. Mater.,* **10**, 2870 (1998).
7. M. Mogensen, N. M. Sammers, and G. A. Tompsett, *Solid State Ionics*, **129**, 63 (2000).
8. J. A. Kilner, *Solid State Ionics,* **129**, 13 (2000).
9. W. Nernst, US patent 685730, 1901.
10. V. V. Kharton, E. N. Naumovich and A. A. Vecher, *J. Solid State Electrochem.*, **3**, 61 (1999).
11. N. M. Minh, *J. Am. Ceram. Soc.*, **76**, 563 (1993).
12. B. C. H. Steele, *Solid State Ionics,* **129**, 95 (2000).
13. K. Huang, R. S. Tichy, J. B. Goodenough, *J. Am. Ceram. Soc.*, **81**, 2565 (1998).
14. N. Jiang and E. D. Wachsman, *J. Am. Ceram. Soc.*, **82**, 3057 (1999).
15. J. M. Ralph, A. C. Schoeler and M. Krumpelt, *J. Mater. Sci.*, **36**, 1161 (2001).
16. V. V. Kharton, A. A. Y aremchenko, E. N. Naumovich, and F. M. B. Marques, *J. Solid State Electrochem,* **4**, 243 (2000).
17. X.-D. Zhou, W. Huebner, I. Kosacki and H. U. Anderson, *J. Am. Ceram. Soc.*, **85**, 1757 (2002).
18. T. Ishihara, H. Matsuda and Y. Takita, *J. Am. Chem. Soc.*, **116**, 3801 (1994).
19. K. Huang, J. Wan, and J. B. Goodenough, *J. Mater. Sci,* **36**, 1093 (2001).
20. S. Indris, P. Heitjans, H. E. Roman and A. Bunde, *Phys. Rev. Lett.*, **84**, 2889 (2000).
21. T. Suzuki, *Microstructure of nanocrystalline undoped and doped cerium oxide thin films and their electrical and optical properties,* University of Missouri-Rolla, Dissertation (2001).
22. H. L. Tuller, *Solid State Ionics,* **131**, 143 (2000),
23. J. B. Goodenough, *Nature,* **404**, 821 (2000).
24. Ph. Lacorre, F. Goutenoire, O. Bohnke, R. Retoux, and Y. Laligant, *Nature,* **404**, 856 (2000).
25. F. Goutenoire, O. Isnard, E. Suard, O. Bohnke, Y. Laligant, R. Retoux and Ph. Lacorre, *J. Mater. Chem.*, **11**, 119 (2001).
26. T. P. Niesen and M. R. De Guire, *J. Electroceramics,* **6**, 169 (2001).
27. J. Will, A. Miterdorfer, C. Kleinlogel, D. Perednis and L. J. Gauckler, *Solid State Ionics,* **131**, 79 (2000).
28. E. T. Ong, B. W. Chung, R. Doshi, J. Guan, G. R. Lear, K. Montgomery and N. Q. Minh, *Ceramic Transactions,* **109**, 77 (2000).
29. M. M. Seabaugh, B. E. McCormick, K. Hasinska, C. T. Holt, S. L. Swartz, and W. L. Dawson, *Ceram. Trans.*, **127**, 91 (2002).
30. F. P. F. van Berkel G. M. Christie, F. H. van Heuveln, J. P. P. Huijsmans, in *Proc. 4th Int. Conf. Solid Oxide Fuel Cells/1995,* M. Dokiya, O. Yamamoto, H. Tagawa, S. C. Singhal, p1062, The Electrochemical Society Proceedings Series, Pennington, NJ.

31. R. Ihringer, J. van Herle, A. J. McEvoy, in *Proc. 5th Int. Conf. Solid Oxide Fuel Cells/1997*, U. Stimmung, S. C. Singhal, H. Tagawa and W. Lehert, p340, The The Electrochemical Society Proceedings Series, Pennington, NJ.
32. U. B. Pal and S. C. Singhal, *J. Electrochem. Soc.*, **137**, 2937 (1990).
33. B. P. Gorman and H. U. Anderson, *J. Am. Ceram. Soc.*, **84**, 890 (2001).
34. B. P. Gorman and H. U. Anderson, *J. Am. Ceram. Soc.*, **85**, 981 (2002).
35. H. U. Anderson, C.-C. Chen, C.-C., and M. N. Nasrallah, U.S. Pat., No. 5,494,700, (1996).
36. P. A. Lessing, *Ceram. Bulltin*, **68**, 1002 (1989).
37. Y. Jiang, A. V. Virkar and F. Zhao, *J. Electrochem. Soc.*, **148**, A1091 (2001).
38. R. van de Krol and H. L. Tuller, *Solid State Ionics*, **150**, 167 (2002).
39. S. Nakayama and M. Sakamoto, *J. Eur. Ceram. Soc.*, **18**, 1413 (1998).
40. S. P. Simner, J. F. Bonnett, N. L. Canfield, K. D. Meinhardt, V. L. Sprenkle, and J. W. Stevenson, *Electrochem. Solid State Lett.*, **5**, A173 (2002).
41. J. B. Yang, W. B. Yelon, W. J. James, Z. Chu, M. Kornecki, Y. X. Xie, X. D. Zhou, H. U. Anderson, A. G. Joshi and S. K. Malik, *Phys. Rev. B*, **66**, 184415 (2002).
42. J. B. Goodenough, *Magnetism and Chemical Bond*, Edited by F. A. Cotton (Interscience Publishers, London, 1976) Vol. 1.
43. H. Takahashi, F. Munakata, and K. Yamanaka, *Phys. Rev. B*, **57**, 15211 (1998).
44. Y. Sun, X. Xu, and Y. Zhang, *Phys. Rev. B*, **62**, 5289 (2000).
45. J. H. Kuo, H. U. Anderson and D. M. Sparlin, *J. Solid State Chem*, **83**, 52 (1989)
46. S. J. Skinner, *Inter. J. Inorg. Mater.*, **3**, 113 (2001).
47. C. W. Tanner, K. Z. Fung, and A. V. Virkar, *J. Electrochem. Soc.*, **144**, 21 (1997).
48. S. B. Adler, J. A. Lane, and B. C. H. Steele, *J. Electrochem. Soc.*, **143**, 3554 (1996).
49. A. J. McEvoy, *Solid State Ionics*, **132**, 159 (2000).
50. P. Mandal and S. Das, *Phys. Rev. B*, **56**, 15073 (1997).
51. J. R. Gebhardt, S. Roy and N. S. Ali, *J. Appl. Phys.*, **85**, 5390 (1999).
52. R. Ganguly, I. K. Gopalakrishnan and J. V. Yakhmi, *J. Phys.: Condens. Matter*, **12**, L719 (2000).

DEFECT CHEMISTRY OF MIXED IONIC/ELECTRONIC P-TYPE OXIDES

Harlan U. Anderson, Xiao-Dong Zhou, Fatih Dogan
Department of Ceramic Engineering, University of Missouri – Rolla

222McNutt Hall, Rolla, MO 65409-0330

Abstract: The p-type perovskite structure oxides are finding use in a number of energy related applications. In particular they are being used as cathodes in fuel cells as well as dense oxygen separation membranes. The defect concentration and defect mobility determine the electrical properties. Since both of these are dependent upon the operating temperature and oxygen activity, it is important to understand how an oxide equilibrates with its environment. In this paper, a defect chemistry model for the oxidation-reduction behavior of p-type perovskites is reviewed with formulations in the (La,Sr)(Cr,Mn,Co,Fe)0_3 system being used as examples.

Key words: (La,Sr)(Cr,Mn,Cr,Co)0_3 perovskite, oxidation-reduction, electrical conductivity, oxygen vacancies.

H.U. Anderson, X.D. Zhou and F. Dogan, "Defect chemistry of mixed ionic/electronic p type oxides", in "Mixed Ionic Electronic Conducting Perovskites for Advanced Energy Systems", 289-298, Edited by N.I. Orlovskaya and N. Browning, Kluwer Academic Publishers, 2004.

1. INTRODUCTION

The perovskite or pseudo-perovskite structure class of oxides is very important since many of them are utilized in electrochemical processes. The structure is basically cubic with the general formula of ABO_3 in which A, the large cation site, may be an alkali, alkaline earth, or rare earth ion, and B, the small cation site, a transition metal cation. The large cations are in 12 fold coordination with oxygen while the small cations fit into octahedral positions. Since these two sites are very different in size, the occupancy of these sites is determined primarily by ionic size rather than valency, so it is possible to substitute selectively for either the A or B ion by introducing isovalent of aliovalent cations. This gives the materials scientist an opportunity to alter the properties of a given oxide by substituting different cations onto either the A or B site. The main criteria which must be followed is the ionic radius of a substitution cation must be close (with ~15%) to a cation for which it substitutes without regard to valency.

In the early 1950's, Verwey and et al. (1) observed that when substitutions are made on to the perovskite lattice, if the valence of the substituting ion is different (ie, it is aliovalent) from that required by the site, then the charge imbalance and overall charge neutrality will be maintained by the formation of electrons, holes or charged vacancies. The compensation process creates carriers which can take part in electrical conductivity. Thus, depending upon whether the basic oxide is a p- or n- type conductor, the substitution of either acceptors or donors, can increase or decrease the carrier concentration. This is very important because it has lead to a number of devices, such as NTC resistors, PTC resistors, electrodes for electrochemical devices, etc.

When a perovskite which contains transition metal ions on the B site is heated to a sufficiently high temperature that it can equilibrate with the ambient oxygen activity, reversible changes in the oxygen content occur as the oxygen activity is varied. This behavior occurs with both p- and n-type perovskites and represents a compensation mechanism in addition to that presented by Verwey and et al. (1). This can cause the neutrality condition to change from electronic to ionic or visa versa.

Thus to completely understand the defect behavior in the perovskite oxides which contain transition metal cations, it is necessary to include the equilibration reaction with the ambient temperature and oxygen activity in addition to the influence of aliovalent effects. This occurs with all perovsites, but for the sake of brevity, in this review only acceptor doped p-type oxides will be considered with appropriate examples included.

2. DEFECT CHEMISTRY

As noted previously, the perovskite oxides can be represented by ABO_3 where the charge related to the A and B sites is +6 with the valence of the B site cation ranging from +3 to +5. In the discussion here, both the A and B sites will be +3 which covers a number of the rare earth perovskites which are important for electrical conductivity and

magnetic applications. For simplicity, the following assumptions are made: 1) the A to B site ratio is one, with the A site occupied by a trivalent rare earth and the B site is occupied by trivalent transition metal ions: Cr, Fe, Mn, Co or mixtures thereof; 2) only fully ionized oxygen vacancies are present; 3) no defect association , 4) no interstitial defects and 5) a divalent acceptor ion, I, can substitute on either the A or B site with the A to B ratio remaining unity. These assumptions can be quite restrictive, but generally nonconformity to them does not affect the general predicted behavior, for example, when defect association occurs, carrier concentration will be altered, but the overall predicted behavior still is valid.

Based on these assumptions and that p-type disorder prevails in nonstoichiometric ABO_3 allows the development of a defect chemistry model. The procedure which is used is to: 1) list the basic defect reactions which can occur: intrinsic, stoichiometric, oxygen excess and oxygen deficient; 2) write the overall neutrality relation and 3) combine the resulting equations to yield a relationship which can be solved for particular temperature and oxygen activity regimes.

The equilibria of interest [using Kröger-Vink (2) notation]:

the Schottky defect reaction;

$$nil = V_A''' + V_B''' + 3V_O^{\bullet\bullet} \qquad K_S = [V_C''']^2[V_O^{\bullet\bullet}]^3 \tag{1}$$

the intrinsic electronic defect reaction:

$$nil = e' + h^{\bullet} \qquad K_i = np = \exp(-\frac{\Delta G_i}{kT}) \tag{2}$$

the oxygen excess reaction

$$\tfrac{3}{2}O_2 = V_A''' + V_B''' + 3VO_O^x + 6h^{\bullet} \qquad K_i = [V_C''']^2 p^6 P_{O_2}^{-3/2} \tag{3}$$

the oxygen deficient reaction;

$$O_O^x = V_O^{\bullet\bullet} + 2e' + \tfrac{1}{2}O_2 \qquad K_{V_O^{\bullet\bullet}} = [V_O^{\bullet\bullet}]n^2 p^6 P_{O_2}^{1/2}. \tag{4}$$

From relations plus the relation for electroneutrality;

$$[I'] + 6[V_C'''] + n = p + 2[V_O'''] \tag{5}$$

the basis equations can be developed to give the overall behavior of the defects in ABO_3 as a function of temperature, oxygen activity and acceptor concentration. Two methods can be used to solve the resulting equations: 1) divide into regions of particular neutrality conditions and solve for that particular region or 2) do not use limiting conditions, but allow a computer to make a numerical solution to the overall equation using the total neutrality condition. In this discussion, only particular solutions will be considered. The results on the global solution are being reported elsewhere (3).

Since the details of the development of the expressions for the defect equations have been previously reported, so only the results are given here (4). Figure 1 illustrates how the defect concentrations change with oxygen activity over six regions of limited neutrality conditions. (assuming the temperature is high enough for the attainment of thermodynamic equilibrium). Table I (4) shows the predicted oxygen activity dependence for the six regions.

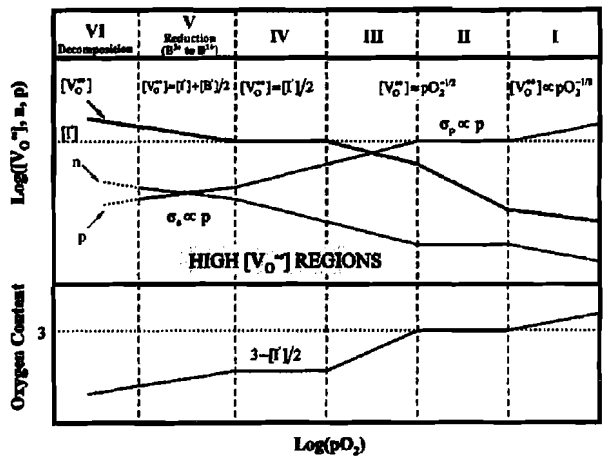

Figure 1: Defect concentration in acceptor substituted ABO_3 as function of oxygen activity at constant temperature. The B site is occupied by a transition metal ion.

Table 1. Table of constant "m" in $([V_O^{\bullet\bullet}], n, p \propto pO_2^m)$ (4)

	VI	V	IV	III	II	I
p	oxide decom-position	1/6	¼	¼	0	3/16
n		-1/6	-1/4	-1/4	0	-3/16
$[V_O^{\bullet\bullet}]$		-1/6	0	~-1/2	-1/2	-1/8
Neutrality condition		$[B_B'] = n = 2[V_O^{\bullet\bullet}]$	$2[V_O^{\bullet\bullet}] = [I_{RE}']$	$p = [I_{RE}'] - 2[V_O^{\bullet\bullet}]$	$p = [I_{RE}']$	$p = 3[V_I'''] + 3[V_B''']$
		HIGH $[V_O^{\bullet\bullet}]$ REGIONS				

During the last 20 years, the electrical conductivity and oxygen vacancy concentration for a number of transition metal containing perovskite structure oxides have been investigated in our laboratory. The following examples represent several of the systems which have been studied. The overall results show that the overall defect chemistry is well represented by the simple approach show above. Most of the exceptions result from defect association or by disproportionation reactions which are typical in Mn containing systems

3. EXAMPLES

3.1 Chromites

Examples of the rare earth chromites are contained in the studies by Flandermeyer (5) and Carini (6) who studied $La(Mg,Cr)O_3$ and $(Y,Ca)CrO_3$ respectively. Figures 2 and 3 show examples of their data which show that the simplified model fit their results quite well. In Flandermeyer's data, evidence of defect association was noted by Van Roosmalen et al. (7) who improved the fit of the experimental data to model by including association. This points out the importance of defect association, however, the simplified model described the overall behavior quite well.

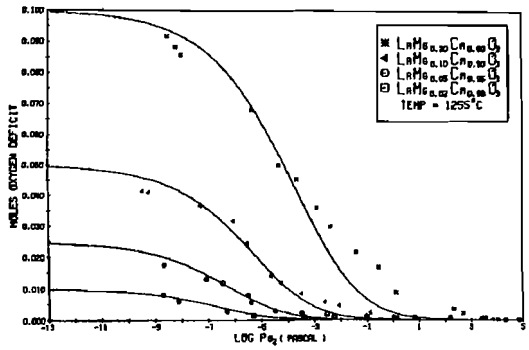

Figure 2: Moles oxygen weight loss per mole samples as a function of log PO_2 and dopant content at 1255°C. (5)

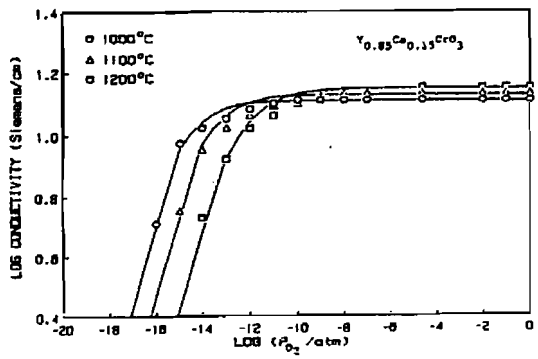

Figure 3: Log conductivity vs. Log PO_2 for $Y_{0.85}Ca_{0.15}CrO_3$ at various temperatures. The solid lines are calculated. (6)

3.2 Manganites

Figure 4 shows results for $(La_{0.8}Sr_{0.2})MnO_3$ (8) which are typical for the Mn containing perovskites. The simplified model appears to fit the experimental data quite well. However, the model predicts a constant oxygen stoichiometry of 2.9 in region IV which does not occur. In order to account for the observed behavior, both Kuo (8) and Stevenson (9) had to invoke thermally excited disproportionation of Mn^{+3} to Mn^{+4} and Mn^{+2}.

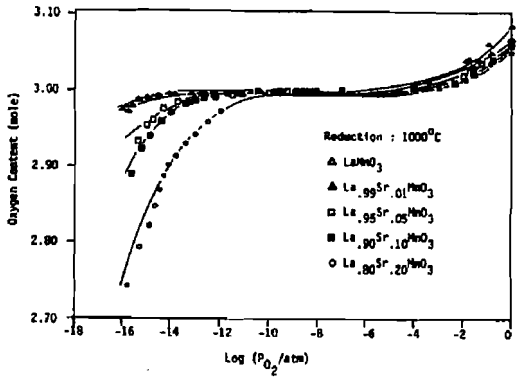

Figure 4: Moles oxygen weight loss per mole sample vs. Log PO_2 for various Sr-dopant levels. The solid lines are calculated from model. (8)

3.3 Ferrites

Compositions within the $(La,Sr)(Fe,Co)O_3$ family have been extensively studied because of their mixed electronic and ionic conductivity. Typical behavior of this system is shown in figures 5 and 6. (10) This family of compositions also follows the simplified model quite well, but as was the case of the manganites, region IV was not observed. This is probably due to continuous reduction of the cations on the B site. It is interesting to note that for most of the compositions, dissociation does not occur until the oxygen stoichiometry reaches the 2.4-2.7 range. This suggests that for the 40% Sr composition, oxygen vacancy content as high as 20% can be expected. This is the reason that high oxygen ion conductivity is observed.

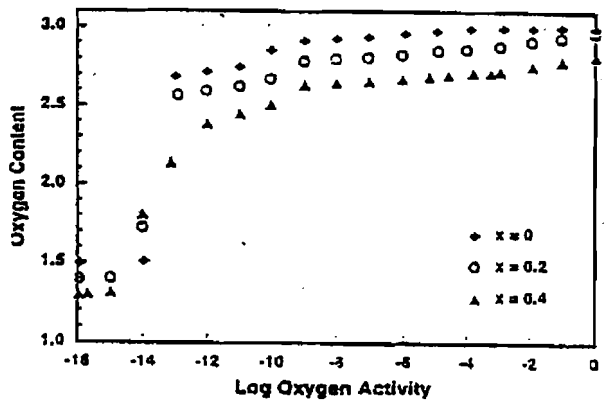

Figure 5: Oxygen content (moles) of $La_{1-x}Sr_xCo_{0.2}Fe_{0.8}O_{3-\delta}$ as a function of oxygen activity and Sr content (moles) at 1200°C. (10)

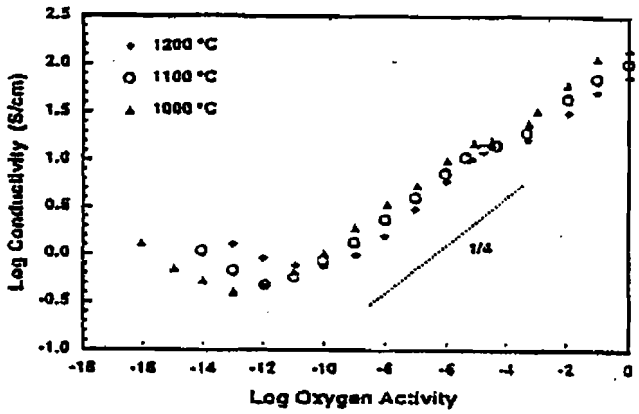

Figure 6: Electrical conductivity of $La_{0.6}Sr_{0.4}Co_{0.2}Fe_{0.8}O_3$ as a function of oxygen activity equilibrated at different temperatures. (10)

4. CONCLUSIONS

a. A defect chemistry model for the oxidation-reduction behavior of p-type perovskite oxides which uses simplified neutrality conditions was developed.
b. The model explains the electrical conductivity of the chromites.
c. In order to explain the behavior of Mn containg perovskites, both site percolation and thermally activated disportionation of $2Mn^{+3} \rightarrow Mn^{+2} + Mn^{+4}$ must be added to the model.
d. The $(La,Sr)(Co,Fe)O_3$ system follows the model and becomes very oxygen nonstoichiometric (10-30%) prior to dissociation.

ACKNOWLEDGEMENTS

The authors wish to thank the Department of Energy and the Gas Research Institute who provided financial support for part of this research.

REFERENCES

1. E. J. W. Verwey, P. W Haaijam, F. C. Romeijh, and G. W.Van Oosterhout, Philips Res. Report 5 173-187 (1950)
2. F. A. Kroger and H. J. Vink, In: Solid State Physics. Eds. By F. Seitz and D. Turnbull, Vol. 3, (Academic Press, New York) , (1965) p 307
3. X-D Zhou and H. U. Anderson, manuscript in preparation
4. H. U. Anderson, Proceedings of the 14th Riso Inter. Symp. On Mater. Sci: High Temp. Electrochm. Behavior of Fast Ion and Mixed Conductors. "Defect Chemistry of p-Type perovskites," eds: F. W. Poulsen, J. J. Bentzen, T. Jacobsen, E. Skou and M. J. L. Ostergard, 1-188, 1993

5. B. K. Flandermeyer, M. M. Nasrallah, A. K. Agarwal and H. U. Anderson, J. Amer. Ceramic Soc. 67, 195-298 (1984)
6. G. F. Carini, H. U. Anderson, D. M. Sparlin, M. M. Nasrallah, Solid State Ionics 49, 233-243, (1991)
7. J. A. M. Roosmalen, J. P. P. Huiusmans, and E. H. P. Cordfunke, J. Solid State Chem. 93, 212-219, (1991)
8. J. H. Kuo, H. U. Anderson, D. M. Sparlin, J. Solid State Chem. 87, 55-63 (1990)
9. J. W. Stevenson, M. M. Nasrallah, H. U. Anderson, and D. M. Sparlin, J Solid State Chem 102, 175-184, (1993)
10. H. U. Anderson, L-W Tai, C. C. Chen, M. M. Nasrallah and W. Huebner, In: Proc. Of the 4th Int'l Symp. On Solid Oxide Fuel Cells, ed S. Singhal, The Electrochemical Society (1994)